

**PERFORMANCE ASSESSMENT AND DESIGN
OPTIMIZATION OF LINEAR SYNCHRONOUS MOTORS
FOR MANUFACTURING APPLICATIONS**

A Thesis
Presented to
The Academic Faculty

by

Nattapon Chayopitak

In Partial Fulfillment
of the Requirements for the Degree
Doctor of Philosophy in the
School of Electrical and Computer Engineering

Georgia Institute of Technology
August 2007

**PERFORMANCE ASSESSMENT AND DESIGN
OPTIMIZATION OF LINEAR SYNCHRONOUS MOTORS
FOR MANUFACTURING APPLICATIONS**

Approved by:

Dr. David G. Taylor, Advisor
School of Electrical and Computer
Engineering
Georgia Institute of Technology

Dr. Andrew F. Peterson
School of Electrical and Computer
Engineering
Georgia Institute of Technology

Dr. Ronald G. Harley
School of Electrical and Computer
Engineering
Georgia Institute of Technology

Dr. Wayne J. Book
School of Mechanical Engineering
Georgia Institute of Technology

Dr. Magnus Egerstedt
School of Electrical and Computer
Engineering
Georgia Institute of Technology

Date Approved: July 3, 2007

ACKNOWLEDGEMENTS

First and foremost I would like to express my deepest appreciation to my advisor, Professor David G. Taylor, for his time, patience and guidance throughout my research endeavor. I am forever grateful for his encyclopedic knowledge, insightful suggestions and invaluable experience during many long hours of discussions. I cannot say thank you enough for his honest and continuing support.

I also would like to thank Professor Harley, Professor Egerstedt, Professor Peterson and Professor Book for their time and patience serving on my thesis committee, and making this thesis possible.

My special gratitude must go to Xianghui Huang, a very first friend I met at Georgia Tech for his true friendship and supports. Thanks to my labmate Raga Ahmed and Matt Horman for their several helps whenever needed and constant words of encouragement. A special thanks also goes to Taweessup Apiwattanapong, Krit Athikulwongse and Vichai Meemongkolkiat, among many other wonderful people I have known during my time in Atlanta, for their helps and friendships.

This thesis work would not have been possible without the financial support from my sponsor, the Ministry of Science and Technology, Government of Thailand. I would like to express my sincere appreciation for receiving the opportunity to study in the United States.

Finally, I am always indebted to my family for their endless support, encouragement and love.

TABLE OF CONTENTS

ACKNOWLEDGEMENTS	iii
LIST OF TABLES	viii
LIST OF FIGURES	ix
SUMMARY	xv
1 INTRODUCTION	1
1.1 Temperature Rise	2
1.2 Linear Motor Technologies	3
1.3 Research Objectives and Literature Review	5
1.3.1 Magnetic Modeling	7
1.3.2 Optimal Performance Assessment	7
1.3.3 Multi-Objective Design Optimization	8
1.4 Thesis Outline	11
1.5 Contributions	12
2 OPTIMAL CONTROL AND OPTIMAL COMMUTATION	14
2.1 Introduction	14
2.2 Idealized Models of Linear Synchronous Motors	15
2.2.1 Dynamic Model	16
2.2.2 Reference Frame Transformation	17
2.3 System Description	18
2.3.1 Point-To-Point Positioning	18
2.3.2 Current Limits	20
2.3.3 Wiring Connections	21
2.3.4 Current Constraint Sets	21
2.4 Optimal Control Problem	24
2.4.1 Minimum Time Control	24
2.4.2 Minimum Copper Loss Control	24

2.5	Analytical Solutions	25
2.5.1	Time-Optimal Control with Spherical Current Limit	25
2.5.2	Minimum Copper Loss Control with Spherical Current Limit	28
2.6	Numerical Solutions	34
2.6.1	Numerical Method	34
2.6.2	Numerical Results	42
2.7	Optimal Commutation Problem	54
2.7.1	Maximum Force Control	55
2.7.2	Minimum-Copper-Loss Force Control without Current Limit	58
2.7.3	Minimum-Copper-Loss Force Control with Current Limits	66
2.7.4	Spatial Average Power Dissipation	67
2.8	Conclusion	72
3	MAGNETIC MODELING	77
3.1	Modeling of Linear Permanent-Magnet Motor	77
3.1.1	Poisson Equation	79
3.1.2	PM Field Calculation	80
3.1.3	Lorentz Force	82
3.1.4	Model Validation	84
3.2	Modeling of Linear Variable Reluctance Motor	85
3.2.1	Steel Permeances	88
3.2.2	Air Permeances and Coils	92
3.2.3	Magnetic Circuit Analysis	95
3.2.4	Model Validation	99
3.3	Conclusion	100
4	OPTIMAL PERFORMANCE ASSESSMENT	101
4.1	Introduction	101
4.2	Performance Assessment of LPM Motors	102
4.2.1	Maximum Force Limit	103

	4.2.2	Spatial Average Power Dissipation	105
	4.2.3	Productivity Trade-Off Curve	110
	4.3	Performance Assessment of LVR Motors	112
	4.3.1	Maximum Force Limit	116
	4.3.2	Spatial Average Power Dissipation	119
	4.3.3	Productivity Trade-Off Curve	121
	4.4	Conclusion	124
5		MULTI-OBJECTIVE DESIGN OPTIMIZATION	128
	5.1	Introduction	128
	5.2	General Problem Statement	129
	5.3	Motor Design System	131
	5.3.1	Synthesis	131
	5.3.2	Analysis	133
	5.3.3	Optimization	133
	5.4	Linear Permanent-Magnet Motor Design	135
	5.4.1	Problem Statement	137
	5.4.2	Design Synthesis	139
	5.4.3	Design Analysis and Optimization	140
	5.4.4	LPM Motor Design Results	142
	5.5	Linear Variable Reluctance Motor Design	150
	5.5.1	Problem Statement	151
	5.5.2	Design Synthesis	153
	5.5.3	Design Analysis and Optimization	154
	5.5.4	LVR Motor Design Results	156
	5.6	Conclusion	158
6		CONCLUSIONS	162
	6.1	Summary of Contributions	162
	6.2	Future Research	165

APPENDIX A	AIR PERMEANCE MODEL	168
APPENDIX B	DESIGN RELATED DERIVATIONS	170
APPENDIX C	THERMAL ANALYSIS OF A LPM MOTOR	184
APPENDIX D	THERMAL ANALYSIS OF A LVR MOTOR	204
REFERENCES	227
VITA	234

LIST OF TABLES

1	Methodology Used to Solved Optimal Control Problems	26
2	Spherical Current Limit with 3- and 6-Wire Connections	43
3	Cubical Current Limit with 3-Wire Connection	47
4	Cubical Current Limit with 6-Wire Connection	47
5	Time-Optimal Control	54
6	Maximum Force Control with Spherical and Cubical Current Limits .	59
7	LPM Motor Parameters	86
8	LVR Motor Parameters	99
9	Dominant Design Parameter Distribution of the LPM Motors	143
10	Selected Dominant Designs of the LPM Motors from the F_s - m Plane	144
11	Dominant Design parameter distribution of the LVR motors	157
12	Selected Dominant Designs of the LVR Motors from the F_s - m Plane .	158
13	Material Density Properties	172
14	Material Thermal Properties	192
15	LPM Motor Parameters	193
16	Boundary Conditions for Steady-State Heat Conduction	200
17	Comparative Thermal Analysis Results, Temperature (K)	202
18	Material Properties	212
19	Motor Parameters	212
20	Boundary Conditions for Steady-State Finite Element Analysis	220
21	Comparative Thermal Analysis Results, Temperature (K)	223
22	Area Averaged and Maximum Temperature (K) from FEA	224

LIST OF FIGURES

1	A classification of linear electric motors.	4
2	Variation of linear synchronous motors with concentrated windings. .	6
3	Cubical current limit set rotating at 0° , 30° and 60° about the u_0 -axis for $U = 1$ A.	22
4	Cubical current limit set in dq -plane at different values of u_0 for $U = 1$ A.	23
5	Minimum travel time for desired travel distance plots of time-optimal and average-power-specified time-optimal results using spherical current limit and 3-wire connection for PM and VR synchronous motors.	35
6	The trajectories of u_q and u_d for $X = 0.05$ m for PM motor using spherical current limit and 3-wire connection.	36
7	The trajectories of u_q and u_d for $X = 0.05$ m for VR motor using spherical current limit and 3-wire connection.	37
8	The trajectories of $f(u_q, u_d)$ for $X = 0.05$ m for PM motor using spherical current limit and 3-wire connection.	38
9	The trajectories of $f(u_q, u_d)$ for $X = 0.05$ m for VR motor using spherical current limit and 3-wire connection.	39
10	Optimal trajectories for $X = 0.05$ m for PM and VR synchronous motors using spherical current limit and 3-wire connection.	40
11	Position, velocity, force and currents for PM motor using spherical current limit with 3-wire or 6-wire connections.	44
12	Position, velocity, force and currents for hybrid motor using spherical current limit with 3-wire or 6-wire connections.	45
13	Position, velocity, force and currents for VR motor using spherical current limit with 3-wire or 6-wire connections.	46
14	Position, velocity, force and currents for PM motor using cubical current limit with 3-wire connection.	48
15	Position, velocity, force and currents for hybrid motor using cubical current limit with 3-wire connection.	49
16	Position, velocity, force and currents for VR motor using cubical current limit with 3-wire connection.	50
17	Position, velocity, force and currents for PM motor using cubical current limit with 6-wire connection.	51

18	Position, velocity, force and currents for hybrid motor using cubical current limit with 6-wire connection.	52
19	Position, velocity, force and currents for VR motor using cubical current limit with 6-wire connection.	53
20	Force maximizing currents and resulting force of the PM motor for 3-wire and 6-wire connection with spherical current limit.	57
21	Force maximizing currents and resulting force of the hybrid motor for 3-wire and 6-wire connection with spherical current limit.	57
22	Force maximizing currents and resulting force of the VR motor for 3-wire and 6-wire connection with spherical current limit.	58
23	Force maximizing currents and resulting force of the PM motor for 3-wire connection with cubical current limit.	59
24	Force maximizing currents and resulting force of the hybrid motor for 3-wire connection with cubical current limit.	60
25	Force maximizing currents and resulting force of the VR motor for 3-wire connection with cubical current limit.	61
26	Force maximizing currents and resulting force of the PM motor for 6-wire connection with cubical current limit.	62
27	Force maximizing currents and resulting force of the hybrid motor for 6-wire connection with cubical current limit.	63
28	Force maximizing currents and resulting force of the VR motor for 6-wire connection with cubical current limit.	64
29	Currents for $f_d = 0.95F_s$ for 3-wire connection for three synchronous motors with cubical current limit.	68
30	Currents for $f_d = 0.95F_s$ for 3-wire connection for three synchronous motors with cubical current limit.	69
31	Currents for $f_d = 0.95F_s$ for 6-wire connection for three synchronous motors with cubical current limit	70
32	Spatial average power dissipation versus desired force command for PM and VR motor with 3/6-wire connection and spherical current limit.	73
33	Spatial average power dissipation versus desired force command for PM and VR motor with 3-wire connection and cubical current limit. .	74
34	Spatial average power dissipation versus desired force command for PM and VR motor with 6-wire connection and cubical current limit. .	75
35	Air-core LPM motor with concentrated windings.	78

36	Schematic diagrams used to derive force model of the LPM motor.	81
37	Force versus position for the LPM motor.	85
38	LVR motor with magnetically coupled phases.	87
39	Steel region with one-dimensional flux flow.	89
40	First-quadrant plot of the odd-symmetric nonlinear magnetization curve characterizing M19 steel.	89
41	Geometry of translator pole teeth and stator bar teeth in unaligned configuration.	91
42	Cross-section areas for toothed regions over half spatial period.	91
43	Flux tube geometries over one tooth pitch for three different orientations.	93
44	Interconnections between tooth permeances with single air gap permeance.	93
45	Interconnections between tooth permeances and separated air gap permeances.	93
46	Magnetic circuit topology representing one-half of the LVR motor.	96
47	Force versus position for the LVR motor.	100
48	Force maximizing currents and resulting force of the LPM motor for $U = 5$ A.	105
49	Force maximizing currents and resulting force of the LPM motor for $U = 2, 4, 6, 8$ A.	106
50	Spatial average power P_x for various values of force command f_d of the LPM motor.	110
51	Two-stage algorithm for determining the trade-off curve $T(X, P)$ using the proposed numerical method.	113
52	Trade-off between P and T for $X = 100$ mm.	113
53	Optimal performance function $T(X, P)$ of the LPM motor.	114
54	The current trajectories of the LPM motor for $X = 100$ mm.	114
55	Force trajectories of the LPM motor for $X = 100$ mm.	115
56	Motion trajectories of the LPM motor for $X = 100$ mm.	115
57	Force maximizing currents and resulting force of the LVR motor for $U = 5$ A, resulting in $F_s = 41.86$ N and $F_a = 134.87$ N.	117

58	Force maximizing currents and resulting force of the LVR motor for $U = 2, 4, 6, 8$ A.	118
59	Minimizing copper-loss currents for $f_d = 0.95F_s = 39.76$ N of the LVR motor.	121
60	Spatial average power P_x for various values of f_d of the LVR motor.	122
61	Optimal trajectories of the ideal VR synchronous motor for $X = 0.05$ m.	123
62	Plot of the time-optimal control trajectory for $X = 0.1$ m of the LVR motor using the maximum force control results at various average power dissipation values.	125
63	The trajectories of position, velocity and force for $X = 0.1$ m of the time-optimal control results for the LVR motor.	125
64	The current trajectories for $X = 0.1$ m of the time-optimal control results for the LVR motor.	126
65	Plot of the time-optimal control trajectories for $X = 0.1$ m and 0.2 m of the LVR motor using the maximum force control results.	126
66	Approximate trade-off curve between minimum travel time and desired travel distance of the LVR motor.	127
67	The proposed computer-aided design structure.	132
68	A trade-off curve between two objective functions.	134
69	Diagram of design parameters for a LPM motor.	136
70	The dominant designs of LPM motors with respect to smooth force and moving mass.	145
71	The dominant designs of LPM motors with respect to average force and moving mass.	146
72	The dominant designs of LPM motors with respect to smooth force and magnet volume per meter.	147
73	The dominant designs of LPM motors with respect to average force and magnet volume per meters.	148
74	The dominant designs of LPM motors with respect to average power loss coefficient and moving mass.	149
75	Diagram of design parameters for a LVR motor.	150
76	The dominant designs of LVR motors with respect to smooth force and moving mass.	159

77	The dominant designs of LVR motors with respect to average force and moving mass.	160
78	The dominant designs of LVR motors with respect to average power slope and moving mass.	161
79	Assumed flux paths between toothed poles at different displacement position.	169
80	Motor diagrams with geometry variables defined.	171
81	Effective circumferential length and winding cross section for winding resistance caculation.	173
82	Diagrams for calculating self inductance of the LPM motor.	173
83	LPM motor with concentrated windings.	185
84	Homogeneous material block and its thermal resistive representation.	187
85	Winding structure and its simplified model.	188
86	Homogeneous layer of winding material model.	188
87	Convective heat transfer surfaces for the steady-state heat transfer analysis for TRM and FEA.	190
88	The thermal resistance model of the LPM motor for steady-state heat transfer analysis.	191
89	Periodic motion trajectory commands.	194
90	Periodic current commands, with rms currents superimposed.	195
91	Derivation of the single-node thermal resistance model of the LPM motor.	198
92	3D FEA solution on slice located at the center of the coil assembly.	201
93	3D FEA solution on the boundary surfaces.	201
94	LVR motor (upper half only).	205
95	Homogeneous block and equivalent thermal resistance.	206
96	Winding structure and its simplified model.	207
97	Homogeneous layer of winding material.	208
98	Airflow over the simplified LVR motor structure.	209
99	Airflow over a flat surface and a noncircular cylinder.	209
100	Teeth of the LVR motor having a fin-like structure.	210

101	Thermal resistance model of the LVR motor for steady-state heat transfer analysis.	211
102	Motion profile using an s-curve.	215
103	Dynamic response during one operating period of 0.8 s, with rms velocity and rms currents superimposed.	216
104	Derivation of the single-node thermal resistance model of the LVR motor.	218
105	Boundary conditions for solving the steady-state incompressible flow Navier-Stokes equations.	221
106	Boundary conditions for solving the steady-state heat transfer equation.	221
107	FEA solution of computational fluid dynamics and heat transfer for the LVR motor.	222
108	Temperature profile of the LVR motor from thermal network model and FEA results for $y = 0.02275$ m.	225
109	Temperature profile of the LVR motor from thermal network model and FEA results for $x = 0.0575$ m.	226

SUMMARY

The major contributions of this thesis are categorized into three areas: (i) magnetic modeling, (ii) optimal performance assessment and (iii) multi-objective design methodology of the linear permanent-magnet (LPM) and linear variable reluctance (LVR) motors for manufacturing automation applications. The target application is to perform repetitive point-to-point positioning tasks on a continuous basis under temperature constraints. Through simplification, the constraint on temperature rise may be replaced by a constraint on average power dissipation, provided that the thermal resistance is constant and known.

The basic framework of analysis is first introduced for a class of idealized linear synchronous (LS) motors, where magnetic saturation and spatial harmonics are neglected, to provide clarity and insight. The physics-based force models for the LPM and LVR motors, including spatial harmonics and magnetic saturation as appropriate, are then developed. Due to magnetic linearity, the force model of the LPM motor is derived from the analytical solution of the Poisson Equation. A nonlinear magnetic circuit analysis model is developed for the LVR motor that includes both spatial harmonics and magnetic saturation. The accuracy of both force models are verified by finite element analysis.

Applying those force models, the optimal performance assessment of the LPM and LVR motors is explored using the mathematical framework discussed for the idealized LS motors. In particular, the relationship between travel time and travel distance is characterized in terms of average power dissipation. The performance assessment methodologies developed here may be applied to any motor technology

used in manufacturing automation applications.

The multi-objective design optimization problem is then defined and software for its solution is developed using Monte-Carlo synthesis, the performance assessment tools and dominance-based sorting. Design results for the LPM and LVR motors are then presented. Future research is discussed as the conclusion of the thesis.

CHAPTER 1

INTRODUCTION

Linear motors are strong candidates for manufacturing automation applications requiring high-performance direct-drive linear position control. Unlike rotary motor drive systems, linear motor drive systems do not require rotary-to-linear transmissions, such as belt or screw; hence they usually provide higher performance [1, 2].

The motivating application for this research arises in the context of manufacturing machines that must perform point-to-point positioning tasks on a continuous basis. In particular, the performance of linear motors in periodic single-axis positioning tasks is often limited by thermal considerations [3]. Regardless of the type of electric motor being used, productivity is increased by reducing travel times, but this requires larger forces, larger current flows, greater heat production, and hence higher coil temperatures. Since coil temperatures must be limited to ensure the integrity of the coil insulation materials and to avoid structural damage, there is a limit to how fast the positioning tasks can be performed. Elaborate cooling systems are typically undesirable since they would add mass and complexity to moving bodies.

Therefore, it is a well-motivated goal to attempt to optimize the achievable (thermally limited) cycle time for periodic motions by a combination of motor design and control design, with an emphasis on magnetic characteristics, excitation waveforms, motion profiles and temperature constraint, so as to reduce the need for (or demands on) a cooling system.

1.1 Temperature Rise

In general, detailed thermal analysis requires accurate evaluation of losses and the solution of partial differential equations (the Heat Equation coupled with Navier-Stokes Equations). However, for purposes of introducing the relationship between losses and temperature rise in repetitive motion applications, a motor may be regarded as a homogeneous body exhibiting a capacity for thermal energy storage and cooled by convection [4]. The mean surface temperature ϑ is governed by the power balance

$$C_p M_t \dot{\vartheta} + C_h A_t \tilde{\vartheta} = p, \quad \tilde{\vartheta} = \vartheta - \vartheta_0 \quad (1)$$

where p is the power dissipation sourcing heat flow, ϑ_0 is the ambient temperature, M_t and C_p are the mass and specific heat of the material experiencing heat flow, A_t is the surface area normal to the direction of heat flow, and C_h is the coefficient of heat transfer which depends on relative air-flow velocity. The average power dissipation $P_{[0,\infty)}$ defined by

$$P_{[0,\infty)} = \lim_{\tau \rightarrow \infty} \frac{1}{\tau} \int_0^\tau p \, dt \quad (2)$$

determines the steady-state temperature Θ according to

$$\Theta = \lim_{t \rightarrow \infty} \vartheta = \vartheta_0 + \frac{1}{C_h A_t} P_{[0,\infty)} \quad (3)$$

Suppose the thermal resistance $1/C_h A_t$ is essentially constant as would be the case with strong fan-based cooling. Then, according to (3), a constraint on Θ is essentially equivalent to a constraint on $P_{[0,\infty)}$.

Suppose that the time interval $[0, \infty)$ is partitioned by time instants $T_i > T_{i-1}$ for $i \geq 1$ with $T_0 = 0$. The average power dissipation on the i th partition is

$$P_{[T_{i-1}, T_i]} = \frac{1}{T_i - T_{i-1}} \int_{T_{i-1}}^{T_i} p \, dt \quad (4)$$

and, consequently, $P_{[0,\infty)}$ may be expressed in the form

$$P_{[0,\infty)} = \lim_{N \rightarrow \infty} \frac{\sum_{i=1}^N (T_i - T_{i-1}) P_{[T_{i-1}, T_i]}}{T_N - T_0} \quad (5)$$

from which it follows that

$$P_{[T_{i-1}, T_i]} = P, \forall i \geq 1 \Rightarrow P_{[0, \infty)} = P \quad (6)$$

In other words, if a motor performs an infinite sequence of tasks and the average power dissipation associated with each task is identical and equal to P , then the choice $P = C_h A_t (\Theta - \vartheta_0)$ will guarantee that $\lim_{t \rightarrow \infty} \vartheta = \Theta$.

This analysis has established the relationship between average power dissipation and temperature rise for repetitive motion systems, under the simplifying assumption that thermal resistance is constant and known. As a result, the constraint on temperature rise may be substituted by a constraint on average power dissipation to reduce complexity.

1.2 *Linear Motor Technologies*

The available linear motor technologies can be classified in similar fashion as their rotary counterparts, as shown in Figure 1. The linear motor technologies chosen for this research are linear synchronous (LS) motors with concentrated windings. Before proceeding with the discussion further, a few terms should be defined. The motor part that contains windings with current flow to create electromagnetic flux is called *active*, whereas the other motor part across the air gap is called *passive* (wound-field motors are not considered). The moving part (active or passive) is called the *translator* and the stationary part (active or passive) is called the *stator*. Linear motor technologies with brushes (DC motors) or any mechanical contacts such as slip rings generally are not suitable for repetitious manufacturing automation applications because of the wear and tear that require regular maintenance or replacement of the brushes. Furthermore, linear induction motors use currents on both sides of the air gap, which adds another source of undesired heating. Therefore, the brushless LS motor technology with passive stator is more suitable and is chosen for this target application.

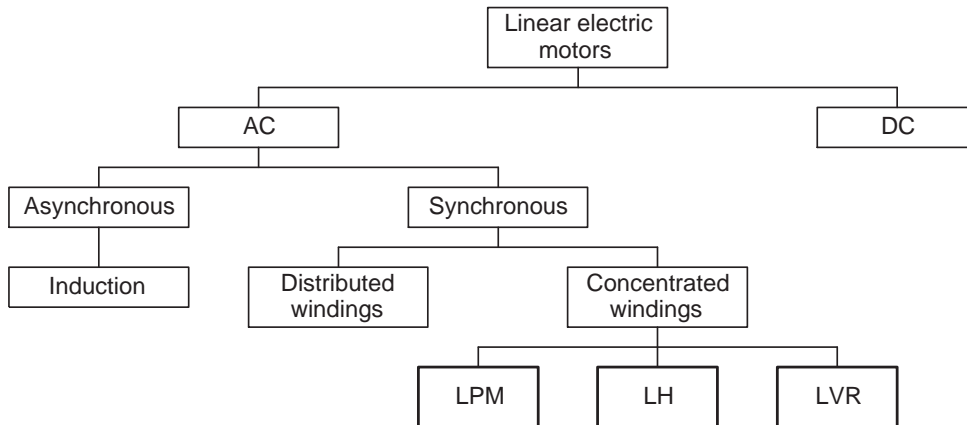


Figure 1: A classification of linear electric motors.

Excluding hysteresis and wound-field synchronous motors, the brushless LS motors (and their rotary counterparts) can be divided into two major categories according to the construction of the passive side and resulting force production mechanism [2]:

- Permanent magnet (PM) material to produce PM alignment force
- Ferromagnetic material with saliency to produce reluctance force

LS motors can be designed to use either mechanism or a combination of the two to produce the total force. Well-known LS motors in the literature that use only PM on the passive side are brushless DC motors and sinewave PM motors [5, 6]. LS motors that only generate reluctance force are known as variable reluctance (VR) motors, synchronous reluctance motors or switched reluctance motors [7]. Several LS motors are designed to produce significant magnitudes of both PM alignment and reluctance forces, for instance Sawyer motors [2, 8], interior PM (IPM) motors [9, 10] and hybrid PM stepping motors [2, 11]. The LS motors in this document are categorized according to their force production mechanism and referred to as LPM, LVR and LH motors for linear permanent magnet, linear variable reluctance and linear hybrid motors, respectively. A diagram of representative configurations of these LS motors with active translators considered in this research is shown in Figure 2. Note that

the reverse designs (active stators) of these LS motors are also possible. Traditionally, VR machines have used concentrated windings whereas PM machines have used distributed windings. However, recent studies show that motors with concentrated windings produce lower heat loss and have the advantages of modularity and reduced construction cost [12, 13, 14]. As a result, two variations of LS motor technology with concentrated windings, namely LPM and LVR motors, are emphasized in this study to limit the scope of the research.

1.3 Research Objectives and Literature Review

Since electric motor design is a multi-objective optimization problem, the primary goal of this research is to develop a computer-based design tool for the design optimization of three-phase LPM and LVR motors for repetitive point-to-point positioning applications under an average power dissipation constraint. This goal gives rise to the following requirements:

- Magnetic modeling of LPM and LVR motors
- Optimal performance assessment of LPM and LVR motors as a basis for comparison between candidate designs
- Multi-objective design optimization methodology

Although a variety of techniques have been reported in the literature to address some of these issues, no research has been conducted to address all aspects in the context of maximizing productivity for manufacturing applications. Note that a recent research area called integrated design optimization [15, 16, 17] refers to a methodology where plant and control system are fully coupled and simultaneously optimized during the design process. In this research, the control system is used only to assess the performance of the plant (the motor).

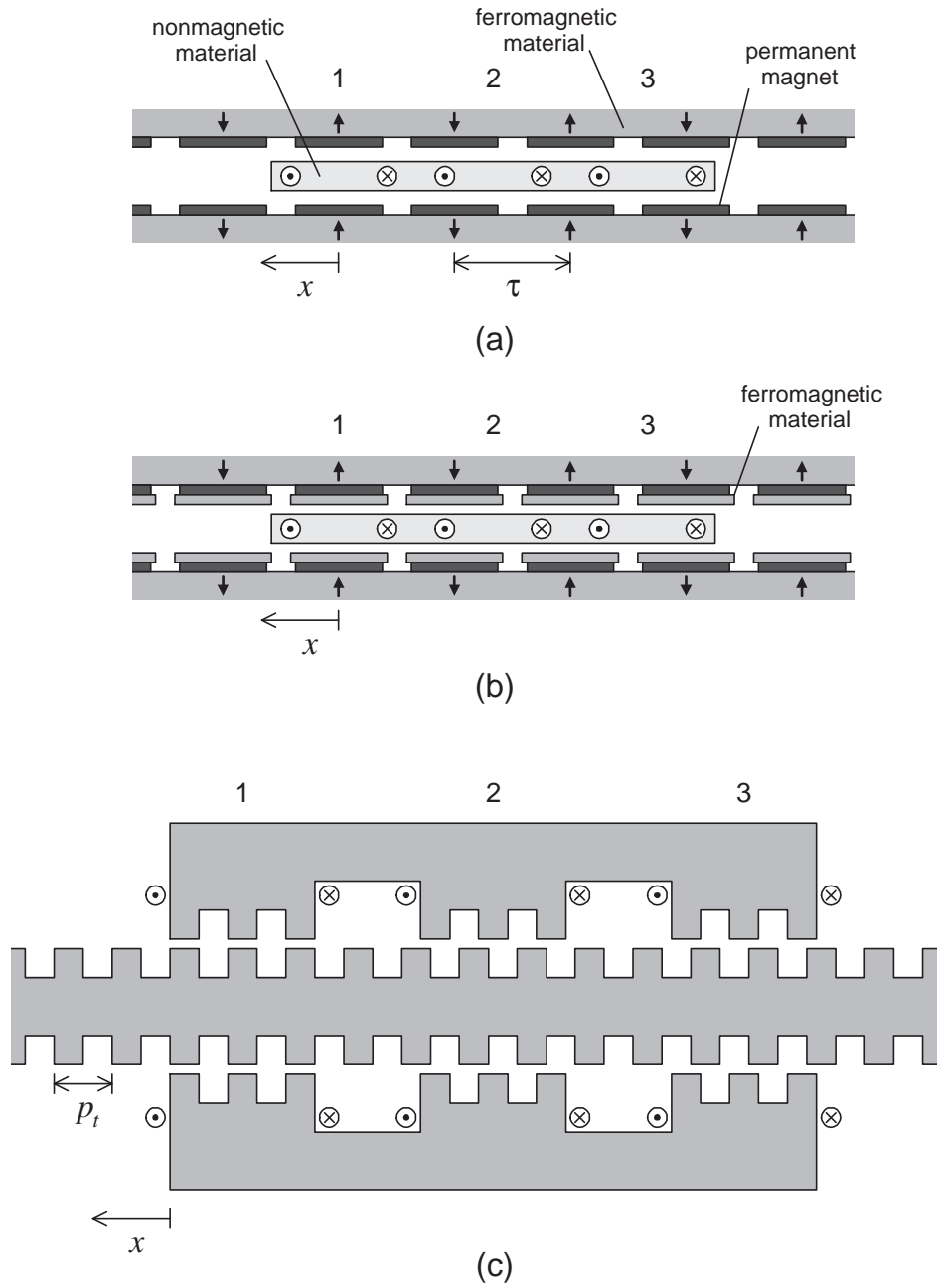


Figure 2: Variation of linear synchronous motors with concentrated windings: (a) LPM motor, (b) LH motor and (c) LVR motor.

1.3.1 Magnetic Modeling

In order to pursue the solution to the motor design problem, all relevant phenomena must be mathematically modeled. Magnetic modeling of electric motors may be based on the analytical solution or numerical solution to the Maxwell Equations. When an accurate analytical solution is too complex to derive, a numerical method is usually employed. Two widely used numerical tools are the very accurate but computationally expensive finite element analysis (FEA) [18, 19] and the less accurate, but computationally efficient magnetic circuit analysis (MCA) [20]. MCA has been a popular method for modeling various types of motors with saturating material, such as rotary PM motors [21, 22] and rotary VR motors [23, 24]. A model of the LPM motor using the analytical solution of the Poisson Equation is reported in [25] and will be adopted in this research. The model of the LVR motor using MCA was first reported in [26] where spatial harmonics and magnetic material saturation are neglected. The comparative studies of the LVR motor using MCA and FEA were then presented in [27], but only spatial harmonics and ideal magnetic material with low current excitation levels are considered in that work. An FEA model of the same motor was later reported in [28] that includes high current excitation levels and saturable magnetic material; however, simultaneous multi-phase excitation is not studied.

1.3.2 Optimal Performance Assessment

Optimization is required to assess the optimal performance of different candidate motor designs. The target application of point-to-point position control under average power dissipation constraints is somewhat related to time-optimal control problems [29, 30]. Although the subject of time-optimal control has a long history, the problem of maximizing the productivity of motors under average power dissipation constraints has not been widely investigated.

A representative approach to minimum-time position control design in single-axis systems is described in [31]. This work considers a rigid load driven by an idealized PM synchronous motor, and the goal is to design a time-optimal control for point-to-point positioning that considers the combined motor/load dynamics and magnitude constraints on the motor's voltages and currents and on the maximum allowable jerk. However, this recent work completely ignores the role of temperature rise as a limitation in positioning applications.

Less closely related works in rigid-link robots performing repetitive tasks with average power dissipation constraints are found in [32, 33] for the multi-axis case with permanent-magnet brush-commutated dc motors, and in [34] for the multi-axis case with separately-excited brush-commutated dc motors. These works focus on a different class of motors and the suggested numerical techniques are not suitable for nonlinear devices like VR motors.

Another topic related to the optimal performance of motors is optimal commutation where system dynamics is neglected. This subject focuses on the optimal design of excitation currents with or without a constraint set. Two optimal commutation problems, maximum force control and minimum-copper-loss force control, are studied in [35] for the LPM motor with cubical current limit and 3/6-wire connections. The fundamental idea of this work will be investigated and applied for motor performance assessment in this research.

1.3.3 Multi-Objective Design Optimization

The proposed motor design problem is distinctly different from traditional design concepts as outlined in [36, 6, 7, 11], specifically in regard to the positioning time goal and average power dissipation constraint. In fact, the traditional design approach involves the use of expert knowledge or past experience, intuition and skills of the designers themselves. To assist with the computational burden, computer-aided design

(CAD) tools are usually employed. Traditional CAD tools [37, 38, 39, 40] make use of specialized computing software to simplify the task of predicting the performance of a given design candidate. Although users of such software benefit from a convenient interface and powerful simulation capabilities, they must still choose the design parameters themselves. In addition, the use of expert knowledge can potentially limit design creativity, and may lead to sub-optimal results.

Much less common is software that automates the selection or refinement of machine design parameters through the use of optimization techniques, namely single-objective [41] or multi-objective [42] optimization. Single-objective optimization relies on the notion that optimal designs are those that minimize some scalar objective function. A limitation of that notion of optimality is the need to handle multiple design objectives in heuristic fashion, such as pre-specifying appropriate weighting factors to balance those objectives. After all, this method yields just one design solution that closely depends on the non-obvious choice of those weighting factors.

Since electric motor design involves several design objectives, the multi-objective optimization technique is naturally more suitable. The advantages of this approach are that (i) design synthesis does not rely on expert design rules or past experience that can limit design creativity and may lead to sub-optimal results; and (ii) optimization provides many candidate designs along with important trade-off information between different objective functions for comparison.

The overall design strategy based on multi-objective optimization involves the repeated use of a three-step procedure of synthesis, analysis and optimization, summarized as follows.

Synthesis

Synthesis of designs can be achieved using stochastic search methods [42, 44] such as Monte-Carlo (MC), genetic algorithm (GA) or particle swarms (PS). All of the

stochastic search methods have the advantage that they generally cover the entire space of design parameters and therefore do not get stuck at local extrema.

MC synthesis is essentially an unguided random synthesis with design parameters determined from a range of possible values using a uniform probability distribution. Examples of motor design results based on MC synthesis include [45, 46] for induction motors and [47, 48] for VR generators.

GA and PS are population-based synthesis methods in which guided random synthesis occurs according to principles inspired by nature. Both GA and PS are capable of generating results faster than MC, but their implementations are also more complex. Examples of motor design results based on GA synthesis include [49, 50, 51] for PM motors and [52, 53, 54] for VR motors. Although [51] studies the same LPM motor topology considered in this thesis, a different set of objectives, which is not directly related to manufacturing applications, is being optimized in that work. A design result based on PS synthesis is reported in [55] for transverse flux PM motor.

Analysis

Analysis of a candidate design is just the evaluation of performance objectives using mathematical models. As pointed out earlier, a primary design goal is to maximize productivity; hence optimal performance assessment must be implemented at this stage to determine all objective functions of each candidate design. Note that an individual objective function may be based on a single-objective optimization problem.

Optimization

Those designs that have been successfully synthesized and analyzed are subjected to dominance testing. Since many design objectives are considered, the performance of a given design is not simply summarized as a scalar value that may be directly compared to the corresponding scalar value of another competing design. Instead, the objective function is vector-valued and the concept of multi-objective optimization is

used to determine dominant designs for the optimization process.

The objective of the overall design process is to create a database with a substantial number of dominant designs, through the repeated application of synthesis, analysis and optimization. The set of dominant designs will reveal the location of Pareto-optimal frontiers where the optimal balance of objectives is achieved on the trade-off curves. On a Pareto-optimal frontier, designs cannot improve one objective without degrading another.

1.4 Thesis Outline

In summary, the objectives of this research are to develop (i) magnetic models of the LPM and LVR motors as shown in Figure 2(a) and 2(c), (ii) the optimal performance assessment methodology to maximize the productivity under average power dissipation constraint as a basis for comparison between different candidate designs and (iii) the computer-aided design tool based on multi-objective optimization concept for manufacturing applications.

The remainder of the thesis is organized as follows: Chapter 2 first derives the mathematical model of idealized LS motors where spatial harmonics and magnetic saturation are neglected. Using that model, the remainder of Chapter 2 explores the solutions of the point-to-point positioning optimal control problem under power dissipation constraints and two related optimal commutation problems with the role of spherical/cubical current limits and 3/6-wire connections fully considered. Analytical results are derived for some simple cases and a numerical method is presented and implemented for all cases of the idealized LS motors. The use of idealized representation provides clarity and invaluable insight to predict the solutions for the “real” motors. Chapter 3 develops the physics-based models for the LPM and LVR motor where spatial harmonics and magnetic saturation are now included. Using those models, the optimal performance assessment of the LPM and LVR motors for manufacturing

applications is explored in Chapter 4 using the mathematical frameworks discussed in Chapter 2. Chapter 5 presents the multi-objective design optimization of the LPM and LVR motors using tools described in Chapter 4. Chapter 6 summarizes the thesis and discusses future research directions. Supplementary materials related to motor modeling and design are provided in Appendices A and B. The thermal analyses of the LPM and LVR motors are finally presented in Appendices C and D, respectively, to demonstrate how the effective thermal resistance can be derived.

1.5 Contributions

This research resulted in the following major contributions:

1. Analytical solution to the problem of minimizing travel time subject to average power dissipation constraint when idealized PM and VR synchronous motors are used for continuous point-to-point positioning with spherical current limit and 3-wire connection.
2. Numerical solution to the problem of minimizing travel time subject to average power dissipation constraint when idealized PM, VR and hybrid synchronous motors are used for continuous point-to-point positioning with spherical/cubical current limit and 3/6-wire connections.
3. Numerical solution to two optimal commutation problems (maximum force control and minimum-copper-loss force control) for idealized PM, VR and hybrid synchronous motors with spherical/cubical current limits and 3/6-wire connections.
4. Explicit model of the LPM and nonlinear MCA model of the LVR motor from their physical specifications.
5. Optimal performance assessment of LPM and LVR motors based on the solutions of the optimal position control and optimal commutation problems.

6. Multi-objective design optimization of LPM and LVR motors for manufacturing applications.
7. Thermal resistance models of the LPM and LVR motors.

Some of these contributions have been published in the form of conference papers [56, 57, 58, 59, 60, 61, 62].

CHAPTER 2

OPTIMAL CONTROL AND OPTIMAL COMMUTATION

2.1 Introduction

This chapter explores the optimal control problems arising in manufacturing applications involving point-to-point positioning tasks. If performed repetitively, point-to-point positioning requires continuous motive forces and hence continuous excitation currents, which in turn generate heat and result in temperature rise. Productivity is increased by reducing travel times, but this requires larger forces and hence higher average power dissipation. Since temperature rise is directly related to power dissipation, there is a limit to how fast the positioning tasks can be performed before the system becomes overheated.

In this chapter, for the sake of clarity, only 3-phase synchronous motors are considered and these are limited to their idealized representation in transformed variables [63] where spatial harmonics and magnetic saturation are neglected. All three types of such motors are included in this study: permanent magnet (PM), variable reluctance (VR) and hybrid. Magnitude limits may be imposed on the current vector as a whole or on the current vector components individually, and the phase windings can be interfaced to a power source using a 3-wire or 6-wire connection. Consequently, there are four possible current constraint sets, each of which is included.

In order to maximize productivity subject to a limit on acceptable average power dissipation, an optimal control problem [29, 30] is formulated. The general optimal control problem specializes for each of the permutations described above. For the simplest cases, this problem is solved analytically; in all cases, a numerical method is used to approximate solutions of this problem.

A static optimization problem called optimal commutation [35] is proposed as a simple alternative way of assessing performance limits of electric motors. Two types of optimal commutation are investigated: (i) maximum force control for determining the motor's continuous force limit corresponding to some given current limits and (ii) minimum-copper-loss force control for determining current profiles that produce a desired force and minimize power dissipation with or without current limit. These two optimal commutation problems are formulated and solved for all four possible current constraint sets (when applicable) described above as well.

The optimal control and optimal commutation problems will be used to assess optimal performance of electric motors from their physical specifications in the subsequent chapters.

2.2 Idealized Models of Linear Synchronous Motors

The mathematical models of LS motors are derived under the idealized assumptions that spatial harmonics and magnetic saturation are negligible. As discussed in Chapter 1, only three-phase LS motors with active translators and concentrated windings are considered and all three variations of LS motors, namely LPM, LVR and LH motors are taken into account in this derivation. According to Figure 2, the conventions applied for this modeling are as follows:

- Phases 1, 2 and 3 are labeled from left to right.
- Positive moving direction is from right to left.
- Direction of positive current is as indicated in Figure 2.
- The position $x = 0$ is the equilibrium position at which the translator rests when some positive current is applied only to phase 1.

2.2.1 Dynamic Model

According to [63], the voltage equation of the LS motor is

$$v = \mathcal{R}i + \frac{d\lambda}{dt} \quad (7)$$

where v is the vector of voltages applied to the coils, i is the vector of currents, λ is the vector of flux linkages, and the winding resistance matrix is given by

$$\mathcal{R} = \begin{bmatrix} R & 0 & 0 \\ 0 & R & 0 \\ 0 & 0 & R \end{bmatrix} \quad (8)$$

where R is the phase winding resistance. Assuming magnetic linearity, the flux linkage is given by

$$\lambda = \lambda_s(x) + \mathcal{L}(x)i \quad (9)$$

where x is mechanical position of the translator, λ_s is the source flux from the PM arrays and \mathcal{L} is the position dependent inductance matrix. For an ideal perfectly sinusoidal machine with geometry shown in Figure 2, λ_s is described by

$$\lambda_s(x) = \lambda_m \begin{bmatrix} \cos(\frac{\pi}{\tau}x) \\ \cos(\frac{\pi}{\tau}x + \frac{2\pi}{3}) \\ \cos(\frac{\pi}{\tau}x - \frac{2\pi}{3}) \end{bmatrix} \quad (10)$$

where λ_m is the maximum flux produced by the PM pole pair and τ is the PM pitch between same polarity as shown in Figure 2, and \mathcal{L} is given by

$$\mathcal{L}(x) = \begin{bmatrix} L_s & -M_s & -M_s \\ -M_s & L_s & -M_s \\ -M_s & -M_s & L_s \end{bmatrix} + L_m \begin{bmatrix} \cos \theta_1 & \cos \theta_2 & \cos \theta_3 \\ \cos \theta_2 & \cos \theta_3 & \cos \theta_1 \\ \cos \theta_3 & \cos \theta_1 & \cos \theta_2 \end{bmatrix} \quad (11)$$

$$\theta_j = \frac{2\pi}{p}x + (j-1)\frac{2\pi}{3}, \quad j = 1, 2, 3 \quad (12)$$

where L_s is the average self inductance, $M_s = \frac{1}{2}L_s$ is the average mutual inductance, L_m is the variation in inductance due to air gap variation, and p is the motor pitch defined as

$$p = \begin{cases} \tau & , \text{ for LPM and LH motor} \\ p_t & , \text{ for LVR motor} \end{cases} \quad (13)$$

where p_t denotes tooth pitch. The force produced by the motor is given by

$$f(x, i) = \frac{d\lambda_s^T(x)}{dx}i + \frac{1}{2}i^T \frac{d\mathcal{L}(x)}{dx}i \quad (14)$$

where the first term is due to magnetic alignment mechanism and the second term is due to the magnetic saliency in the air gap. For the configurations shown in Figure 2, cogging force is not present.

2.2.2 Reference Frame Transformation

A change of variables may be introduced at this stage to eliminate the dependence on position x to further simplify the model. This operation is purely for mathematical convenience. The orthonormal transformation matrix [63]

$$S(x) = \sqrt{\frac{2}{3}} \begin{bmatrix} \cos(\frac{\pi}{p}x) & \cos(\frac{\pi}{p}x + \frac{2\pi}{3}) & \cos(\frac{\pi}{p}x - \frac{2\pi}{3}) \\ -\sin(\frac{\pi}{p}x) & -\sin(\frac{\pi}{p}x + \frac{2\pi}{3}) & -\sin(\frac{\pi}{p}x - \frac{2\pi}{3}) \\ \frac{1}{\sqrt{2}} & \frac{1}{\sqrt{2}} & \frac{1}{\sqrt{2}} \end{bmatrix} \quad (15)$$

maps physical variables into a new reference frame according to

$$\underbrace{[\sigma_d \ \sigma_q \ \sigma_0]^T}_{\tilde{\sigma}^T} = S(x) \underbrace{[\sigma_1 \ \sigma_2 \ \sigma_3]^T}_{\sigma^T} \quad (16)$$

where $\tilde{\sigma}$ is a vector of the so-called d -axis, q -axis and 0-axis variables for voltage, current or flux, and σ is a vector of the original voltage, current or flux variables. Note that S is orthonormal and hence its inverse is equal to its transpose. Application

of this transformation to the voltage and force equations results in

$$v_d = Ri_d - \alpha L_q i_q \frac{dx}{dt} + L_d \frac{di_d}{dt} \quad (17)$$

$$v_q = Ri_q + \alpha L_d i_d \frac{dx}{dt} + L_q \frac{di_q}{dt} \quad (18)$$

$$v_0 = Ri_0 \quad (19)$$

where (v_q, v_d, v_0) and (i_q, i_d, i_0) are the q -axis, d -axis and 0-axis components of voltages and currents, respectively; L_d and L_q are given by

$$L_d = L_s + M_s + \frac{3}{2}L_m \quad (20)$$

$$L_q = L_s + M_s - \frac{3}{2}L_m \quad (21)$$

and the constant parameter α is

$$\alpha = \frac{\pi}{p} \quad (22)$$

The force function is given by

$$f(i_q, i_d) = K_a i_q + K_r i_q i_d \quad (23)$$

where the alignment force constant K_a and the reluctance force constant K_r are given by

$$K_a = \sqrt{\frac{3}{2}} \alpha \lambda_m \quad (24)$$

$$K_r = \alpha(L_d - L_q) \quad (25)$$

Note that the dependence on position x has been completely eliminated from (14), and the obtained force equation is essentially equivalent to that of idealized rotary synchronous motors.

2.3 System Description

2.3.1 Point-To-Point Positioning

The position control problem considered here involves a frictionless single-axis motion system. The motive force is provided by a synchronous motor, constructed from

linear magnetic materials with geometry that yields spatially sinusoidal magnetic characteristics. The dynamic model is

$$M\ddot{x} = f(u_q, u_d) \quad (26)$$

where x denotes position, M is the moving mass, and the force function depends on the type of synchronous motor according to

$$f(u_q, u_d) = \begin{cases} K_a u_q & , \text{ PM motor} \\ K_r u_q u_d & , \text{ VR motor} \\ K_a u_q + K_r u_q u_d & , \text{ hybrid motor} \end{cases} \quad (27)$$

where K_a is the alignment force constant, K_r is the reluctance force constant and $u_{q/d}$ are the q/d -axis current command components. The point-to-point positioning tasks correspond to the boundary conditions

$$\begin{bmatrix} x(0) \\ \dot{x}(0) \end{bmatrix} = \begin{bmatrix} 0 \\ 0 \end{bmatrix}, \quad \begin{bmatrix} x(T) \\ \dot{x}(T) \end{bmatrix} = \begin{bmatrix} X \\ 0 \end{bmatrix} \quad (28)$$

where T is the travel time and X is the travel distance. In (26)-(27), the actual currents $i_{q/d}$ have been replaced by the current command signals $u_{q/d}$ to reflect the use of high-gain current loops which result in $i_{q/d} \approx u_{q/d}$.

Recall from (16) that the current variables appearing in (26), along with another current variable u_0 known as the 0-axis current component, are related to the physical currents (u_1, u_2, u_3) flowing through the three phase windings by a coordinate transformation of the form

$$\underbrace{\begin{bmatrix} u_d & u_q & u_0 \end{bmatrix}^T}_{\tilde{u}^T} = S(x) \underbrace{\begin{bmatrix} u_1 & u_2 & u_3 \end{bmatrix}^T}_{u^T} \quad (29)$$

Temperature rise is determined in part by the average power dissipation in the phase windings, given by

$$P = \frac{R}{T} \int_0^T u^T u dt \quad (30)$$

where R denotes coil resistance. Since $S(x)$ is an orthonormal matrix, it follows that

$$u^T u = (S^T(x)\tilde{u})^T (S^T(x)\tilde{u}) = \tilde{u}^T \tilde{u} \quad (31)$$

for all x . Hence, in terms of the current variables used in (26), average power dissipation is proportional to the integral of $\tilde{u}^T \tilde{u}$; this fact will be exploited in the formulation of the minimum copper loss control problem.

2.3.2 Current Limits

The physical currents u must necessarily be limited; an ultimate limit is imposed by the power source, but another more-restrictive limit is imposed by the controller to guarantee safe operation. There is more than one way to introduce the current limit U imposed by the controller. If the limit is imposed on the current vector as a whole, then a spherical limit set

$$\mathcal{U}_s := \{u : u^T u \leq U^2\} \quad (32)$$

$$= \{\tilde{u} : \tilde{u}^T \tilde{u} \leq U^2\} \quad (33)$$

is obtained; when expressed in terms of \tilde{u} , the boundaries of \mathcal{U}_s are independent of x . If the limit is imposed on the current vector components individually, then a cubical limit set

$$\mathcal{U}_c := \{u : |u_j| \leq U, j = 1, 2, 3\} \quad (34)$$

$$= \{\tilde{u} : |S_j(x)\tilde{u}| \leq U, j = 1, 2, 3\} \quad (35)$$

is obtained, where $S_j(x)$ denotes the j th row of $S(x)$; when expressed in terms of \tilde{u} , the boundaries of \mathcal{U}_c depend on x .

Figure 3 illustrates the geometrical representation of \mathcal{U}_c with respect to \tilde{u} , for $x = 0$, $x = p/6$ and $x = p/3$, where p is the motor pitch. The tilted cube rotates about the u_0 -axis by angles 0° , 30° and 60° . Figure 4 shows the cross sections in the dq -plane corresponding to different values of u_0 . At $u_0 = 0$, the cross section is a

regular hexagon; for $|u_0| < U/\sqrt{3}$, it is a hexagon; for $|u_0| \geq U/\sqrt{3}$, it is a triangle; and for maximum value $|u_0| = \pm U\sqrt{3}$, it is a point.

2.3.3 Wiring Connections

Three-phase synchronous motors have three phase windings and hence six wire ends for interfacing to a power source. From the perspective of power source design, a 6-wire connection is more versatile but a 3-wire connection is more economical. The 3-wire connection requires the free wire end from all phase windings to be interconnected as a floating node, so in this case the currents are confined to the set

$$\mathcal{U}_0 := \{u : u_1 + u_2 + u_3 = 0\} \quad (36)$$

$$= \{\tilde{u} : u_0 = 0\} \quad (37)$$

Considering \mathcal{U}_s , the dq -plane cross section is circular, and its radius is maximum at $u_0 = 0$; when $\tilde{u} \in \mathcal{U}_s$ the choice $u_0 = 0$ is advantageous for producing large forces with small losses, and the use of a 3-wire connection would not be a restriction. Considering \mathcal{U}_c , however, the dq -plane cross sections favorable for producing large forces generally correspond to $u_0 \neq 0$, e.g. the “largest” cross section generated by sweeping x corresponds to $|u_0| = U/\sqrt{3}$; this type of operation requires a 6-wire connection, and also contributes an additional component to losses, so when $u \in \mathcal{U}_c$ the optimal excitation is not easily determined.

2.3.4 Current Constraint Sets

In summary, with two types of current limits and two types of wiring connections, the four current constraint sets to be imposed on the optimal control problem will be

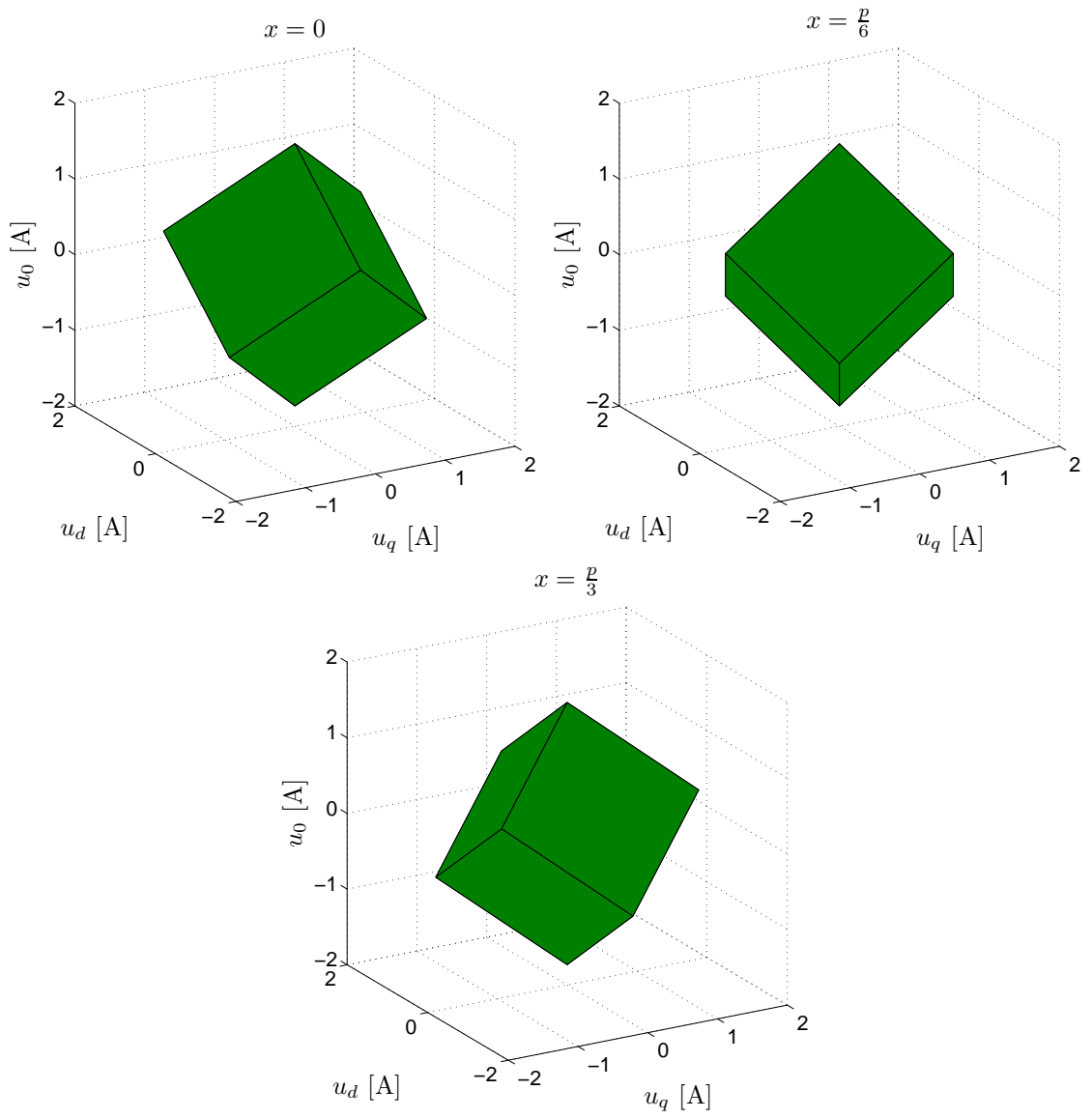


Figure 3: Cubical current limit set rotating at 0° , 30° and 60° about the u_0 -axis for $U = 1$ A.

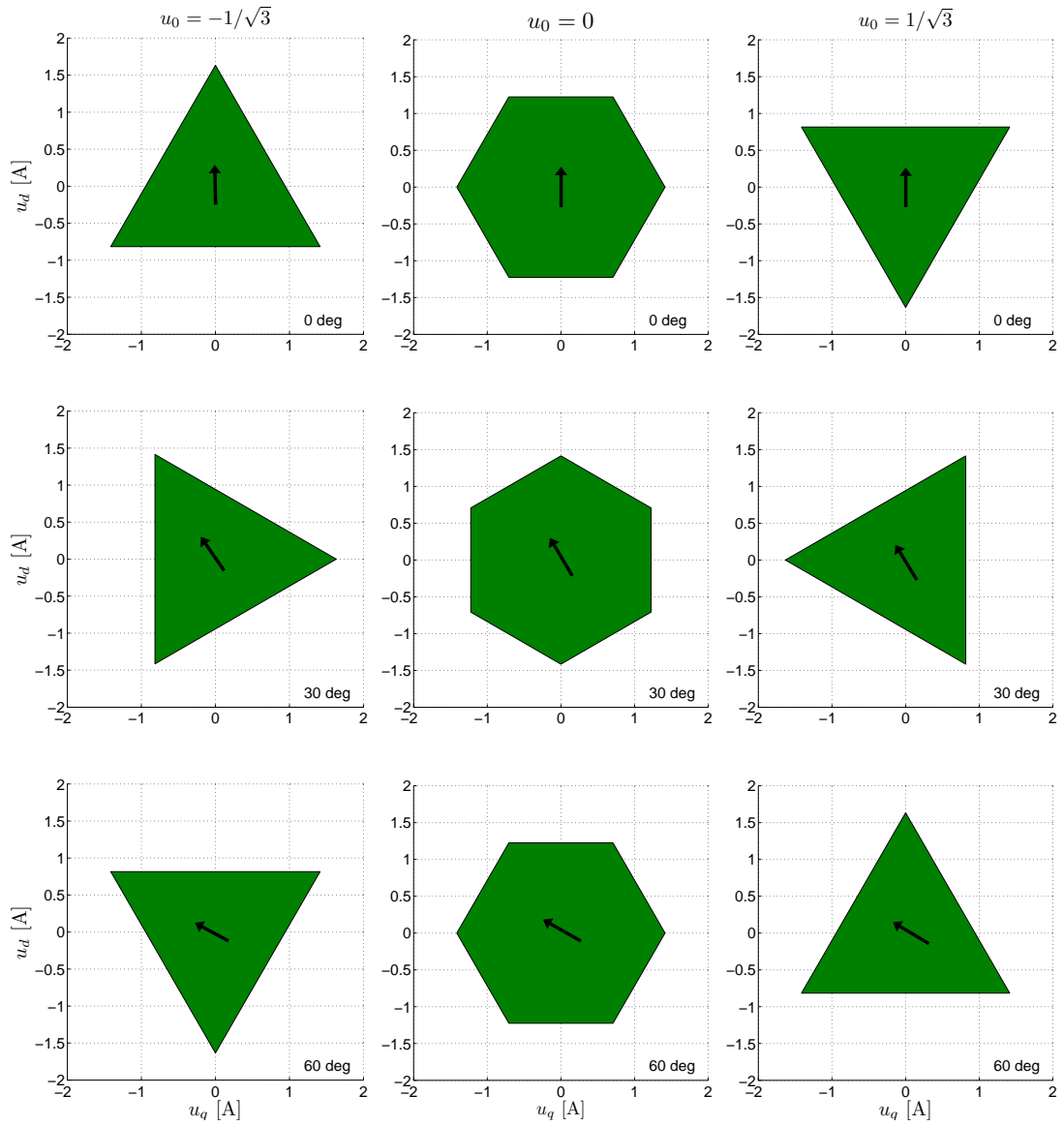


Figure 4: Cubical current limit set in dq -plane at different values of u_0 for $U = 1$ A.

generically denoted by \mathcal{U} and defined by

$$\mathcal{U} = \begin{cases} \mathcal{U}_s \cap \mathcal{U}_0 & , \text{ vector limit with 3-wire} \\ \mathcal{U}_s & , \text{ vector limit with 6-wire} \\ \mathcal{U}_c \cap \mathcal{U}_0 & , \text{ scalar limit with 3-wire} \\ \mathcal{U}_c & , \text{ scalar limit with 6-wire} \end{cases} \quad (38)$$

According to (33) and (35), \mathcal{U}_s and \mathcal{U}_c have been defined in terms of a common parameter U such that $\mathcal{U}_s \subset \mathcal{U}_c$. Hence, $\mathcal{U} = \mathcal{U}_c$ represents the least restrictive case.

2.4 Optimal Control Problem

2.4.1 Minimum Time Control

The minimum possible travel time T_* , along with the associated average power dissipation P_* , is obtained by solving the optimal control problem

$$\text{minimize} \quad T = \int_0^T 1 \, dt \quad (39)$$

$$\text{subject to} \quad (26), (28), \tilde{u} \in \mathcal{U} \quad (40)$$

Although the solution of this problem gives the minimal possible travel time T_* , it will be shown later that this also results in the maximum average power dissipation P_* . If the allowable average power dissipation is restricted to $P < P_*$ to limit temperature rise, then the problem formulation given below is more appropriate.

2.4.2 Minimum Copper Loss Control

Since T_* is the minimum achievable travel time for given values of M , K_a , K_r , U and X , there will be infinitely many solutions to the positioning problem if $T > T_*$. For this case, the objective here is to find the unique solution, from among all possible solutions, that minimizes T subject to an equality constraint on P . Direct solution of this average-power-specified time-optimal control problem would require that the motor dynamics be augmented with an additional state equation to account for the equality constraint on P .

In this research, an alternative solution method is pursued in order to avoid the need for augmenting the motor dynamics and, consequently, adding dimension to the associated two-point boundary value problem. For fixed values of M , K_a , K_r , U and X , all possible solutions to the positioning problem are characterized by points located within a feasible region of the (P, T) -plane. The boundary of the feasible region is defined by the function $T_{\min}(P)$ or the function $P_{\min}(T)$, depending on the assignment of independent/dependent axes. These functions define the same boundary and are related by

$$T_{\min}(P) = P_{\min}^{-1}(P) , P_{\min}(T) = T_{\min}^{-1}(T) \quad (41)$$

Consequently, the approach taken here is to solve the minimum average power dissipation optimal control problem with any fixed $T > T_*$, for which the dimension of the associated two-point boundary value problem is minimal. Solutions of this problem are located on the above-described boundary and, consequently, are also solutions to the average-power-specified time-optimal control problem.

Motivated by the considerations described above, the objective now is to solve the optimal control problem

$$\text{minimize} \quad P = \frac{R}{T} \int_0^T \tilde{u}^T \tilde{u} dt \quad (42)$$

$$\text{subject to} \quad (26), (28), \tilde{u} \in \mathcal{U} \quad (43)$$

for fixed $T > T_*$.

Analytical and numerical solutions for (39)-(40) and (42)-(43) are obtained for different cases as summarized in Table 1.

2.5 Analytical Solutions

2.5.1 Time-Optimal Control with Spherical Current Limit

First, the minimum possible travel time T_* , along with the associated average power dissipation P_* , will be obtained by solving the optimal control problem (39)-(40) with

Table 1: Methodology Used to Solved Optimal Control Problems

Motor Type	Minimum Time Control				Minimum Copper Loss Control			
	$\mathcal{U}_s \cap \mathcal{U}_0$	\mathcal{U}_s	$\mathcal{U}_c \cap \mathcal{U}_0$	\mathcal{U}_c	$\mathcal{U}_s \cap \mathcal{U}_0$	\mathcal{U}_s	$\mathcal{U}_c \cap \mathcal{U}_0$	\mathcal{U}_c
PM	✓	○	○	○	✓	○	○	○
VR	✓	○	○	○	✓	○	○	○
Hybrid	✓	○	○	○	○	○	○	○

✓ = symbolic and numerical results ○ = numerical results only

$\tilde{u} \in \mathcal{U}_s \cap \mathcal{U}_0$. By letting $x_1 = x$ and $x_2 = \dot{x}$, the Hamiltonian function

$$H = 1 + \lambda_1 x_2 + \lambda_2 \frac{1}{M} f(u_q, u_d) \quad (44)$$

leads to the co-state dynamics

$$\dot{\lambda}_1 = -\frac{\partial H}{\partial x_1} = 0 \quad (45)$$

$$\dot{\lambda}_2 = -\frac{\partial H}{\partial x_2} = -\lambda_1 \quad (46)$$

with solutions of the form

$$\lambda_1 = c_1 \quad (47)$$

$$\lambda_2 = c_2 - c_1 t \quad (48)$$

where c_1 and c_2 are constants. Pontryagin's minimum principle states that the optimal control minimizes H subject to $\tilde{u} \in \mathcal{U}_s \cap \mathcal{U}_0$ so the optimal control will be the signum function of λ_2 given by

$$(u_q, u_d) = \begin{cases} (+u_{q\star}, +u_{d\star}) & , \lambda_2 < 0 \\ (0, 0) & , \lambda_2 = 0 \\ (-u_{q\star}, +u_{d\star}) & , \lambda_2 > 0 \end{cases} \quad (49)$$

where

$$u_{q\star} = \frac{\sqrt{2}}{4K_r} \left(-K_a^2 + 4K_r^2 U^2 + K_a (K_a^2 + 8K_r^2 U^2)^{\frac{1}{2}} \right)^{\frac{1}{2}} \quad (50)$$

$$u_{d\star} = \frac{1}{4K_r} \left(-K_a + (K_a^2 + 8K_r^2 U^2)^{\frac{1}{2}} \right) \quad (51)$$

As two special cases, this reduces to

$$(u_q, u_d) = \begin{cases} (+U, 0) & , \lambda_2 < 0 \\ (0, 0) & , \lambda_2 = 0 \\ (-U, 0) & , \lambda_2 > 0 \end{cases} \quad (52)$$

when $K_r = 0$ for the PM motor, and

$$(u_q, u_d) = \begin{cases} \left(\frac{+U}{\sqrt{2}}, \frac{+U}{\sqrt{2}} \right) & , \lambda_2 < 0 \\ (0, 0) & , \lambda_2 = 0 \\ \left(\frac{-U}{\sqrt{2}}, \frac{+U}{\sqrt{2}} \right) & , \lambda_2 > 0 \end{cases} \quad (53)$$

when $K_a = 0$ for the VR motor.

From (48), λ_2 and hence u_q can change signs at most once and thus its possible sign sequences are $\{+\}$, $\{-\}$, $\{+, -\}$ and $\{-, +\}$. The geometry of the possible trajectories, constructed in the (x_1, x_2) -plane using (26), leads to the conclusion that the only valid sign sequence for u_q is $\{+, -\}$ and the switch point occurs at $x_1 = \frac{1}{2}X$ or, equivalently, at $t = \frac{1}{2}T_*$. Therefore, the piecewise-constant optimal control may be expressed in the form

$$(u_q, u_d) = \begin{cases} (+u_{q*}, +u_{d*}) & , t \in [0, \frac{1}{2}T_*) \\ (-u_{q*}, +u_{d*}) & , t \in [\frac{1}{2}T_*, T_*) \\ (0, 0) & , \text{otherwise} \end{cases} \quad (54)$$

for the hybrid motor,

$$(u_q, u_d) = \begin{cases} (+U, 0) & , t \in [0, \frac{1}{2}T_*) \\ (-U, 0) & , t \in [\frac{1}{2}T_*, T_*) \\ (0, 0) & , \text{otherwise} \end{cases} \quad (55)$$

for the PM motor, and

$$(u_q, u_d) = \begin{cases} \left(\frac{+U}{\sqrt{2}}, \frac{+U}{\sqrt{2}} \right) & , t \in [0, \frac{1}{2}T_*) \\ \left(\frac{-U}{\sqrt{2}}, \frac{+U}{\sqrt{2}} \right) & , t \in [\frac{1}{2}T_*, T_*) \\ (0, 0) & , \text{otherwise} \end{cases} \quad (56)$$

for the VR motor. This optimal control results in travel time

$$T_{\star} = \left(\frac{4X}{A} \right)^{\frac{1}{2}} \quad (57)$$

where $A = |f(u_{q\star}, u_{d\star})/M|$, and explicitly for two special cases

$$T_{\star} = \begin{cases} \left(\frac{4MX}{K_a U} \right)^{\frac{1}{2}}, & \text{PM motor} \\ \left(\frac{8MX}{K_r U^2} \right)^{\frac{1}{2}}, & \text{VR motor} \end{cases} \quad (58)$$

The average power dissipation is given by

$$P_{\star} = RU^2, \text{ for PM, VR and hybrid motor} \quad (59)$$

If $(u_q, u_d) \in \mathcal{U}_s \cap \mathcal{U}_0$, then T_{\star} is the minimum possible T and P_{\star} is the maximum possible P . Furthermore,

$$\lim_{U \rightarrow \infty} T_{\star} = 0, \quad \lim_{U \rightarrow \infty} P_{\star} = \infty \quad (60)$$

for all three motors.

2.5.2 Minimum Copper Loss Control with Spherical Current Limit

In this section, the symbolic solutions are developed only for the PM and VR synchronous motor for (42)-(43) with $\tilde{u} \in \mathcal{U}_s \cap \mathcal{U}_0$. By letting $x_1 = x$ and $x_2 = \dot{x}$, the Hamiltonian function

$$H = \frac{R}{T} (u_q^2 + u_d^2) + \lambda_1 x_2 + \lambda_2 \frac{1}{M} f(u_q, u_d) \quad (61)$$

leads to the co-state dynamics

$$\dot{\lambda}_1 = -\frac{\partial H}{\partial x_1} = 0 \quad (62)$$

$$\dot{\lambda}_2 = -\frac{\partial H}{\partial x_2} = -\lambda_1 \quad (63)$$

with solutions of the form

$$\lambda_1 = c_1 \quad (64)$$

$$\lambda_2 = c_2 - c_1 t \quad (65)$$

where c_1 and c_2 are constants. Pontryagin's minimum principle states that the optimal control minimizes H subject to $(u_q, u_d) \in \mathcal{U}_s \cap \mathcal{U}_0$. The two cases are considered separately.

2.5.2.1 PM Synchronous Motor

According to (27) and (61), the optimal control will be the saturation function of λ_2 given by

$$(u_q, u_d) = \begin{cases} (+U, 0) & , \lambda_2 \leq -\frac{2MR}{K_a T} U \\ \left(-\frac{K_a T}{2MR} \lambda_2, 0\right) & , |\lambda_2| < \frac{2MR}{K_a T} U \\ (-U, 0) & , \lambda_2 \geq +\frac{2MR}{K_a T} U \end{cases} \quad (66)$$

From (65), and the symmetry about $x_1 = \frac{1}{2}X$ and $t = \frac{1}{2}T$ required due to boundary conditions (28), optimal control (66) may be expressed in more explicit form. If saturation occurs

$$(u_q, u_d) = \begin{cases} (+U, 0) & , t \in [0, T_s) \\ \left(\frac{U(T-2t)}{T-2T_s}, 0\right) & , t \in [T_s, T - T_s) \\ (-U, 0) & , t \in [T - T_s, T) \\ (0, 0) & , \text{otherwise} \end{cases} \quad (67)$$

where $0 \leq T_s \leq \frac{1}{2}T$ denotes the duration of saturation at the beginning and end of motion. If saturation does not occur

$$(u_q, u_d) = \begin{cases} \left(\frac{6MX(T-2t)}{K_a T^3}, 0\right) & , t \in [0, T) \\ (0, 0) & , \text{otherwise} \end{cases} \quad (68)$$

Since control saturation may or may not occur, two cases must be considered. The choice of $T \geq T_*$ will fall into one of the two sets

$$\mathcal{T}_s = \left[T_*, \sqrt{\frac{3}{2}} T_* \right] , \quad \mathcal{T}_u = \left(\sqrt{\frac{3}{2}} T_*, \infty \right) \quad (69)$$

If $T \in \mathcal{T}_s$ then the control will be saturated, whereas if $T \in \mathcal{T}_u$ then the control will be unsaturated. The two cases may also be distinguished according to the value of $P \leq P_\star$ induced by the choice of $T \geq T_\star$ using the sets

$$\mathcal{P}_u = (0, \frac{1}{3}P_\star) , \quad \mathcal{P}_s = [\frac{1}{3}P_\star, P_\star] \quad (70)$$

If $P \in \mathcal{P}_s$ then the control will be saturated, whereas if $P \in \mathcal{P}_u$ then the control will be unsaturated.

The result of applying optimal control (67)-(68) to (26) is most conveniently described in terms of functions that depend on T_\star and P_\star . These functions are defined by

$$\alpha(T) = \begin{cases} 1 - \frac{2}{\sqrt{3}} \left(1 - \left(\frac{T_\star}{T}\right)^2\right)^{\frac{1}{2}} , & T \in \mathcal{T}_s \\ \frac{3}{4} \left(\frac{T_\star}{T}\right)^4 , & T \in \mathcal{T}_u \end{cases} \quad (71)$$

where $\alpha(T) \in [\frac{1}{3}, 1]$ for $T \in \mathcal{T}_s$ and $\alpha(T) \in (0, \frac{1}{3})$ for $T \in \mathcal{T}_u$;

$$\beta(P) = \begin{cases} \left(1 - \frac{3}{4} \left(1 - \frac{P}{P_\star}\right)^2\right)^{-\frac{1}{2}} , & P \in \mathcal{P}_s \\ \left(\frac{3}{4}\right)^{\frac{1}{4}} \left(\frac{P}{P_\star}\right)^{-\frac{1}{4}} , & P \in \mathcal{P}_u \end{cases} \quad (72)$$

where $\beta(P) \in [1, \sqrt{\frac{3}{2}}]$ for $P \in \mathcal{P}_s$ and $\beta(P) \in (\sqrt{\frac{3}{2}}, \infty)$ for $P \in \mathcal{P}_u$. The only undetermined parameter in (67)-(68) is T_s and, in order to guarantee $x_1(T) = X$, it is selected such that

$$T_s = \begin{cases} \frac{1}{2}T \left(1 - \sqrt{3} \left(1 - \left(\frac{T_\star}{T}\right)^2\right)^{\frac{1}{2}}\right) , & T \in \mathcal{T}_s \\ 0 , & T \in \mathcal{T}_u \end{cases} \quad (73)$$

Using (67)-(68) with (73), the resulting average power dissipation (42) directly evaluates to

$$P_{\min}(T) = P_\star \alpha(T) \quad (74)$$

Making use of the relation (41), inversion of (74) leads to the corresponding result

$$T_{\min}(P) = T_\star \beta(P) \quad (75)$$

Although derived indirectly, (75) provides a means to evaluate the minimum possible travel time for a desired travel distance subject to the requirement that specified average power P is generated. According to (3) and (6), the result (75) also provides the minimum possible travel times for an infinite sequence of motions consistent with a specified steady-state temperature.

It is also of interest to determine the nature of solutions in the limit as arbitrarily large excitation currents are permitted. If U is increased sufficiently then the optimal control will never saturate, so the above general results cover this case as a special case. The limiting results are given by

$$\lim_{U \rightarrow \infty} P_{\min}(T) = \frac{12M^2RX^2}{K_a^2T^4} \quad (76)$$

$$\lim_{U \rightarrow \infty} T_{\min}(P) = \left(\frac{12M^2RX^2}{K_a^2P} \right)^{\frac{1}{4}} \quad (77)$$

Unlike the limiting results of the time-optimal control given in (60), the average-power-specified time-optimal control leads to finite and nonzero limit values for P and T .

2.5.2.2 VR Synchronous Motor

According to (27) and (61), the optimal control will be the deadzone function of λ_2 given by

$$(u_q, u_d) = \begin{cases} \left(\frac{+U}{\sqrt{2}}, \frac{+U}{\sqrt{2}} \right) & , \lambda_2 \leq -\frac{2MR}{K_rT} \\ (0, 0) & , |\lambda_2| < \frac{2MR}{K_rT} \\ \left(\frac{-U}{\sqrt{2}}, \frac{+U}{\sqrt{2}} \right) & , \lambda_2 \geq +\frac{2MR}{K_rT} \end{cases} \quad (78)$$

From (65), and the symmetry about $x_1 = \frac{1}{2}X$ and $t = \frac{1}{2}T$ required due to boundary conditions (28), the optimal control (78) may be expressed in the explicit form

$$(u_q, u_d) = \begin{cases} \left(\frac{+U}{\sqrt{2}}, \frac{+U}{\sqrt{2}} \right) & , t \in [0, T_s) \\ (0, 0) & , t \in [T_s, T - T_s) \\ \left(\frac{-U}{\sqrt{2}}, \frac{+U}{\sqrt{2}} \right) & , t \in [T - T_s, T) \\ (0, 0) & , \text{otherwise} \end{cases} \quad (79)$$

where $0 < T_s \leq \frac{1}{2}T$ denotes the duration of saturation that occurs at the beginning and end of motion.

The result of applying optimal control (79) to (26) is most conveniently described in terms of functions that depend on T_\star and P_\star . These functions are defined by

$$\alpha(T) = 1 - \left(1 - \left(\frac{T_\star}{T} \right)^2 \right)^{\frac{1}{2}} \in (0, 1] \quad (80)$$

$$\beta(P) = \left(1 - \left(1 - \frac{P}{P_\star} \right)^2 \right)^{-\frac{1}{2}} \in [1, \infty) \quad (81)$$

The only undetermined parameter in (79) is T_s and, in order to guarantee $x_1(T) = X$, it is selected such that

$$T_s = \frac{1}{2}T\alpha(T) \quad (82)$$

Using (79) with (82), the resulting average power dissipation (42) directly evaluates to

$$P_{\min}(T) = P_\star\alpha(T) \quad (83)$$

Making use of the relation (41), inversion of (83) leads to the corresponding result

$$T_{\min}(P) = T_\star\beta(P) \quad (84)$$

Although derived indirectly, (84) provides a means to evaluate the minimum possible travel time for a desired travel distance subject to the requirement that specified

average power P is generated. According to (3) and (6), the result (84) also provides the minimum possible travel times for an infinite sequence of motions consistent with a specified steady-state temperature.

It is also of interest to determine the nature of solutions in the limit as arbitrarily large excitation currents are permitted. As U is increased the optimal control will continue to demand saturated rectangular current pulses, but their height will be increased and their width will be decreased. In fact, the effect of increasing U on the current pulses is to obtain

$$\lim_{U \rightarrow \infty} u_q(t) = \left(\frac{MX}{K_r T} \right)^{\frac{1}{2}} \left(\delta(t)^{\frac{1}{2}} - \delta(t - T)^{\frac{1}{2}} \right) \quad (85)$$

$$\lim_{U \rightarrow \infty} u_d(t) = \left(\frac{MX}{K_r T} \right)^{\frac{1}{2}} \left(\delta(t)^{\frac{1}{2}} + \delta(t - T)^{\frac{1}{2}} \right) \quad (86)$$

Despite the impulsive nature of the limiting currents, the corresponding limits for average power dissipation and travel time are well-defined and given by

$$\lim_{U \rightarrow \infty} P_{\min}(T) = \frac{4MRX}{K_r T^2} \quad (87)$$

$$\lim_{U \rightarrow \infty} T_{\min}(P) = \left(\frac{4MRX}{K_r P} \right)^{\frac{1}{2}} \quad (88)$$

Unlike the limiting results of the time-optimal control given in (60), the average-power-specified time-optimal control leads to finite and nonzero limit values for P and T .

2.5.2.3 Comparative Results

The results of the time-optimal control and average-power-specified time-optimal control for PM and VR synchronous motors are compared in Figures 5-10. The parameters are selected to be: $R = 5 \Omega$, $U = 5 \text{ A}$, $M = 1 \text{ kg}$ and $(K_a, K_r) = (4 \text{ N/A}, 1.6 \text{ N/A}^2)$, which result in both motors having the same maximum force of 20 N.

Using relationships (75) and (84), the trade-off curves $T(X, P)$ between the minimum travel time and the desired travel distance operating at different allowable power

dissipation levels are shown in Figure 5. Note that T_* is implicitly parameterized by X from (58), and is achieved by dissipating the same maximum power $P_* = 125$ W by both PM and VR motors according to (59). The presented power dissipation levels are selected to be at (100%, 75%, 50%, 25%) of P_* .

The current trajectories for both PM and VR motors at $X = 0.05$ m are shown in Figures 6-7, and the forces produced by such currents are plotted in Figures 8-9. Notice that at $P = 31.25$ W (i.e. 25% of P_*), the currents are not saturated for the PM motor, whereas VR motors always operate using saturated currents. In this particular example, the PM motor requires smaller travel time T when the same power dissipation $P < P_*$ is permitted.

The optimal trajectories are plotted in Figure 10. The constant velocity (x_2) periods of the VR motor correspond to the duration of zero force production during the “cruising” stage.

2.6 Numerical Solutions

A numerical method is presented here to solve (42)-(43) when the force function f and/or current constraint set \mathcal{U} are too complex to determine the symbolic solution.

2.6.1 Numerical Method

Consider the general optimal control problem

$$\text{minimize} \quad J = \int_0^T L(x, u) dt \quad (89)$$

$$\text{subject to} \quad \dot{x} = F(x, u) \quad (90)$$

$$x(0) = x_0, \quad x(T) = x_T \quad (91)$$

$$u \in \mathcal{U} \quad (92)$$

which covers (42)-(43) as a special case. Approximate solutions may be computed by formulating a nonlinear programming problem using collocation [64, 65, 66]. Trajectories $u(t)$ and $x(t)$ are approximated on a mesh $0 = t_1 < t_2 < \dots < t_N = T$

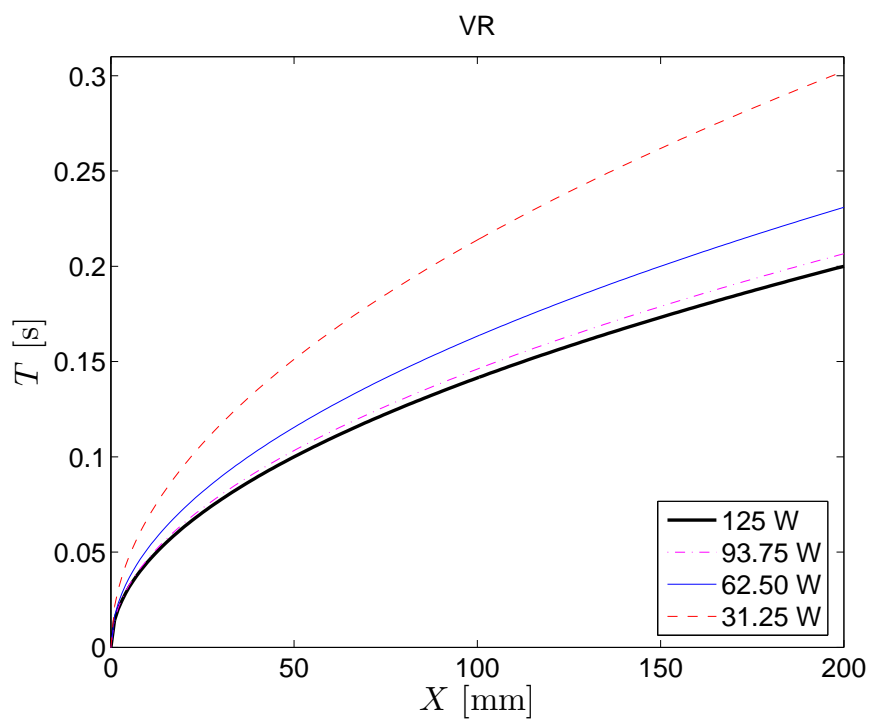
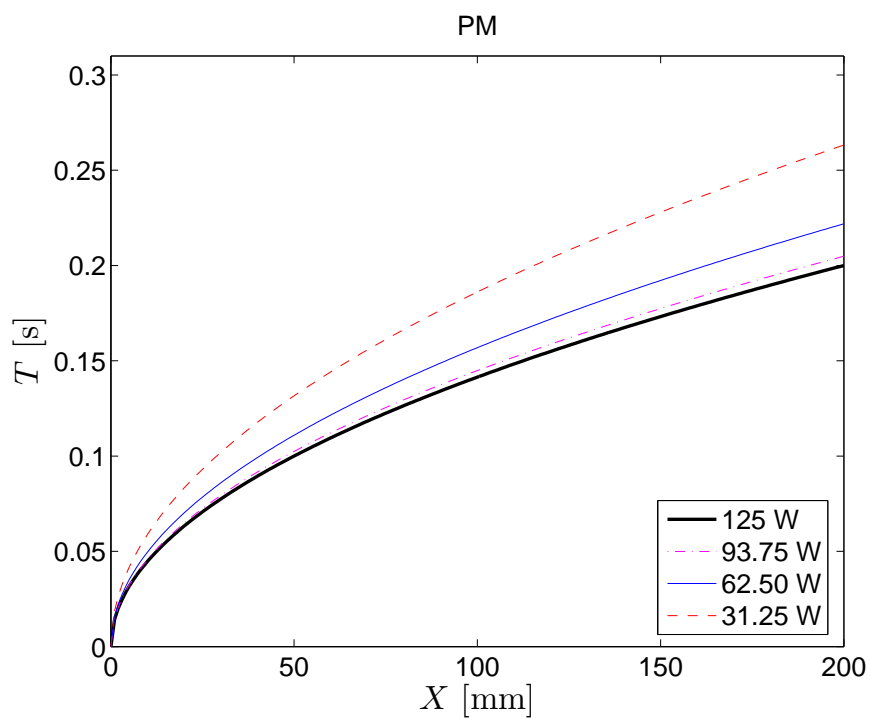


Figure 5: Minimum travel time for desired travel distance plots of time-optimal and average-power-specified time-optimal results using spherical current limit and 3-wire connection for PM and VR synchronous motors.

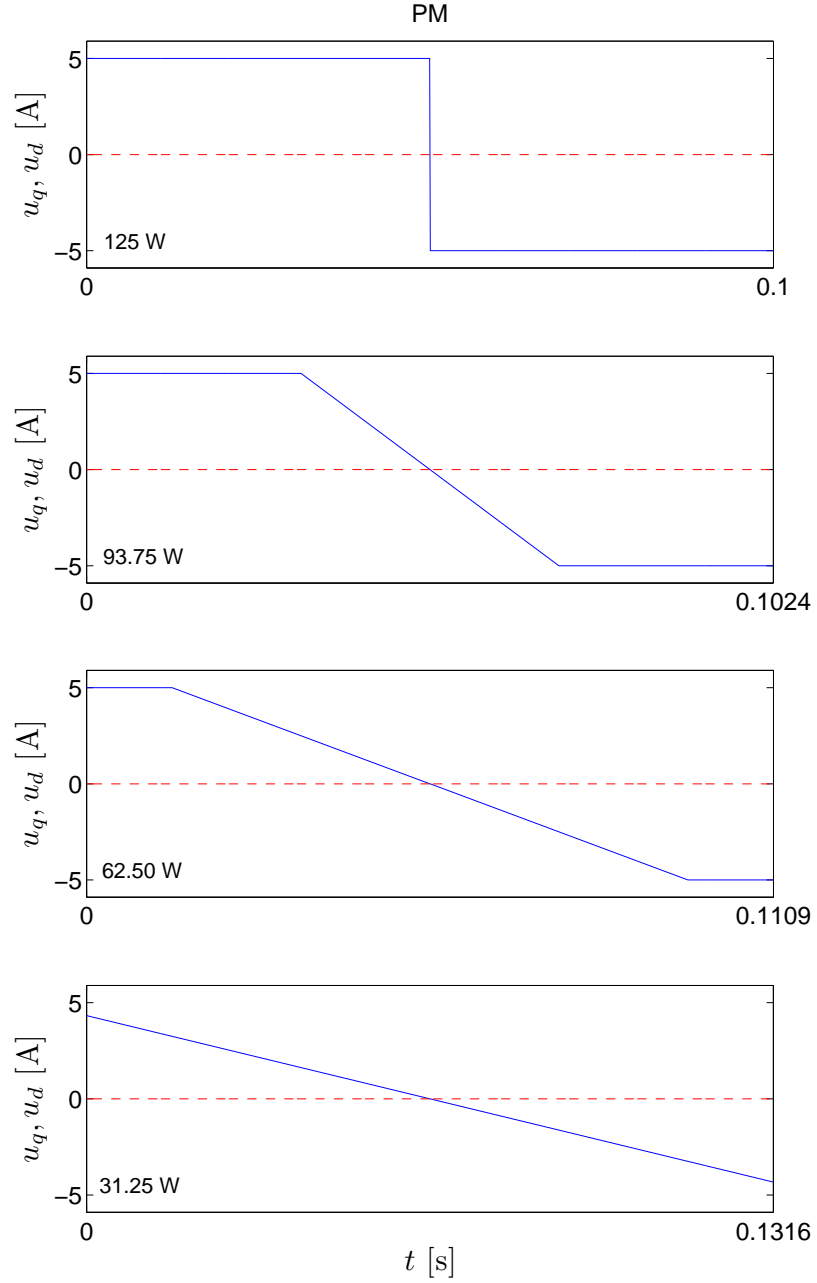


Figure 6: The trajectories of u_q (solid) and u_d (dashed) for $X = 0.05$ m for PM motor using spherical current limit and 3-wire connection.

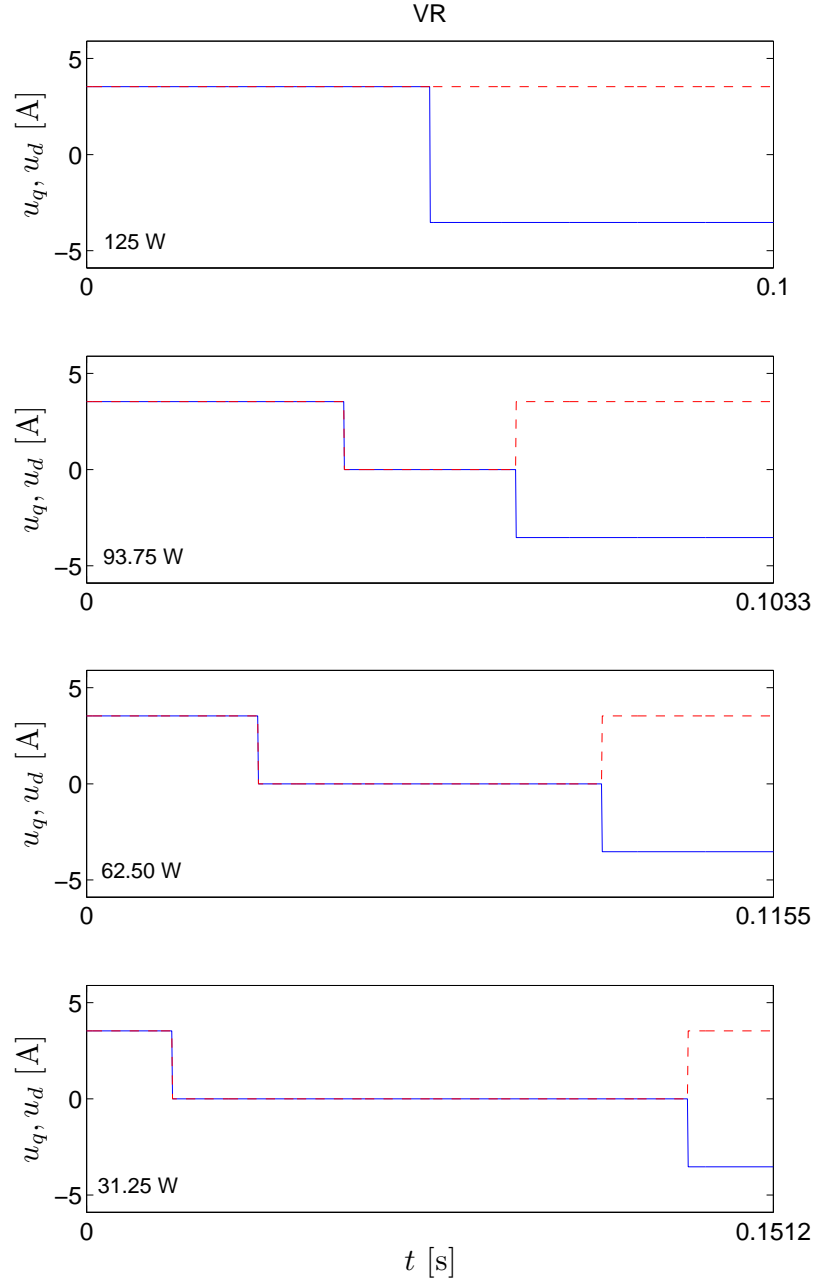


Figure 7: The trajectories of u_q (solid) and u_d (dashed) for $X = 0.05$ m for VR motor using spherical current limit and 3-wire connection.

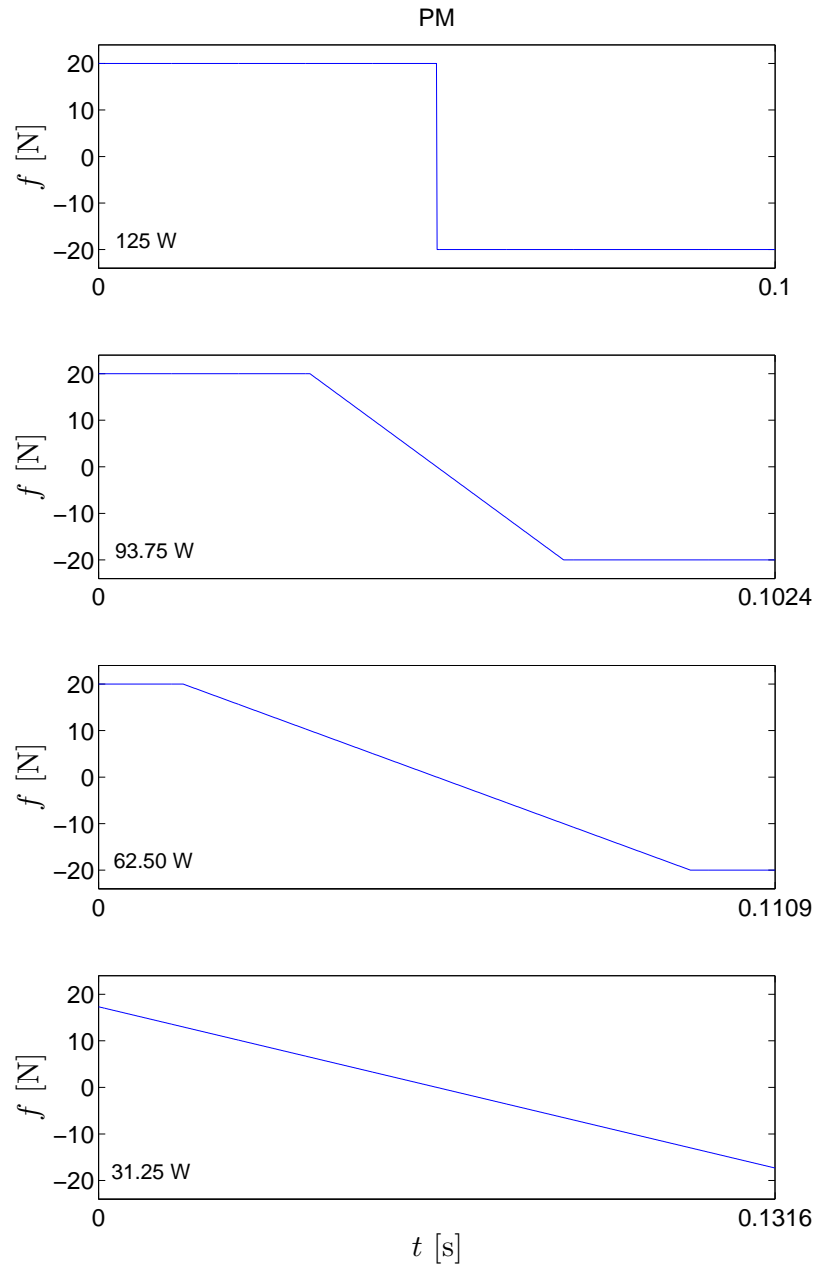


Figure 8: The trajectories of $f(u_q, u_d)$ for $X = 0.05$ m for PM motor using spherical current limit and 3-wire connection.

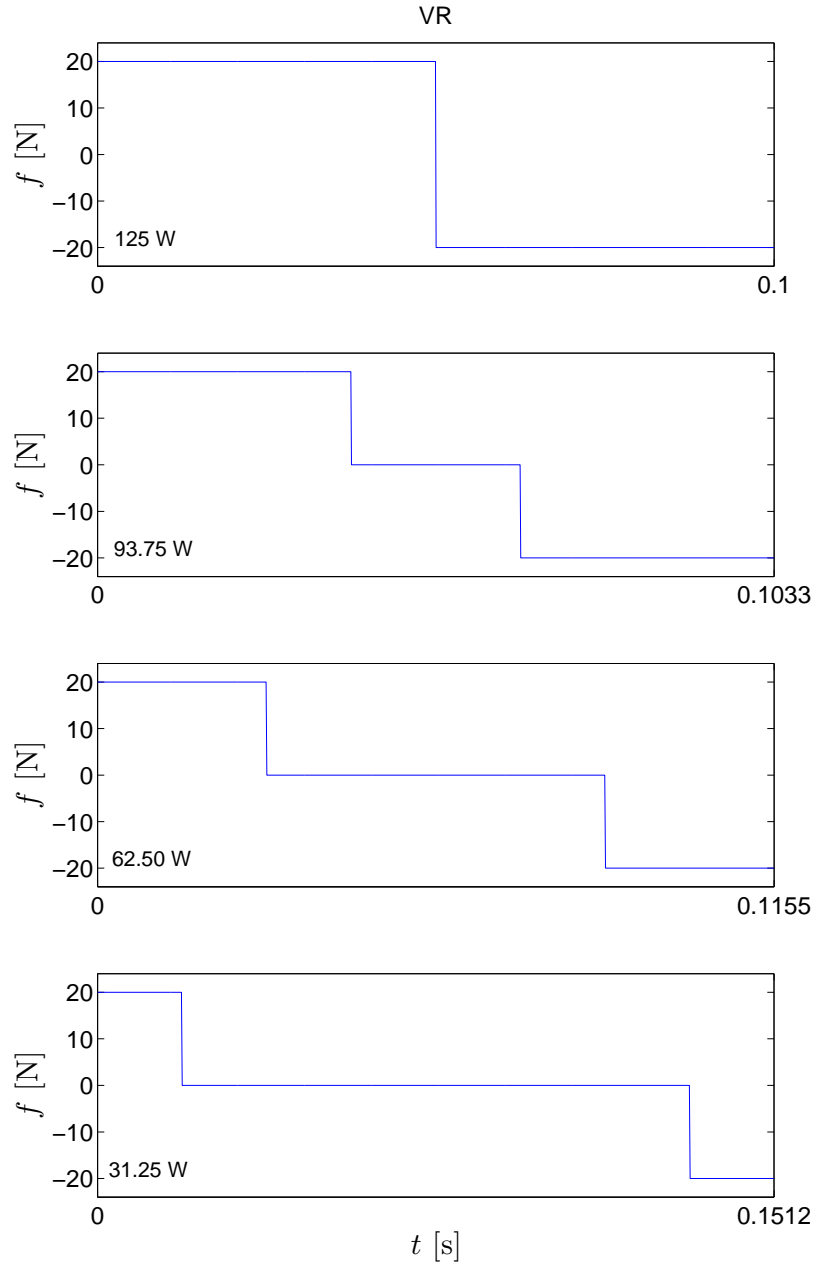


Figure 9: The trajectories of $f(u_q, u_d)$ for $X = 0.05$ m for VR motor using spherical current limit and 3-wire connection.

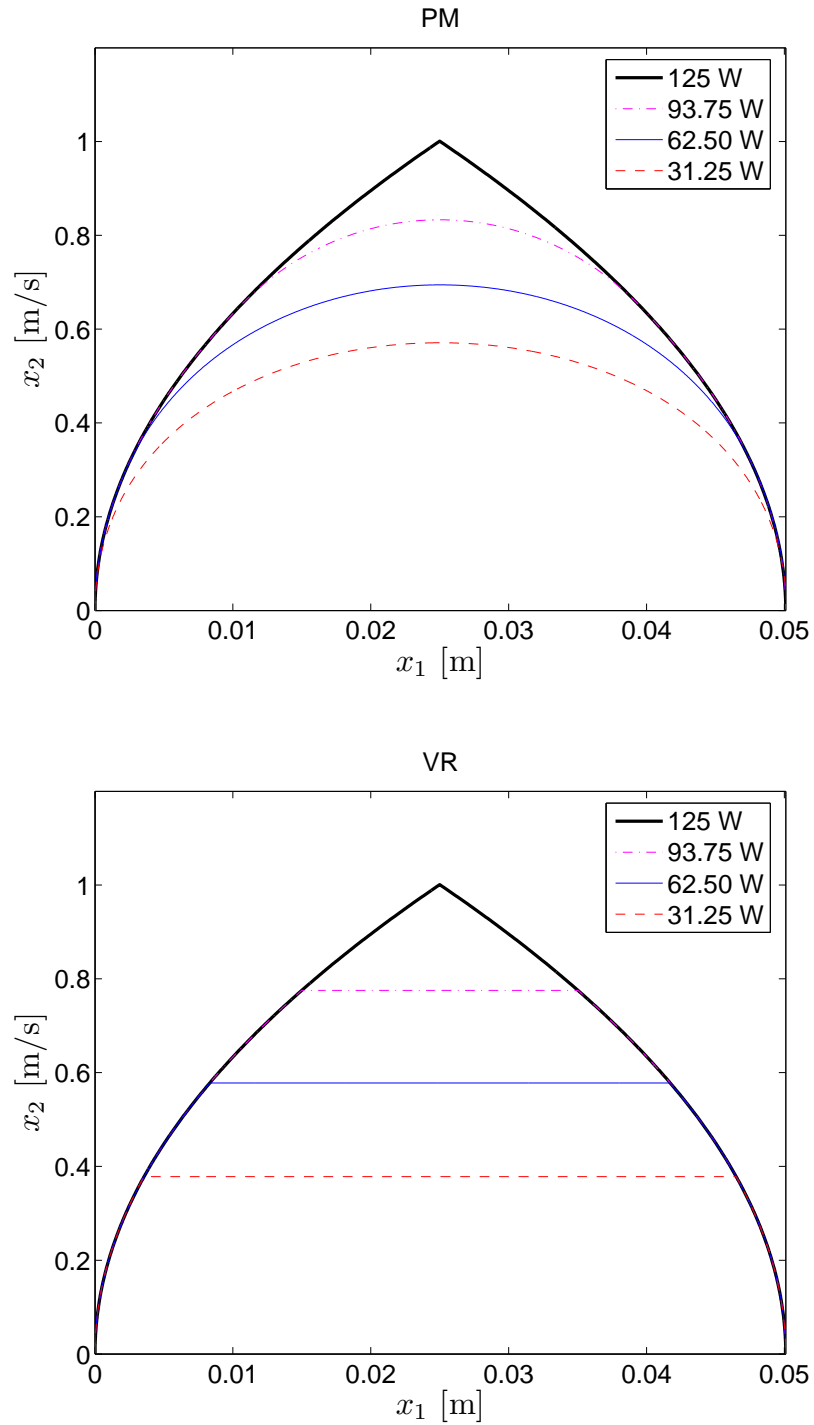


Figure 10: Optimal trajectories for $X = 0.05$ m for PM and VR synchronous motors using spherical current limit and 3-wire connection.

with spacing $h_j = t_{j+1} - t_j$, such that $\hat{u}_j \approx u(t_j)$ and $\hat{x}_j \approx x(t_j)$. The nonlinear programming problem will iterate the vector

$$y = \left[\hat{u}_1^T \quad \cdots \quad \hat{u}_N^T \quad \hat{x}_1^T \quad \cdots \quad \hat{x}_N^T \right]^T \quad (93)$$

and $u(t)$ and $x(t)$ will be recovered by interpolation. For $u(t)$ the interpolation formula

$$u(t) \approx \hat{u}_j + \frac{t - t_j}{h_j} (\hat{u}_{j+1} - \hat{u}_j), \quad t_j \leq t \leq t_{j+1} \quad (94)$$

guarantees that $u(t)$ interpolates to computed values \hat{u}_j at $t = t_j$. For $x(t)$ the interpolation formula is

$$x(t) \approx \sum_{i=0}^3 c_{i,j} \left(\frac{t - t_j}{h_j} \right)^i, \quad t_j \leq t \leq t_{j+1} \quad (95)$$

To guarantee that $x(t)$ interpolates to computed values \hat{x}_j at $t = t_j$, it is necessary to impose the constraints

$$c_{0,j} = \hat{x}_j \quad (96)$$

$$c_{0,j} + c_{1,j} + c_{2,j} + c_{3,j} = \hat{x}_{j+1} \quad (97)$$

To guarantee that $x(t)$ satisfies the differential equation at $t = t_j$, it is necessary to impose the constraints

$$c_{1,j}/h_j = \hat{F}_j \quad (98)$$

$$(c_{1,j} + 2c_{2,j} + 3c_{3,j})/h_j = \hat{F}_{j+1} \quad (99)$$

where $\hat{F}_j = F(\hat{x}_j, \hat{u}_j)$. Solving the combined system of constraint equations leads to

$$c_{0,j} = \hat{x}_j \quad (100)$$

$$c_{1,j} = h_j \hat{F}_j \quad (101)$$

$$c_{2,j} = 3(\hat{x}_{j+1} - \hat{x}_j) - h_j(\hat{F}_{j+1} + 2\hat{F}_j) \quad (102)$$

$$c_{3,j} = -2(\hat{x}_{j+1} - \hat{x}_j) + h_j(\hat{F}_{j+1} + \hat{F}_j) \quad (103)$$

To formulate differential equation constraints at mesh midpoints, note that at $t_{c,j} = \frac{1}{2}(t_j + t_{j+1})$

$$u(t_{c,j}) \approx \frac{1}{2}(\hat{u}_j + \hat{u}_{j+1}) =: \hat{u}_{j+\frac{1}{2}} \quad (104)$$

$$x(t_{c,j}) \approx c_{0,j} + \frac{1}{2}c_{1,j} + \frac{1}{4}c_{2,j} + \frac{1}{8}c_{3,j} =: \hat{x}_{j+\frac{1}{2}} \quad (105)$$

$$\dot{x}(t_{c,j}) \approx (c_{1,j} + c_{2,j} + \frac{3}{4}c_{3,j})/h_j =: \hat{x}_{j+\frac{1}{2}} \quad (106)$$

and

$$F(x(t_{c,j}), u(t_{c,j})) \approx F(\hat{x}_{j+\frac{1}{2}}, \hat{u}_{j+\frac{1}{2}}) =: \hat{F}_{j+\frac{1}{2}} \quad (107)$$

Approximating J by trapezoidal integration, (89)-(92) is now transformed into the form

$$\text{minimize} \quad \hat{J} = \sum_{j=1}^{N-1} \frac{h_j}{2} (\hat{L}_j + \hat{L}_{j+1}) \quad (108)$$

$$\text{subject to} \quad \hat{x}_{j+\frac{1}{2}} = \hat{F}_{j+\frac{1}{2}}, \quad j = 1, \dots, N-1 \quad (109)$$

$$\hat{x}_1 = x_0, \quad \hat{x}_N = x_T \quad (110)$$

$$\hat{u}_j \in \mathcal{U}, \quad j = 1, \dots, N \quad (111)$$

where $\hat{L}_j = L(\hat{x}_j, \hat{u}_j)$. This numerical method was implemented in MATLAB with Optimization Toolbox to solve the derived nonlinear programming problem.

2.6.2 Numerical Results

Numerical solutions of (42)-(43) for $T > T_*$ are obtained for four cases of \mathcal{U} . The parameter values are chosen as follows: $M = 1$ kg, $X = 0.05$ m, $p = 0.01$ m, $R = 5$ Ω , $U = 5$ A, $K_a = 4$ N/A for the PM motor, $K_r = 1.6$ N/A² for the VR motor and $(K_a, K_r) = (1.238$ N/A, 1.238 N/A²) for the hybrid motor. The force constants are chosen such that each motor has the same maximum force of 20 N for $\tilde{u} \in \mathcal{U}_s$. The numerical method uses $N = 41$; due to discretization, it is unable to reproduce the jump discontinuities in current known to characterize the analytical solution for the VR motor with $\tilde{u} \in \mathcal{U}_s$.

Table 2: Spherical Current Limit with 3- and 6-Wire Connections

T [s]	P [W]		
	PM	Hybrid	VR
0.125	38.4473	48.9770	50.4405
0.120	45.2691	54.9892	56.3573
0.115	53.7847	62.5023	63.7484
0.110	64.9417	72.3381	73.4401
0.105	81.0885	86.6096	87.4481
0.100*	125	125	125

* Analytical results.

Plots of position, velocity, force and currents for each synchronous motor, with $\tilde{u} \in \mathcal{U}_s$ and either 3-wire or 6-wire connection, are shown in Figures 11-13. Both 3-wire and 6-wire connection yield identical results. All three motors accelerate and decelerate with constant ripple-free forces, but otherwise the shape of the force trajectory depends on the type of motor. All the motors operate with $u_0 = 0$ which is consistent with previous discussions. Values of average power dissipation $P < P_*$ for various values of $T > T_*$ are listed in Table 2. In this case, for any fixed T , the VR motor generates the most heat and the PM motor generates the least heat.

Plots of position, velocity, force and currents for each synchronous motor, with $\tilde{u} \in \mathcal{U}_c$, are shown in Figure 14-16 for 3-wire connection and in Figures 17-19 for 6-wire connection. The 3-wire and 6-wire results differ from each other, with higher peak forces for the 6-wire connection. In both cases all three motors accelerate and decelerate with nonconstant forces exhibiting ripple, and the shape of the force trajectory depends on the type of motor. Values of average power dissipation $P < P_*$ for various values of $T > T_*$ are listed in Tables 3 and 4 for the 3-wire and 6-wire connections. For any fixed T , $\tilde{u} \in \mathcal{U}_c$ yields lower cost than $\tilde{u} \in \mathcal{U}_s$, and $\tilde{u} \in \mathcal{U}_c$ with 6-wire connection yields lower cost than $\tilde{u} \in \mathcal{U}_c$ with 3-wire connection. These results are consistent with previous discussions. For any fixed T , with $\tilde{u} \in \mathcal{U}_c$ the VR motor

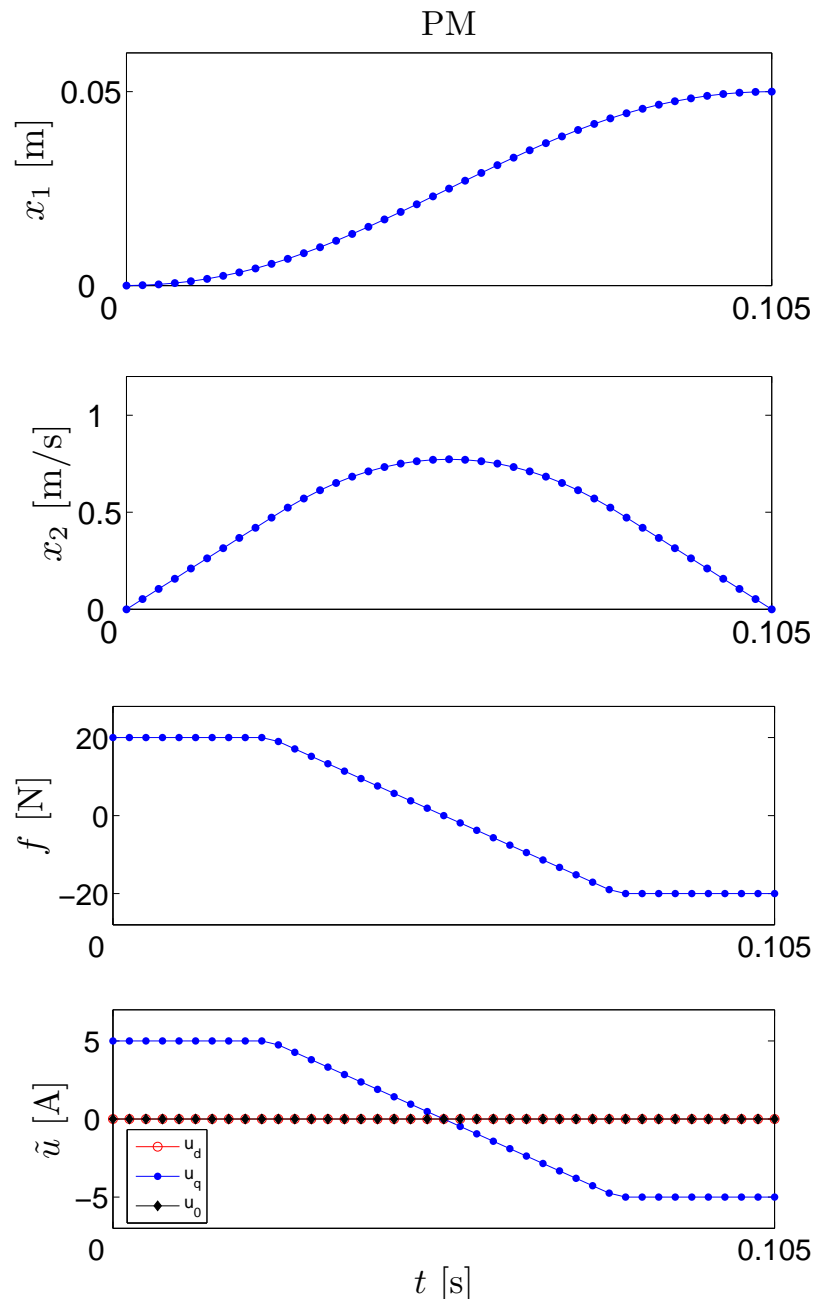


Figure 11: Position, velocity, force and currents for PM motor using spherical current limit with 3-wire or 6-wire connections.

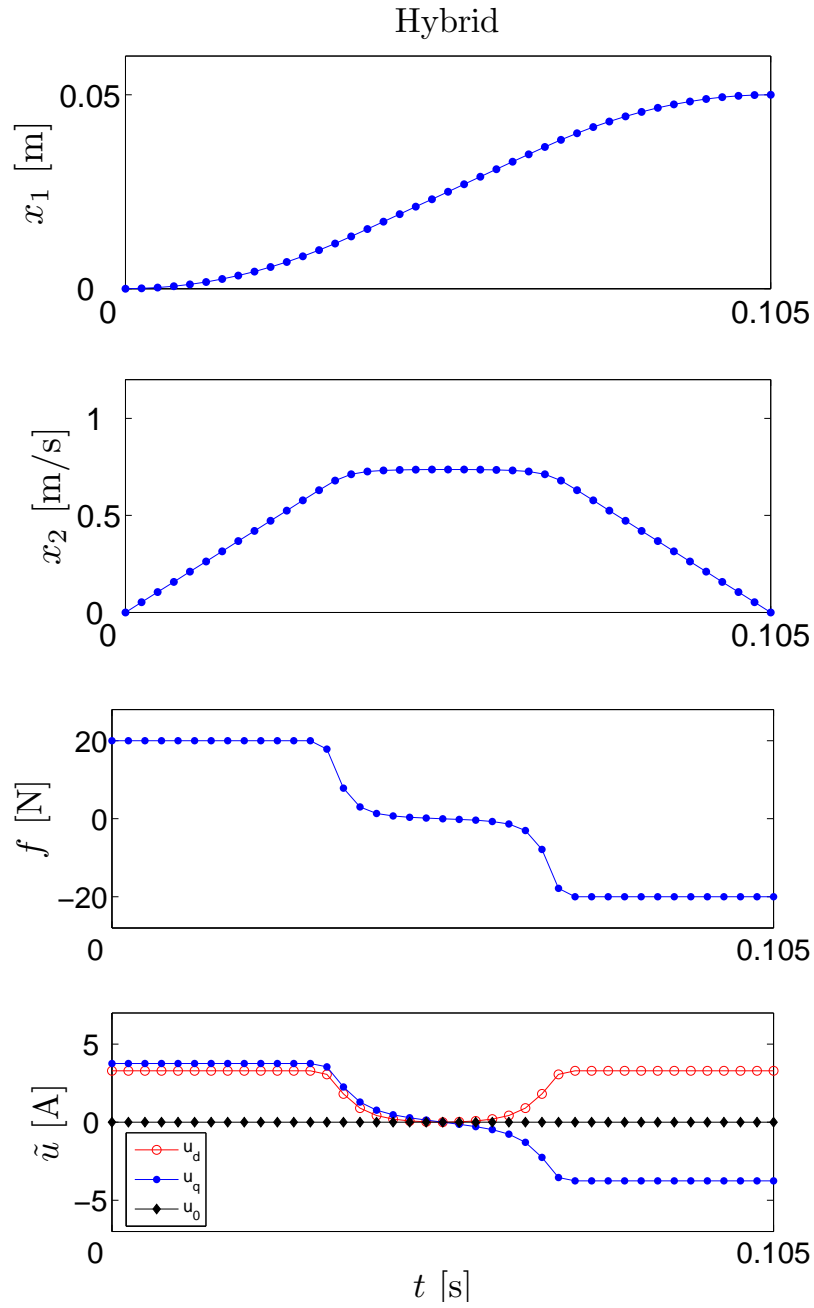


Figure 12: Position, velocity, force and currents for hybrid motor using spherical current limit with 3-wire or 6-wire connections.

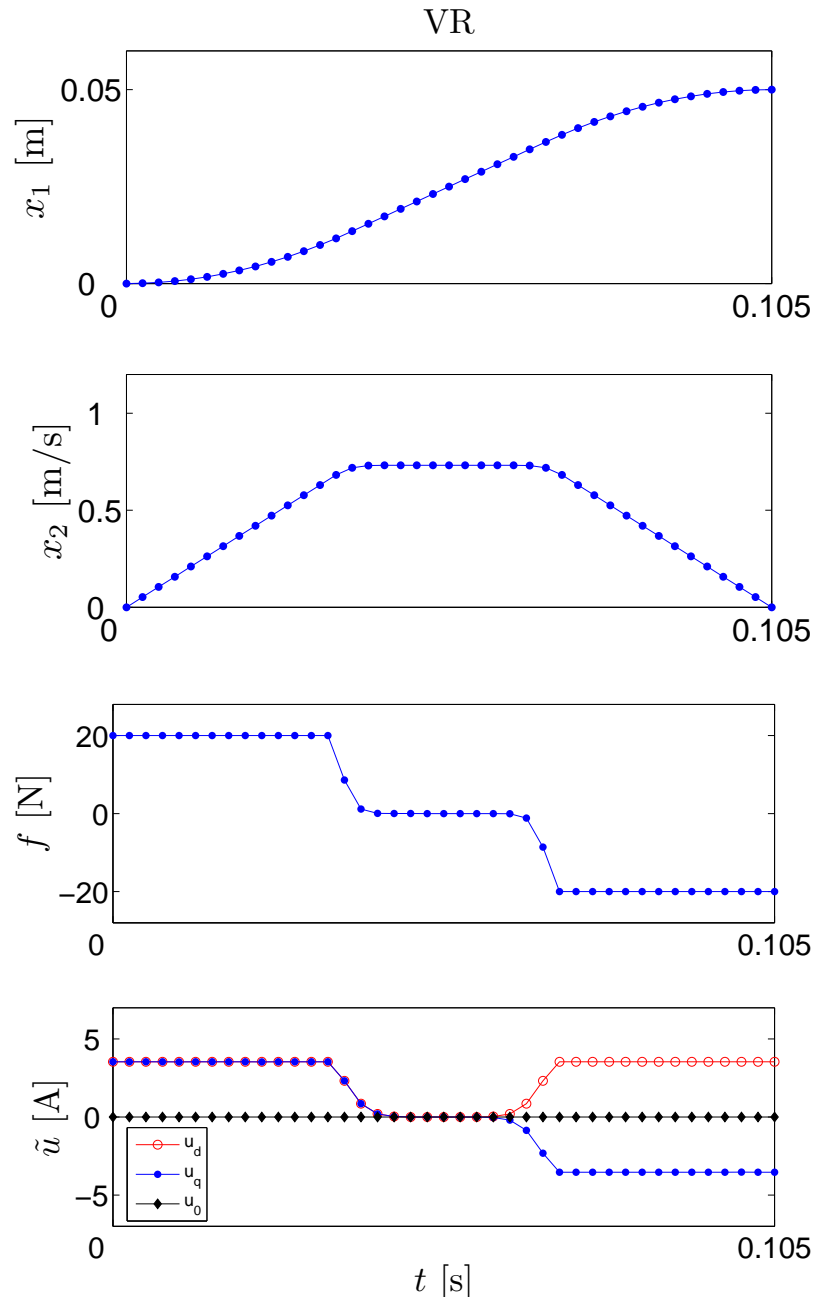


Figure 13: Position, velocity, force and currents for VR motor using spherical current limit with 3-wire or 6-wire connections.

Table 3: Cubical Current Limit with 3-Wire Connection

T [s]	P [W]		
	PM	Hybrid	VR
0.110	64.1113	63.7530	61.7573
0.105	77.2233	71.9397	69.1315
0.100	93.8916	81.9955	78.1598
0.095	116.6171	95.0292	89.7284
0.090	151.9896	112.3206	104.6511
0.085	-	137.2831	125.2064

Table 4: Cubical Current Limit with 6-Wire Connection

T [s]	P [W]		
	PM	Hybrid	VR
0.110	64.1113	62.8830	60.3468
0.105	77.2233	70.5193	67.0976
0.100	93.8864	79.6731	75.1880
0.095	116.1864	90.8084	85.0090
0.090	148.3871	104.6864	97.0913
0.085	201.8867	122.5108	112.4806

generates the least heat and the PM motor generates the most heat.

Solutions to the time-optimal control problem (39)-(40) are approximated by solving (42)-(43) as follows. First, a sufficiently large value of T is chosen so that the nonlinear programming problem will converge. Then successively smaller values of T are chosen and the nonlinear programming problem is run to check for convergence. This procedure repeats until convergence fails to occur, and T_* is approximated by the previous value of T in the sequence. The results obtained using this method are listed in Table 5. The tabulated results using $\tilde{u} \in \mathcal{U}_s$ are reasonably accurate in comparison with the analytical results; approximation errors in P_* are less than 5%. As expected, T_* is smallest for $\tilde{u} \in \mathcal{U}_c$.

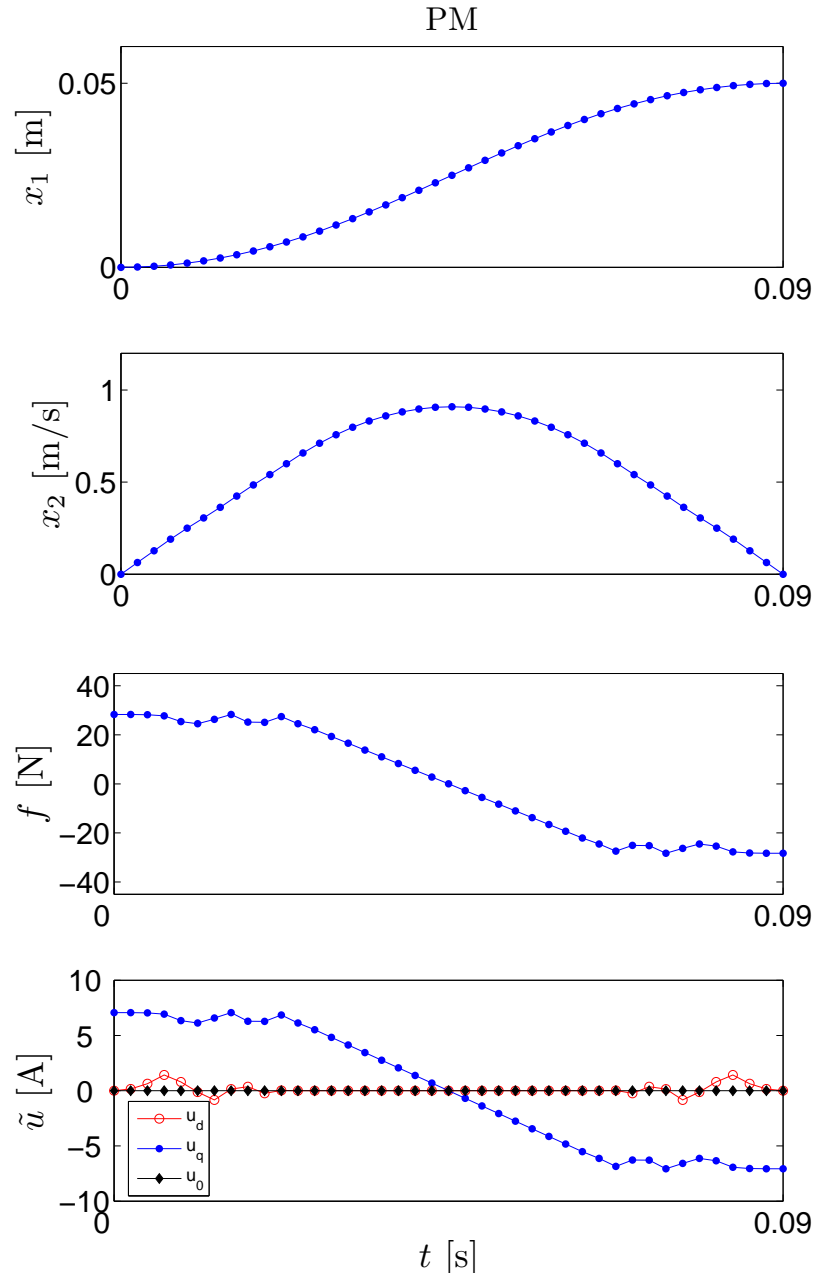


Figure 14: Position, velocity, force and currents for PM motor using cubical current limit with 3-wire connection.

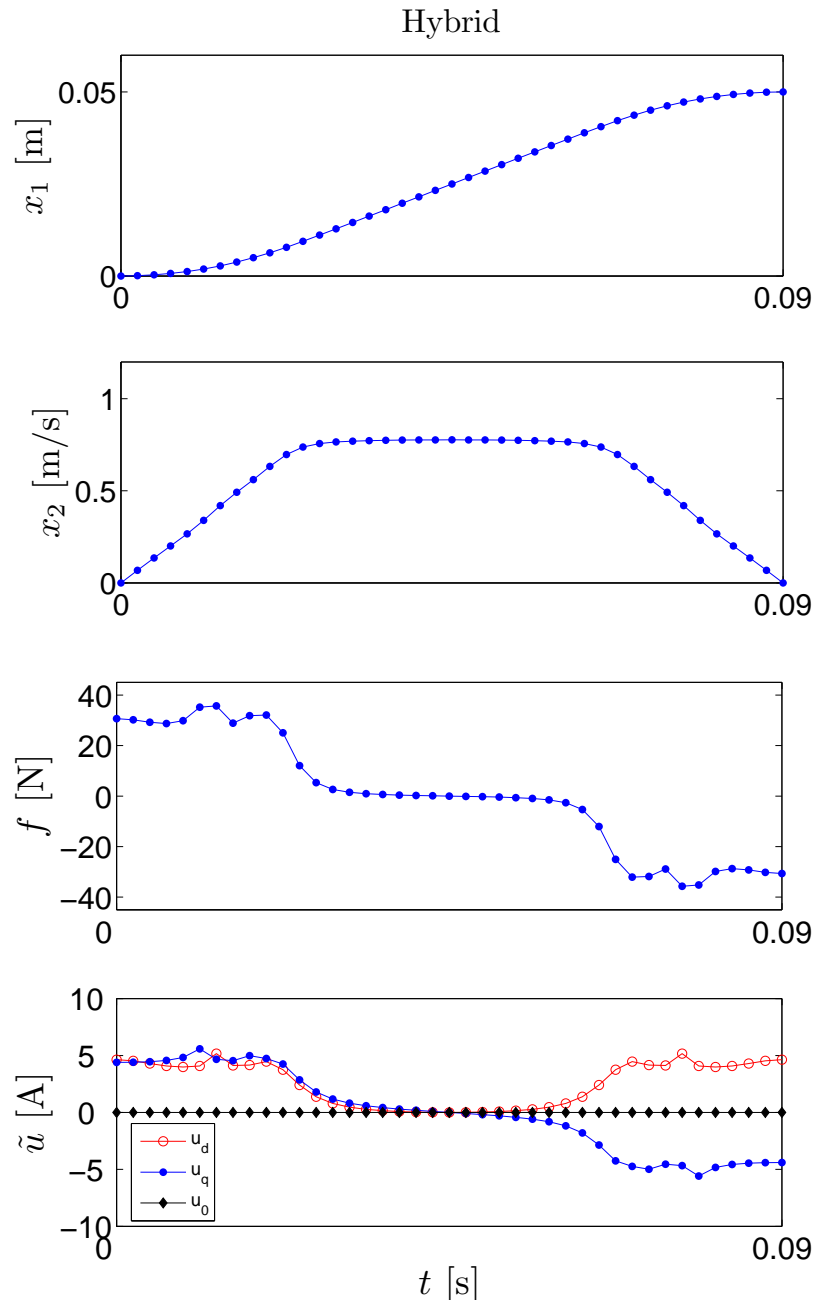


Figure 15: Position, velocity, force and currents for hybrid motor using cubical current limit with 3-wire connection.

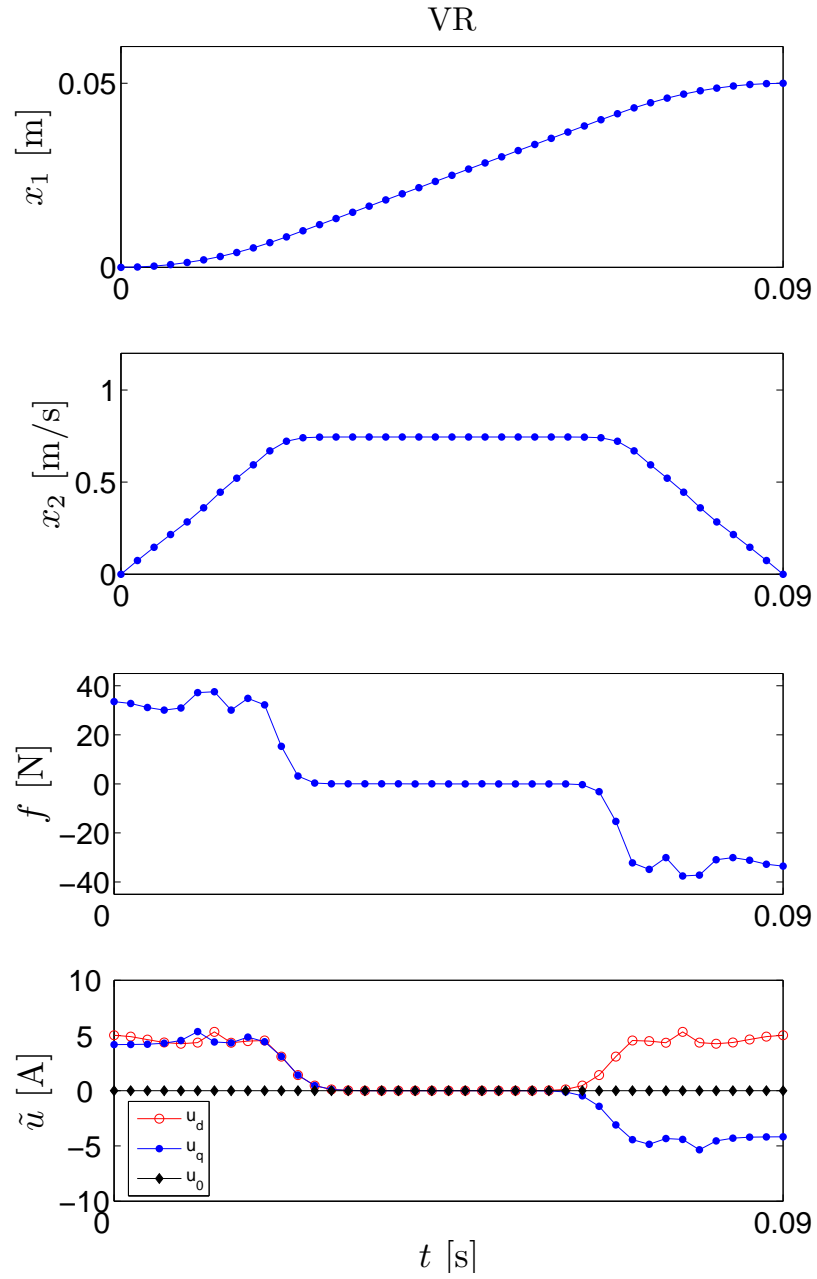


Figure 16: Position, velocity, force and currents for VR motor using cubical current limit with 3-wire connection.

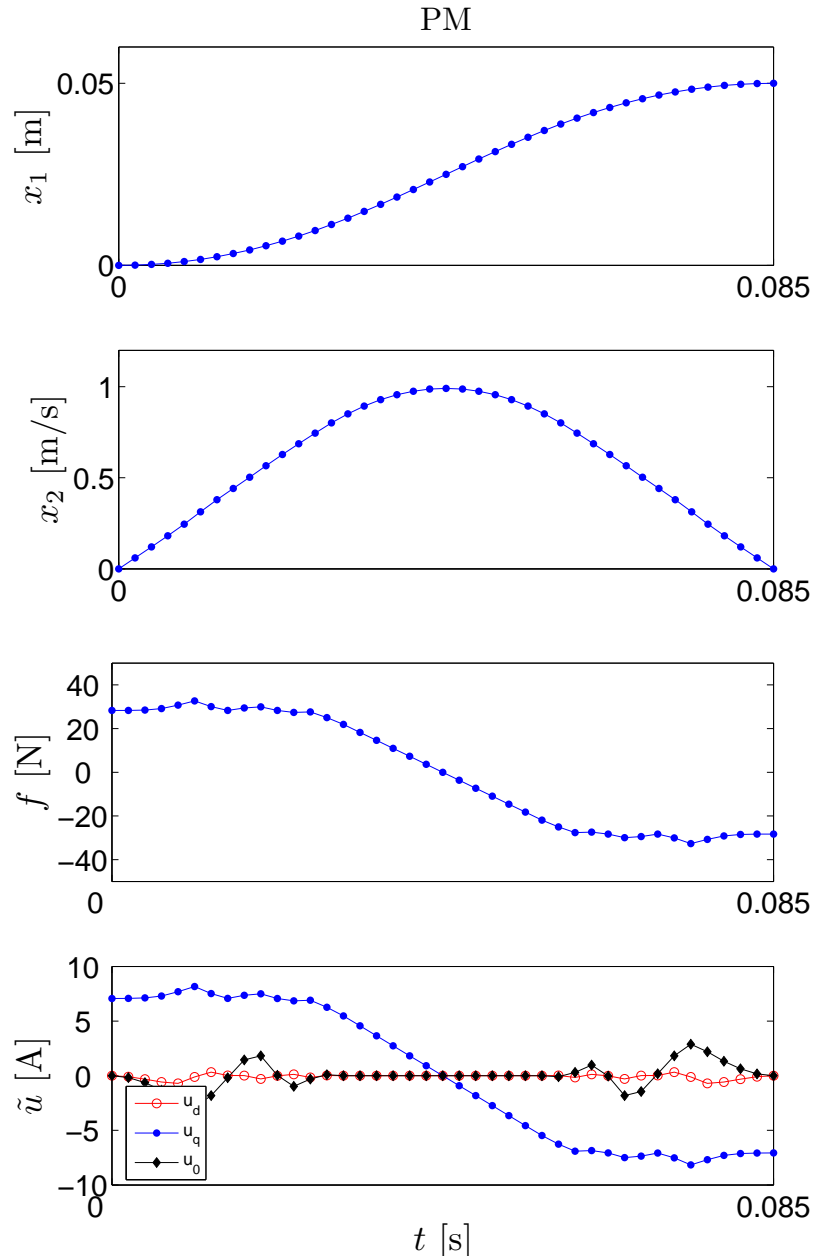


Figure 17: Position, velocity, force and currents for PM motor using cubical current limit with 6-wire connection.

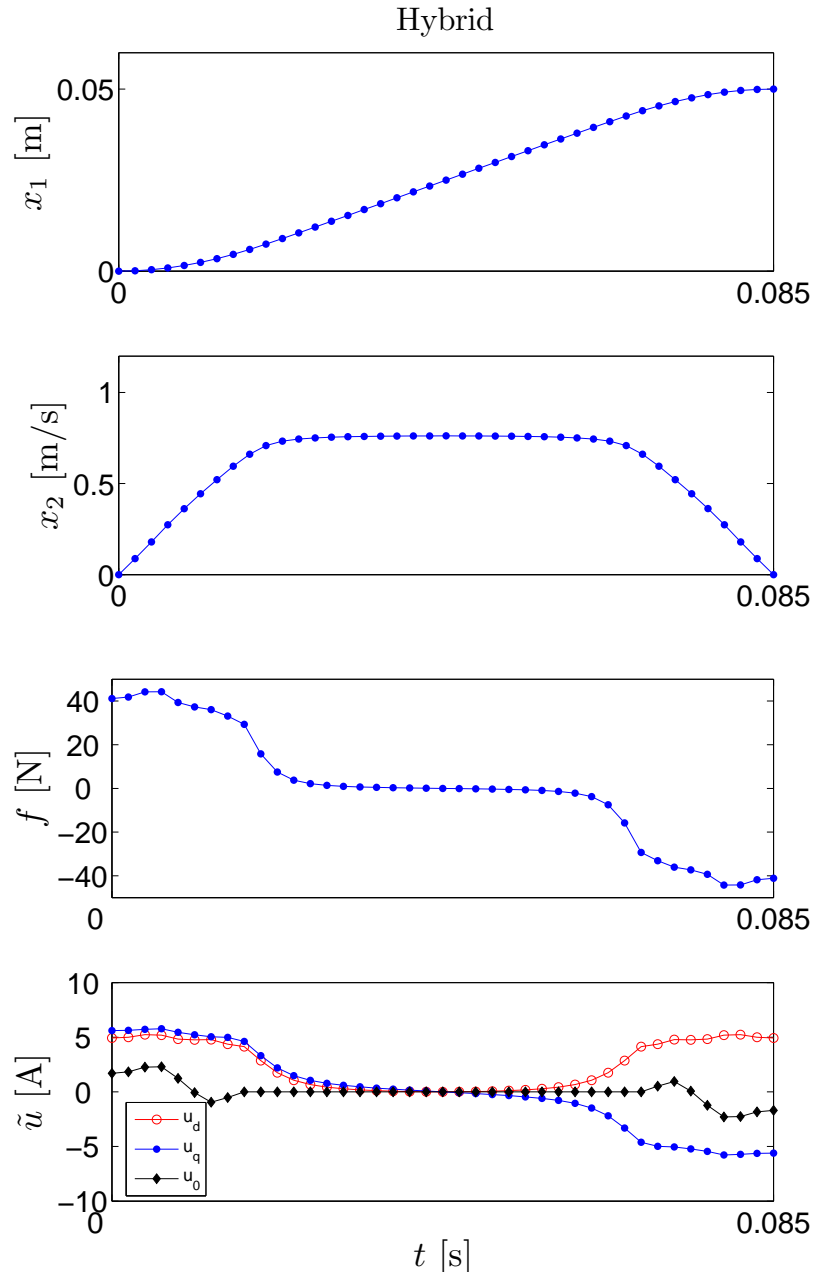


Figure 18: Position, velocity, force and currents for hybrid motor using cubical current limit with 6-wire connection.

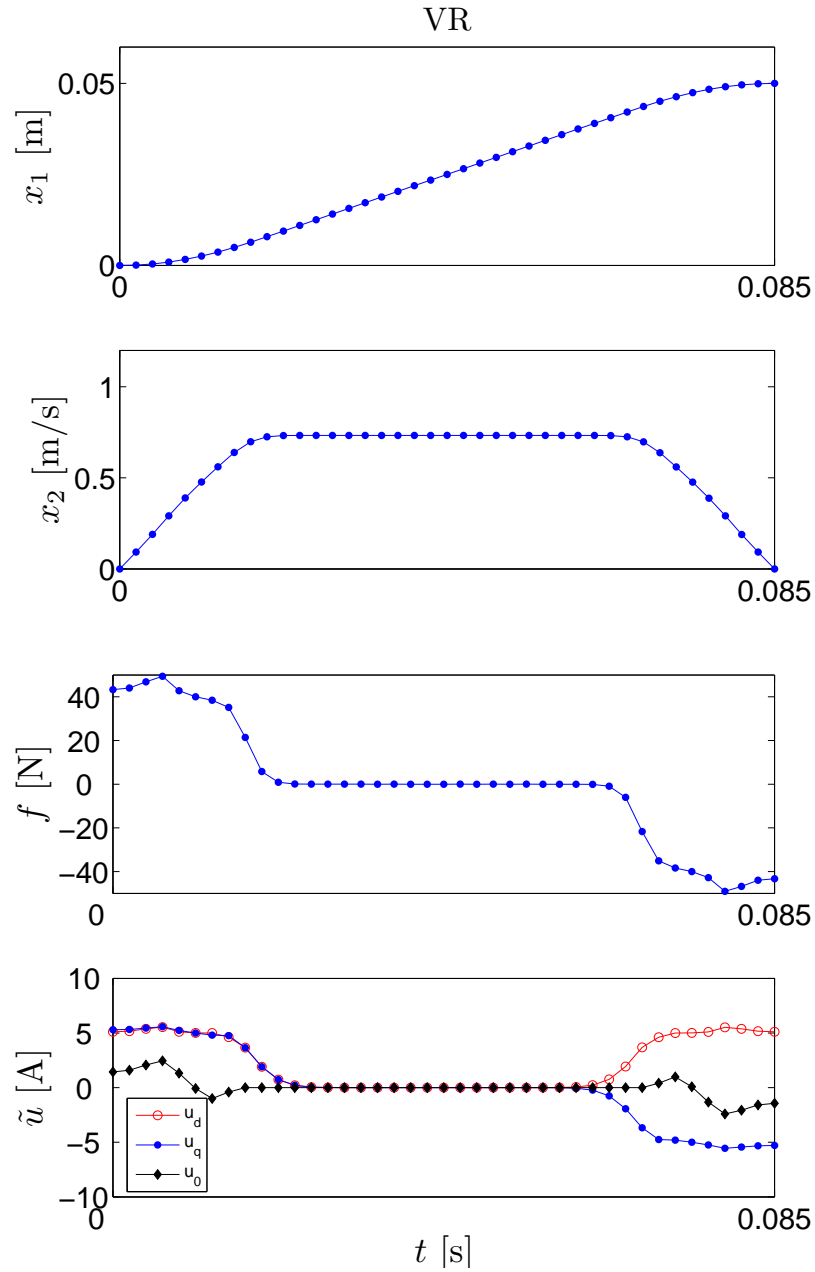


Figure 19: Position, velocity, force and currents for VR motor using cubical current limit with 6-wire connection.

Table 5: Time-Optimal Control

	Sphere		Cube	
	3-wire*	6-wire	3-wire	6-wire
PM:				
T_\star [s]	0.1001	0.1001	0.0857	0.0807
P_\star [W]	119.30	119.30	241.28	339.42
Hybrid:				
T_\star [s]	0.1001	0.1001	0.0790	0.0673
P_\star [W]	120.83	120.83	216.12	326.15
VR:				
T_\star [s]	0.1001	0.1001	0.0766	0.0647
P_\star [W]	120.83	120.83	221.66	331.27

* Analytical results are $T_\star = 0.1$ s and $P_\star = 125$ W for all three motors.

2.7 Optimal Commutation Problem

The commutation problem is concerned with the relationship between force and excitation current. Since there are three phase currents (for a three-phase motor) that combine to produce force, there are many combinations of currents that produce a desired force. Hence, this force control problem may be posed as an optimization problem to determine the optimal commutation strategy.

Two types of optimal commutation problems being investigated here are: (i) maximum force control problem for determining the motor's continuous force limit corresponding to some given current limits and (ii) minimum-copper-loss force control problem for determining current profiles that produce a desired force and minimize power dissipation with or without current limits. These two optimal commutation problems are formulated and solved numerically for 3-wire or 6-wire connection with spherical or cubical current limit. Analytical solutions are also presented for select cases to provide insight and clarity. The optimization results indicate that cubical

current limit and 6-wire are preferable if the goal is to maximize the range of ripple-free and/or average force, or to produce force with minimized losses.

2.7.1 Maximum Force Control

The first optimization problem considered is the maximum force control problem for determining the maximum force at any given position within current limit. The problem is stated for each $x \in [0, 2p]$ as

$$\begin{aligned} & \text{maximize} \quad \pm f(\tilde{u}) \\ & \text{subject to} \quad \tilde{u} \in \mathcal{U} \end{aligned} \tag{112}$$

where the sign of the objective function is chosen to match the desired force sign. Note that the statement of the problem would be meaningless if current limit is not included because the motor, as a force source in theory, can produce an infinite force output if infinite current inputs are given. The solution to this optimization problem has application in time-optimal control because it provides the continuous maximum force corresponding to a given continuous current limit.

Let the solution of the maximum force control problem be denoted by $(\tilde{u}^*(x), f^*(x))$. Three quantities of interest derived from the corresponding solution are maximum smooth force F_s , maximum average force F_a and maximum overall force F_m . Maximum smooth force, or equivalently maximum ripple-free force, is determined according to

$$F_s = \min_{x \in [0, 2p]} f^*(x) \tag{113}$$

Maximum average force is determined according to

$$F_a = \frac{1}{2p} \int_0^{2p} f^*(x) dx \tag{114}$$

and maximum overall force is determined as

$$F_m = \max_{x \in [0, 2p]} f^*(x) \tag{115}$$

In particular, F_s and F_a are considered to accommodate a range of applications. Force ripple may be a concern in some applications, in which case the smaller measure F_s would be appropriate. In other applications, the significant responses may be driven primarily by average rather than instantaneous force, in which case the larger measure F_a would be more appropriate.

Numerical results have been obtained for the same three types of synchronous motors with the maximum force of 20 N for $\tilde{u} \in \mathcal{U}_s$, $p = 0.01$ m and $U = 5$ A. Numerical solutions of (112) are obtained for four cases of \mathcal{U} . Numerical optimization was performed using MATLAB with Optimization Toolbox. The plots of corresponding physical currents are calculated by (29).

Plots of force maximizing currents and resulting (positive) force for each synchronous motor, with $\tilde{u} \in \mathcal{U}_s$ and either 3-wire or 6-wire connection, are shown in Figures 20-22. Both 3-wire and 6-wire connections yield identical results and the maximum force for all cases is 20 N as expected.

Plots of force maximizing currents and resulting force for each synchronous motor, with $\tilde{u} \in \mathcal{U}_c$, are shown in Figures 23-25 for 3-wire connection and in Figures 26-28 for 6-wire connection. The 3-wire and 6-wire results differ from each other and the maximized force for the 6-wire connection exceeds the maximized force for the 3-wire connection at every position for all synchronous motors.

For PM motor in Figure 23 and Figure 26, the optimal physical currents are square waves and the resulting force has a semi-circle like shape in the force ripples. The motor operates with $u_0 = 0$ for 3-wire connection and $u_0 = \pm U/\sqrt{3}$ for 6-wire connection. These results are consistent with previous discussion.

For VR motor in Figure 25 and Figure 28, the optimal physical currents are trapezoidal and the resulting maximized force varies sinusoidally about a maximized average value. The motor operates with $u_0 = 0$ for 3-wire connection and u_0 varies between $+U/\sqrt{3}$ and $-U/\sqrt{3}$ for 6-wire connection.

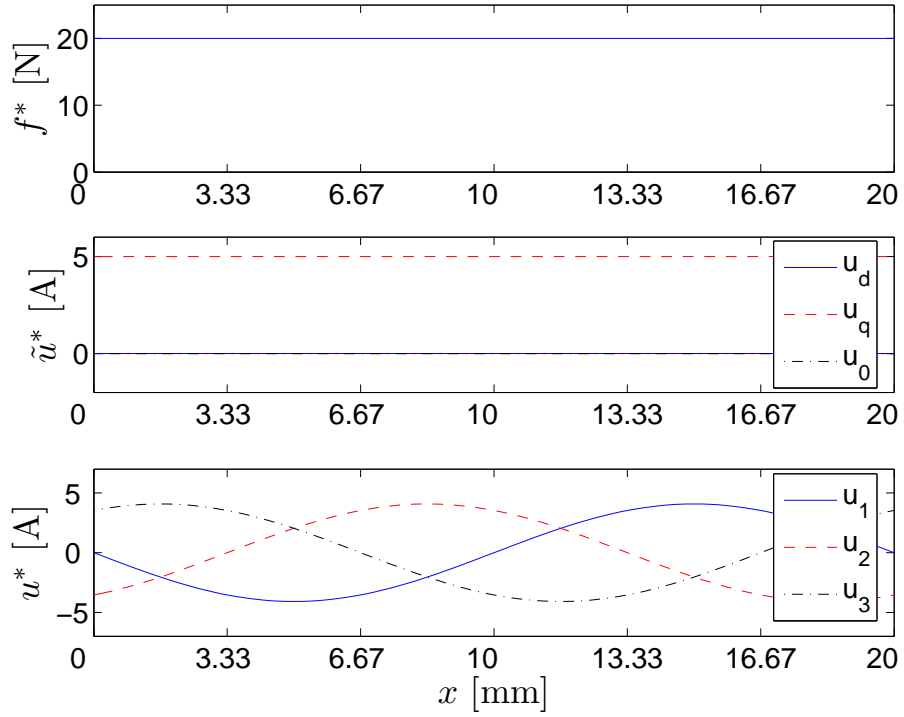


Figure 20: Force maximizing currents and resulting force of the PM motor for 3-wire and 6-wire connection with spherical current limit.

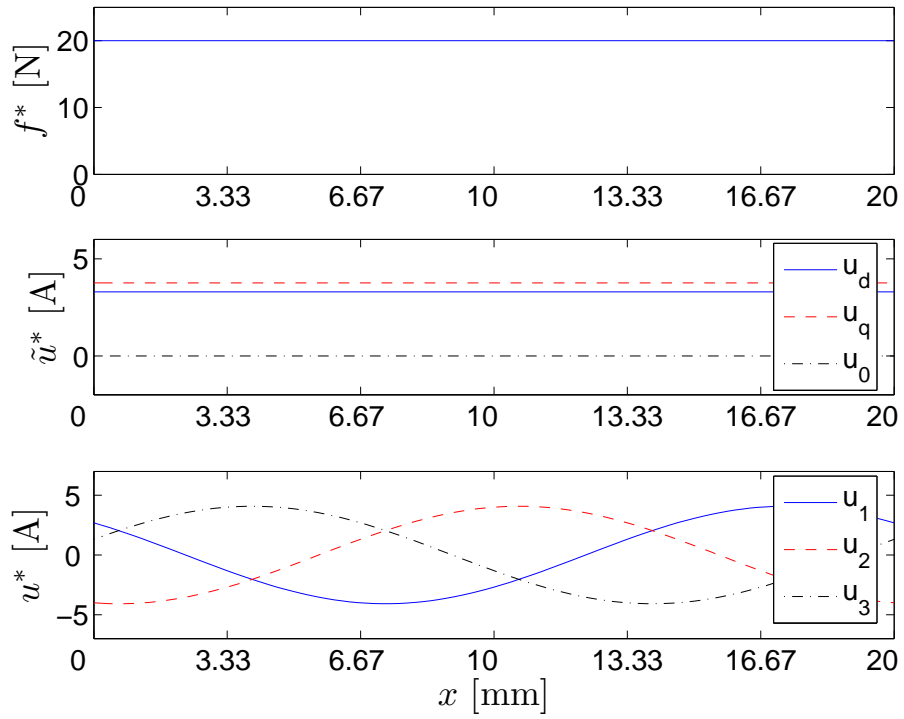


Figure 21: Force maximizing currents and resulting force of the hybrid motor for 3-wire and 6-wire connection with spherical current limit.

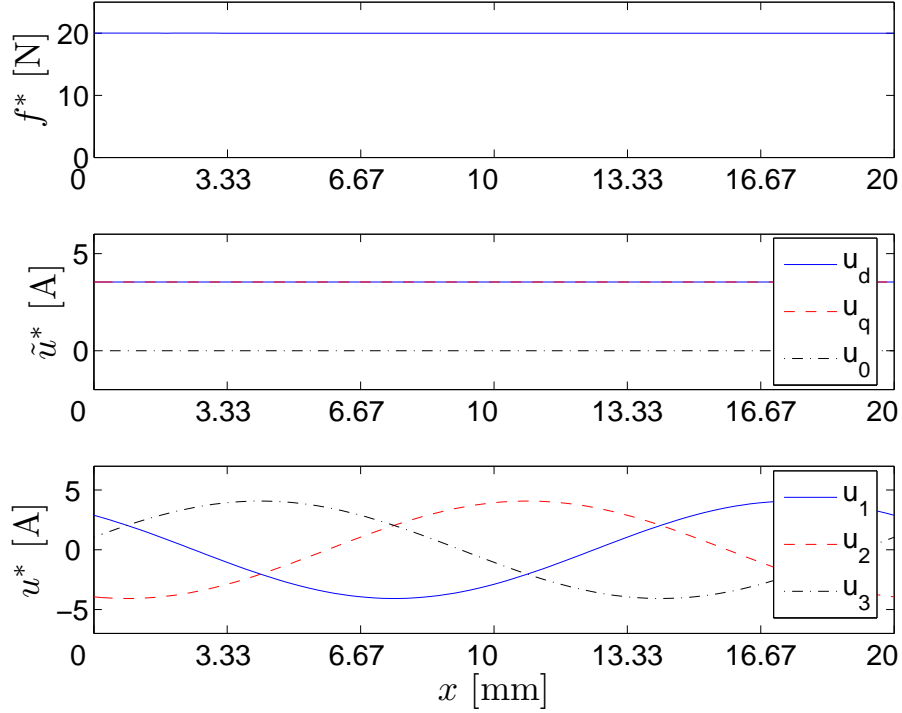


Figure 22: Force maximizing currents and resulting force of the VR motor for 3-wire and 6-wire connection with spherical current limit.

For the hybrid motor in Figure 24 and Figure 27, the optimal current profile is more “similar” to the VR than the PM motor with small phase shift, depending on the ratio of the force constant K_a and K_r . The corresponding numerical values of F_s , F_a and F_m for all cases are listed in Table 6. All values for the 6-wire connection exceed the maximized force for the 3-wire using cubical current limit. Notice the continuity condition where F_m for the 3-wire connection is equal to F_s for the 6-wire connection.

2.7.2 Minimum-Copper-Loss Force Control without Current Limit

Motivated by the desire to limit production of heat for the target application, the next optimal commutation problem considered is to find currents that produce a given desired force with minimum power dissipation. First, the commutation scheme selected here minimizes instantaneous copper loss and does not consider any current

Table 6: Maximum Force Control with Spherical and Cubical Current Limits

Sphere		Cube					
3/6-wire		3-wire			6-wire		
$F_s/F_a/F_m$		F_s	F_a	F_m	F_s	F_a	F_m
PM	20	24.49	27.01	28.28	28.28	31.19	32.66
Hybrid	20	28.72	32.95	37.29	37.29	42.84	48.56
VR	20	30.00	34.84	40.00	40.00	46.45	53.33

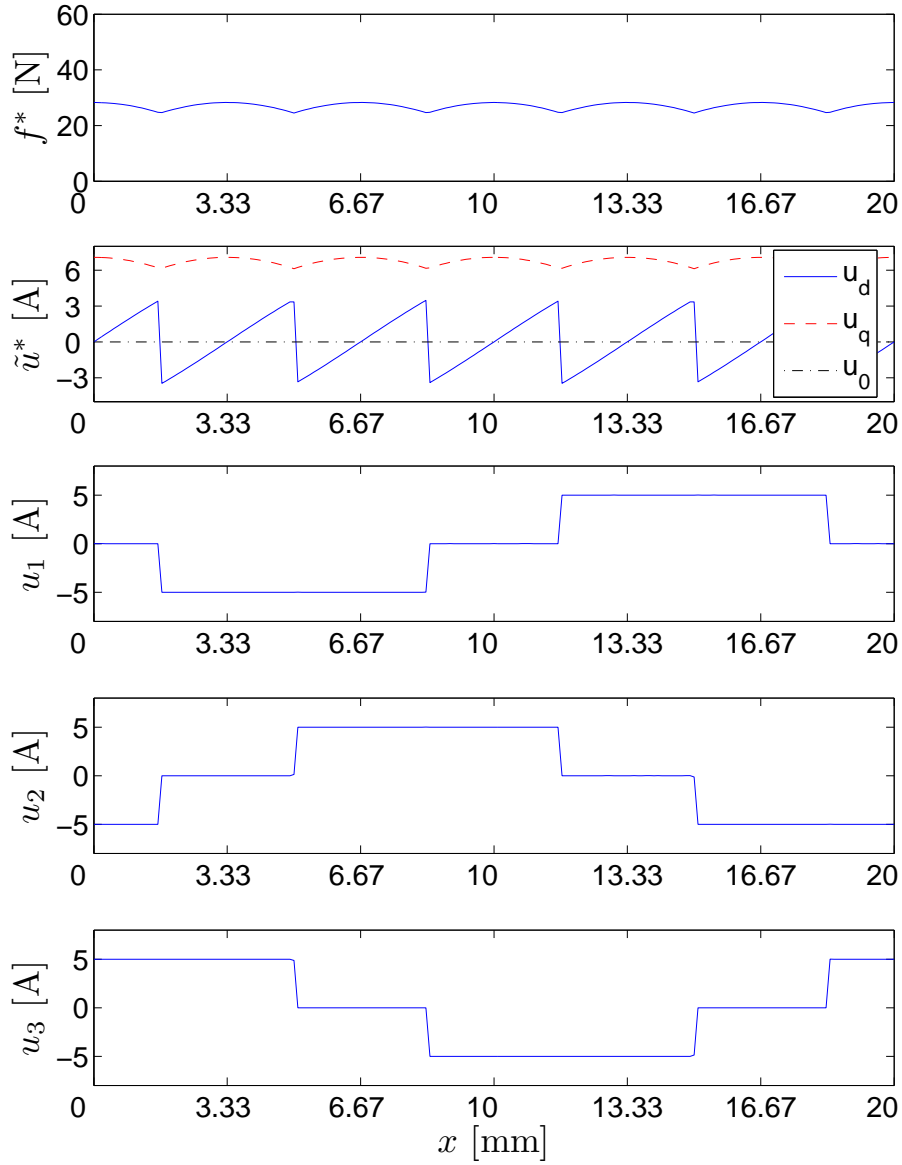


Figure 23: Force maximizing currents and resulting force of the PM motor for 3-wire connection with cubical current limit.

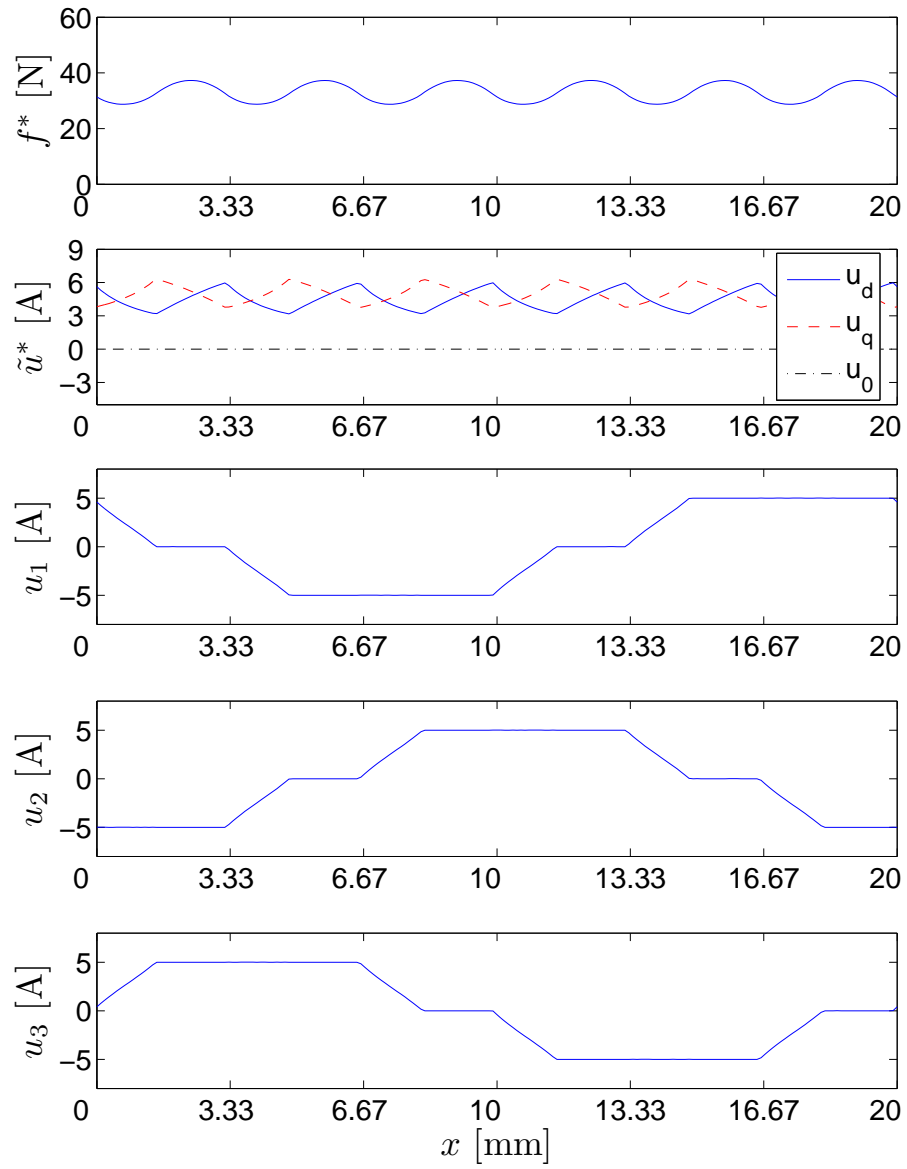


Figure 24: Force maximizing currents and resulting force of the hybrid motor for 3-wire connection with cubical current limit.

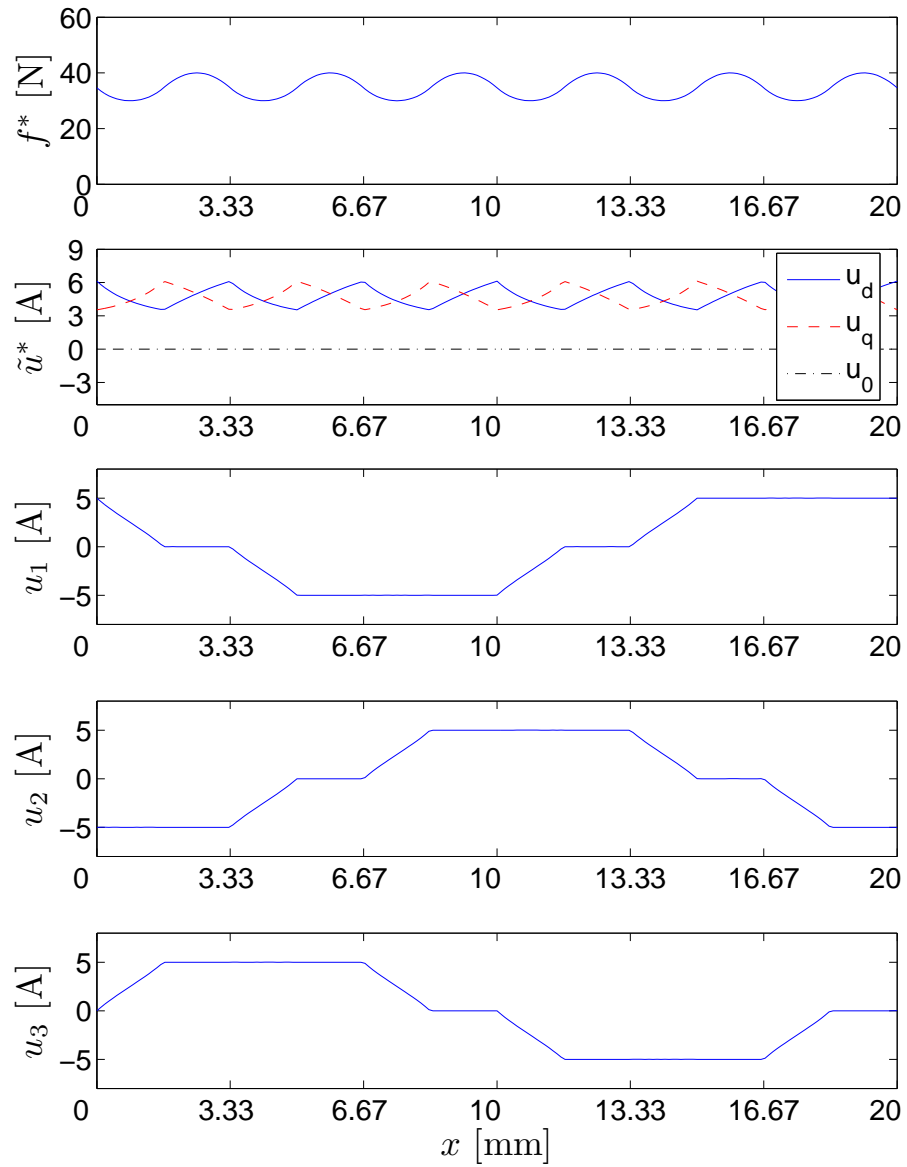


Figure 25: Force maximizing currents and resulting force of the VR motor for 3-wire connection with cubical current limit.

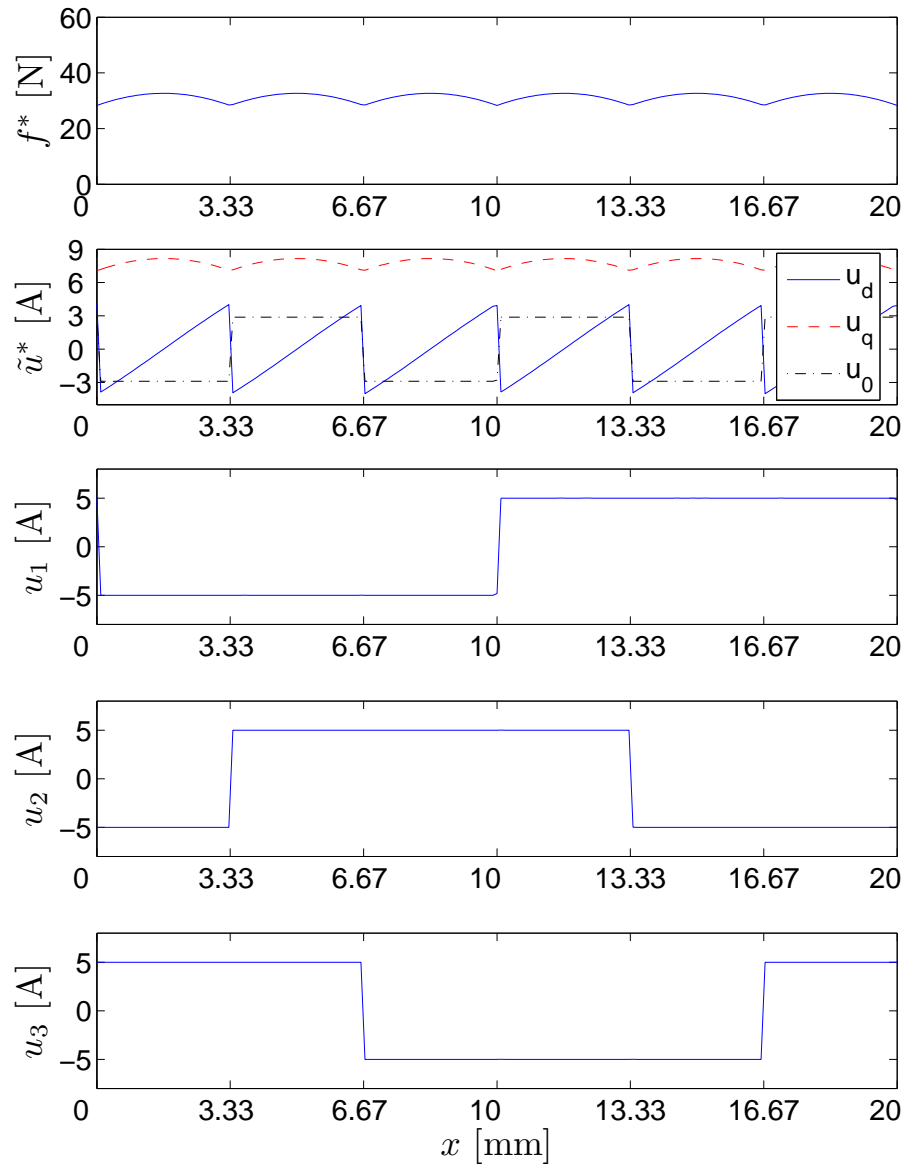


Figure 26: Force maximizing currents and resulting force of the PM motor for 6-wire connection with cubical current limit.

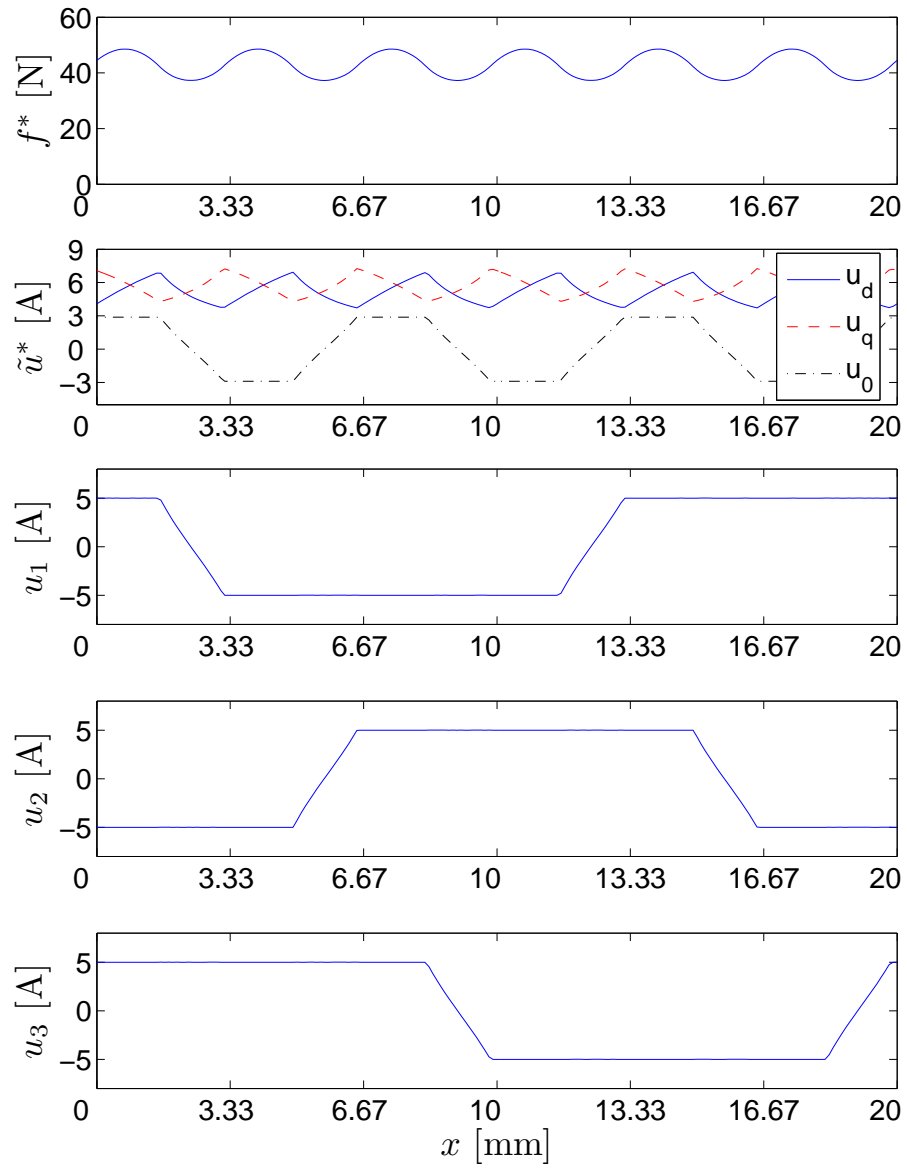


Figure 27: Force maximizing currents and resulting force of the hybrid motor for 6-wire connection with cubical current limit.

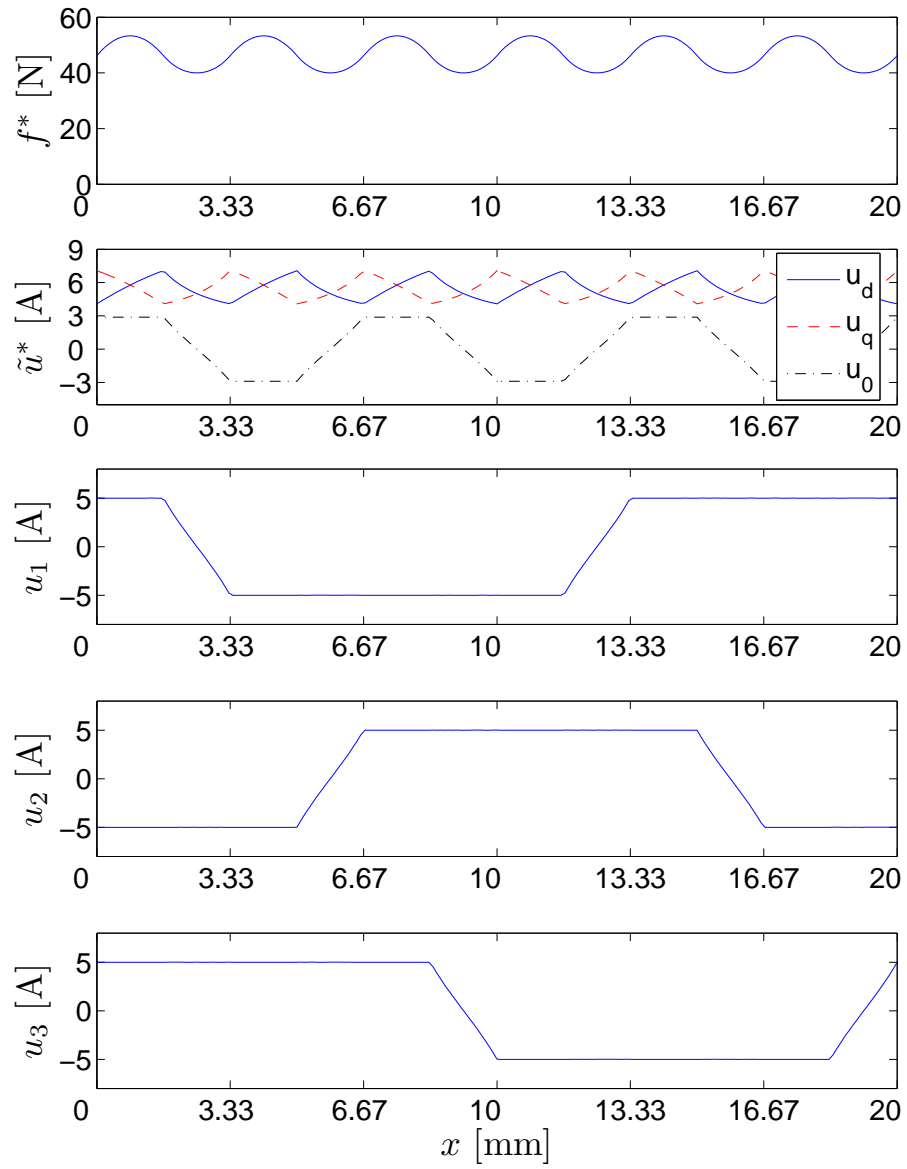


Figure 28: Force maximizing currents and resulting force of the VR motor for 6-wire connection with cubical current limit.

limit. This problem can be stated for each $x \in [0, 2p]$ as

$$\begin{aligned} & \text{minimize} \quad \tilde{u}^T \tilde{u} \\ & \text{subject to} \quad f(\tilde{u}) = f_d \end{aligned} \quad (116)$$

where f_d is any given desired force command. Although this problem falls into the general category of nonlinear constrained optimization problems [41] where it is customary to introduce the Lagrangian at this point, the special structure of (116) may be exploited to simplify the problem.

Using force model (27), where PM, VR and hybrid motors are accounted for,

$$K_a u_q + K_r u_q u_d = u_q (K_a + K_r u_d) = f_d \Rightarrow u_q = \frac{f_d}{K_a + K_r u_d} \quad (117)$$

hence (116) reduces to

$$\text{minimize} \quad \left(\frac{f_d}{K_a + K_r u_d} \right)^2 + u_d^2 \quad (118)$$

which is merely a single variable optimization problem. By applying derivative with respect to u_d , the first-order necessary condition and the optimal solution may be obtained. Three separate cases are separately considered as follows:

If $K_r = 0$ (PM motor), the solution is

$$u_d = 0 \quad (119)$$

$$u_q = f_d / K_a \quad (120)$$

$$u_0 = 0 \quad (121)$$

If $K_a = 0$ (VR motor), the solution is

$$u_d = \sqrt{|f_d| / K_r} \quad (122)$$

$$u_q = \text{sign}(f_d) \sqrt{|f_d| / K_r} \quad (123)$$

$$u_0 = 0 \quad (124)$$

If $K_a \neq 0$ and $K_r \neq 0$ (hybrid motor), the complexity of the problem prohibits a simple explicit solution formula. However, application of the first-order necessary condition leads to

$$u_d = \nu \quad (125)$$

$$u_q = \frac{f_d}{K_a + K_r \nu} \quad (126)$$

$$u_0 = 0 \quad (127)$$

where ν is a solution of

$$\nu(K_a + K_r \nu)^3 = K_r f_d^2 \quad (128)$$

Since (128) admits four solutions, the value of ν to be used in (125)-(126) is the real solution of (128) that minimizes

$$\nu^2(K_a + K_r \nu)^2 \quad (129)$$

Note that the solutions for the PM and VR motors are captured as special cases of the solution for the hybrid motor and all solutions lie on the $u_0 = 0$ plane (i.e. both 3-wire and 6-wire connections are equivalent).

2.7.3 Minimum-Copper-Loss Force Control with Current Limits

The next optimal commutation problem considered is to find magnitude-constrained currents that produce a given desired force and also minimize the power dissipation due to copper loss. The problem now includes current limit and can be stated for each $x \in [0, 2p]$ as

$$\begin{aligned} & \text{minimize} && \tilde{u}^T \tilde{u} \\ & \text{subject to} && f(\tilde{u}) = f_d \\ & && \tilde{u} \in \mathcal{U} \end{aligned} \quad (130)$$

where the given desired force command satisfies $f_d \leq F_s$ where F_s is the ripple-free force limit defined in (113). Due to the complexity introduced by current limits, only numerical results are pursued.

The minimum-copper-loss force control problems have been solved for the same three types of synchronous motors with the maximum force of 20 N for $\tilde{u} \in \mathcal{U}_s$, $p = 0.01$ m and $U = 5$ A. The optimal excitation currents are solved for $f_d = 0.95F_s$ for all three synchronous motors, with reference to Table 6. Numerical optimization was performed using MATLAB with Optimization Toolbox. The optimal excitation currents are denoted by \tilde{u}^* with the corresponding physical currents calculated by (29).

Plots of optimal excitation currents for each synchronous motor with $\tilde{u} \in \mathcal{U}_s$ and either 3-wire or 6-wire connection, are shown in Figure 29. Both 3-wire and 6-wire connection yield identical results and the optimal d/q -axis currents are constant corresponding to sinusoidal physical currents. For both 3-wire and 6-wire connections, it is apparent that the force command cannot exceed $F_s = 20$ N and $u_0 = 0$ for all cases which is consistent with previous discussions.

Plots of optimal excitation currents for each synchronous motor with $\tilde{u} \in \mathcal{U}_c$ are shown in Figure 30 for 3-wire connection and in Figure 31 for 6-wire connection. In the 6-wire case, larger force commands are possible since u_0 can be non-zero and hence the optimal currents are not restricted to the u_0 plane.

2.7.4 Spatial Average Power Dissipation

Consider the spatial average power dissipation defined as

$$P_x(f_d) = \frac{R}{2p} \int_0^{2p} \tilde{u}^{*T} \tilde{u}^* dx \quad (131)$$

where \tilde{u}^* is the solution to the minimum-copper-loss commutation problem just discussed (with or without current limit). Since \tilde{u}^* depends on f_d , P_x inherently also depends on f_d . Although at first glance P_x does not seem to relate to the dynamic behavior of the motor, in fact P_x has a very special interpretation under constant velocity mode of operation.

Let $X = 2p$ be the spatial period and T be the time period corresponding at

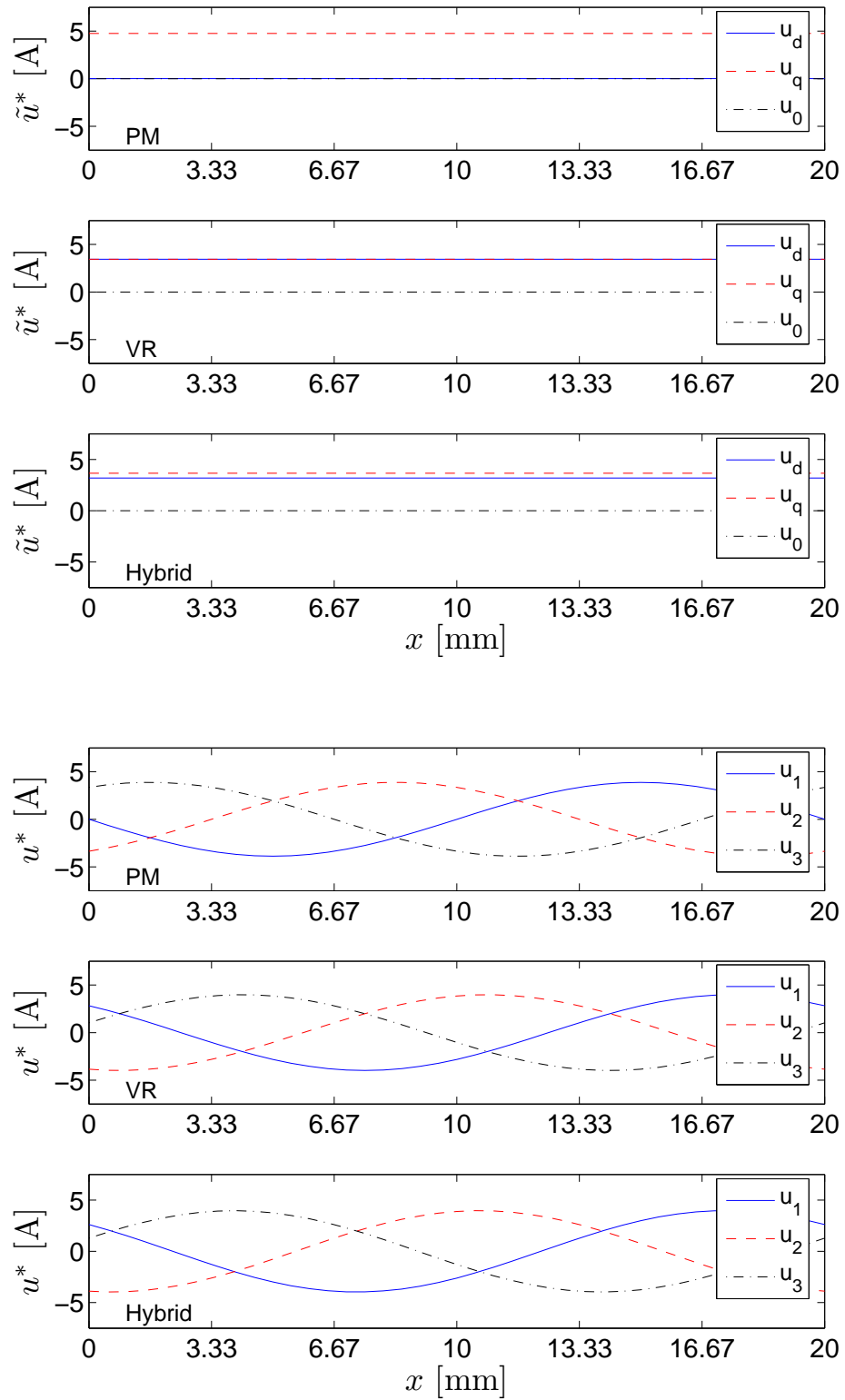


Figure 29: Currents for $f_d = 0.95F_s$ for 3-wire and 6-wire connection for three synchronous motors with spherical current limit ($F_s = 20$ N for all cases).

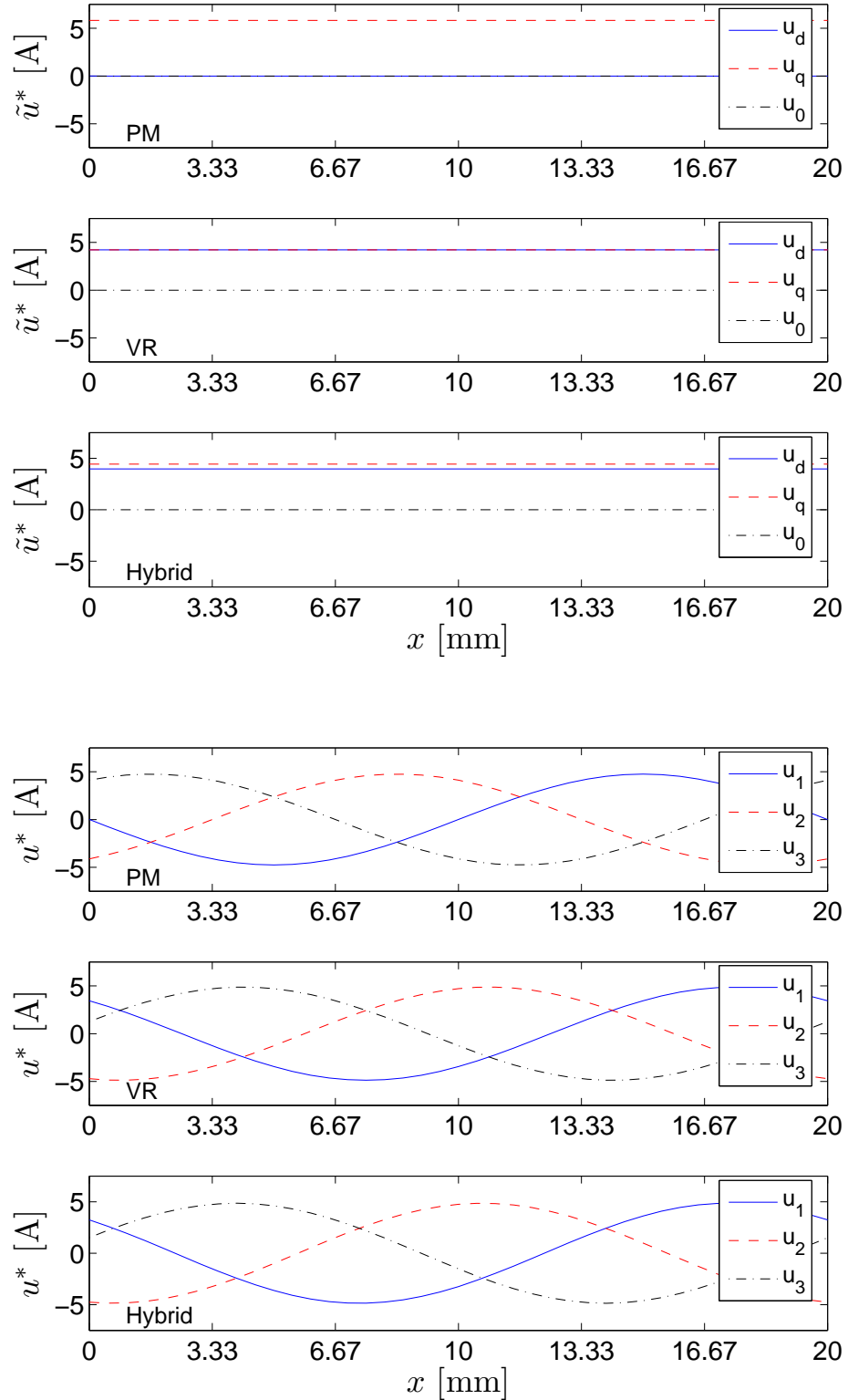


Figure 30: Currents for $f_d = 0.95F_s$ for 3-wire connection for three synchronous motors with cubical current limit (see Table 6 for the corresponding values of F_s for each motor).

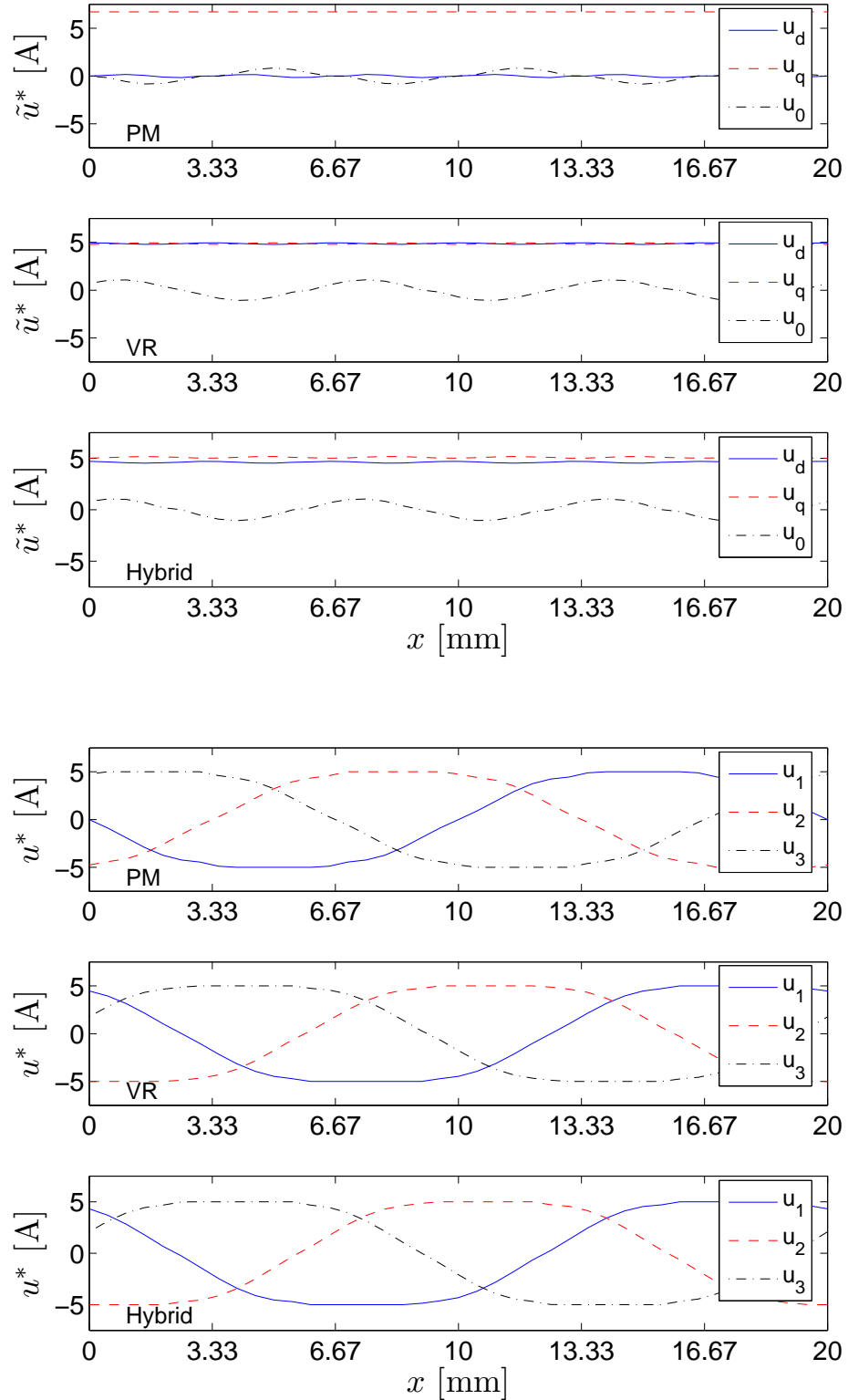


Figure 31: Currents for $f_d = 0.95F_s$ for 6-wire connection for three synchronous motors with cubical current limit (see Table 6 for the corresponding values of F_s for each motor).

constant velocity v . Consider the change of variables

$$\frac{dx}{dt} = v = \frac{X}{T} \Rightarrow \begin{cases} x = 0 & \rightarrow t = 0 \\ x = X & \rightarrow t = T \end{cases} \quad (132)$$

Then the spatial average power

$$\begin{aligned} P_x &= \frac{R}{X} \int_0^X \tilde{u}^T \tilde{u} \, dx \\ &= \frac{R}{vT} \int_0^T \tilde{u}^T \tilde{u} \, v \, dt \\ &= \frac{R}{T} \int_0^T \tilde{u}^T \tilde{u} \, dt \quad := P \end{aligned}$$

is equivalent to the average power previously defined in (30)-(31) using the time variable. Two cases of PM and VR motor are considered next due to availability of their explicit solutions.

From (119)-(121), (122)-(124) and (131), the spatial average powers of the PM and VR motor without current limit are given by

$$P_x(f_d) = \begin{cases} \frac{R}{K_a^2} f_d^2 & , \text{ PM motor} \\ \frac{2R}{K_r} f_d & , \text{ VR motor} \end{cases} \quad (133)$$

which is a parabola for PM motor and a straight line for VR motor on the P_x - f_d plane.

The spatial average powers of the PM and VR motor with current limit must rely on numerical solutions. Note that in this case the P_x - f_d curve is only defined for $f_d \leq F_s$. For each value of f_d , there is a corresponding value of P_x ; hence for $0 \leq f_d \leq F_s$, there also exists a corresponding P_x - f_d curve.

The comparative results for the PM and VR motor are shown in Figure 32 for spherical current limit with both 3-wire and 6-wire connection. The results for cubical current limit are shown in Figure 33 for 3-wire connection and Figure 34 for 6-wire connection. The numerical results are obtained for $0 \leq f_d \leq 0.99F_s$. When f_d is small, both minimum-copper-loss commutation problems with and without current limit

admit the same solutions. When the value of f_d increases near F_s , a small deviation between the two solutions becomes noticeable only for 6-wire connection with cubical current limit. Since magnetic saturation and spatial harmonics are absent from the ideal force model, these deviations are caused by the active current constraints.

In addition, the average slope of the P_x - f_d curve for $0 \leq f_d \leq F_s$, defined as

$$s = \frac{1}{F_s} \int_0^{F_s} \frac{dP_x}{df_d} df_d = \frac{1}{F_s} P_x \Big|_{F_s} = \frac{P_x(F_s)}{F_s} \quad (134)$$

is also shown for PM motor cases, whereas the average slope is not shown for VR motor cases due to overlapping.

In all figures, a data point which belongs to the minimum-copper-loss *average* force control problem is also shown for comparison. This problem accepts desired force command $f_d > F_s$ and satisfies the force command on average. The plots indicate that the solutions to this problem dissipate more heat when the cubical current limit is used and dissipate the same amount of heat when the spherical current limit is used.

2.8 Conclusion

The minimum-copper-loss position control problem has been formulated and solved analytically and numerically for a class of synchronous motors. The results provide insight regarding the distinctions between synchronous motor types, their current limits and their winding connections, in the context of optimal control. The optimal control results indicate that cubical current limit and 6-wire are preferable if the goal is to minimize the average power dissipation subject to the same travel time and same travel distance.

In addition, two optimal commutation problems, maximum force control and minimum-copper-loss force control, are formulated and solved for the same class of synchronous motors. The optimization results also indicate that cubical current limit and 6-wire are preferable if the goal is to maximize the range of ripple-free and/or

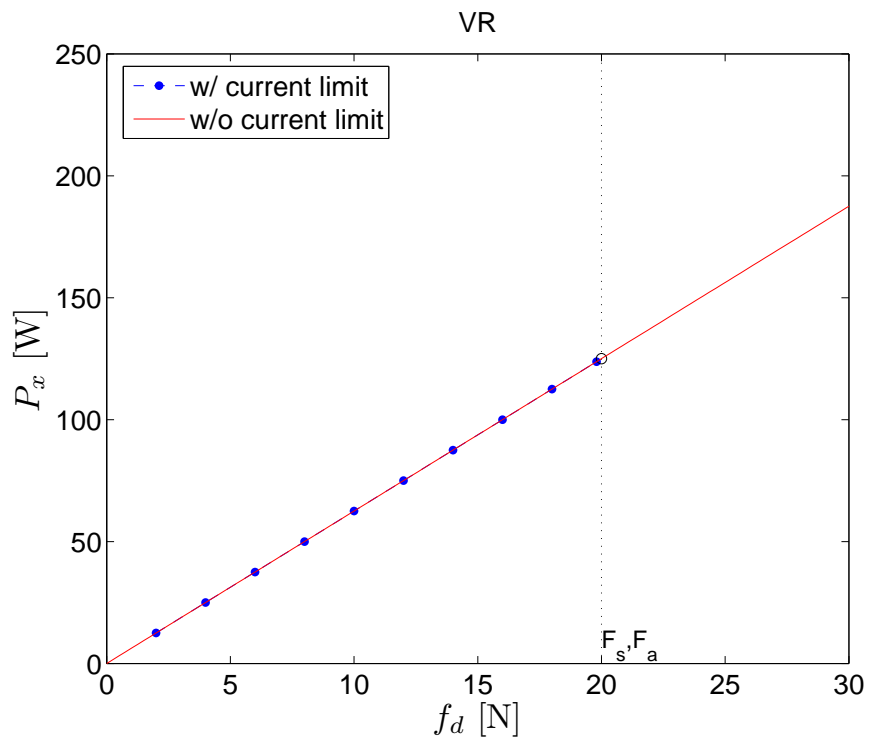
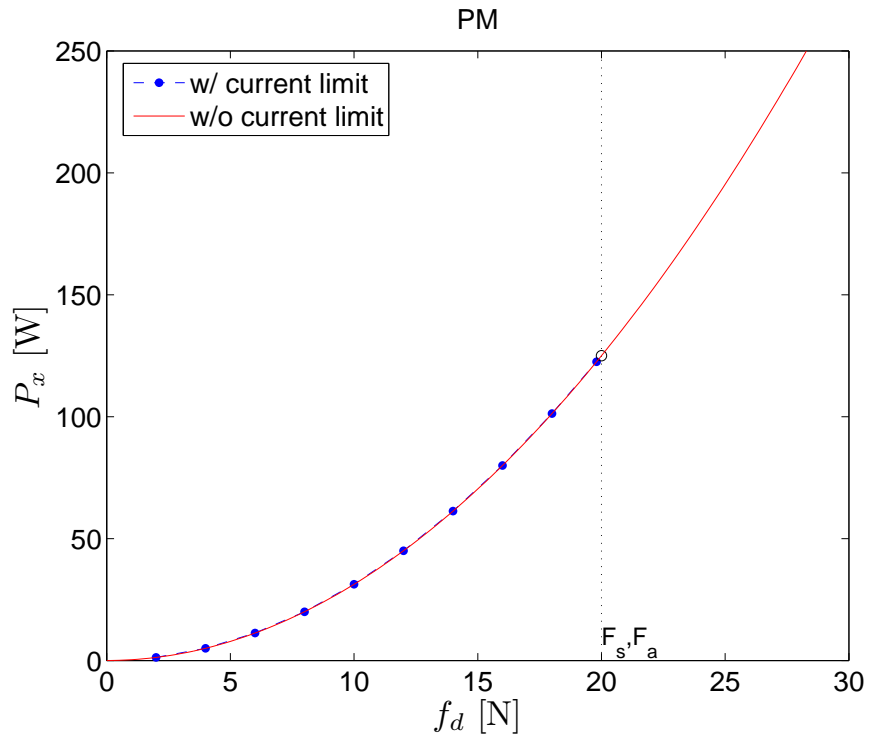


Figure 32: Spatial average power dissipation versus desired force command for PM and VR motor with 3/6-wire connection and spherical current limit.

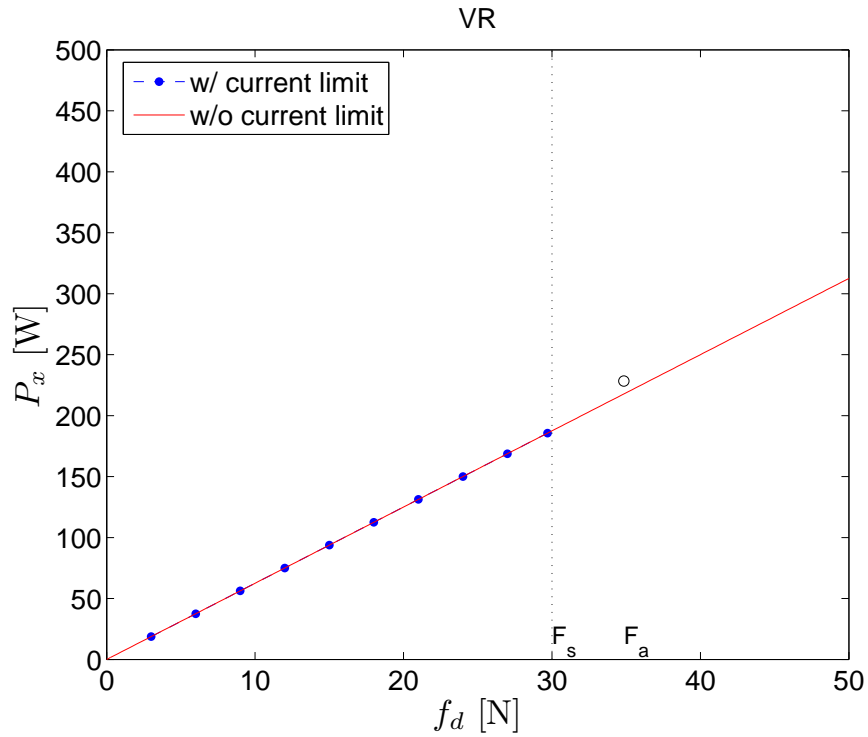
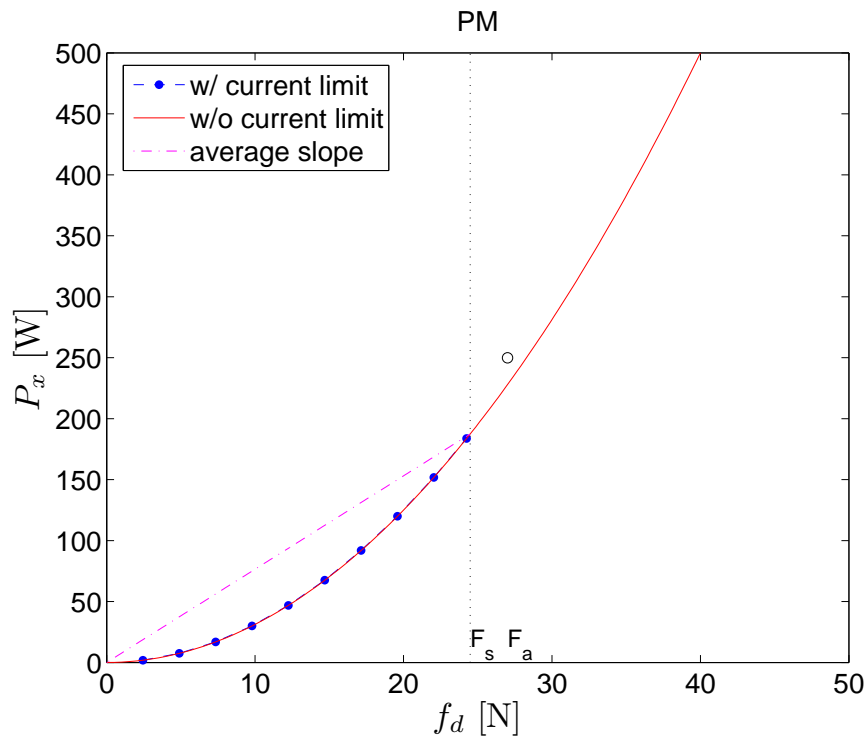


Figure 33: Spatial average power dissipation versus desired force command for PM and VR motor with 3-wire connection and cubical current limit.

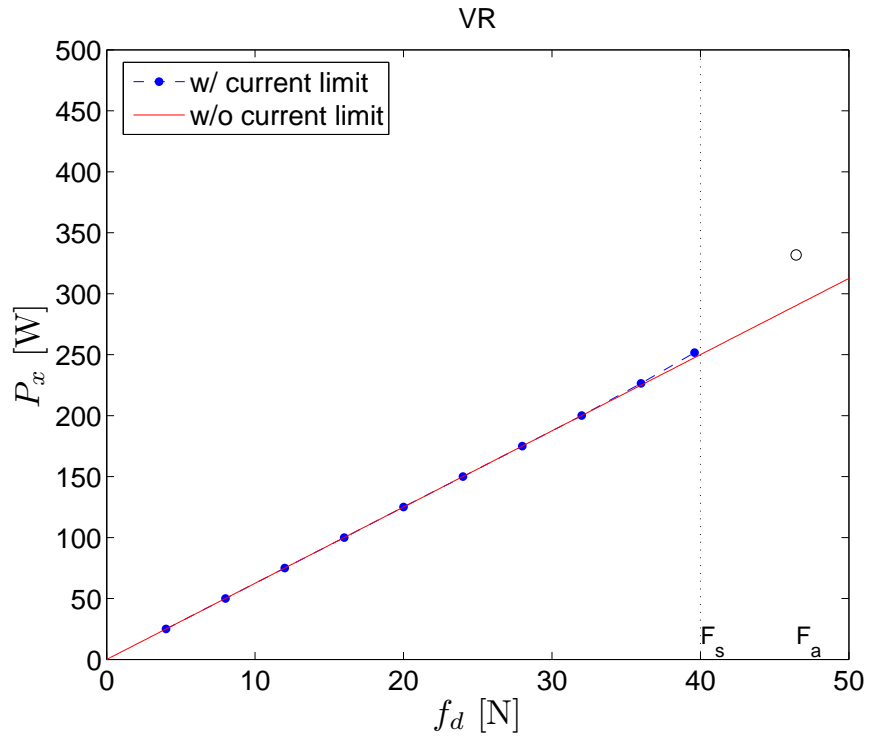
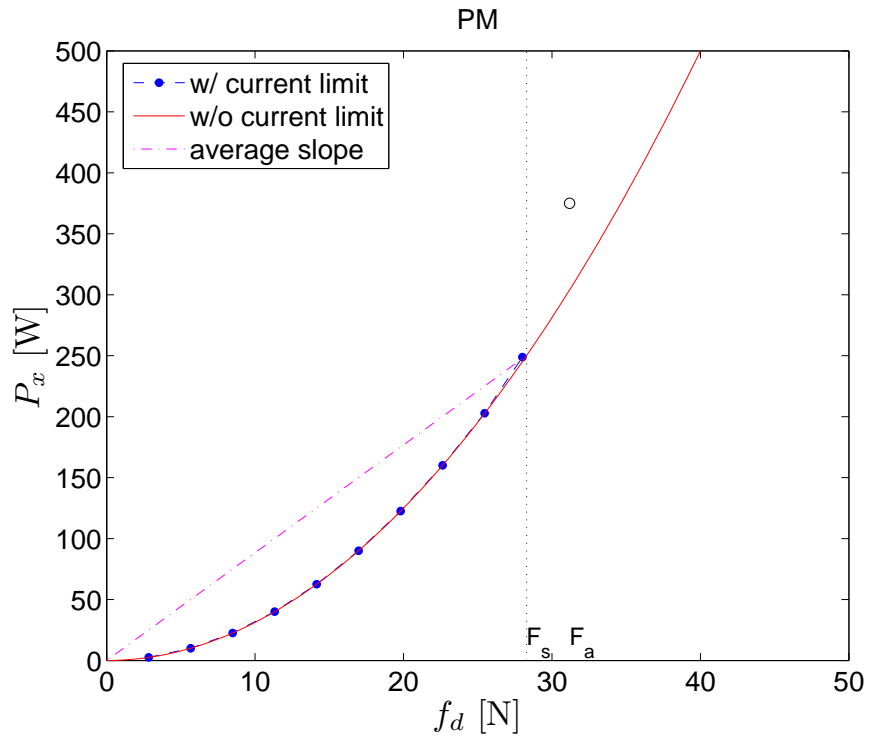


Figure 34: Spatial average power dissipation versus desired force command for PM and VR motor with 6-wire connection and cubical current limit.

average force. These results will be used later to assess the performance of the motors during the motor design process.

Since the force equation is essentially equivalent to that of idealized rotary synchronous motors, the analysis is valid for both linear and rotary motors and hence the term “linear” is dropped for convenience.

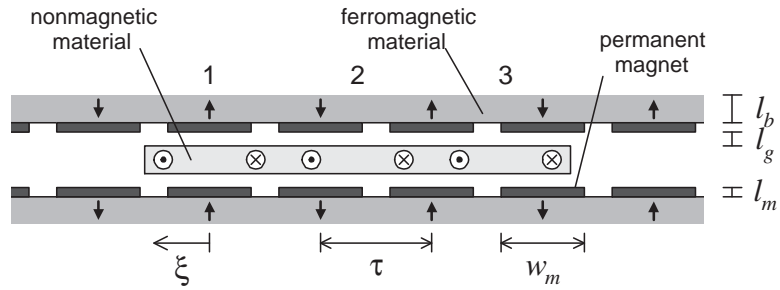
CHAPTER 3

MAGNETIC MODELING

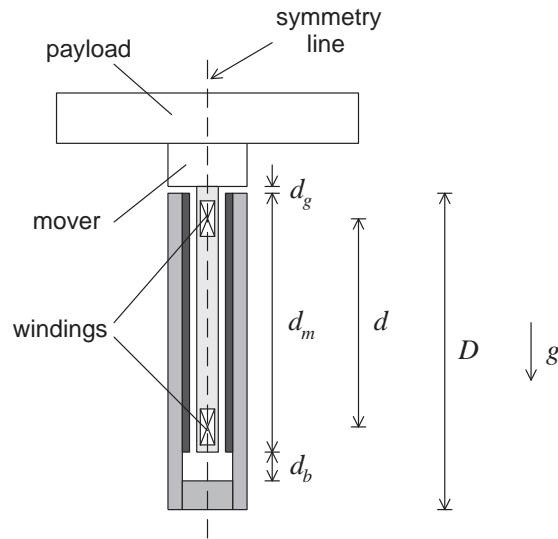
The physics-based force models for LPM and LVR motors are derived in this chapter. For the LPM motor, the Poisson equation is solved to determine the air gap flux density according to [25], and an integration of this flux density is performed to evaluate the Lorentz force. Only spatial harmonics are considered due to magnetic linearity from the construction of the coil assembly with nonmagnetic materials. For the LVR motor, the force model is based on nonlinear magnetic circuit analysis (MCA) [20] to account for spatial harmonics and material saturation. The accuracy of the force models of the LPM and LVR motors are compared with results from finite element analysis (FEA) [18, 19].

3.1 Modeling of Linear Permanent-Magnet Motor

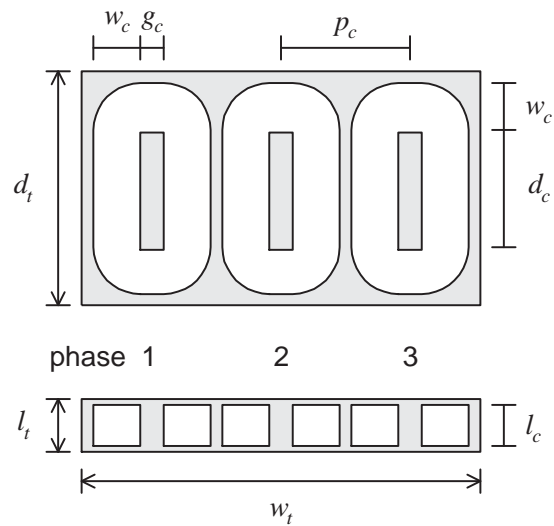
The LPM motor under consideration is shown in Figure 35. The stator consists of ferromagnetic material formed in a U-shaped frame on which PM pairs are placed with alternating polarity. The payload is attached to the moving coil assembly which consists of three concentrated coil windings encapsulated in a casing of nonmagnetic material (e.g. epoxy resin), resulting in zero cogging force. Coil pitch p_c and magnet pitch τ are related by $p_c = \frac{4}{3}\tau$. Position ξ is defined such that $\xi = 0$ is an equilibrium position imposed by positive current in phase 1 and increasing ξ corresponds to leftward motion.



(a) Top view, with payload removed.



(b) Front view, with payload attached.



(c) Concentrated windings encased in epoxy.

Figure 35: Air-core LPM motor with concentrated windings.

3.1.1 Poisson Equation

The classical description of static magnetic fields is provided by Maxwell's equations

$$\nabla \times \mathbf{H} = \mathbf{J} \quad (135)$$

$$\nabla \cdot \mathbf{B} = 0 \quad (136)$$

where \mathbf{H} is magnetic field intensity, \mathbf{B} is magnetic flux density and \mathbf{J} is current density.

\mathbf{B} and \mathbf{H} satisfy the constitutive relation

$$\mathbf{B} = \mu \mathbf{H} \quad (137)$$

where μ denotes material permeability. Boundary conditions that must be satisfied between two regions are

$$\hat{\mathbf{n}} \times (\mathbf{H}_1 - \mathbf{H}_2) = \mathbf{K} \quad (138)$$

$$\hat{\mathbf{n}} \cdot (\mathbf{B}_1 - \mathbf{B}_2) = 0 \quad (139)$$

where $\hat{\mathbf{n}}$ is a unit vector normal to the boundary surface directed from region 2 to region 1 and \mathbf{K} represents surface current density.

Since the divergence of the curl of any vector \mathbf{A} must always be zero, it follows from (136) that there exists a so-called magnetic vector potential \mathbf{A} such that

$$\mathbf{B} = \nabla \times \mathbf{A} \quad (140)$$

Substituting (137) and (140) into (135) yields

$$\nabla \times \left(\frac{1}{\mu} \nabla \times \mathbf{A} \right) = \mathbf{J} \quad (141)$$

If $\mathbf{J} = J \hat{\mathbf{z}}$, then $\mathbf{A} = A \hat{\mathbf{z}}$, and (141) reduces to

$$-\nabla \cdot \left(\frac{1}{\mu} \nabla A \right) = J \quad (142)$$

which may be written in the expanded form

$$\frac{\partial}{\partial x} \left(\frac{1}{\mu} \frac{\partial A}{\partial x} \right) + \frac{\partial}{\partial y} \left(\frac{1}{\mu} \frac{\partial A}{\partial y} \right) = -J \quad (143)$$

Equation (143) is the scalar Poisson equation [67].

3.1.2 PM Field Calculation

According to Figure 35, the static magnetic field established by the PM array is approximately planar in the region where the coils are located, and thus it may be accurately approximated by solving (143). The derivation is based on Figure 36(a) which defines the two regions of interest, Figure 36(b) which models the PM excitation by equivalent currents, and Figure 36(c) which represents these equivalent currents as a periodic train of impulse functions. This formulation assumes that (i) the stator is infinitely long in the x -direction, (ii) that end-effects are negligible in the z -direction, (iii) that the permeability of the PM material is equal to the permeability of free space μ_0 , and (iv) that the permeability of the back iron material is infinite. Under these assumptions, (143) specializes to

$$\frac{\partial^2 A_1}{\partial x^2} + \frac{\partial^2 A_1}{\partial y^2} = 0 \quad (144)$$

$$\frac{\partial^2 A_2}{\partial x^2} + \frac{\partial^2 A_2}{\partial y^2} = -\mu_0 J_2 \quad (145)$$

where the subscripts identify regions and the equivalent current density of the PM array is the source; boundary conditions (138)-(139) specialize to

$$\left\{ \begin{array}{ll} H_{1x} = 0 & , \quad y = g_s \\ H_{1x} = H_{2x} \text{ and } B_{1y} = B_{2y} & , \quad y = l_m \\ H_{2x} = 0 & , \quad y = 0 \end{array} \right. \quad (146)$$

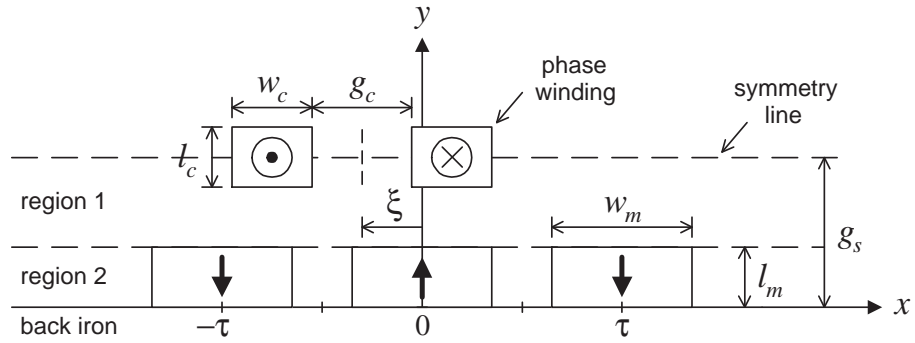
Note that the entire air gap region, including the region occupied by the moving coil assembly, is nonmagnetic.

The equivalent current density of the PM array may be expressed as the Fourier series

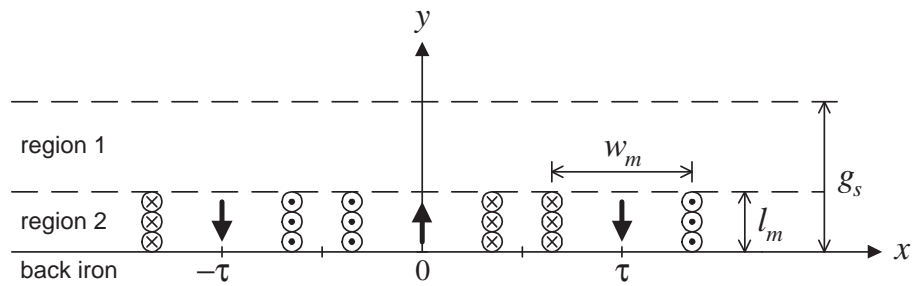
$$J_2 = \sum_{n=1,3,\dots}^{\infty} \alpha_n \sin(nkx) \quad (147)$$

with coefficients

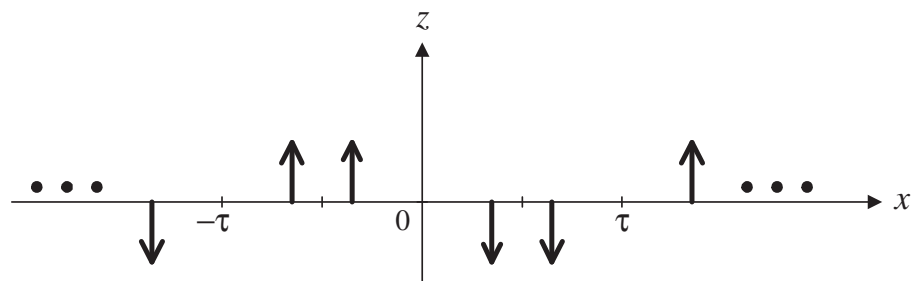
$$\alpha_n = -\frac{4B_r}{\tau\mu_0} \sin\left(\frac{1}{2}nk w_m\right) \quad (148)$$



(a) The two regions defining the problem domain.



(b) Equivalent current distribution for PM array in (x, y) -plane.



(c) Equivalent current distribution for PM array in (x, z) -plane.

Figure 36: Schematic diagrams used to derive force model of the LPM motor.

where B_r is the residual flux density of the PM material and $k = \pi/\tau$ is the spatial frequency. Given this excitation, the solution of (144)-(145) satisfying (146) is

$$A_1 = \mu_0 \sum_{n=1,3,\dots}^{\infty} \frac{\alpha_n}{(nk)^2} \cdot \left(\frac{\sinh(nkl_m)}{\sinh(nkg_s)} \cosh(nk(g_s - y)) \right) \cdot \sin(nkx) \quad (149)$$

$$A_2 = \mu_0 \sum_{n=1,3,\dots}^{\infty} \frac{\alpha_n}{(nk)^2} \cdot \left(1 - \frac{\sinh(nk(g_s - l_m))}{\sinh(nkg_s)} \cosh(nky) \right) \cdot \sin(nkx) \quad (150)$$

Following (140), the curl of (149) provides the air gap flux density in the form

$$B_{1x} = -\mu_0 \sum_{n=1,3,\dots}^{\infty} \frac{\alpha_n}{nk} \cdot \frac{\sinh(nkl_m)}{\sinh(nkg_s)} \cdot \sinh(nk(g_s - y)) \cdot \sin(nkx) \quad (151)$$

$$B_{1y} = -\mu_0 \sum_{n=1,3,\dots}^{\infty} \frac{\alpha_n}{nk} \cdot \frac{\sinh(nkl_m)}{\sinh(nkg_s)} \cdot \cosh(nk(g_s - y)) \cdot \cos(nkx) \quad (152)$$

The air gap flux density plays a critical role in determining the force produced on the coil assembly.

3.1.3 Lorentz Force

The force exerted by a PM-sourced static magnetic field with flux density \mathbf{B} on conductors carrying current density \mathbf{J} is the so-called Lorentz force \mathbf{F} given by

$$\mathbf{F} = \int_v \mathbf{J} \times \mathbf{B} \, dv \quad (153)$$

which specializes to

$$F = - \int_v J_z B_y \, dv \quad (154)$$

if current is z -directed and motion is x -directed [67]. For a single N -turn coil with z -direction length of L carrying current I , (154) reduces to

$$F = -NILB_{\text{avg}} \quad (155)$$

with

$$B_{\text{avg}} = \frac{1}{A_c} \left(\int_{a^+} B_y \, da - \int_{a^-} B_y \, da \right) \quad (156)$$

where areas a^+ and a^- on which integration is performed coincide with the cross sections of area $A_c = w_c l_c$ of the two coil sides. Note that (155)-(156) extends to multi-coil rigid assemblies using superposition, where B_{avg} is computed directly from the PM field alone. Although coil currents induce additive contributions to the PM field, they do not induce any net contributions to force; all such current-induced forces sum to zero.

Evaluation of the first integral of (156) with (152) and the relative coil position $\xi_j = \xi - (j-1)\frac{4}{3}\tau$, where $j = 1, 2, 3$, yields

$$\begin{aligned}
\int_{a^+} B_y da &= 2 \int_{(g_s - \frac{l_c}{2})}^{g_s} \int_{(-\frac{g_c}{2} - w_c - \xi_j)}^{(-\frac{g_c}{2} - \xi_j)} B_{1y} dx dy \\
&= -2\mu_0 \sum_{n=1,3,\dots}^{\infty} \frac{\alpha_n}{(nk)^3} \cdot \frac{\sinh(nkl_m)}{\sinh(nkg_s)} \cdot \left[\sinh(nk(g_s - y_s)) \right]_{(g_s - \frac{l_c}{2})}^{g_s} \\
&\quad \cdot \left[\sin(nkx_s) \right]_{(-\frac{g_c}{2} - w_c - \xi_j)}^{(-\frac{g_c}{2} - \xi_j)} \\
&= -2\mu_0 \sum_{n=1,3,\dots}^{\infty} \frac{\alpha_n}{(nk)^3} \cdot \frac{\sinh(nkl_m)}{\sinh(nkg_s)} \cdot \left[-\sinh\left(\frac{1}{2}nkl_c\right) \right] \\
&\quad \cdot \left[2 \cos\left(\frac{1}{2}nk(g_c - w_c - 2\xi_j)\right) \sin\left(\frac{1}{2}nkw_c\right) \right] \\
&= 4\mu_0 \sum_{n=1,3,\dots}^{\infty} \beta_n \cos\left(\frac{1}{2}nk(g_c - w_c - 2\xi_j)\right)
\end{aligned}$$

where

$$\beta_n = \frac{\alpha_n}{(nk)^3} \cdot \frac{\sinh(nkl_m)}{\sinh(nkg_s)} \cdot \sinh\left(\frac{1}{2}nkl_c\right) \cdot \sin\left(\frac{1}{2}nkw_c\right) \quad (157)$$

Similarly, evaluation of the second integral of (156) yields

$$\begin{aligned}
\int_{a^-} B_y da &= 2 \int_{(g_s - \frac{l_c}{2})}^{g_s} \int_{(\frac{g_c}{2} - \xi_j)}^{(\frac{g_c}{2} + w_c - \xi_j)} B_{1y} dx dy \\
&= 4\mu_0 \sum_{n=1,3,\dots}^{\infty} \beta_n \cos\left(\frac{1}{2}nk(g_c + w_c - 2\xi_j)\right)
\end{aligned}$$

It follows that

$$B_{\text{avg}} = 8\mu_0 \sum_{n=1,3,\dots}^{\infty} \beta_n \sin\left(\frac{1}{2}nk(g_c + w_c)\right) \cdot \sin(nk\xi_j) \quad (158)$$

and hence the force produced by each phase according to (155) is

$$f_j = -\frac{8\mu_0 N d i_j}{A_c} \sum_{n=1,3,\dots}^{\infty} \beta_n \sin\left(\frac{1}{2}nk(g_c + w_c)\right) \cdot \sin(nk\xi_j) \quad (159)$$

Ultimately the total force function is obtained by the sum of forces from all three phases that takes the form

$$f(\xi, i) = \sum_{j=1}^3 K_j(\xi) i_j \quad (160)$$

where the spatial characteristics of the phases are summarized by the Fourier series

$$K_j(\xi) = \sum_{n=1,3,\dots}^{\infty} \gamma_n \sin\left(nk\left(\xi - (j-1)\frac{4}{3}\tau\right)\right) \quad (161)$$

with coefficients

$$\begin{aligned} \gamma_n = & -\frac{18Ndp_c^2 B_r}{w_c l_c (n\pi)^3} \cdot \frac{\sinh(nkl_m)}{\sinh(nkg_s)} \cdot \sinh\left(\frac{1}{2}nkl_c\right) \cdot \sin\left(\frac{1}{2}nkw_m\right) \cdot \sin\left(\frac{1}{2}nkw_c\right) \\ & \cdot \sin\left(\frac{1}{2}nk(g_c + w_c)\right) \end{aligned} \quad (162)$$

A sign change has been made to account for the fact that position ξ increases in the negative x -direction. The physics-based approach to the development of (160)-(162) has obvious value from the point of view of motor design, since the force model explicitly exhibits the influence of each critical dimension and material parameter.

3.1.4 Model Validation

The specific LPM motor of interest is the one specified in Table 7. The proposed force model is validated by FEA; 2D magnetostatic analysis was performed using commercial software from Ansoft. For the FEA, saturable M19 steel is assumed for the stator back iron material and the permeability of the PM material is assumed to be $1.05\mu_0$ with $B_r = 1.2$ T.

Comparative results obtained for four current levels, applied only to phase 1, over the one-half PM pitch interval from $\xi = 0$ mm to 46.5 mm are shown in Figure 37. Forces computed using (160) with truncation at $n = 11$ appear to be in very good

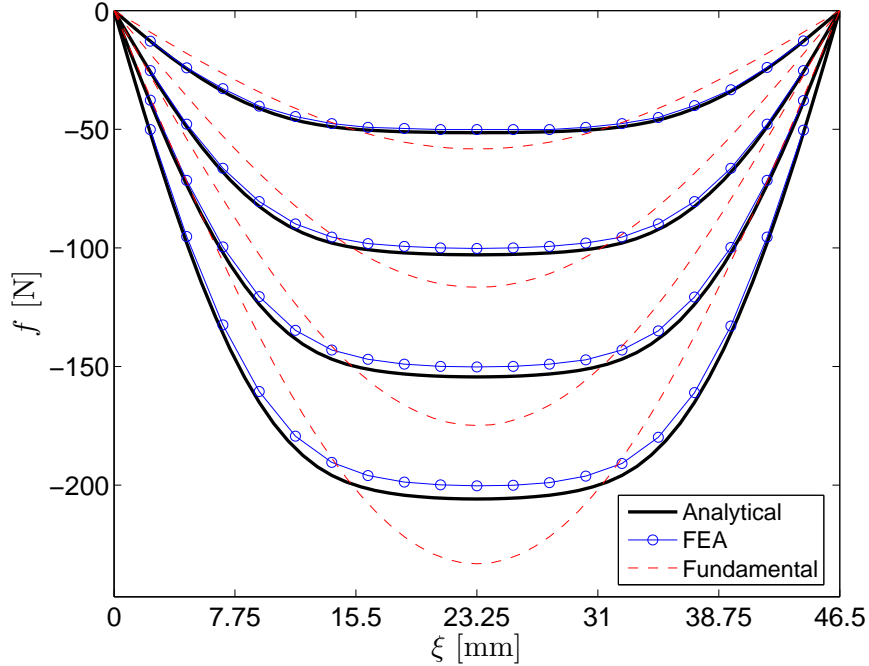


Figure 37: Force versus position for the LPM motor with excitation $i_1 = 2, 4, 6, 8$ A.

agreement with FEA at all excitation levels with a maximum error of less than 2%. Therefore, the simplifying assumptions (primarily that the permeability of PM material is μ_0 and the permeability of back iron material is infinite) do not compromise the accuracy of the force model. Note that the force profile is non-sinusoidal; the fundamental components of the Fourier series are shown for comparison. This LPM motor is not dq-transformable due to the presence of significant spatial harmonics.

3.2 Modeling of Linear Variable Reluctance Motor

The three-phase LVR motor under consideration is shown in Figure 38. The stator and translator consist of ferromagnetic material. Each phase winding is a series connection of two concentrated coils placed on opposing poles of the two E-cores. The phases of this configuration are magnetically coupled, since the flux induced by exciting one phase links the turns of the other phases as it traverses closed paths through magnetic material. The two-sided design results in zero normal force.

Table 7: LPM Motor Parameters

Parameter	Symbol	Value
Coil assembly:		
Coil pitch	p_c	62 mm
Coil width	w_c	15 mm
Coil length	l_c	9.3 mm
Coil gap	g_c	28 mm
Coil depth	d_c	100 mm
Total width	w_t	186 mm
Total length	l_t	10.3 mm
Total depth	d_t	134 mm
Effective depth	d	115 mm
Vertical cover	$(l_t - l_c)/2$	0.5 mm
Horizontal cover	$(d_t - d_c - 2w_c)/2$	2 mm
Coil size (AWG)	w	20
Number of turns	N	200
Phase resistance	R	2 Ω
Stator:		
Back iron depth	D	164 mm
Back iron length	l_b	10 mm
Magnet depth	d_m	134 mm
Magnet pitch	τ	46.5 mm
Magnet width	w_m	40 mm
Magnet length	l_m	5 mm
Air gap length	l_g	0.5 mm
Clearance gap depth	d_g	2 mm
Stator base depth	d_b	15 mm
Residual flux density	B_r	1.2 T

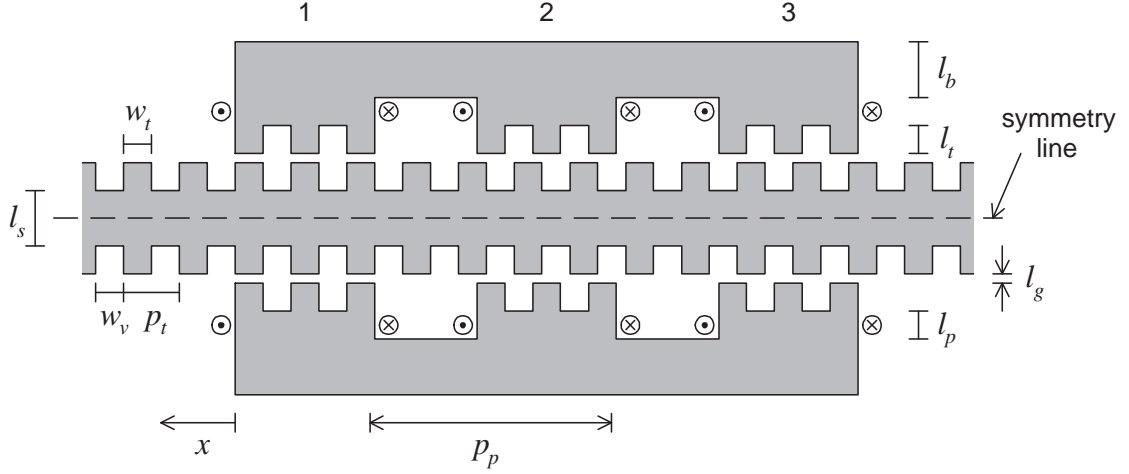


Figure 38: LVR motor with magnetically coupled phases.

This type of motor must have a feasible arrangement of poles and teeth. The pole pitch p_p and the tooth pitch p_t must satisfy

$$p_p = (n_t + n_s + \frac{1}{3})p_t \quad (163)$$

where n_t is the number of teeth per pole and n_s is an integer greater than one. The tooth width w_t and the valley width w_v must satisfy

$$w_t = p_t(2 + \alpha)/6 \quad (164)$$

$$w_v = p_t(4 - \alpha)/6 \quad (165)$$

where $\alpha \in [0, 1]$ is a free parameter corresponding to the ratio of w_t and p_t between $\frac{1}{3}$ and $\frac{1}{2}$. The value of n_s determines the space available for windings, whereas the value of α determines the air gap geometry. In Figure 38, the choices are $n_t = 3$, $n_s = 1$ and $\alpha = 1$. An accurate model of this motor must account for saturation of magnetic material and magnetic coupling between phases. Here, position x is defined such that $x = 0$ is an equilibrium position imposed by positive current in phase 1 and increasing x corresponds to leftward motion.

3.2.1 Steel Permeances

3.2.1.1 Steel Model

Steel regions within the LVR motor will be modeled by one-dimensional nonlinear permeance elements [20]. Consider a rectangular block of homogeneous isotropic magnetic material as shown in Figure 39(a), having length l and cross section area A . Flux Φ is assumed to flow only in the direction of the x -axis, and to be uniformly distributed across equipotential surfaces parallel to the yz -plane. The corresponding nonlinear permeance element is shown in Figure 39(b), where F_i and F_j denote the potentials associated with the left and right cross sections, respectively. The magnetic field intensity H is determined by the potential difference according to $H = (F_i - F_j) / l$, and the magnetic flux density B is determined by the nonlinear magnetization curve \mathcal{N} characterizing the material, i.e. $B = \mathcal{N}(H)$. The resulting flux is given by $\Phi = BA$. Hence, each steel region is modeled by a nonlinear relation of the form

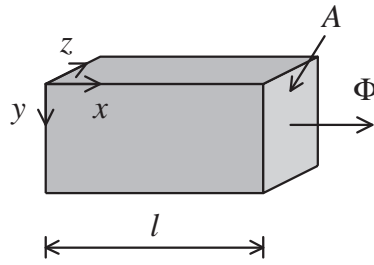
$$\Phi_{i,j} = \mathcal{N} \left(\frac{F_i - F_j}{l} \right) A \quad (166)$$

and, consequently, each such region must be chosen so as to justify the previously listed assumptions.

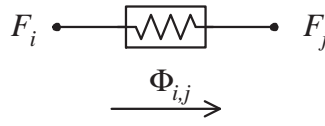
MCA amounts to solving a system of nonlinear algebraic equations wherein all nonlinearities arise from \mathcal{N} . For M19 steel, \mathcal{N} is as shown in Figure 40. A cubic splines representation of \mathcal{N} will be employed in the numerical method to follow, since this guarantees the desirable property of continuous first derivatives.

3.2.1.2 Effective Cross Section Area

It is essential to model all steel regions with reasonable accuracy, but also to reduce complexity by using a minimum number of permeance elements; thus, compromises must be made. The most critical regions are the teeth, since they are likely to exhibit the highest levels of localized material saturation. Therefore, when (166) is used to



(a)



(b)

Figure 39: Steel region with one-dimensional flux flow: (a) magnetic material block; (b) corresponding nonlinear permeance element.

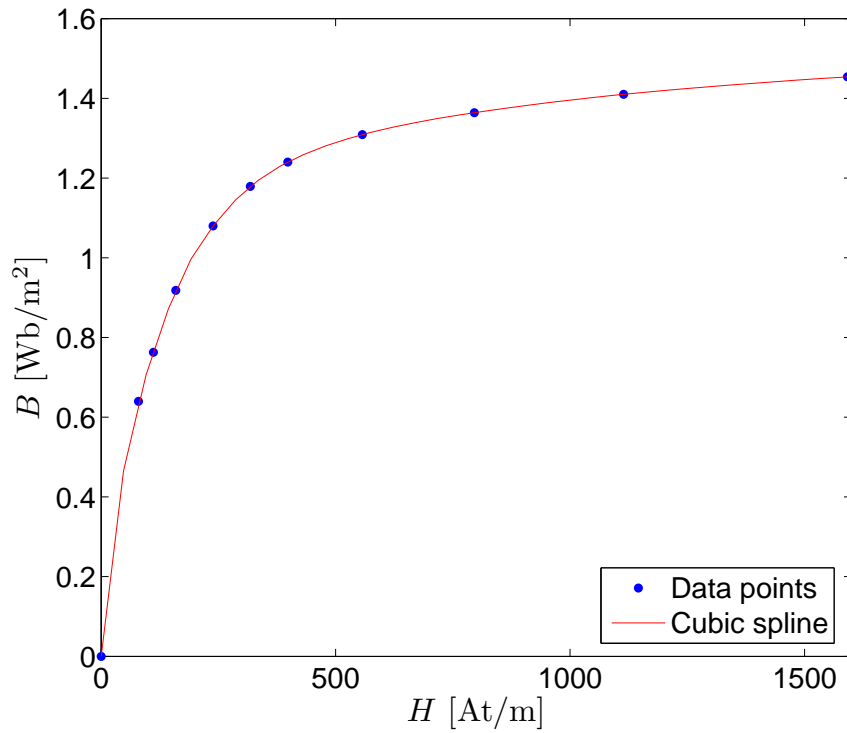


Figure 40: First-quadrant plot of the odd-symmetric nonlinear magnetization curve $B = \mathcal{N}(H)$ characterizing M19 steel.

model teeth in particular, an effective value $A_e \leq A$ will be used to represent the fractional area of material located along the anticipated flux path.

Consider the tooth geometry shown in Figure 41. Feasible values for w_t and w_v are identified by $w_t/(w_t + w_v) \in [\frac{1}{3}, \frac{1}{2}]$. The orientation of opposing teeth varies as a periodic function of x , with period $w_t + w_v$. The teeth are fully aligned at $x = 0$ and fully unaligned at $x = \frac{1}{2}(w_t + w_v)$. Between these extremes, overlap is present if $x \in [0, w_t]$ and absent if $x \in [w_t, \frac{1}{2}(w_t + w_v)]$.

In the aligned orientation $x = 0$, most of the flux passes between opposing teeth through rectangular air gap regions having cross section area dw_t , where d denotes depth. The distribution of flux within a tooth is essentially uniform. If n teeth per pole are modeled by a single permeance, then $A_e = ndw_t$.

In the unaligned orientations $x \in [w_t, \frac{1}{2}(w_t + w_v)]$, most of the flux crosses the air gap along the path of shortest length from tooth corner to tooth corner. The distribution of flux within a tooth is nonuniform, with the highest flux density occurring at tooth corners. It is assumed that the flux path within a tooth excludes a triangular region defined by the two corners and a third vertex. This vertex is located halfway between the tooth midpoint and the tooth base, in order to balance the limiting cases of fully intersecting flux paths and non-intersecting flux paths. Using these assumptions, $\frac{5}{8}$ of the tooth volume is occupied by flux. If n teeth per pole are modeled by a single permeance, then $A_e = \frac{5}{8}ndw_t$.

Motivated by the discussion above, toothed regions are modeled by (166) with $A = A_e(x)$ where

$$A_e(x) = \begin{cases} nd(w_t - \frac{3}{8}x) & , x \in [0, w_t] \\ \frac{5}{8}ndw_t & , x \in [w_t, \frac{1}{2}(w_t + w_v)] \end{cases} \quad (167)$$

The piecewise-linear shape of $A_e(x)$ is plotted in Figure 42. Use of x -dependent cross section area has been motivated by other researchers, e.g. see [23, 24, 40].

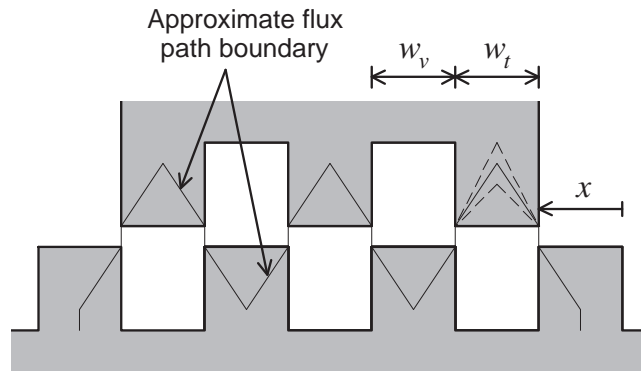


Figure 41: Geometry of translator pole teeth and stator bar teeth in unaligned configuration (depicted for special case $w_t = w_v$).

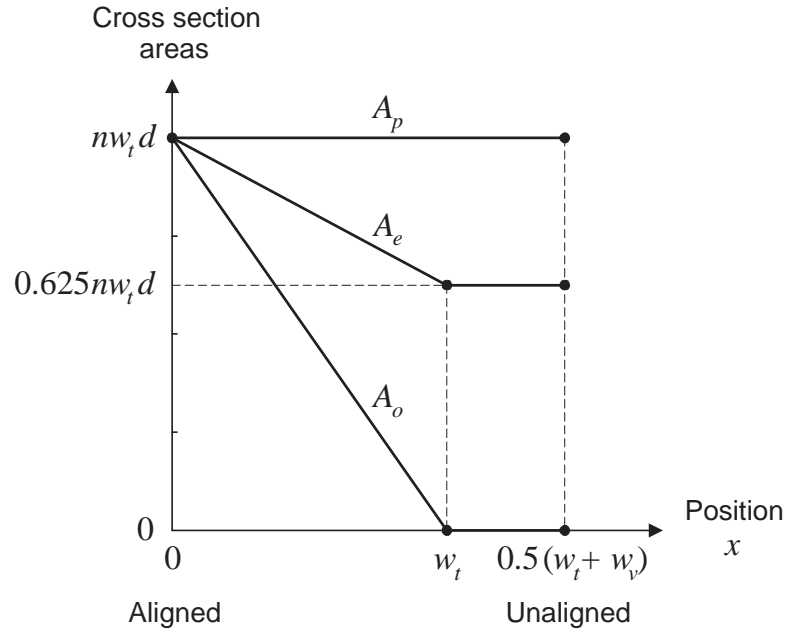


Figure 42: Cross-section areas for toothed regions over half spatial period: physical area A_p ; effective area A_e ; overlap area A_o .

3.2.2 Air Permeances and Coils

3.2.2.1 Gap Permeances

The air gap model used in this research assumes that flux flows across the air gap through flux tubes shaped by straight lines and circular arcs. Representative flux tubes are shown in Figure 43, over one tooth pitch, for several orientations of opposing teeth. The permeance of each flux tube is computed analytically using

$$P_{\text{tube}} = \mu_0 \int \frac{dA}{l} \quad (168)$$

where μ_0 is the permeability of air, l is the length of the tube and dA is the differential cross section of the tube. Evaluation of (168) for all possible cases leads to explicit position-dependent expressions for the permeance $P_{\text{tube}}(x)$ and spatial derivative of permeance $P'_{\text{tube}}(x)$ of any given flux tube. The explicit formulas of the flux tube model used in this research were introduced in [68] and are summarized in Appendix A.

For the LVR motor of Figure 38, there are six air gap regions, two for each pole pair, and each of these multi-tooth regions will be covered by a number of flux tubes. The simplest option would be to represent the toothed regions of the pole tips by single nodes as shown in Figure 44, in which case all flux tubes associated with each such node would be combined in parallel to obtain a single effective gap permeance $P_g(x)$ and gap permeance derivative $P'_g(x)$. The problem with such an approach is that it does not adequately account for the localized effect of tooth corner saturation.

In this research, flux tubes are separated into two distinct groups; overlap flux tubes and fringing flux tubes. These two groups are treated separately, yielding two effective permeances and permeance derivatives for each of the six air gap regions. Consequently, toothed regions can include two nodes having distinct potentials, and this refinement permits the flux density within a tooth to vary from tooth tip to tooth base. This approach is illustrated in Figure 45, where the overlap component

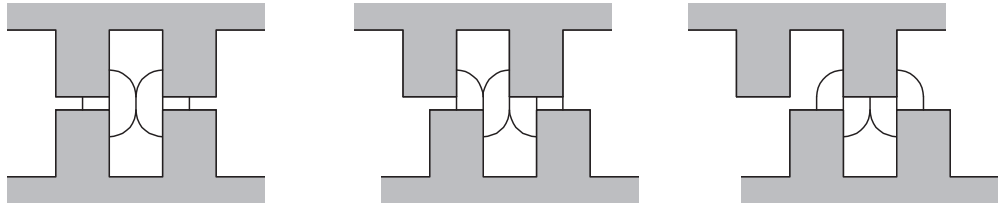


Figure 43: Flux tube geometries over one tooth pitch for three different orientations (depicted for special case $w_t = w_v$).

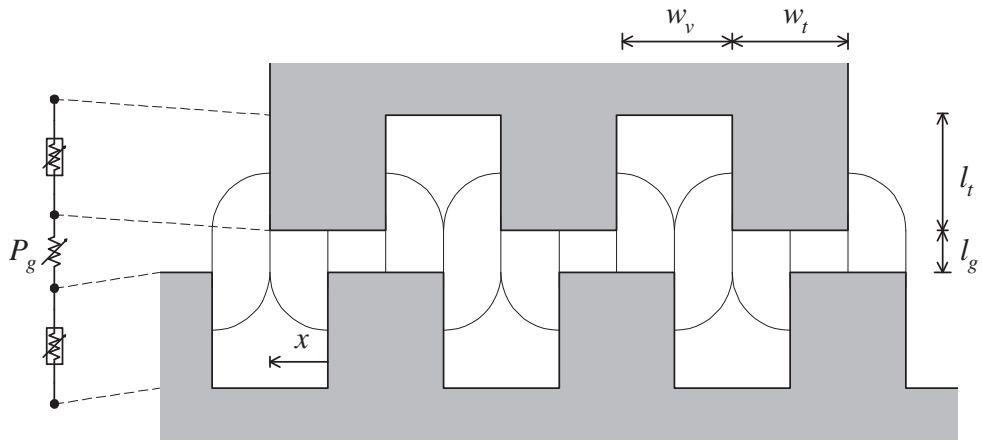


Figure 44: Interconnections between tooth permeances with single air gap permeance (depicted for special case $w_t = w_v$).

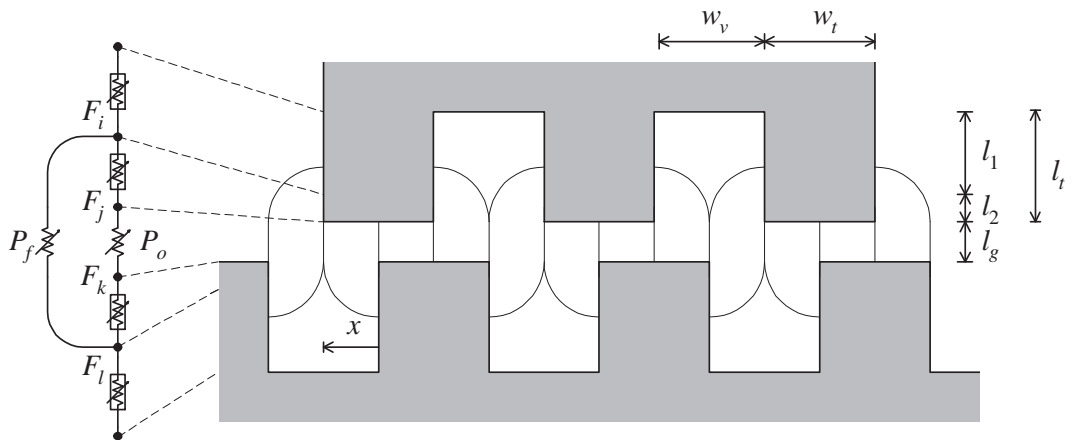


Figure 45: Interconnections between tooth permeances and separated air gap permeances (depicted for special case $w_t = w_v$).

of gap permeance $P_o(x)$ accounts for regions of overlap between opposing teeth and the fringing component of gap permeance $P_f(x)$ accounts for regions on which fringing occurs. The corresponding spatial derivative components are $P'_o(x)$ and $P'_f(x)$. Toothed regions of steel are represented by two nonlinear permeances. These nonlinear permeances vary with x according to their effective area $A_e(x)$ from (167). The constant lengths of these nonlinear permeances are denoted by l_1 and l_2 , where the sum $l_1 + l_2$ equals the tooth length l_t and where $l_2 = \frac{1}{4}w_v$ defines the average penetration distance of fringing flux along the tooth sides.

3.2.2.2 Leakage Permeances

Leakage permeances are introduced to account for the fact that not all flux will cross the air gap. Two leakage paths are considered. First, some fraction of pole flux will tend to return to the back iron rather than cross the gap. An approximation of this effect can be introduced by including the permeance

$$P_{\text{pb}} = \frac{\mu_0 8d}{\pi} \quad (169)$$

between the tip and base of each pole. Second, some fraction of pole flux will tend to flow to an adjacent pole rather than cross the gap. An approximation of this effect can be introduced by including the permeance

$$P_{\text{pp}} = \frac{\mu_0 l_p d}{p_p - ((n-1)p_t + w_t)} \quad (170)$$

between neighboring pole tips, where l_p , p_p and p_t denote pole length, pole pitch and tooth pitch, respectively.

3.2.2.3 Coils

The mmf sources corresponding to the phase winding are modeled by

$$\text{mmf}_j = \frac{1}{2} N i_j \quad (171)$$

where N denotes the number of turns for each series-connected phase winding and i_j is the phase- j current for $j = 1, 2, 3$. Since symmetry is imposed in the network topology, only half of the turns is implemented.

3.2.3 Magnetic Circuit Analysis

3.2.3.1 Network Topology

From Figure 38, the LVR motor exhibits a form of symmetry with respect to the stator centerline. As a consequence, it is sufficient to construct a magnetic circuit representing only the flux paths on one side of the stator centerline, with constant potential imposed along the stator centerline. The use of symmetry reduces the complexity of the magnetic circuit by a factor of two.

The half-motor magnetic circuit representation is chosen as shown in Figure 46. Flux paths through steel appear as nonlinear permeances, whereas flux paths through air appear as linear permeances. In the vicinity of teeth, both nonlinear steel permeances and linear air permeances depend explicitly on position. Coils appear as mmf sources. This network topology captures all of the pre-assumed flux paths. Each node represents an equipotential cross section surface orthogonal to the plane in which the figure is drawn. The magnetically coupled nature of this LVR motor is clearly evident.

3.2.3.2 Implementation

The system of modified nodal equations corresponding to the network of Figure 46 is derived by imposing conservation of flux at each node [69, 20]. Since the network includes nonlinear elements, this results in a system of 24 nonlinear nodal equations and 3 auxiliary equations

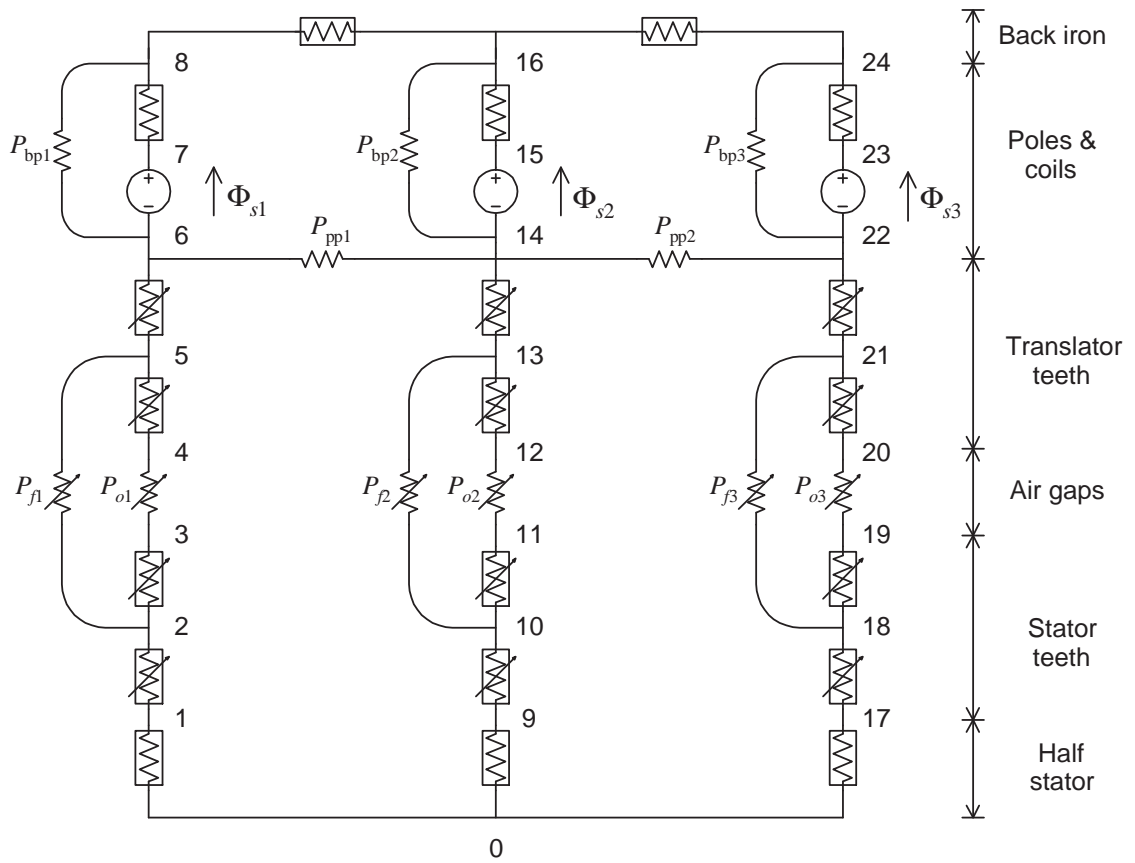


Figure 46: Magnetic circuit topology representing one-half of the LVR motor, wherein symmetry has imposed constant potential along the stator centerline.

$$\begin{aligned}
\text{node 1:} & \quad 0 = \Phi_{1,0} + \Phi_{1,2} \\
\text{node 2:} & \quad 0 = \Phi_{2,1} + \Phi_{2,3} + P_{f1}(F_2 - F_5) \\
\text{node 3:} & \quad 0 = \Phi_{3,2} + P_{o1}(F_3 - F_4) \\
\text{node 4:} & \quad 0 = P_{o1}(F_4 - F_3) + \Phi_{4,5} \\
\text{node 5:} & \quad 0 = P_{f1}(F_5 - F_2) + \Phi_{5,4} + \Phi_{5,6} \\
\text{node 6:} & \quad 0 = \Phi_{6,5} + P_{pb1}(F_6 - F_8) + P_{pp1}(F_6 - F_{14}) + \Phi_{s1} \\
\text{node 7:} & \quad 0 = \Phi_{7,8} - P_{s1} \\
\text{node 8:} & \quad 0 = P_{pb1}(F_8 - F_6) + \Phi_{8,7} + \Phi_{8,16} \\
\text{node 9:} & \quad 0 = \Phi_{9,0} + \Phi_{9,10} \\
\text{node 10:} & \quad 0 = \Phi_{10,9} + \Phi_{10,11} + P_{f1}(F_{10} - F_{13}) \\
\text{node 11:} & \quad 0 = \Phi_{11,10} + P_{o2}(F_{11} - F_{12}) \\
\text{node 12:} & \quad 0 = P_{o2}(F_{12} - F_{11}) + \Phi_{12,13} \\
\text{node 13:} & \quad 0 = P_{f2}(F_{13} - F_{10}) + \Phi_{13,12} + \Phi_{13,14} \\
\text{node 14:} & \quad 0 = P_{pp1}(F_{14} - F_6) + \Phi_{14,13} + P_{pp2}(F_{14} - F_{22}) + \Phi_{s2} \\
\text{node 15:} & \quad 0 = \Phi_{15,16} - \Phi_{s2} \\
\text{node 16:} & \quad 0 = \Phi_{16,8} + P_{pb2}(F_{16} - F_{14}) + \Phi_{16,15} + \Phi_{16,24} \\
\text{node 17:} & \quad 0 = \Phi_{17,0} + \Phi_{17,18} \\
\text{node 18:} & \quad 0 = \Phi_{18,17} + \Phi_{18,19} + P_{f3}(F_{18} - F_{21}) \\
\text{node 19:} & \quad 0 = \Phi_{19,18} + P_{o3}(F_{19} - F_{20}) \\
\text{node 20:} & \quad 0 = P_{o3}(F_{20} - F_{19}) + \Phi_{20,21}
\end{aligned}$$

$$\begin{aligned}
\text{node 21:} \quad 0 &= P_{f3}(F_{21} - F_{18}) + \Phi_{21,20} + \Phi_{21,22} \\
\text{node 22:} \quad 0 &= P_{pp2}(F_{22} - F_{14}) + \Phi_{23,21} + P_{pb3}(F_{22} - F_{24}) + \Phi_{s3} \\
\text{node 23:} \quad 0 &= \Phi_{23,24} - \Phi_{s3} \\
\text{node 24:} \quad 0 &= \Phi_{24,16} + P_{pb3}(F_{24} - F_{22}) + \Phi_{24,23} \\
0 &= F_5 - F_4 - \frac{1}{2}Ni_1 \\
0 &= F_{15} - F_{14} - \frac{1}{2}Ni_2 \\
0 &= F_{23} - F_{22} - \frac{1}{2}Ni_3
\end{aligned}$$

or compactly in the form

$$G(y) = 0 \tag{172}$$

where y is a vector containing node potentials and source fluxes, i.e.

$$y = [F_1 \quad \dots \quad F_{24} \quad \Phi_{s1} \quad \Phi_{s2} \quad \Phi_{s3}]^T \tag{173}$$

Given a specification of motor geometry and material properties, (172) may be formulated and iteratively solved by Newton's method for any desired position and excitation.

The force produced on a pole, f_p , may be obtained from the corresponding node potentials and gap permeance derivatives according to

$$f_p = (F_j - F_k)^2 P'_o + (F_i - F_l)^2 P'_f \tag{174}$$

with reference to Figure 45. The total force produced is the sum of the three pole forces. Note that the half-motor feature of Figure 46 is fully accounted for in (174).

In (174), the terms P'_o and P'_f exhibit sign changes at critical positions and hence determine the polarity of pole force produced as a function of position. It is interesting to note that P'_o and P'_f are actually discontinuous at these critical positions, even though the spatial derivative of $P_o + P_f$ is a continuous function of position. Note, however, that the mmf-squared factors are typically many orders of magnitude larger

Table 8: LVR Motor Parameters

Parameter	Symbol	Value
Device depth	d	50 mm
Tooth width	w_t	5 mm
Valley width	w_v	5 mm
Tooth pitch	p_t	10 mm
Pole pitch	p_p	$\frac{130}{3}$ mm
Tooth length	l_t	5 mm
Pole length	l_p	10 mm
Back length	l_b	15 mm
Stator length	l_s	15 mm
Air gap length	l_g	$\frac{1}{4}$ mm
Wire size (AWG)	w	21
Turns per phase	N	200
Phase resistance	R	1.44 Ω

than the permeance-derivative factors, so the size of discontinuity introduced by (174) is typically negligible. For the numerical problem considered in the following section, the discontinuity is practically imperceptible.

3.2.4 Model Validation

The proposed modeling technique has been implemented in MATLAB. The motor geometry is listed in Table 8, and the magnetic material is M19. Results are obtained for four current levels, applied only to phase 1, over the one-half tooth pitch interval from the aligned position at $x = 0$ mm to the unaligned position at $x = 5$ mm. Plots of total force are shown in Figure 47, where data obtained by FEA in [28] are shown for comparison. Forces computed using the proposed model appear to be very accurate at the lower excitation levels. As the excitation levels are increased, the proposed model appears to provide relatively lower accuracy for force. At the maximum current of 8 A, the flux density reaches 1.4 Wb/m², indicating deep saturation according to Figure 40.

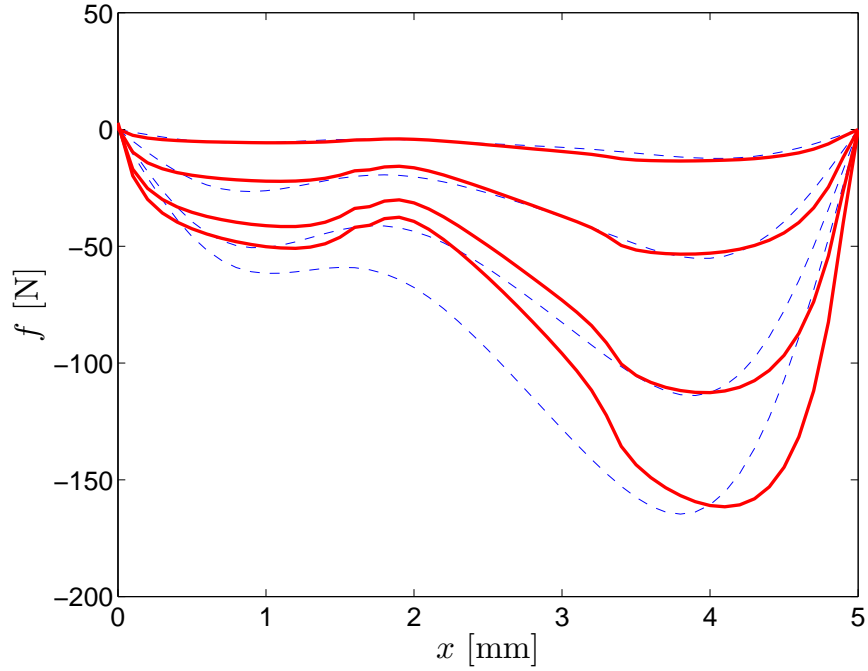


Figure 47: Force versus position for the LVR motor with currents $i_1 = 2, 4, 6, 8$ A (solid = MCA, dashed = FEA).

3.3 Conclusion

The physics-based force models of the LPM and LVR motor have been developed in this chapter. For the LPM motor, the force model is obtained using the analytical solution of the Poisson Equation. For the LPM motor, the nonlinear MCA approach is taken to derive the force model. Both modeling approaches are much more computationally efficient than FEA, yet they are also reasonably accurate in comparison. Although the results presented here are only for single-phase excitation, consideration of multi-phase excitation is possible without introducing further complexity. These physics-based force models will be used to assess motor performances in order to relate the achievable performance levels to motor design variables, i.e. dimensions and material properties.

CHAPTER 4

OPTIMAL PERFORMANCE ASSESSMENT

4.1 Introduction

Performance assessment is crucial during the motor design process as a basis for comparison between different candidate designs. Depending on motor technologies and target applications, the performance of candidate designs can be assessed by various characteristics, which together constitute a “performance vector.” For instance, a performance vector of an induction motor designed for constant speed application may consist of efficiency, maximum speed, maximum torque and torque ripple, whereas a performance vector of a linear motor designed for point-to-point positioning application may consist of moving mass, maximum force and efficiency. Although some of these performance characteristics are common to all motor design purposes, some characteristics are more important for certain applications than the others. For example, designing a large size motor for continuous mode of operation should consider all sources of power dissipation such as copper losses, mechanical losses, hysteresis losses and eddy-current losses to assess the efficiency performance with sufficient accuracy, whereas when designing small size motors for occasional use in appliances, it may be sufficient to consider only copper losses.

The objective of this chapter is to assess the performance of the LPM and LVR motor, for use in manufacturing automation applications in terms of magnetostatic performance and achievable productivity. The target application involves point-to-point positioning tasks on a continuous basis, so productivity is limited in large part by thermal constraints imposed to ensure the integrity of the motor coils; for any fixed

motor, faster cycling requires greater heat production which results in higher steady-state coil temperatures. Hence, there is a limit to how fast the positioning tasks can be performed. Some aspects of this problem have been previously discussed in Chapter 2 for ideal LS motors. Extensions, as presented here, include use of realistic models of motor force production from physical specifications to account for magnetic saturation and spatial harmonics.

This chapter considers three approaches to assess the optimal performance: (i) maximum force limit, (ii) spatial average power dissipation and (iii) productivity trade-off curve. The first two approaches, based on solving uncoupled static optimization problems to obtain magnetostatic performance characteristics, are computationally efficient but less directly related to the target application. The third approach is directly related to the target application but it is more computationally expensive to obtain the productivity trade-off curves. Since the physics-based force functions of the LPM and LVR motors are derived from different principles that further result in different final formulations, the performance assessments of the LPM and LVR motors are discussed separately. All numerical results were obtained for the LPM and LVR motors modeled in Chapter 3, using MATLAB with Optimization Toolbox.

4.2 Performance Assessment of LPM Motors

Three performance assessments of LPM motors are described in the following sections. The maximum force limit is first presented and is based on solving constrained optimization problems numerically to obtain magnetostatic performance characteristics. This is the only performance assessment method that is applicable for both the LPM and LVR motors. The spatial average power dissipation is next presented and is calculated directly without solving the constrained optimization problem numerically, due to magnetic linearity of the force function for the LPM motors. The productivity

trade-off curve is finally discussed and is derived based on solving multiple optimal control problems numerically. Only 6-wire connection and cubical current limit (when applicable) is considered due to its highest performance.

4.2.1 Maximum Force Limit

The first performance assessment considered is the maximum force capability of the LPM motor. Two values of interest are maximum smooth force F_s and maximum average force F_a . These quantities can be determined by solving an optimization problem in order to find the magnitude-constrained currents that maximize the magnitude of force produced at any given position over one spatial period.

4.2.1.1 Problem Formulation

For a 6-wire connection between motor and inverter and cubical current limit, this problem may be stated for each position $x \in [0, 2\tau]$ in the form

$$\begin{aligned} & \text{maximize} && f(x, u) \\ & \text{subject to} && |u_j| \leq U \quad , \quad j = 1, 2, 3 \end{aligned} \tag{175}$$

where τ is the magnet pitch of the LPM motor, the force function of the LPM motor is available in a special structure (162) as

$$f(x, u) = \sum_{j=1}^3 K_j(x)u_j = K(x)^T u \tag{176}$$

where

$$K(x) = [K_1(x) \quad K_2(x) \quad K_3(x)]^T \tag{177}$$

$$u = [u_1 \quad u_2 \quad u_3]^T \tag{178}$$

and U is the current limit. The main features distinguishing this version of the problem from the one addressed in Chapter 2 are the use of physical current variables (instead of the transformed dq -variables) and the general form of the force function $f(x, u)$ that includes spatial harmonics (magnetic saturation is not present and hence

not modeled for the LPM motor). The corresponding solution will be denoted by $(u^*(x), f^*(x))$. Maximum smooth force, or equivalently maximum ripple-free force, is then determined according to

$$F_s = \min_{x \in [0, 2\tau]} f^*(x) \quad (179)$$

Maximum average force is determined according to

$$F_a = \frac{1}{2\tau} \int_0^{2\tau} f^*(x) dx \quad (180)$$

These two measures of force production capability are considered, in order to accommodate a range of applications. Force ripple may be a concern in some applications, in which case the smaller measure F_s would be appropriate. In other applications, the significant responses may be driven primarily by average rather than instantaneous force, in which case the larger measure F_a would be more appropriate.

For comparison between two different designs, one design is better than another design if, for the same moving mass, its values of F_a and F_s are both higher because it can produce higher force and higher acceleration. This implies that it can finish the positioning tasks faster and hence yields a higher productivity, given that no other constraint (e.g. power or thermal limit) is imposed. If only either F_a or F_s is higher, neither of the two motors is obviously superior to the other.

4.2.1.2 Numerical Results

The maximum (positive) force capability of the LPM motor is determined for $U = 5$ A. The plots of the maximized force $f^*(x)$ with corresponding currents $u^*(x)$ are shown in Figure 48. The optimal current profiles are square waves where one current switches every $\frac{1}{3}\tau$ resulting in two of the three currents having the same sign. The maximized force has a semi-circle like ripple with the period of $\frac{1}{3}\tau$ and the peak force values appear at every $\frac{1}{6}\tau$ after the current switching. These results are consistent with those obtained for the ideal PM motor previously discussed. The maximum

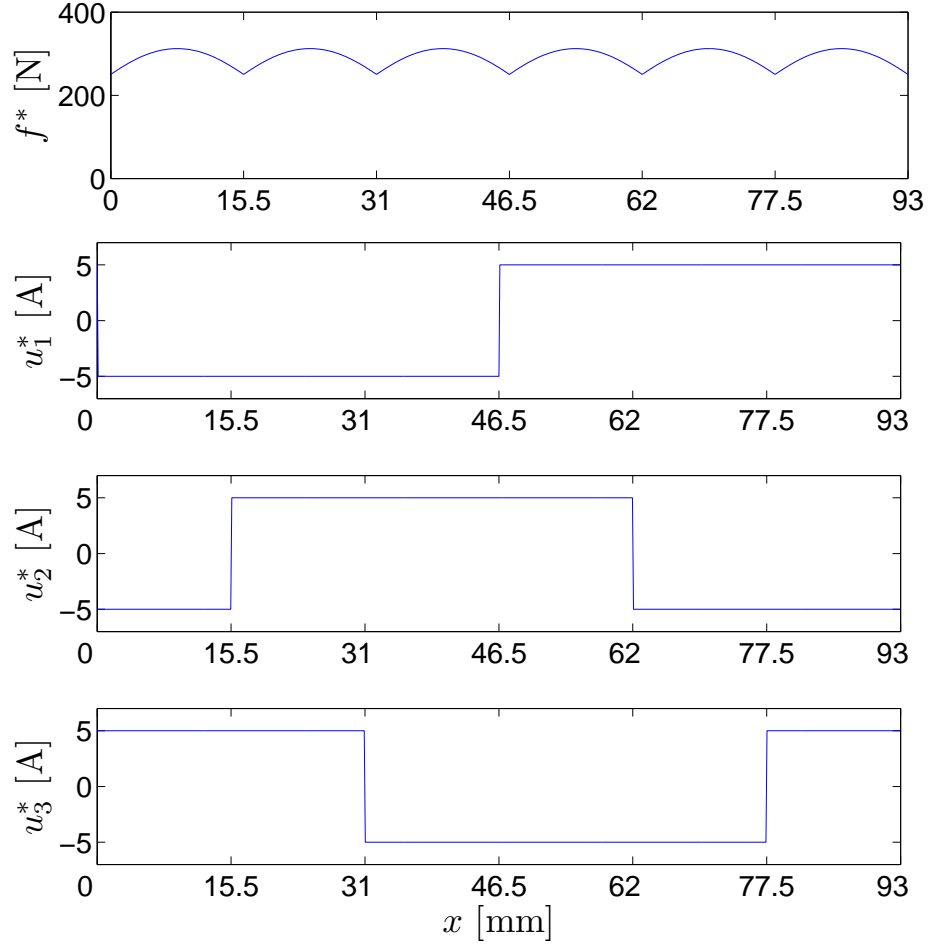


Figure 48: Force maximizing currents and resulting force of the LPM motor for $U = 5$ A, resulting in $F_s = 250.14$ N and $F_a = 290.62$ N.

smooth force and the maximum average force are 250.14 N and 290.62 N, respectively. The plots of the maximized force $f^*(x)$ with corresponding currents $u^*(x)$ for $U = 2, 4, 6, 8$ A are shown in Figure 49. The force ripples become larger as U increases, but the plots are equally spaced due to the absence of steel saturation.

4.2.2 Spatial Average Power Dissipation

The second performance assessment considered is the spatial average power dissipation. This quantity can be determined by solving multiple minimum-copper-loss force control problems.

Since two versions of the problem exist, i.e. with and without current limit, a

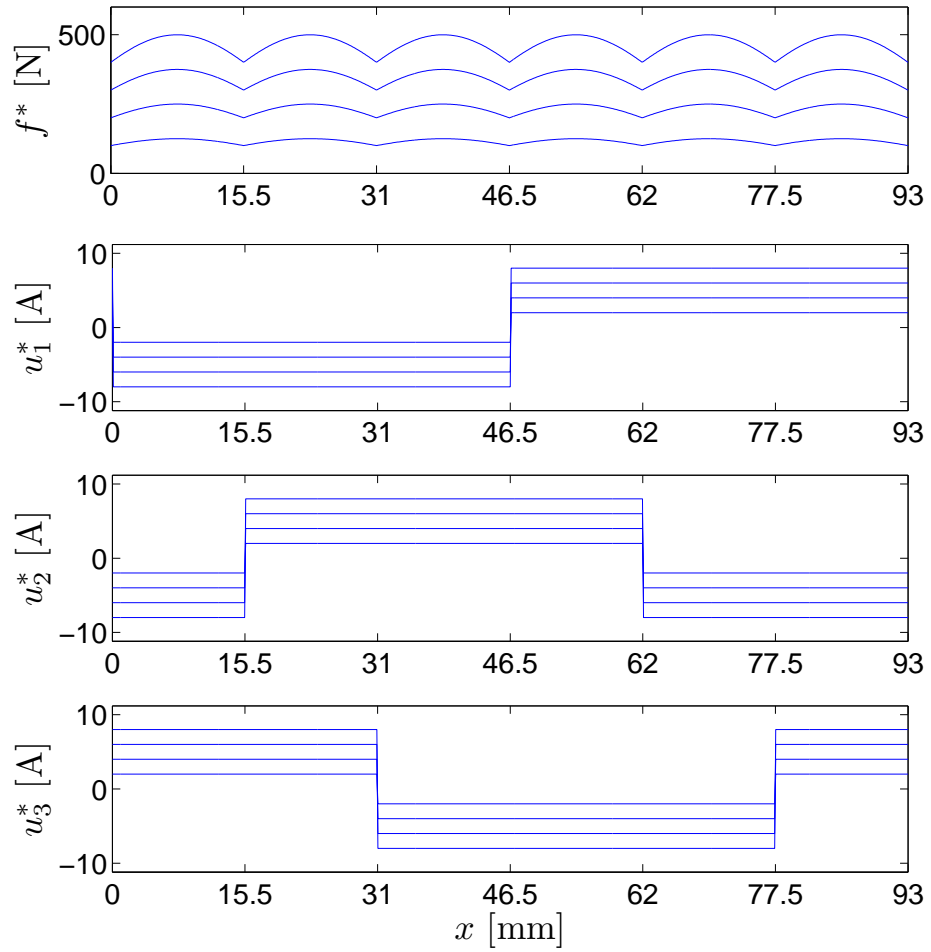


Figure 49: Force maximizing currents and resulting force of the LPM motor for $U = 2, 4, 6, 8$ A.

decision must be made whether or not to consider both cases or select only one of the two available choices. First consider the results of the ideal PM motor for 6-wire connection shown in Figure 34 of Chapter 2. Note that the solutions for both cases are identical to each other until the desired force command f_d approaches F_s . Even at $f_d = F_s$, only a small deviation is noticeable. However, the computational burden between the two methods is significantly different.

Since the force model of the LPM motor includes only spatial harmonics, but not magnetic saturation, it is also possible to exploit the special structure of the force model of the LPM motor to obtain a closed-form solution. Consequently, the whole P_x - f_d curve can be determined much more quickly by solving the problem version without current limit. In contrast, the problem version with current limit must rely on solving many successive constrained optimization problems numerically to characterize the whole P_x - f_d curve due to additional complexity from current limit. The average slope, which must rely on the solutions of the problem version with current limit, is obviously less advantageous for the same reason.

Therefore, the determination of spatial average power dissipation for the LPM motor will be based on solutions of the minimum-copper-loss force control problem without current limit for two reasons: (i) much less extensive computation is required due to the existence of a closed-form solution and (ii) only a small deviation exists between the two approaches.

4.2.2.1 Problem Formulation

For a 6-wire connection between motor and inverter, the minimum-copper-loss force control problem without current limit can be defined for each $x \in [0, 2\tau]$ in the form

$$\begin{aligned} & \text{minimize} && u^T u \\ & \text{subject to} && K(x)^T u = f_d \end{aligned} \tag{181}$$

The objective is to determine the corresponding value of the spatial average power dissipation given by

$$P_x(f_d) = \frac{R}{2\tau} \int_0^{2\tau} u^{*T} u^* dx \quad (182)$$

where R is the winding resistance and u^* is the solution of (181). Note that u^* implicitly depends on f_d causing a dependence of P_x on f_d . Since the force function of the LPM motor is available with linear magnetic structure, u^* can be determined analytically using nonlinear constrained optimization techniques [41].

The Lagrangian of (181) is

$$L = u^T u + \lambda (K(x)^T u - f_d) \quad (183)$$

where λ is the Lagrange multiplier. The necessary conditions are

$$\frac{\partial L}{\partial u} = 2u + \lambda K(x) = 0 \quad (184)$$

$$\frac{\partial L}{\partial \lambda} = K(x)^T u - f_d = 0 \quad (185)$$

Multiply (184) by $K(x)$ to obtain

$$2K(x)^T u + \lambda K(x)^T K(x) = 0$$

and substitute (185) to obtain

$$2f_d + \lambda K(x)^T K(x) = 0$$

so that

$$\lambda = -\frac{2f_d}{K(x)^T K(x)}$$

Finally substitute this into (184) to obtain

$$2u - \frac{2f_d}{K(x)^T K(x)} K(x) = 0$$

and solve to obtain

$$u^* = \frac{K(x)}{K(x)^T K(x)} f_d \quad (186)$$

Consequently, from (182) and (186) the spatial average power dissipation is determined to be

$$P_x = \frac{Rf_d^2}{2\tau} \int_0^{2\tau} \frac{1}{K^T(x)K(x)} dx \quad (187)$$

which is a parabola. Recall from (133) in Chapter 2 that this curve is also a parabola for the ideal PM motor. As a result, the performance assessment is defined to be the *coefficient* that characterizes the parabola curve, i.e.

$$c = \frac{R}{2\tau} \int_0^{2\tau} \frac{1}{K(x)^T K(x)} dx \quad (188)$$

to effectively represent the whole P_x - f_d curve. This coefficient can be computed numerically once $K(x)$ is known.

For comparison between two different designs, the first design is better than the second design if, for the same smooth force capability (i.e. same F_s and moving mass), its value of c is smaller than the other's because it can dissipate less heat while producing the same force over the same range $f_d \leq F_s$. This implies that the first motor can be given higher force commands so that it can finish the positioning tasks faster and hence yields a higher productivity, while still dissipating heat less than or equal to the second motor.

4.2.2.2 Numerical Results

The plot of P_x for various values of f_d of the LPM motor is shown in Figure 50 with $R = 2 \Omega$. These results are consistent with those obtained for the ideal PM motor. The average power coefficient of the P_x - f_d curve is $c = 1.545 \text{ mW/N}^2$. For comparison, the spatial average power corresponding to F_a , which is calculated from the force maximizing currents, is also shown. This data point belongs to the minimum-copper-loss *average* force control problem that finds the magnitude-constrained currents that produce a given desired average force and further minimizes the power dissipated in the winding resistances. At F_a , the solution of this problem dissipates higher

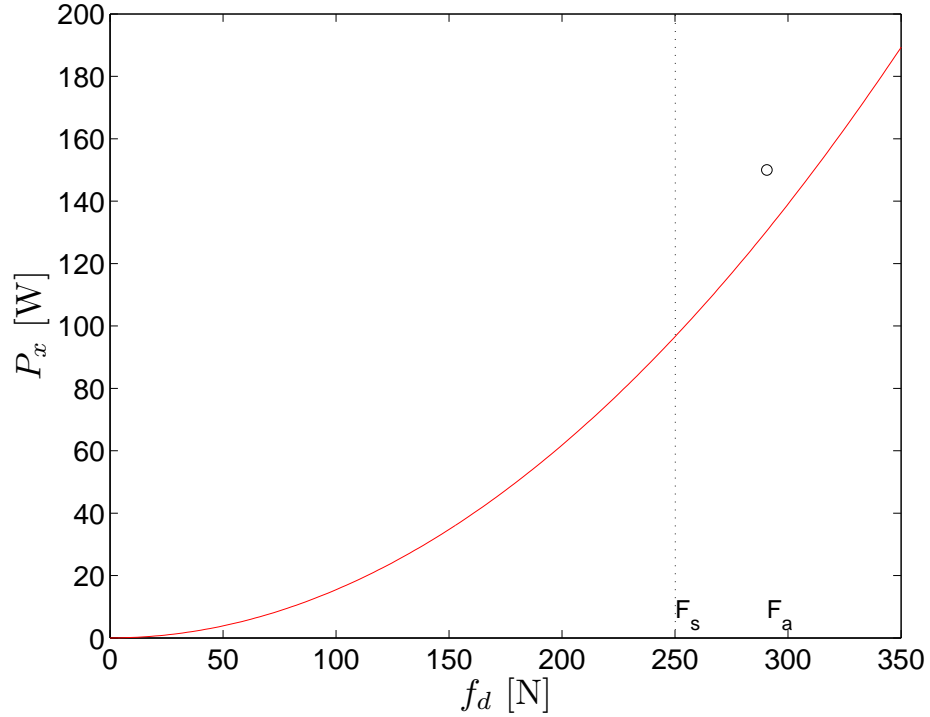


Figure 50: Spatial average power P_x for various values of f_d of the LPM motor with average power coefficient $c = 1.545 \text{ mW/N}^2$.

heat because current limit is included in the problem formulation resulting in fewer available degrees of freedom for the optimal solution.

4.2.3 Productivity Trade-Off Curve

To directly assess the productivity of the motor under average power dissipation constraints, the performance objectives are to minimize the positioning time over a range of desired travel distance for a range of power dissipation. Specifically, the goal is to evaluate the trade-off function $T(X, P)$ that identifies how long the motor will take (i.e. T) to complete a single-stroke motion of desire length (i.e. X) such that the heat-minimizing current waveforms will yield the budgeted average-power (i.e. P). The evaluation of $T(X, P)$ is achieved by solving the family of minimum-copper-loss optimal control problems.

4.2.3.1 Problem Formulation

As previously discussed in Section 2.4, there are computational advantages to finding the minimum T given P in an indirect way. Consider the problem of finding the minimum P given T (for any feasible T); the solutions of this problem are consistent with the solutions of the original problem, in the sense that both solutions trace the same curve in the (T, P) plane. For convenience, this problem is restated here as

$$\text{minimize} \quad P = \frac{R}{T} \int_0^T (u_1^2 + u_2^2 + u_3^2) dt \quad (189)$$

$$\text{subject to} \quad M\ddot{x} = f(x, u) \quad (190)$$

$$(x, \dot{x}) = \begin{cases} (0, 0) & , \quad t = 0 \\ (X, 0) & , \quad t = T \end{cases} \quad (191)$$

$$|u_j| \leq U \quad , \quad j = 1, 2, 3 \quad (192)$$

The main features distinguishing this version of the problem from the one addressed in Chapter 2 are that the physical current variables are used and the force function $f(x, u)$ has a general form. The numerical method proposed for use here is previously presented in Section 2.6.1. Although the proposed problem formulation and numerical method are numerically efficient, the overall computation might not be practical if $f(x, u)$ is too computationally expensive to evaluate.

For comparison between two different designs, one motor design is better than another motor design if, for a fixed P of interest, its T versus X curve lies closer to the origin. The possibility of crossing curves exists, in which case neither of the two motors is universally better than the other.

4.2.3.2 Numerical Results

To evaluate the trade-off curve $T(X, P)$, the optimal control problem (189)-(192) is solved multiple times for $U = 5$ A using the numerical method described in Section 2.6.1. As indicated in Figure 51, the algorithm has two stages. In stage 1, values of the function $P_{\min}(T, X)$ are obtained by computing solutions of (189)-(192) for

various values of T and X ; the range of T values is lower bounded by $T_\star(X)$ and is chosen to correspond with the range of P values of interest. In stage 2, interpolation is used to extract T values corresponding to a grid of X and P values, thus producing a tabulated representation of the desired function $T(X, P)$.

For the example illustrated here, the function $T_\star(X)$ was approximated by $\widehat{T}_\star(X) = \sqrt{4MX/F_a}$ where F_a denotes the maximum average force (over x) achievable given U . The value of F_a may be approximated or computed by solving a static optimization problem; the computed value used here is 290.62 N. Although such approximations of $T_\star(X)$ are entirely optional, they may be useful for selection of suitable values of T . For stage 1, the grid for T was based on several specified values of the approximated ratio $T/\widehat{T}_\star(X)$, where the grid values for X ranged from 25 mm to 200 mm in steps of 25 mm. The corresponding minimized values of P for $X = 100$ mm are shown in Figure 52. For stage 2, the grid values for X remain unchanged and the grid values for P are taken to be (100, 75, 50) W. The numerically obtained representation of $T(X, P)$ for the LPM motor is shown in Figure 53. These data quantify the intuitive notion that faster positioning can be achieved by permitting higher losses.

The currents, forces and motion paths of the LPM motor for $X = 100$ mm and various values of P are shown in Figures 54-56. Note that the travel time values obtained from the interpolated solutions of $T(X, P)$ are merely approximations; hence, the actual costs calculated from the numerical method are not perfectly matched with the selected values of (100, 75, 50) W due to interpolation error.

4.3 Performance Assessment of LVR Motors

Three performance assessments of the LVR motor, namely maximum force limit, spatial average power dissipation and productivity trade-off curve, are discussed in the following sections. The maximum force limit is based on solving constrained optimization problems numerically to obtain magnetostatic performance characteristics;

```

% Stage 1
for various values of  $X$ 
  for various values of  $T$ 
    solve the optimal control problem (42)-(43)
  end
end
store function  $P_{\min}(T, X)$ 

% Stage 2
for various values of  $X$ 
  for various values of  $P$ 
    solve for  $T$  from  $P_{\min}(T, X) = P$ 
  end
end
store function  $T(X, P)$ 

```

Figure 51: Two-stage algorithm for determining the trade-off curve $T(X, P)$ using the proposed numerical method.

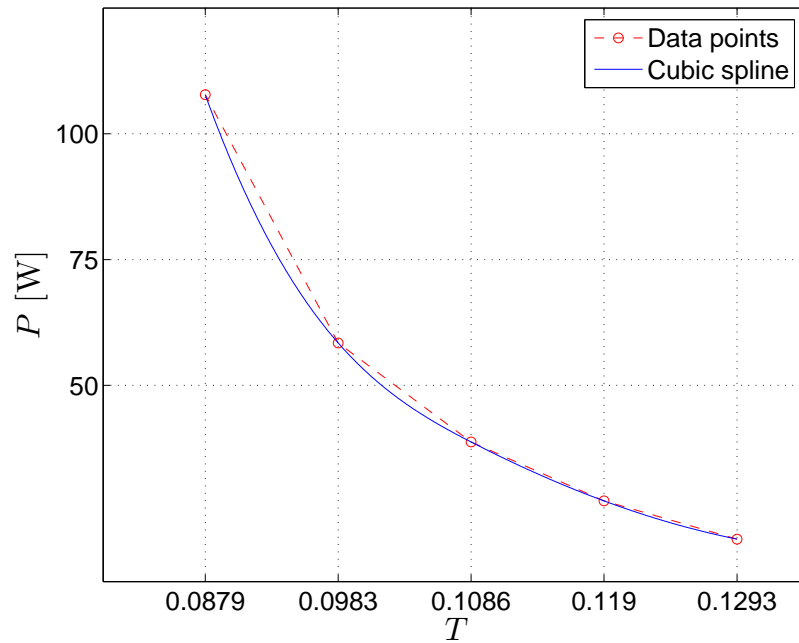


Figure 52: Trade-off between P and T for $X = 100$ mm.

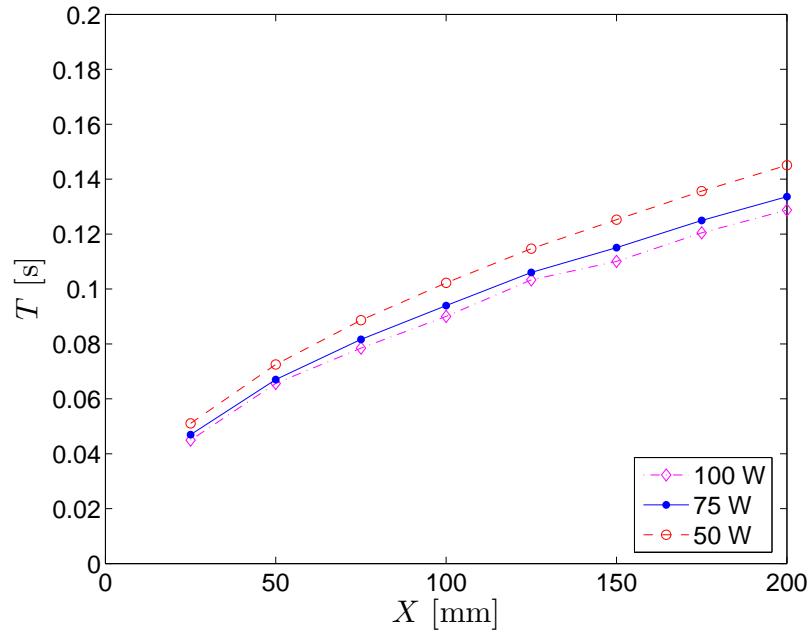


Figure 53: Optimal performance function $T(X, P)$ of the LPM motor.

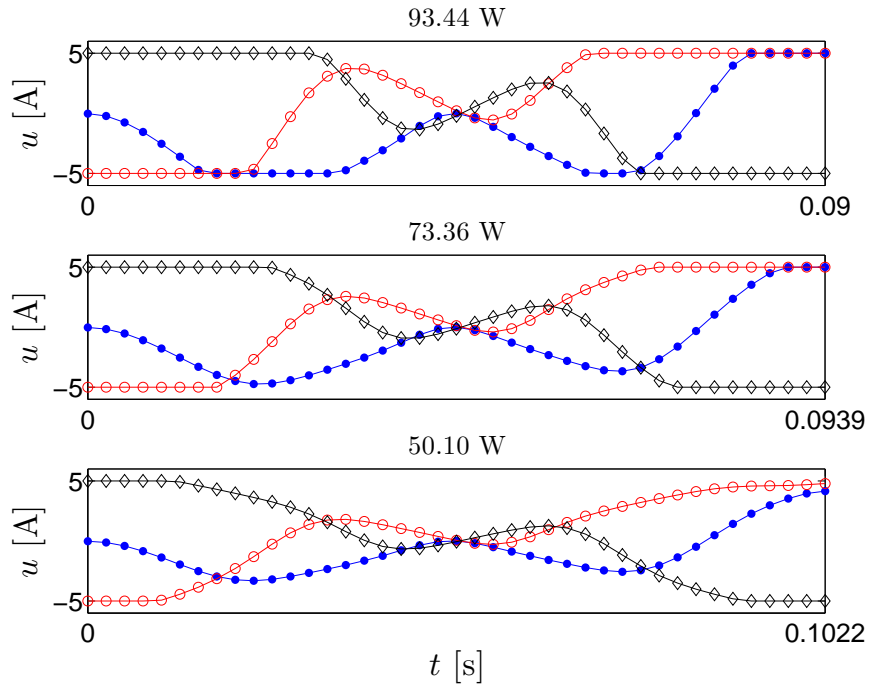


Figure 54: The current trajectories of the LPM motor for $X = 100$ mm ($u_1 =$ dots, $u_2 =$ circles and $u_3 =$ diamonds).

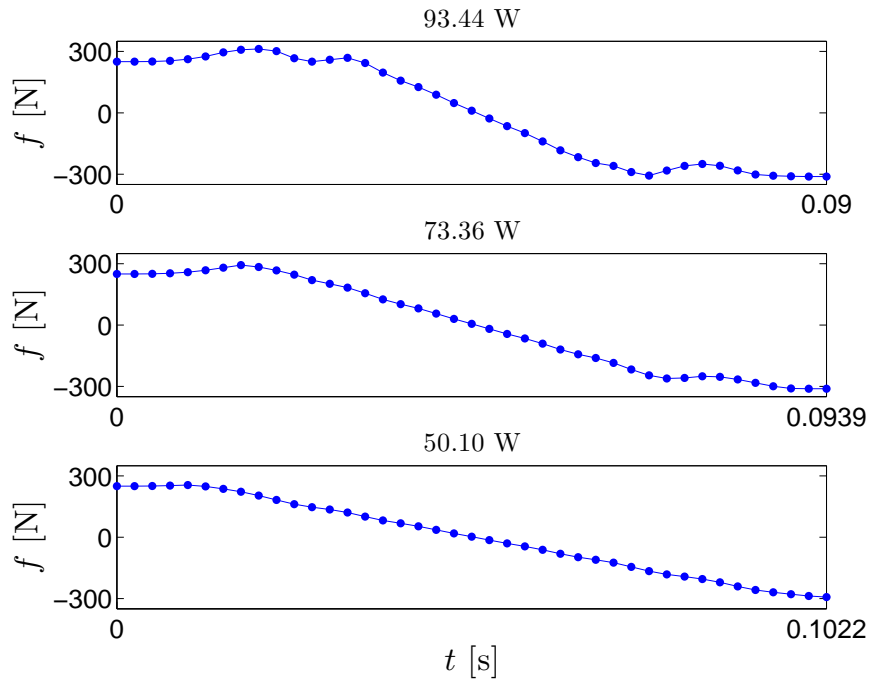


Figure 55: Force trajectories of the LPM motor for $X = 100$ mm.

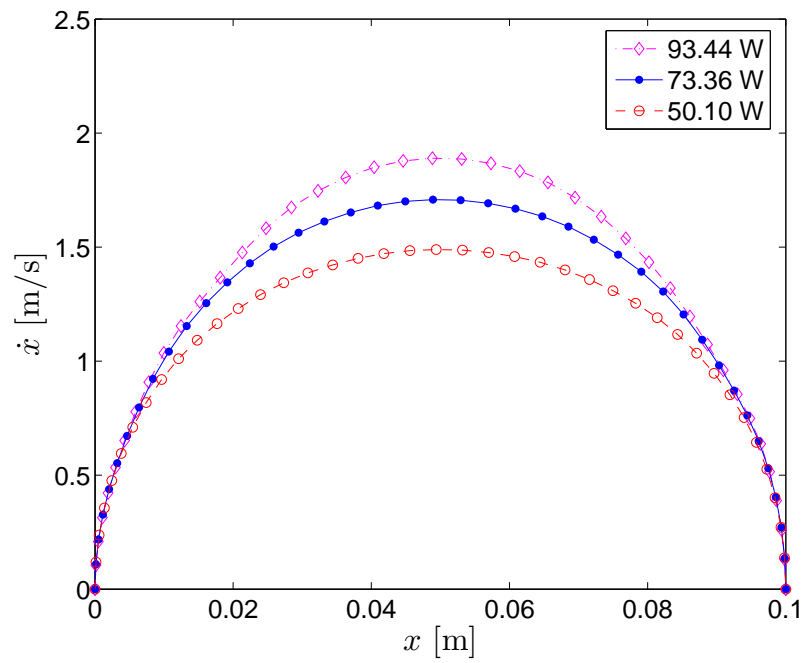


Figure 56: Motion trajectories of the LPM motor for $X = 100$ mm.

this method is the same as for the LPM motor. Due to magnetic saturation and spatial harmonics, the spatial average power dissipation is derived from solving constrained optimization problems. Because of the expensive cost for evaluating the force function of the LVR motor, the productivity trade-off curve is not based on solving multiple optimal control problems as for the LPM motor. An alternative approach, inspired by the analytical results previously presented in Chapter 2, is instead suggested. This proposed methodology derives the productivity trade-off curves based on a sub-optimal control scheme that can be extended using other control schemes including optimal control.

4.3.1 Maximum Force Limit

As for the LPM motor, the maximum force capability of the LVR motor is determined by solving the static optimization problem (175) where $f(x, u)$ is now the force function of the LVR motor and where τ is replaced by the tooth pitch p_t . Two corresponding values of interest, F_s and F_a , are calculated according to (179)-(180), also with τ replaced by p_t .

The maximum force limit performance is first explored to determine the maximum (positive) force capability of the LVR motor for $U = 5$ A. The plots of the maximized force $f^*(x)$ with corresponding currents $u^*(x)$ are shown in Figure 57. The optimal current profiles, which include spatial harmonics and steel saturation, are perturbations from the results for the ideal VR motor previously discussed. The resulting maximum smooth force and the maximum average force are 41.86 N and 134.87 N, respectively. The plots of the maximized force $f^*(x)$ with corresponding currents $u^*(x)$ for $U = 2, 4, 6, 8$ A are shown in Figure 58. The force ripples become larger and the presence of steel saturation is apparent since each plot lies closer to the adjacent plot as U increases.

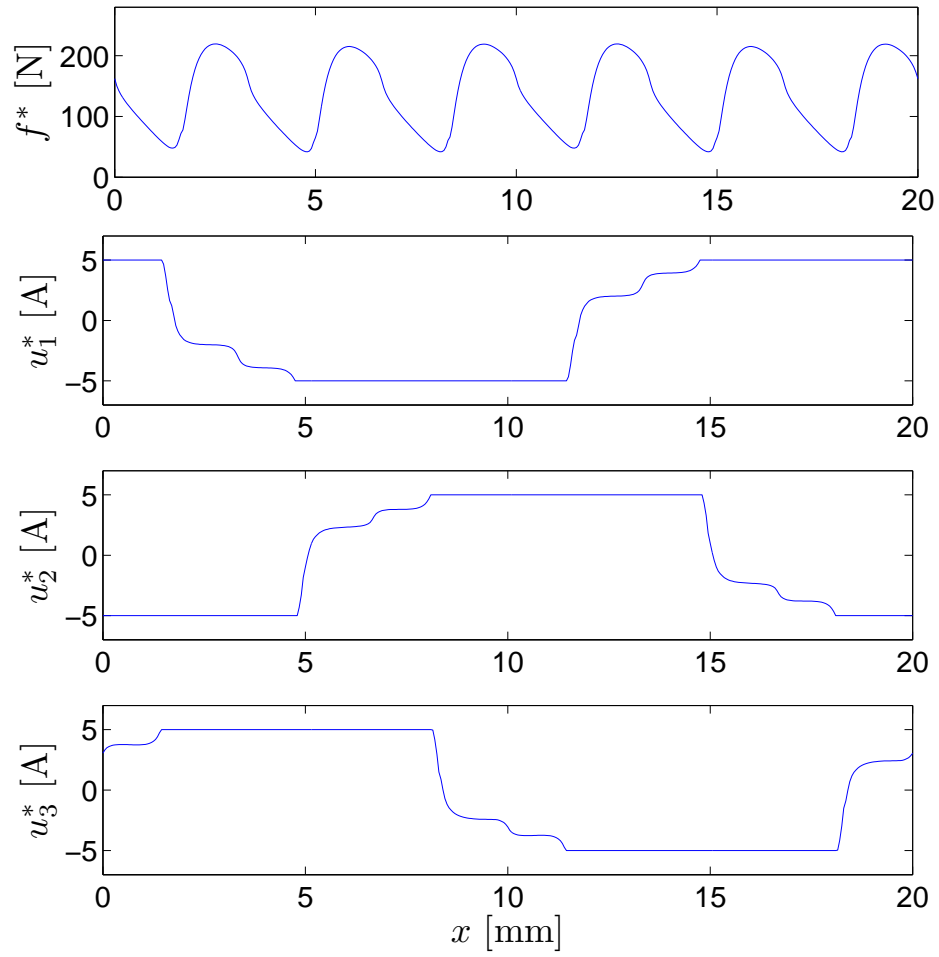


Figure 57: Force maximizing currents and resulting force of the LVR motor for $U = 5$ A, resulting in $F_s = 41.86$ N and $F_a = 134.87$ N.

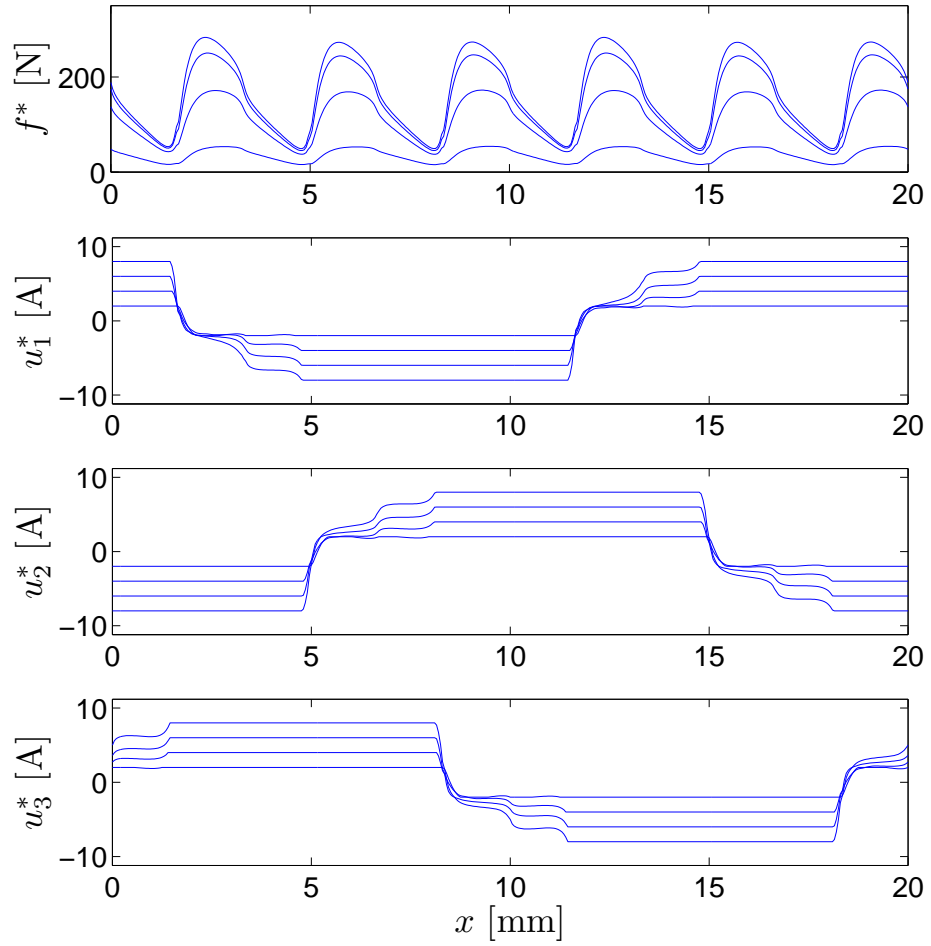


Figure 58: Force maximizing currents and resulting force of the LVR motor for $U = 2, 4, 6, 8$ A.

4.3.2 Spatial Average Power Dissipation

The second performance assessment considered is the spatial average power dissipation. This quantity can be determined by solving the minimum-copper-loss force control problem.

Since two versions of the problem exist, namely with and without current limit, a decision must be made whether or not to consider both cases or choose between the two available choices. Unlike the LPM motor whose force model exhibits a special structure that can be exploited due to magnetic linearity, no such advantage exists for the LVR motor due to the presence of both magnetic saturation and spatial harmonics. Since the primary concern for the target application is the smooth force capability, the minimum-copper-loss commutation problem with current limit is solved directly to determine the corresponding P_x - f_d curve.

4.3.2.1 Problem Formulation

For a 6-wire connection between motor and inverter, the minimum-copper-loss force control problem with cubical current limit can be stated for each $x \in [0, 2p_t]$ in the form

$$\text{minimize} \quad u^T u \quad (193)$$

$$\text{subject to} \quad f(x, u) = f_d \quad (194)$$

$$|u_j| \leq U \quad , \quad j = 1, 2, 3 \quad (195)$$

where the desired continuous force command satisfies $f_d \leq F_s$. The spatial average power dissipation is calculated by

$$P_x(f_d) = \frac{R}{2p_t} \int_0^{2p_t} u^{*T} u^* dx \quad (196)$$

where u^* is the solution to the minimum-copper-loss commutation problem for $x \in [0, 2p_t]$.

For each value of f_d , there is a corresponding value of P_x ; hence for a range of f_d , there exists a corresponding P_x - f_d curve. According to the results of the ideal VR motor shown in Figure 34 of Chapter 2, the general shape of the P_x - f_d curve is a straight line. However, the actual shape for the LVR motor would be a perturbation from a straight line because of steel saturation and spatial harmonics. Therefore, the performance assessment may be defined to be the *average slope* of the P_x - f_d curve, i.e.

$$s = \frac{1}{F_s} \int_0^{F_s} \frac{dP_x}{df_d} df_d = \frac{1}{F_s} P_x \Big|_{F_s} = \frac{P_x(F_s)}{F_s} \quad (197)$$

This average slope preserves the information of the general shape of the P_x - f_d curve when the current excitations are small (mostly linear) and also captures the nonlinear effects when the current excitation is high.

Similar to the LPM motor, for comparison between two different motor designs, the first design is better than the second design if, for the same F_s and moving mass, its value of s is smaller than the other's because it can dissipate less heat while producing the same force.

4.3.2.2 Numerical Results

The minimum copper-loss-force control is explored to determine the spatial average power loss of the LVR motor for $U = 5$ A and $R = 1.44$ Ω . The optimal excitation currents are solved for $f_d = 0.95F_s$ to account for numerical error. The plots of the currents $u^*(x)$ with corresponding power dissipation $Ru^{*T}u^*(x)$ are shown in Figure 59. These results are consistent with those obtained for the ideal VR motor previously discussed in Chapter 2. The spatial average power is 20.53 W and the resulting average slope is $s = 0.5161$ W/N.

For comparison, the plot of the spatial average power of the LVR motor for various values of f_d is shown in Figure 60. The P_x - f_d curve is linear for small values of f_d and becomes nonlinear when the value of f_d increases because the LVR motor

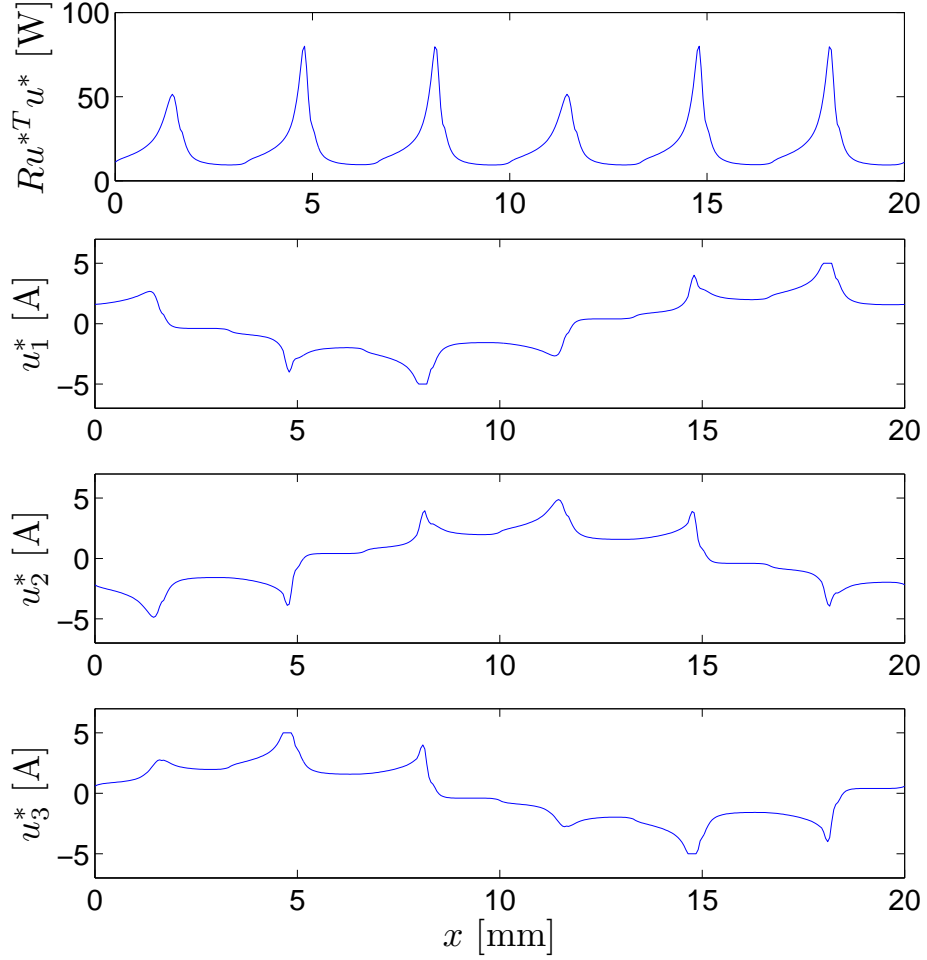


Figure 59: Minimizing copper-loss currents for $f_d = 0.95F_s = 39.76$ N of the LVR motor, resulting in $P_x = 20.53$ W and $s = 0.5161$ W/N.

requires much higher increment of currents to produce smaller increment in force once the steel is saturated at higher f_d . The spatial average power corresponding to F_a calculated from the force maximizing currents is also shown for comparison. This data point belongs to the minimum-copper-loss average force control problem as previously discussed.

4.3.3 Productivity Trade-Off Curve

Since the force function $f(x, u)$ of the LVR motor is much more complex and computationally expensive to evaluate, the numerical method presented in Section 2.6.1 and the algorithm shown in Figure 51 for the LPM motor are not practical to derive

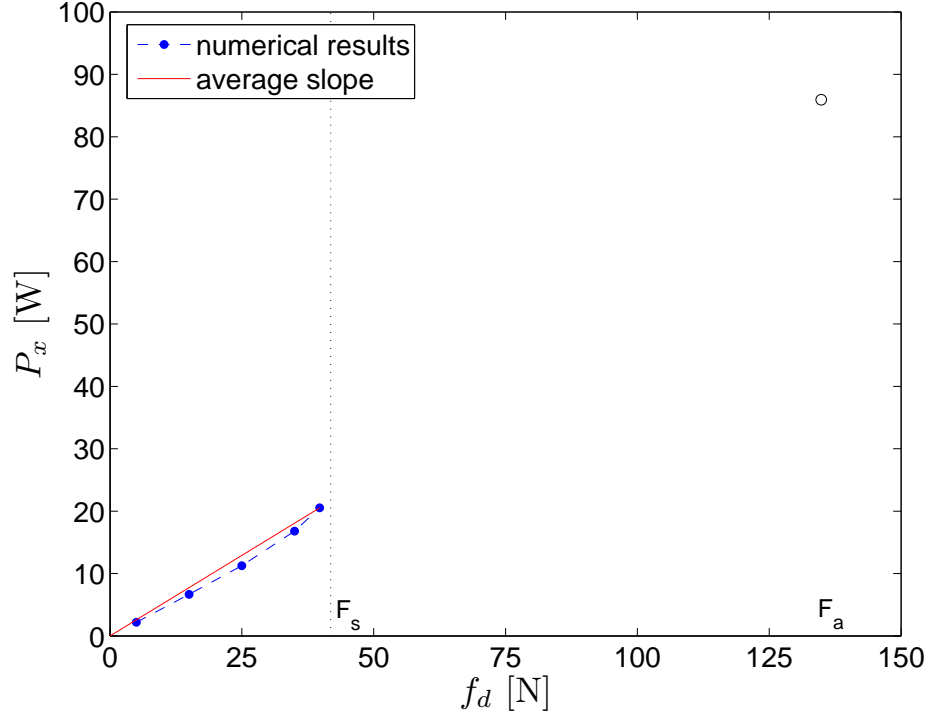


Figure 60: Spatial average power P_x for various values of f_d of the LVR motor.

the productivity trade-off curves $T(X, P)$ for the LVR motor. Instead, an alternative approach, inspired by the analytical results for the ideal VR motor, is proposed to obtain the $T(X, P)$ curves based on a sub-optimal control scheme.

4.3.3.1 Sub-Optimal Control Implementation

Consider the optimal control result, presented in Chapter 2 and repeated here for convenience, for the ideal VR motor as shown in Figure 61. The two “bang” portions of the trajectory are confined by the time-optimal control result, and the motor travels with constant velocity during the middle “off” portion for $P < P_*$. Hence, to derive an approximate solution to the optimal control problem for the LVR motor, the two bang portions can be determined using the (positive) maximum force and (negative) minimum force commutation results. The middle off portion is then determined by connecting a horizontal straight line corresponding to the cruising phase (constant velocity).

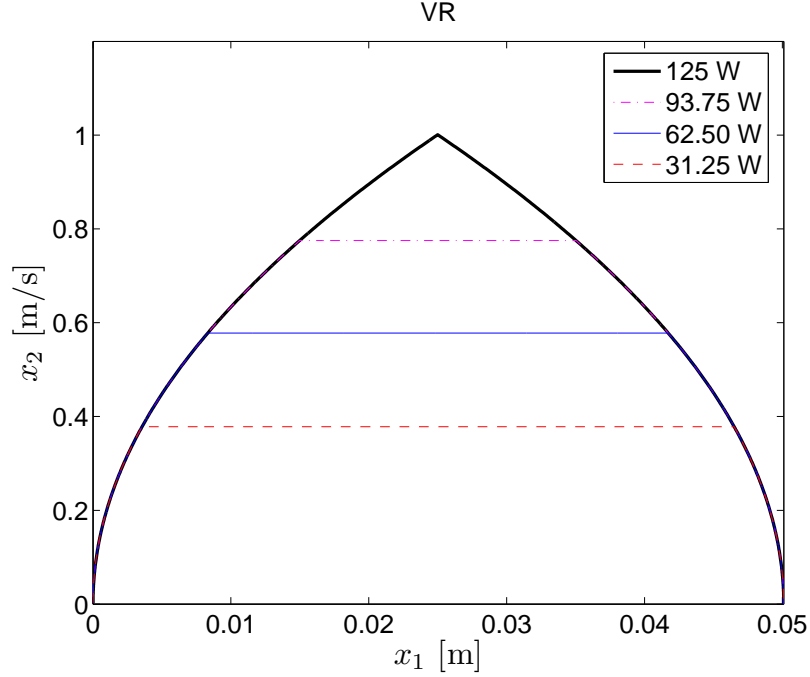


Figure 61: Optimal trajectories of the ideal VR synchronous motor for $X = 0.05$ m.

To pursue this approach, two numerical integrations from both ends (forward integration from $t = 0$ and backward integration from $t = T$) are required in order to ensure that boundary conditions are met. The forward integration problem is approximated by the Forward Euler formula

$$\begin{bmatrix} x_1^{n+1} \\ x_2^{n+1} \end{bmatrix} = \begin{bmatrix} x_1^n \\ x_2^n \end{bmatrix} + \Delta t \begin{bmatrix} x_2^n \\ \frac{1}{M} f^+(x_1^n) \end{bmatrix} \quad (198)$$

where x_1^n and x_2^n are the position and velocity at time step n , Δt is the forward integration step size and f^+ is the solution of the maximum (positive) force commutation problem. The backward integration is achieved by applying a change of variables, $\tau = T - t$, so that $t = T$ corresponds to $\tau = 0$ and $d\tau/dt = -1$, resulting in the Forward Euler formula

$$\begin{bmatrix} x_1^{n+1} \\ x_2^{n+1} \end{bmatrix} = \begin{bmatrix} x_1^n \\ x_2^n \end{bmatrix} - \Delta \tau \begin{bmatrix} x_2^n \\ \frac{1}{M} f^-(x_1^n) \end{bmatrix} \quad (199)$$

where $\Delta \tau$ is the backward integration step size and f^- is the solution of the minimum

(negative) force commutation problem.

4.3.3.2 Numerical Results

The positive time and negative time integration problems can be solved separately on the computer. The resulting trajectories are plotted on the position-velocity phase plane and the point where two trajectories intersect is a good estimate of the switching time for the time-optimal control.

The trajectories of the minimum copper loss control are then estimated by connecting the two trajectories with horizontal straight lines, as illustrated in Figure 62 for $X = 100$ mm. The corresponding values of the average power dissipation are 86.49, 67.85, 45.93, 23.78 and 5.76 W. The trajectory plots of the time-optimal control for position, velocity, force and currents versus time are shown in Figures 63-64. Although the force ripple magnitude is large, the position is less affected than the velocity or the acceleration (not shown) due to the low pass filtering effect of the double integration. Note that the switching time is not at the mid point of the motion due to asymmetry during the acceleration and deceleration phases. The force and current trajectories are all discontinuous at the switching time.

The proposed alternative method is applied to solve for several X values, as depicted in Figure 65. The corresponding values of P and T are calculated for each X and the stored functional values of $P_{\min}(T, X)$ are interpolated and solved for $P = (75, 62.5, 50)$ W. The resulting trade-off curves $T(X, P)$ of the LVR motor are shown in Figure 66. The plots also exhibit the same trend obtained for the LPM motor where higher productivity can be achieved (lower T) by expending more heat (higher P).

4.4 Conclusion

The assessment of optimal control performance for LPM and LVR motors has been pursued for point-to-point positioning applications. Three approaches of optimal

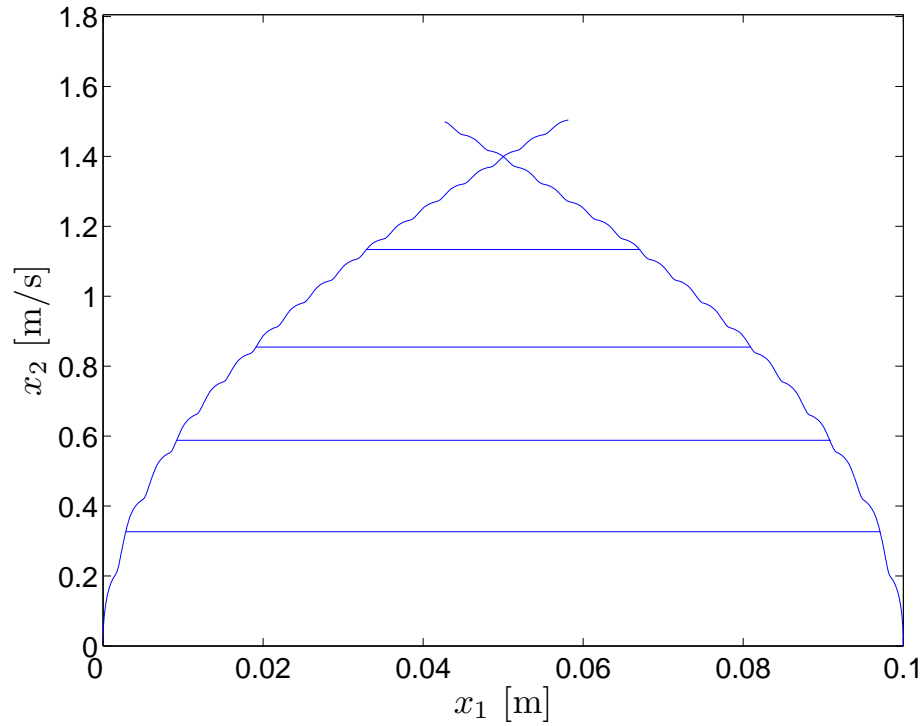


Figure 62: Plot of the time-optimal control trajectory for $X = 0.1$ m of the LVR motor using the maximum force control results at various average power dissipation values.

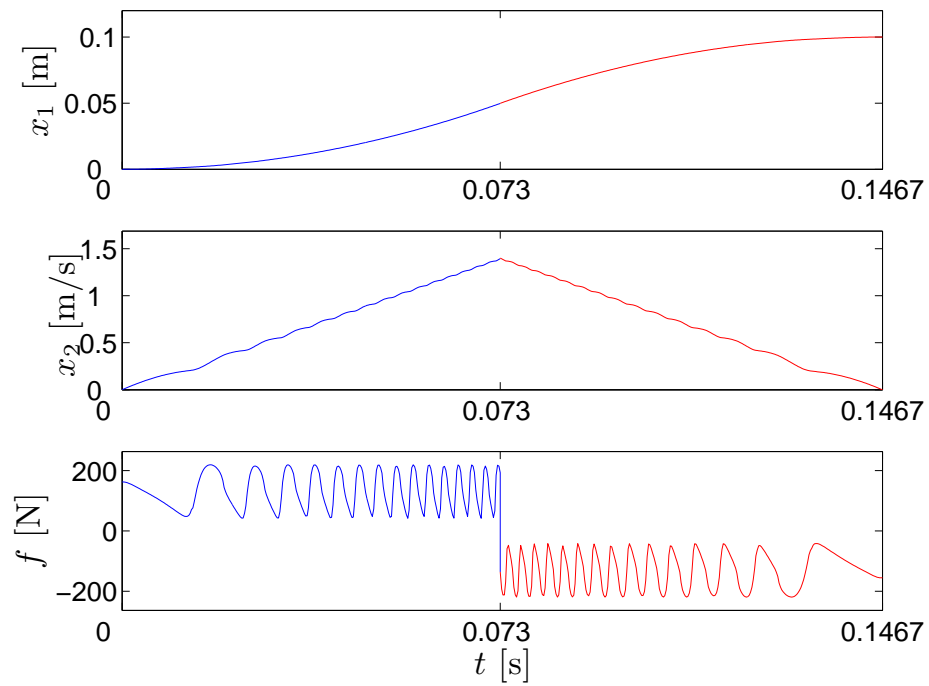


Figure 63: The trajectories of position, velocity and force for $X = 0.1$ m of the time-optimal control results for the LVR motor.

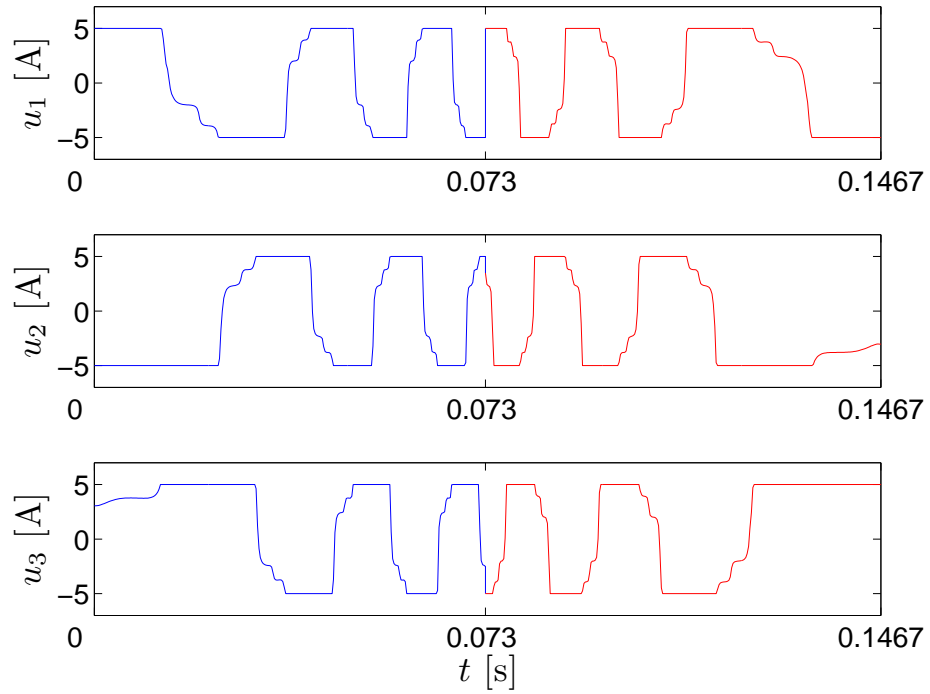


Figure 64: The current trajectories for $X = 0.1$ m of the time-optimal control results for the LVR motor.

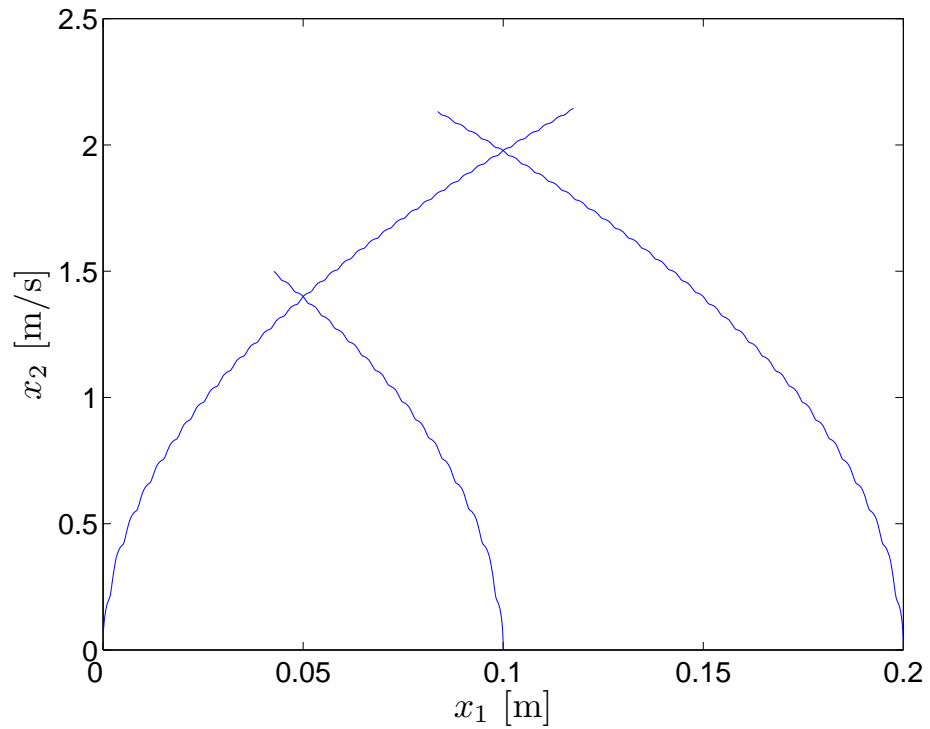


Figure 65: Plot of the time-optimal control trajectories for $X = 0.1$ m and 0.2 m of the LVR motor using the maximum force control results.

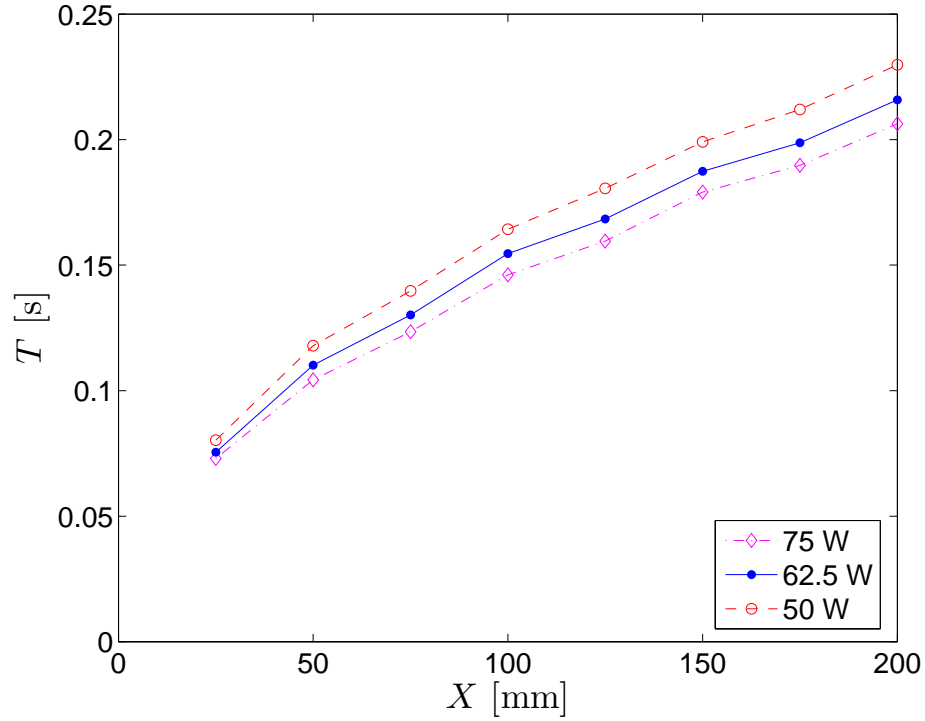


Figure 66: Approximate trade-off curve between minimum travel time and desired travel distance of the LVR motor.

performance assessment, namely maximum force limit, spatial average power dissipation and productivity trade-off curve are considered. Such approaches may be used to guide the design of the motor along with the design of its control system. The performance assessment methodology developed here may be applied to any motor technology used in manufacturing automation applications. Note that only the first two assessment approaches will be implemented for the design of the LPM and LVR motors in the following chapter because of their numerical efficiency.

CHAPTER 5

MULTI-OBJECTIVE DESIGN OPTIMIZATION

5.1 Introduction

The objective of this chapter is to develop the automated computer-aided design methodology for the LPM and LVR motors based on the multi-objective optimization principle. The general design procedure includes three main steps: synthesis, analysis and optimization. The synthesis of designs is achieved using stochastic search methods, which have the advantage of covering the entire search space of design parameters without getting stuck at local extrema as may occur in single-objective optimization problems. The applications of the multi-objective optimization techniques for motor designs by other researchers are already discussed in Section 1.3.3.

In this research, Monte-Carlo (unguided random) synthesis is chosen due to its advantage of not relying on expert rules or past experience that may limit design creativity. The analysis of designs is based on solving several single-objective optimization problems to determine performance measures that broadly characterize each candidate design for later design optimization comparison, as demonstrated in Chapter 3. The multi-objective optimization feature of this approach allows evaluation of design trade-offs along Pareto-optimal frontiers. With manufacturing automation as the target application, the design goal is to search for motors characterized by maximum acceleration and minimum average power dissipation subject to constraints on current density, flux density, speed and voltage.

The design optimization of the LPM and LVR motors, although similar in several aspects, is discussed in different sections due to differences in physical construction and modes of operation. For instance, the LPM motors require permanent-magnets

for construction while the LVR motors do not. On the other hand, the LVR motors usually operate in the saturation region of the BH-curve whereas the LPM motors operate in the linear region that respectively results in nonlinear and linear behaviors. This leads to a different number of objective functions and constraints for the design optimization for each type of motor. Nonetheless, the bases for analyzing candidate designs for both types of motors share some similarities because the design objectives aim for the same target application.

5.2 General Problem Statement

The multi-objective design optimization problem [42] can be stated in a general form as

$$\begin{aligned}
 & \text{minimize/maximize } F_i(\theta) && , \quad i = 1, 2, \dots, I \\
 & \text{subject to } g_j(\theta) \leq 0 && , \quad j = 1, 2, \dots, J \\
 & h_k(\theta) = 0 && , \quad k = 1, 2, \dots, K \\
 & L_m \leq \theta_m \leq U_m && , \quad m = 1, 2, \dots, M
 \end{aligned} \tag{200}$$

where θ is a vector of design parameters, F is a vector of objective functions to be optimized, g is a vector of inequality constraints, h is a vector of equality constraints, and L and U are vectors of lower bounds and upper bounds, respectively.

This optimization problem seeks the θ that simultaneously optimizes all objective functions F_i of interest (e.g. minimize moving mass, maximize force). The solution to this optimization problem is not a single design if some of the performance metrics are competing with one another (e.g. a smaller moving mass motor cannot produce high force) and hence a so-called Pareto-optimal set of solutions is obtained in which any objective function can be improved only by degrading another objective function. If the objective functions are non-competing to one another (e.g. minimizing mass and minimizing volume), the problem yields only one optimal solution located at the boundary. In general, the non-competing nature among different objective functions might not be obvious.

Multi-objective optimization has a long history as summarized in [42]. However, a multi-objective optimization was often posed as a single-objective optimization in the past using some “fix-ups” to address the multi-objective nature of the problem. The two most common fix-ups are the weighted sum method and the so-called ϵ -constraint method. For the weighted sum method, multiple objectives are grouped together using some pre-determined weighting factors resulting in single objective function to be optimized. Apparently, the optimal solution depends heavily on those pre-determined factors. For the ϵ -constraint method, a single objective is chosen among the available multiple objectives and the remaining objectives are considered as constraints with some pre-determined limits. Here, the optimal solution also depends heavily on the choice of the selected objective function and those pre-determined constraint limits. These types of fix-ups usually create difficulties for choosing the pre-determined values that could potentially lead to sub-optimal solutions.

In addition to no artificial fix-ups being added, the other two main features of multi-objective optimization that are distinctively different from single-objective optimization are the overall optimization goals to: (i) determine solutions as near as possible to the Pareto-optimal frontier and (ii) determine solutions as diverse as possible by covering the entire search space. These two features are not present in single-objective optimization that focuses on searching for only one optimal solution from the entire search space. Multi-objective optimization gives rise to many optimal solutions along Pareto-optimal frontiers; hence it is important to have a sufficient number of solutions spreading over the entire search space to guarantee that a good set of solutions has been achieved.

Since the designs of the LPM and LVR motors for the target application have several objectives (i.e. maximizing acceleration and minimizing power dissipation), it is best to address them in terms of multi-objective optimization problems. Note that to maximize acceleration, moving mass must be minimized and force must be

maximized.

5.3 Motor Design System

The structure for solving the multi-objective design optimization problem is illustrated in Figure 67. The general procedure includes three main steps: synthesis, analysis, and optimization. First, the objective function vector F (e.g. mass, force, average power dissipation), inequality constraints g (e.g. maximum mass, minimum force), equality constraints h (e.g. maximum current density, maximum velocity), and feasible ranges for geometrical parameters L and U must be specified. Then the three steps of synthesis, analysis and optimization take place in sequence many times until the space of design parameters has been sufficiently explored. Some of the designs will need to be discarded because they do not meet the requirements specified by the designer. Designs meeting all requirements are tested in sequence for possible inclusion in a database of “good” designs. Ultimately, this procedure reveals the location of Pareto-optimal frontiers associated with the attributes of interest. The three distinct steps (synthesis, analysis, and optimization) are summarized below.

5.3.1 Synthesis

Synthesis of designs can be achieved using stochastic search methods such as Monte-Carlo (MC), genetic algorithm or particle swarms. All of the stochastic search methods have the advantage that they generally cover the entire space of design parameters and therefore they do not get stuck at local extrema.

In particular, MC synthesis or unguided random synthesis is chosen in this research. Although the unguided nature of the MC synthesis has the disadvantage that good designs are generated less often and hence the computational efficiency is low in comparison with other stochastic search methods, it has the advantage that there is virtually no reliance on expert rules and hence creativity is fully promoted.

The MC synthesis process generates a random set of design parameters from

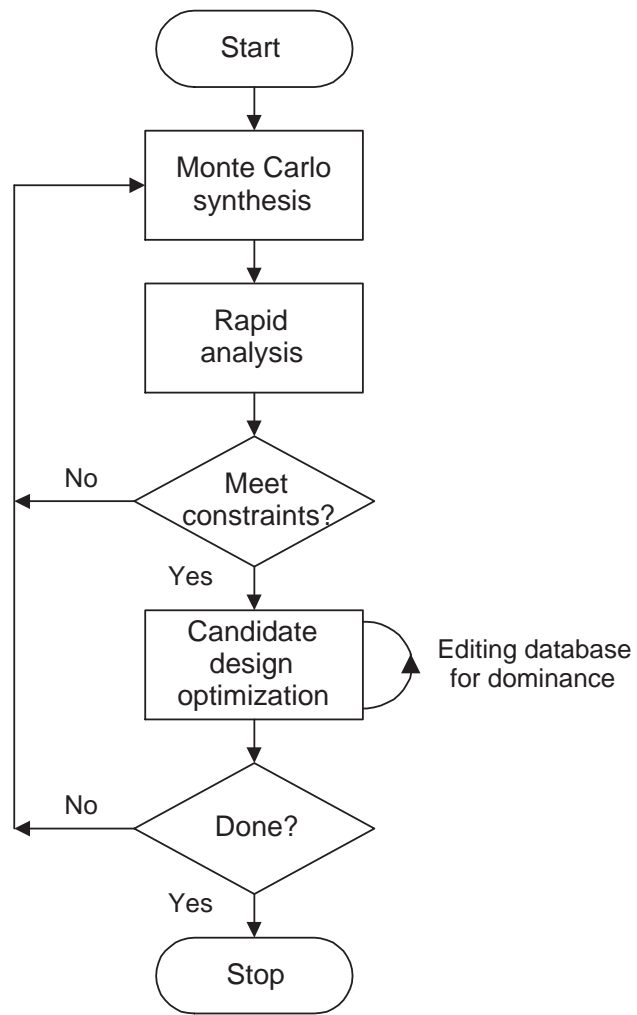


Figure 67: The proposed computer-aided design structure.

permissible ranges using uniform distribution. The design parameters with the most influence on the design must be synthesized first, and then used to set the permissible ranges for the subsequent choices of the remaining design parameters. Optimization based on MC synthesis may be time consuming because a large number of designs is needed to cover the design space. Hence, some design rules and/or expert knowledge may be implemented here to limit the size of the design space, but only at the risk of limiting design creativity. As computational capabilities improve, this trade-off can be expected to diminish. After all design parameters are randomly synthesized, the next step is to analyze the performance of the candidate design.

5.3.2 Analysis

Analysis of a candidate design is the evaluation of the objective functions using mathematical models. As pointed out earlier, a primary design goal is to maximize productivity; hence optimal performance assessment must be implemented at this stage to determine all objective functions of each candidate design. The analysis of candidate designs requires rapid computations because of the aforementioned large number of designs being randomly synthesized. For the linear motor drive system, it is appropriate to use the physics-based analytical model of the LPM motors or nodal network model for the LVR motors. Note that an individual objective function may be based on a single-objective optimization problem.

5.3.3 Optimization

Those designs that have been successfully synthesized and analyzed are subjected to dominance testing. Since many design objectives are considered, the performance of a given design is not simply summarized as a scalar value that may be directly compared to the corresponding scalar value of another competing design. Instead, the objective function is vector-valued and the concept of dominance is used to sort designs into a non-dominated set and a dominated set. Given two designs, the first

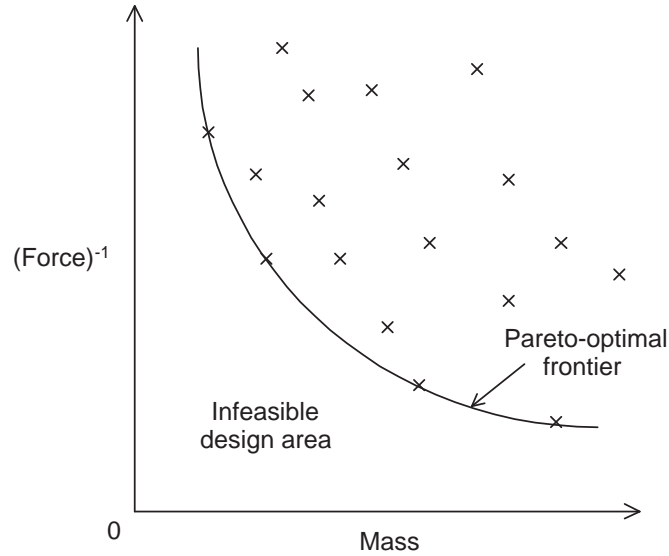


Figure 68: A trade-off curve between two objective functions.

design is said to dominate the second design if (i) the first design performs no worse than the second design with respect to all objective functions and (ii) the first design performs strictly better than the second design with respect to at least one objective function. For a given population of designs, a particular design is a member of the dominated set if it is dominated by any other design in the population. A design that is not dominated by any other design in the population is a member of the non-dominated set.

The objective of the overall design process is to create a substantial number of dominant designs, through the repeated application of synthesis, analysis and optimization. The members of the non-dominated set will reveal the location of Pareto-optimal frontiers where the optimal balance of objective functions is achieved on the trade-off curves. The plot of a typical trade-off curve for two objective functions (force and mass) is shown in Figure 68. The origin represents an ideal machine, i.e. a motor with zero mass that could provide infinite force. On a Pareto-optimal frontier, designs cannot improve one objective function without degrading another. The designs that lie above the performance frontier are dominant in other objective functions and no

design exists in the infeasible design area.

The designs of LPM and LVR motors using these concepts are discussed separately in the following sections.

5.4 Linear Permanent-Magnet Motor Design

The diagram of a three-phase LPM motor under consideration is shown in Figure 69. Although the LPM motor is installed with a stationary U-frame and bearing systems, the analysis of the LPM motor performance requires only the design parameters associated with the moving mass and force model. All other design parameters can be fixed or neglected during the design process and then properly selected later as a post-process without affecting the analysis results. For instance, the back iron thickness is being fixed because it plays no role in the force model with the infinite permeability in steel assumption. Furthermore, the mover is assumed to be a solid aluminum block with fixed depth to simplify the model. The objective functions for the LPM motor design optimization are: moving mass, smooth force, average force, average power and magnet volume per meter. The statement of the problem will be presented first and followed by the detailed discussions of design synthesis, analysis, optimization and final design results.

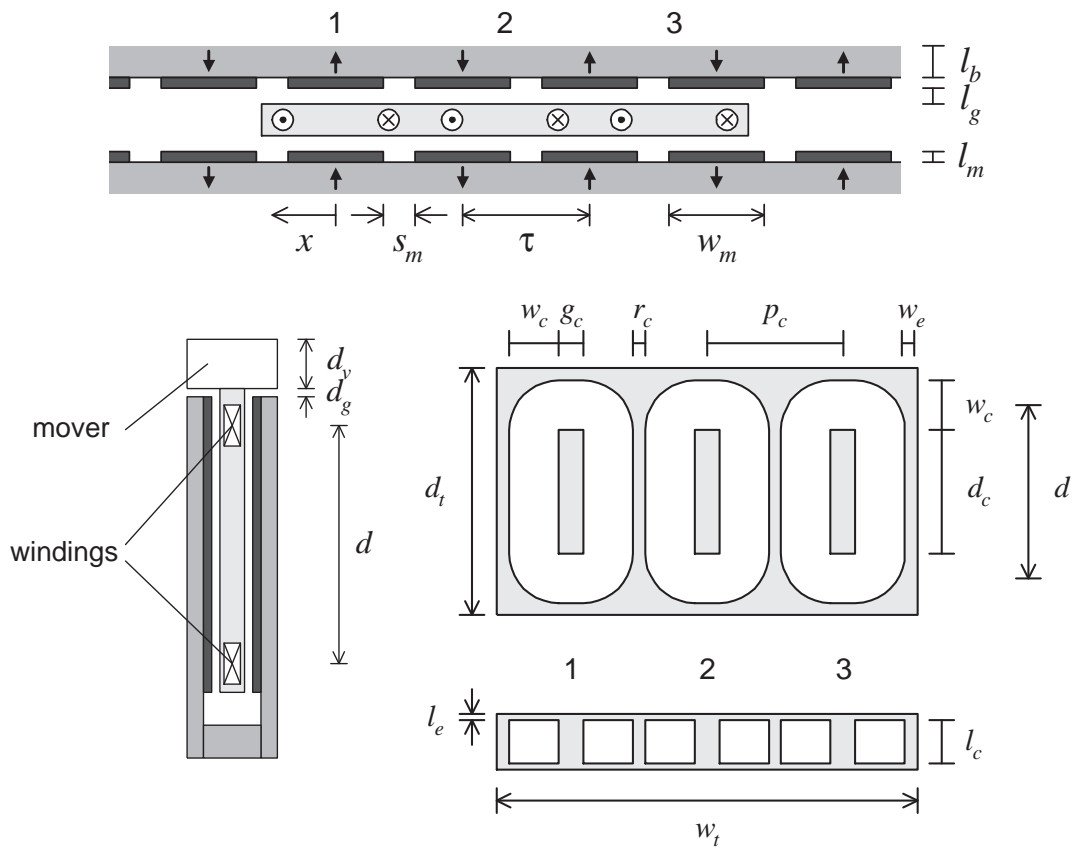


Figure 69: Diagram of design parameters for a LPM motor.

5.4.1 Problem Statement

The LPM motor is characterized by a vector of design parameters, as shown in Figure 69. This vector of design parameters may be defined as

$$\theta = \begin{bmatrix} \tau \\ l_m \\ l_c \\ l_g \\ d_c \\ s_m \\ g_c \\ w_c \\ w \end{bmatrix} \begin{array}{l} \text{(magnet pitch)} \\ \text{(magnet length)} \\ \text{(coil length)} \\ \text{(air gap length)} \\ \text{(coil depth)} \\ \text{(magnet space)} \\ \text{(coil gap)} \\ \text{(coil width)} \\ \text{(wire size, integer)} \end{array}$$

where the dashed lines indicate the sequential order in which the random synthesis takes place. For any feasible θ , there will be corresponding values for motor performance functions to be optimized.

The multi-objective design optimization problem of the LPM motor is given by

$$\begin{array}{ll} \text{minimize} & m \quad \text{(moving mass)} \\ \text{maximize} & F_s \quad \text{(smooth force)} \\ \text{maximize} & F_a \quad \text{(average force)} \\ \text{minimize} & c \quad \text{(average power coefficient)} \\ \text{minimize} & V \quad \text{(magnet volume per meter)} \end{array}$$

subject to the inequality constraints

$$\begin{array}{ll} m \leq & 15 \text{ kg} \quad \text{(maximum mass)} \\ F_s \geq & 10 \text{ N} \quad \text{(minimum smooth force)} \\ v_{\max} \leq & 270 \text{ V} \quad \text{(maximum voltage)} \\ \text{dia}(w) < & l_c \quad \text{(maximum wire diameter)} \end{array}$$

the equality constraints

$$\begin{aligned}
r_c &= 1 \text{ mm} && \text{(minimum side room between coils)} \\
d_g &= 4 \text{ mm} && \text{(clearance gap depth)} \\
d_v &= 20 \text{ mm} && \text{(mover depth)} \\
l_e &= 0.5 \text{ mm} && \text{(epoxy case length)} \\
w_e &= 2 \text{ mm} && \text{(epoxy case width)} \\
s_c &= 0.7 && \text{(coil space factor)} \\
J_{\max} &= 5 \text{ A/mm}^2 && \text{(maximum current density)} \\
\dot{x}_{\max} &= 1.8 \text{ m/s} && \text{(maximum velocity)}
\end{aligned}$$

and the bounds on the variable design parameters

$$\begin{aligned}
10 \text{ mm} &\leq \tau \leq 80 \text{ mm} \\
1 \text{ mm} &\leq l_m \leq 15 \text{ mm} \\
1 \text{ mm} &\leq l_c \leq 25 \text{ mm} \\
0.2 \text{ mm} &\leq l_g \leq 1.6 \text{ mm} \\
15 \text{ mm} &\leq d_c \leq 150 \text{ mm} \\
1 \text{ mm} &\leq s_m \leq 0.2\tau \\
2.5 \text{ mm} &\leq g_c \leq \frac{4}{3}\tau - r_c - 2 \text{ dia}(w = 11)/s_c \\
\text{dia}(w = 11)/s_c &\leq w_c \leq (\frac{4}{3}\tau - r_c - g_c)/2 \\
11 \text{ AWG} &\leq w \leq 30 \text{ AWG}
\end{aligned}$$

The materials are copper and bonding materials for coils, epoxy for coil assembly cases, aluminum for movers and NdFeB permanent-magnets with residual flux density $B_r = 1.2 \text{ T}$ for stators. These specific choices of materials are selected to limit the search space. In this problem formulation, some design parameters are set as equality constraints also to limit the search space but one could vary certain design parameters by including them in θ to increase the size of the search space. The details for synthesizing design parameters are described in the following sections.

5.4.2 Design Synthesis

The MC synthesis process is used to generate a random set of design parameters from the permissible range. Random synthesis for the LPM motor design involves a four-step process where the design parameters with the most influence on the design must be synthesized first, and then used to set the permissible ranges for the subsequent choices of the remaining design parameters.

In the first step, the following five design parameters are randomly selected with uniform probability distributions: τ , l_m , l_c , l_g and d_c .

In the second step, the bound for magnet space s_m can be set after τ is known. To guarantee that at least one turn of the biggest wire considered (AWG 11) will fit horizontally, the constraint on the upper bound of the coil gap is set to

$$g_c \leq \frac{4}{3}\tau - r_c - 2 \text{dia}(w = 11)/s_c \quad (201)$$

and the lower bound is set arbitrarily.

In the third step, the bound for the coil width w_c is set accordingly after g_c is known. The random choices of w_c and l_c introduce limitations on the available coil area for the final step selection.

To guarantee that at least one turn will fit the coil area, the wire diameter must be less than l_c . Take AWG_{\min} to be the smallest AWG value, greater than or equal to AWG 11, that satisfies this constraint on wire diameter. For each w value between AWG_{\min} and AWG 30, determine the corresponding value of N according to

$$N = \frac{s_c w_c l_p}{A_w(w)} \quad (202)$$

where A_w is the conductor area. Each such (w, N) pair is then checked for feasibility, using an idealized model of the LPM motor assumed to be operating with excitation that minimizes instantaneous copper losses. To this end, a current limit is first established by

$$i_{\max} = A_w J_{\max} \quad (203)$$

This current limit is consistent with the specified limits on current density $J_{\max} = 5$ A/mm² to limit the temperature rise for the inside coil structure of the LPM motors [70]. Operation with maximum current at radian frequency $\omega = \frac{\pi}{\tau} \dot{x}_{\max}$ is then possible if

$$v_{\max} = \sqrt{R^2 + (\omega L)^2} i_{\max} \leq V_{\max} \quad (204)$$

where L is the coil self inductance. The coil parameters (w, N) are then selected randomly with uniform probability distribution from among the feasible candidates identified above. The detailed derivations are given in Appendix B.

5.4.3 Design Analysis and Optimization

After design parameters for a candidate solution have been randomly synthesized, the next step is to perform analysis to calculate the vector of objective functions. The objective functions related to manufacturing application are already discussed and demonstrated for a LPM motor in Chapter 4. The additional details to calculate other objective functions are included in Appendix B.

The first objective function is determined by

$$m = \text{moving mass} \quad (205)$$

The associated force function of the LPM motor

$$f(x, i) = K(x)^T i$$

is based on physical properties as presented in Chapter 3. Two objective functions associated with achievable force, the “smooth” limit and the “average” limit, are calculated according to

$$F_s = \min_{x \in [0, 2\tau]} f^*(x) \quad (206)$$

$$F_a = \frac{1}{2\tau} \int_0^{2\tau} f^*(x) dx \quad (207)$$

where $f^*(x)$ is the solution to the maximum force commutation problem

$$\begin{aligned} & \text{maximize} && f(x, i) \\ & \text{subject to} && |i_j| \leq i_{\max} \quad , \quad j = 1, 2, 3 \end{aligned}$$

for each $x \in [0, 2\tau]$ and i_{\max} is given by (203). Next recall the spatial average power dissipation, previously defined as

$$P_x(f_d) = \frac{R}{2\tau} \int_0^{2\tau} i^{*T} i^* dx$$

where R is the phase resistance and i^* is the solution to the minimum copper loss commutation problem without current limit

$$\begin{aligned} & \text{minimize} && i^{*T} i \\ & \text{subject to} && f(x, i) = f_d \end{aligned}$$

for each $x \in [0, 2\tau]$ and any desired force f_d . The objective function associated with this performance measure is defined as the average power coefficient of the P_x - f_d parabola curve, i.e.

$$c = \frac{R}{2\tau} \int_0^{2\tau} \frac{1}{K(x)^T K(x)} dx \quad (208)$$

The final objective function to be considered is

$$V = \text{magnet volume per meter} \quad (209)$$

which is included in the LPM motor design to prevent the over-usage of permanent magnet materials [51].

This set of objective functions identifies limits on achievable acceleration (minimum moving mass and maximum force), average power dissipation with constant velocity operation mode and magnet usage due to constraints imposed on current density, velocity and voltage. These objective functions are clearly competing and therefore the solution to this optimization problem is not a single design. To limit the search, the constraints $F_s \geq 10$ N and $m \leq 15$ kg are imposed.

The stages of synthesis and analysis eliminate some designs because they cannot satisfy all of the specified constraints. Those designs that have been successfully synthesized and analyzed are subjected to optimization, using multi-objective dominance testing. More specifically, designs reaching this stage of consideration will be compared to each other to form a database of non-dominated designs. The logic applied to build the database is as follows: candidate designs that are superior in one or more objective functions (i.e. being non-dominated) are added to the database; candidate designs that are inferior in all objective functions (i.e. being dominated) are deleted from the database. A database maintaining software can be implemented on a computer using this logic description.

5.4.4 LPM Motor Design Results

The procedure described above was employed for a total of 120000 trials. Of these, 42484 trials were rejected due to small force and none was rejected due to large mass. Hence, 77516 candidate designs were identified and, of these, 1863 belonged to the non-dominated set. The database of 1863 dominant designs is characterized statistically by Table 9.

Figure 70 shows the dominant designs with respect to smooth force and moving mass in two formats; reciprocal smooth force $1/F_s$ on the top and smooth force F_s on the bottom. Figure 71 shows the dominant designs with respect to average force and moving mass, with reciprocal average force $1/F_a$ on the top and average force F_a on the bottom. The Pareto-optimal frontiers are particularly apparent when reciprocal force is plotted against mass, since the origin represents the unachievable ideal.

Since smooth force and average force are strongly interrelated, both Figure 70 and Figure 71 look similar to each other due to small ripple force. The trade-off between force and mass along the performance frontiers is clear in these plots.

Figure 72 shows the dominant designs with respect to smooth force and magnet

Table 9: Dominant Design Parameter Distribution of the LPM Motors

Parameter	Mean	STD	Min	Max
τ (mm)	54.61	18.92	10.05	79.96
l_c (mm)	9.22	5.96	1.01	24.97
l_m (mm)	5.37	3.64	1.00	14.98
l_g (mm)	0.63	0.34	0.20	1.60
d_c (mm)	102.15	35.35	15.04	149.99
s_m (mm)	6.26	3.70	1.00	15.75
g_c (mm)	18.67	12.04	2.55	74.30
w_c (mm)	23.80	10.39	3.77	49.54
w (AWG)	20.53	5.57	11	30
N	635.21	919.77	3	6355

volume per meter in two formats; reciprocal smooth force $1/F_s$ on the top and smooth force F_s on the bottom. Figure 73 shows the dominant designs with respect to average force and magnet volume per meter, with reciprocal average force $1/F_a$ on the top and average force F_a on the bottom. The Pareto-optimal frontiers are also apparent and the distribution of dominant designs is clearly different from Figures 70-71. The trade-off between force and magnet usage along the performance frontiers is also evident in these plots.

The dominant designs with respect to average power coefficient and mass are shown in Figure 74. The trade-off suggests that the motors with larger mass tend to generate lower average power dissipation.

Comparative details for several dominant designs selected from the database, including attributes and design parameters, are shown in Table 10. For this selection, smooth and average acceleration values fall in the ranges 6.15-14.71 g and 6.74-16.62 g, respectively, where $g = 9.8 \text{ m/s}^2$. These acceleration values depend heavily on the constraints imposed within the design software. Other characteristics are tabulated as well, including values for phase resistance and self inductance L . These selected results show that smaller wire sizes are preferable for the design objectives under

Table 10: Selected Dominant Designs of the LPM Motors from the F_s - m Plane

m (kg)	0.19	1.33	2.44	4.34	5.52	7.61	8.97	11.27
F_s (N)	11.41	162.13	346.24	625.25	738.96	878.82	1030.90	1079.70
F_a (N)	12.51	181.85	389.16	706.52	824.98	981.28	1152.00	1195.80
V (cm ²)	11.36	35.37	44.79	61.18	54.04	47.78	49.75	41.98
c (mW/N ²)	12.57	0.81	0.38	0.22	0.23	0.24	0.20	0.23
F_s/m (g)	6.15	12.47	14.47	14.71	13.66	11.78	11.72	9.77
F_a/m (g)	6.74	13.98	16.26	16.62	15.25	13.16	13.10	10.83
i_{\max} (A)	0.32	4.11	1.02	0.81	2.59	2.05	4.11	2.59
v_{\max} (V)	2.51	2.72	24.84	63.47	33.28	73.15	42.50	95.67
R (Ω)	7.81	0.64	21.68	65.29	9.41	22.00	6.27	20.57
L (mH)	1.25	1.30	112.45	599.13	105.06	323.46	115.13	429.21
τ (mm)	12.49	39.28	58.22	78.58	67.73	65.15	79.21	78.94
l_c (mm)	2.34	6.22	6.51	8.40	12.49	19.35	20.63	23.94
l_m (mm)	5.75	12.63	12.31	14.98	13.24	12.09	14.11	12.27
l_g (mm)	0.42	0.39	0.40	0.50	0.89	0.35	0.31	1.08
d_c (mm)	134.92	128.96	145.38	146.84	149.78	145.84	123.13	149.29
s_m (mm)	1.92	2.68	2.41	2.11	2.64	2.80	4.71	9.81
g_c (mm)	7.86	14.64	22.75	33.40	15.83	12.66	24.10	18.94
w_c (mm)	3.86	16.57	26.50	34.50	35.74	35.15	38.50	39.18
w (AWG)	29	18	24	25	20	21	18	20
N (turns)	98	87	590	1250	604	1160	676	1269

consideration.

Careful consideration must be made when viewing the results shown in Table 10 for two reasons. First, these acceleration values are deceptive because they do not include the payload mass, which could be several times higher than the moving mass of the LPM motors. These LPM motors have small moving mass, due to the absence of ferromagnetic steel in the translators. Therefore, the actual acceleration could be much lower than the values presented. Second, the comparison between different motor designs is not fully possible because thermal resistances (for Watt to Kelvin conversion) are not calculated. These thermal resistances and the average power coefficient (for Newton to Watt conversion) are required to calculate the force capability of each motor operating at the same temperature for a direct comparison.

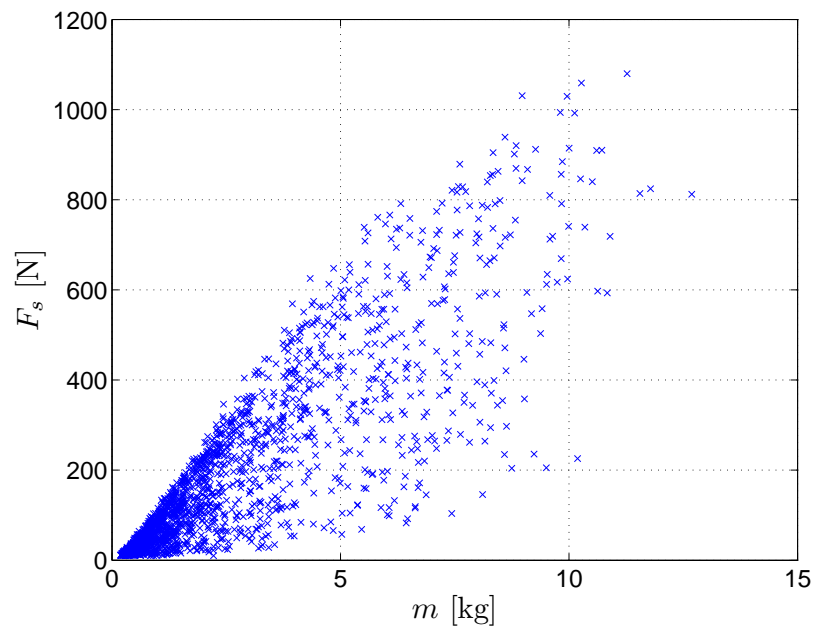
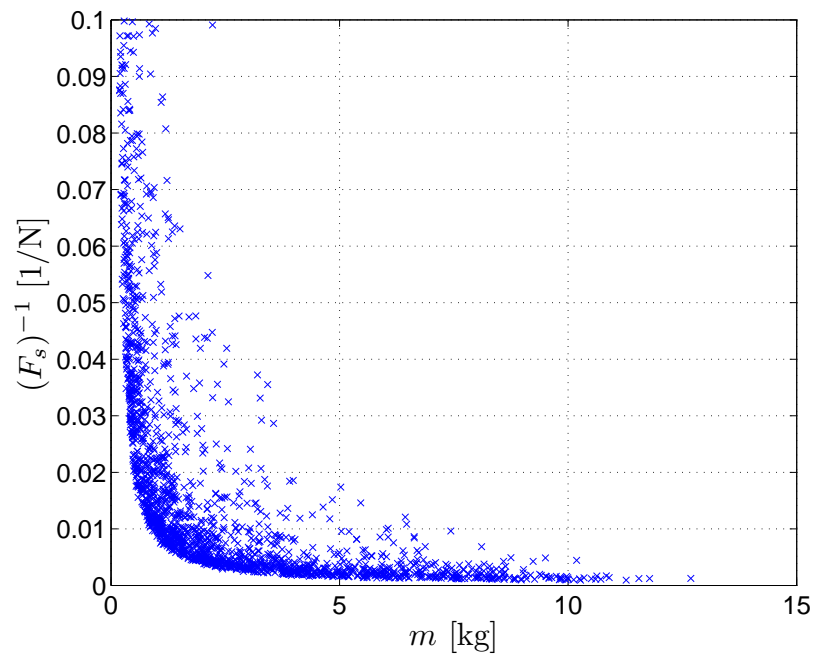


Figure 70: The dominant designs of LPM motors with respect to smooth force and moving mass.

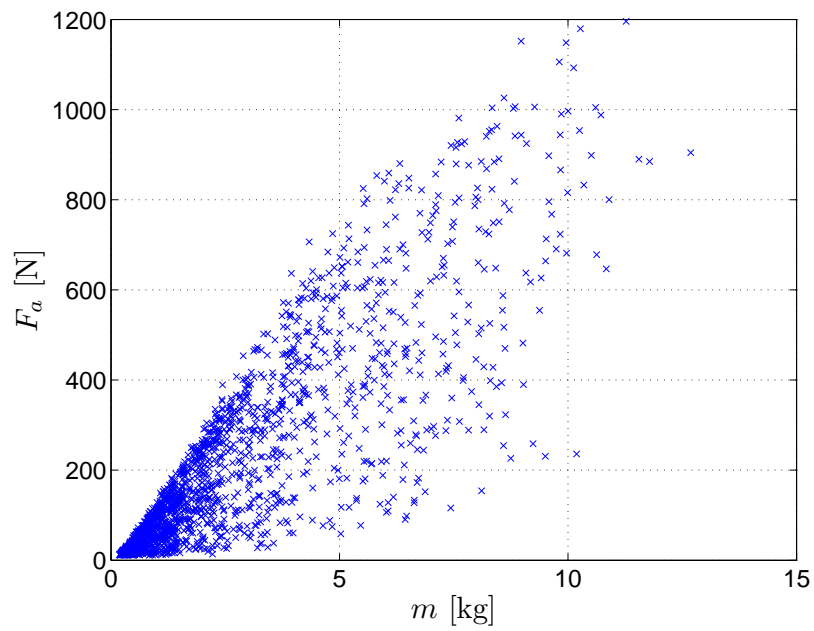
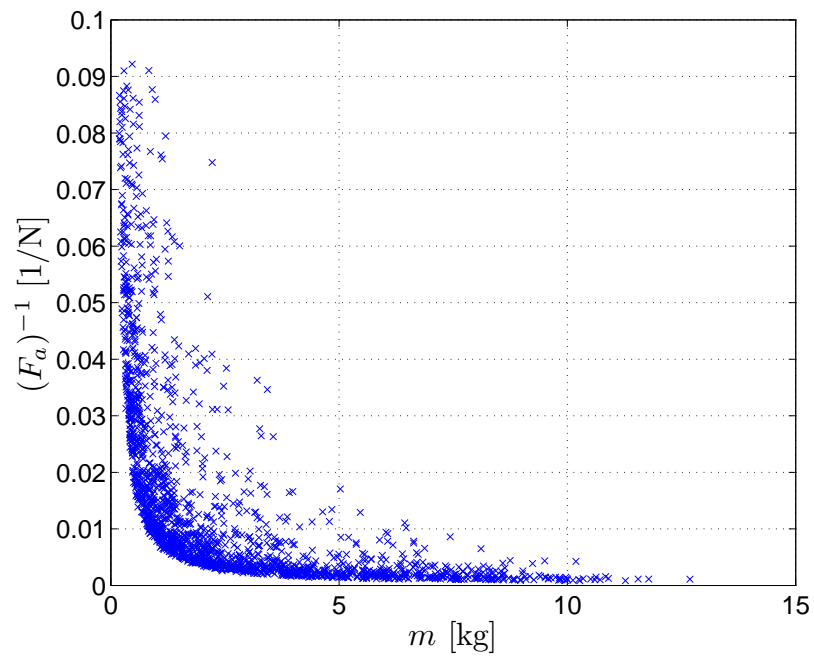


Figure 71: The dominant designs of LPM motors with respect to average force and moving mass.

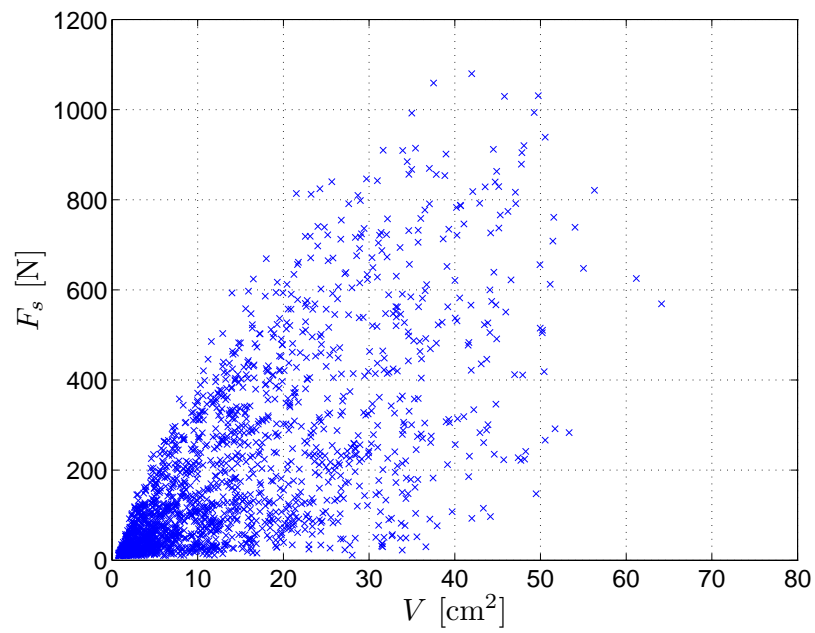
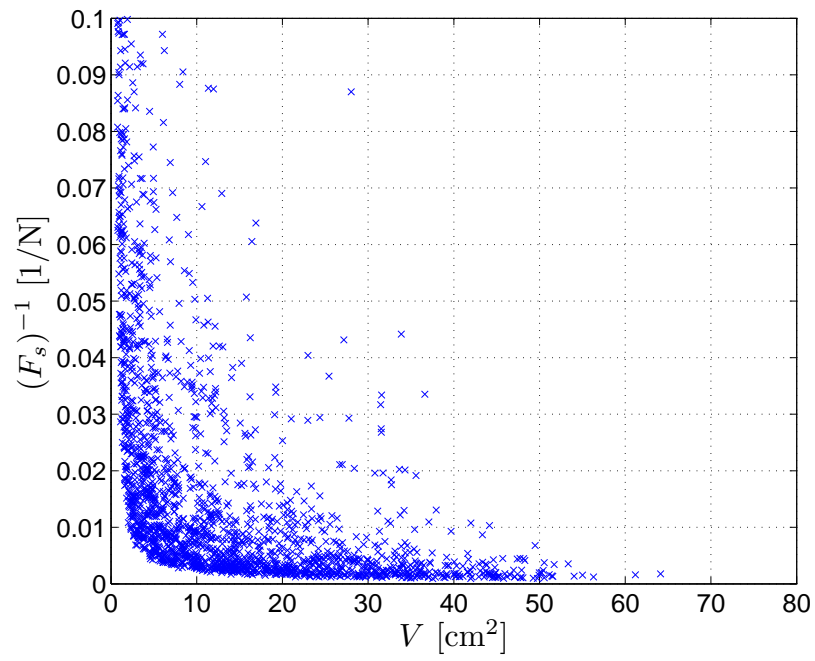


Figure 72: The dominant designs of LPM motors with respect to smooth force and magnet volume per meter.

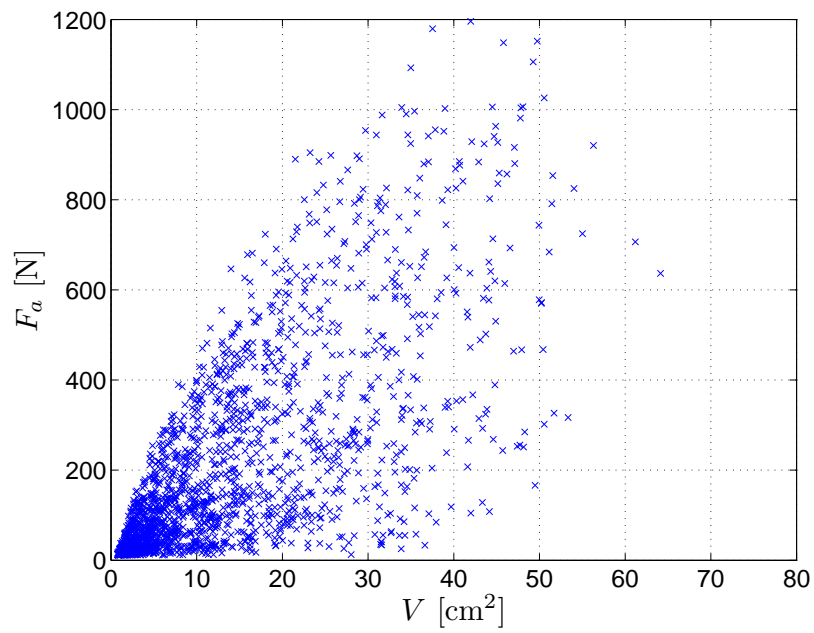
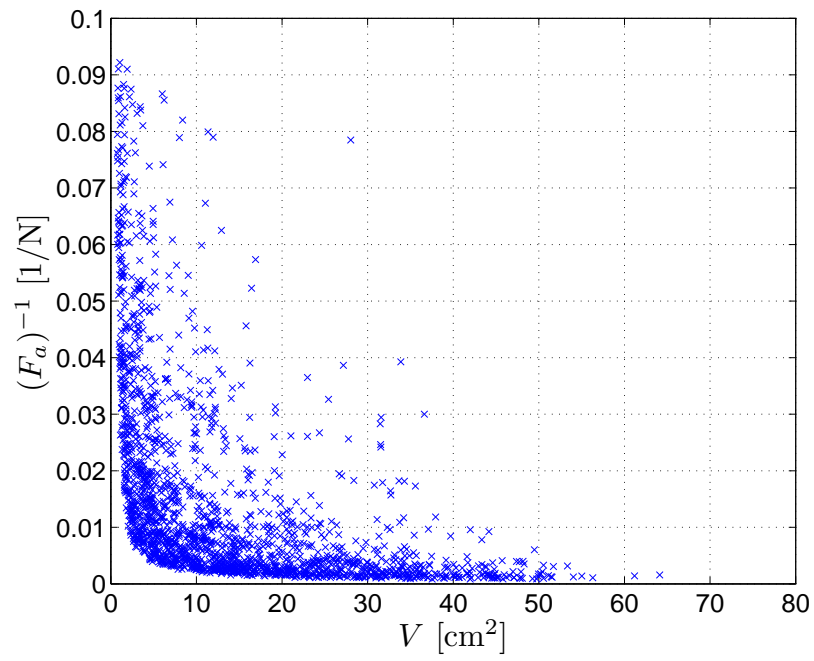


Figure 73: The dominant designs of LPM motors with respect to average force and magnet volume per meters.

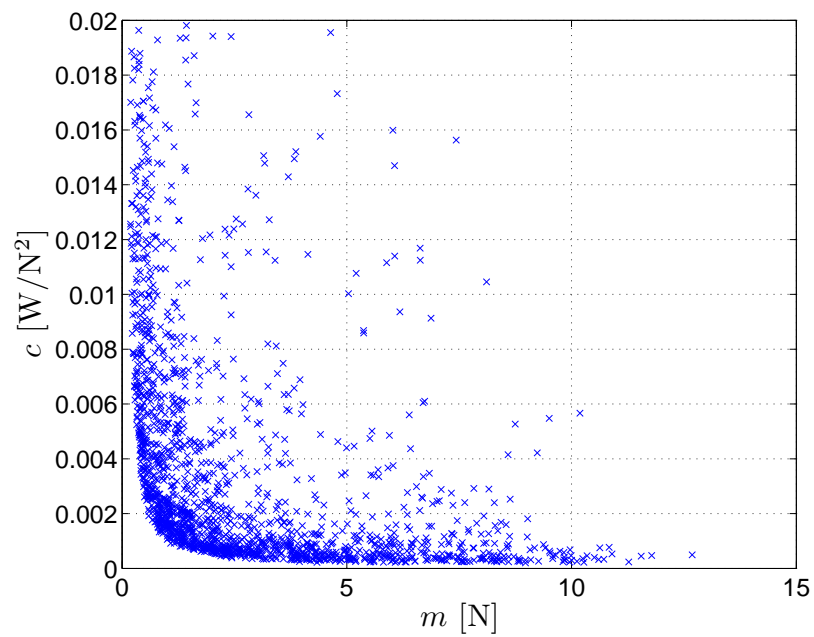
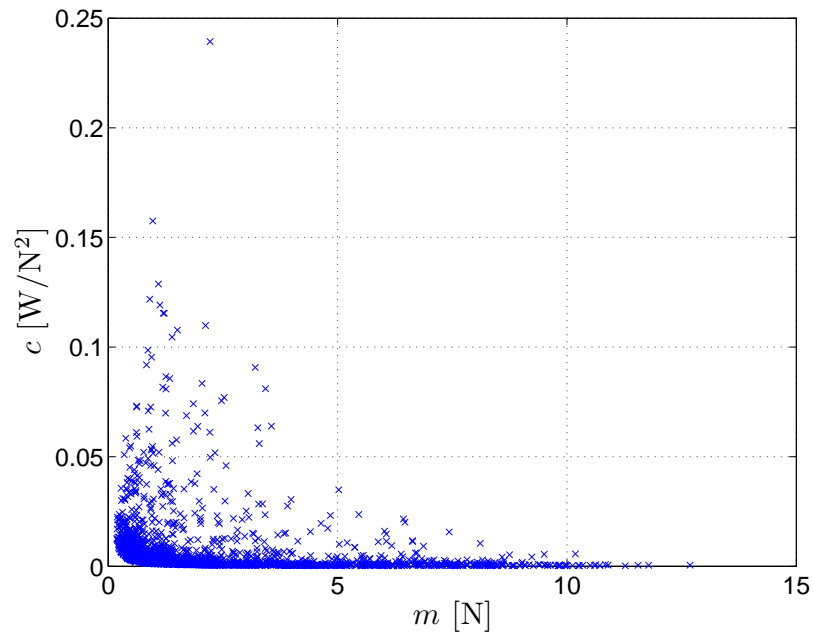


Figure 74: The dominant designs of LPM motors with respect to average power loss coefficient and moving mass.

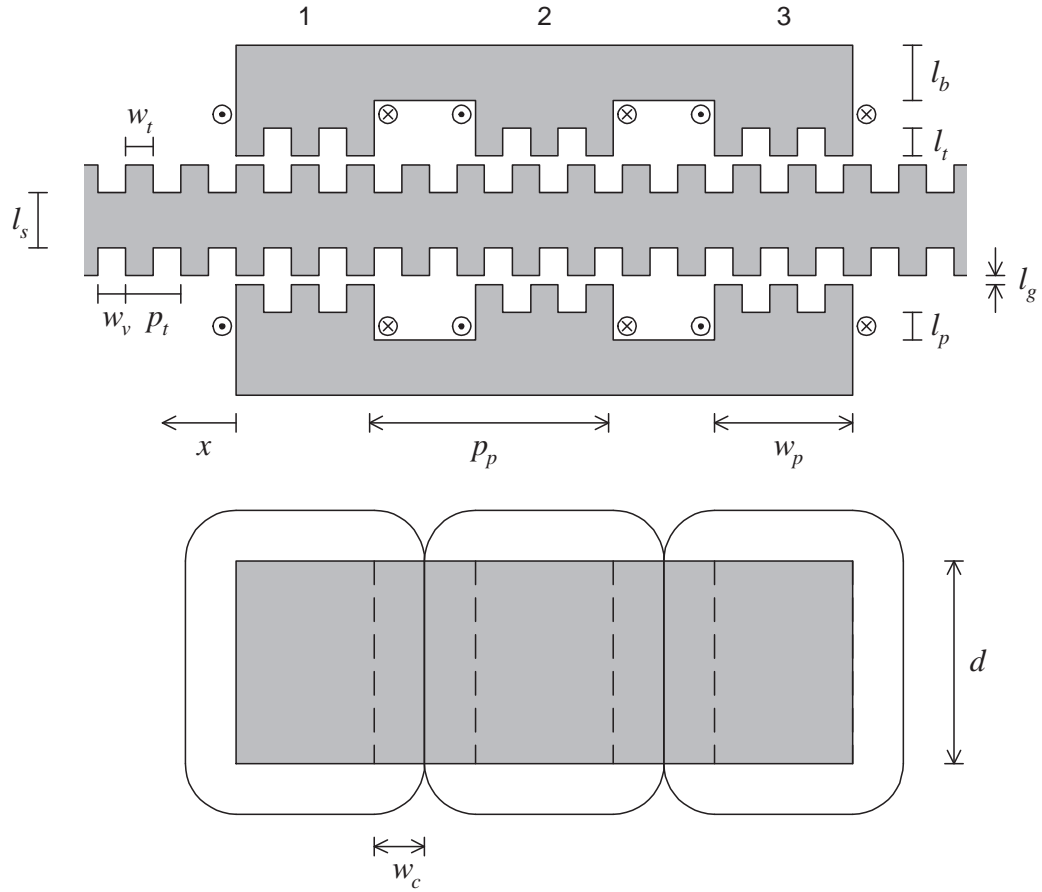


Figure 75: Diagram of design parameters for a LVR motor with $n_t = 3$ and $n_s = 1$.

5.5 Linear Variable Reluctance Motor Design

The diagram of a three-phase LVR motor under consideration is shown in Figure 75. Although the LVR motor is installed with bearing systems that hold the two-sided structure, the analysis of LVR motor performance requires only the design parameters associated with moving mass and force model. The attributes for the LVR motor design optimization are: moving mass, smooth force, average force and spatial average power. The statement of the problem will be presented first and followed by the detailed discussions of design synthesis, analysis, optimization and final design results.

5.5.1 Problem Statement

The LVR motor is characterized by a vector of design parameters, as shown in Figure 75. This vector of design parameters is given by

$$\theta = \begin{bmatrix} p_t \\ l_p \\ l_b \\ d \\ n_t \\ n_s \\ \text{---} \\ l_t \\ l_g \\ l_s \\ w \end{bmatrix} \begin{array}{l} \text{(tooth pitch)} \\ \text{(pole length)} \\ \text{(back iron length)} \\ \text{(depth)} \\ \text{(teeth/pole, integer)} \\ \text{(space index, integer)} \\ \\ \text{(tooth length)} \\ \text{(air gap length)} \\ \text{(stator length, = } l_b) \\ \text{(wire size, integer)} \end{array} \quad (210)$$

where the dashed line indicates the sequential order in which the random synthesis takes place. For any feasible θ , there will be corresponding values for motor performance functions to be optimized.

The multi-objective design optimization problem of the LVR motor is given by

$$\begin{array}{ll} \text{minimize} & m \quad \text{(moving mass)} \\ \text{maximize} & F_s \quad \text{(smooth force)} \\ \text{maximize} & F_a \quad \text{(average force)} \\ \text{minimize} & s \quad \text{(average power slope)} \end{array}$$

subject to the inequality constraints

$$\begin{array}{ll} m \leq 25 \text{ kg} & \text{(maximum mass)} \\ F_s \geq 10 \text{ N} & \text{(minimum smooth force)} \\ v_{\max} \leq 270 \text{ V} & \text{(maximum voltage)} \\ \text{dia}(w) < \min \left(l_p, \left(n_s + \frac{5}{6} \right) \frac{p_t}{2} \right) & \text{(maximum wire diameter)} \end{array}$$

the equality constraints

$$\begin{aligned}
 n_p &= 3 && \text{(number of phases)} \\
 r_t &= 0.5 && \text{(ratio of tooth width and tooth pitch)} \\
 s_c &= 0.7 && \text{(coil space factor)} \\
 J_{\max} &= 10 \text{ A/mm}^2 && \text{(maximum current density)} \\
 B_{\max} &= 2 \text{ T} && \text{(maximum flux density)} \\
 \dot{x}_{\max} &= 1.8 \text{ m/s} && \text{(maximum velocity)}
 \end{aligned}$$

and the bounds on the variable design parameters

$$\begin{aligned}
 2.5 \text{ mm} &\leq p_t \leq 40 \text{ mm} \\
 1 \text{ mm} &\leq l_p \leq 50 \text{ mm} \\
 5 \text{ mm} &\leq l_b \leq 50 \text{ mm} \\
 15 \text{ mm} &\leq d \leq 150 \text{ mm} \\
 2 &\leq n_t \leq 8 \\
 1 &\leq n_s \leq 4 \\
 \max(1 \text{ mm}, \frac{p_t}{4}) &\leq l_t \leq 20 \text{ mm} \\
 0.1 \text{ mm} &\leq l_g \leq \min(\frac{p_t}{25}, 0.8 \text{ mm}) \\
 11 \text{ AWG} &\leq w \leq 30 \text{ AWG}
 \end{aligned}$$

The materials are copper and bonding materials for coils and M19 steel for translators and stators. These specific choices of materials are selected to limit the search space. In this problem formulation, some design parameters are set as equality constraints to limit the search space but one could vary certain design parameters by including them in θ to increase the size of the search space. The details of synthesizing design parameters are described in the following section.

5.5.2 Design Synthesis

The MC synthesis process is used to generate a random set of design parameters from permissible range. Random synthesis for the LVR motor design involves a two-step process where the design parameters with the most influence on the design must be synthesized first, and then used to set the permissible ranges for the subsequent choices of the remaining design parameters.

In the first step, the following eight design parameters are randomly selected with uniform probability distributions: p_t , l_p , l_b , d , n_t and n_s . These random choices introduce limitations on the available coil area. The pole pitch p_p is given by

$$p_p = (n_t + n_s + \frac{1}{3})p_t \quad (211)$$

For the choice of tooth ratio $r_t = 0.5$, the tooth width and the valley width are equal to $w_t = w_v = \frac{1}{2}p_t$. The pole width w_p and the available coil width w_c are given by

$$w_p = n_t w_t + (n_t - 1)w_v = (2n_t - 1)\frac{p_t}{2} \quad (212)$$

$$w_c = (p_p - w_p)/2 = (n_s + \frac{5}{6})\frac{p_t}{2} \quad (213)$$

and thus the coil area is $w_c l_p$.

In the second step, the additional constraints $l_t \geq \frac{1}{4}p_t$ and $l_g \leq \frac{1}{25}p_t$ are imposed in order to ensure the accuracy of the air gap model used for analysis before being randomly selected with uniform probability distribution within these bounds. Note that the stator length l_s is made proportional to the back iron length l_b to ensure sufficient stiffness to support the motor weight. Since the thickness of the stator bar usually does not significantly influence the force production of the motor (in comparison to the air gap), this approximation does not affect the overall performance of the motor.

The coil design parameters w and the number of turns in each coil, N , are selected according to the following procedure. To guarantee that at least one turn will fit

around each pole, the wire diameter must be less than $\min(w_c, l_p)$. Take AWG_{\min} to be the smallest AWG value, greater than or equal to AWG 11, that satisfies this constraint on wire diameter. For each AWG value between AWG_{\min} and AWG 30, determine the corresponding value of N according to

$$N = \frac{2s_c w_c l_p}{\text{dia}(w)} \quad (214)$$

where the factor of two accounts for the two-sided topology. Each such (w, N) pair is then checked for feasibility, using an idealized synchronous reluctance model of the LVR motor assumed to be operating with excitation that minimizes instantaneous copper losses. To this end, a current limit is first established by

$$i_{\max} = \min \left\{ N A_p \left(\frac{L_d^2 + L_q^2}{2} \right)^{-\frac{1}{2}} B_{\max}, A_w J_{\max} \right\} \quad (215)$$

where $A_p = n_t r_t p_t d$ is the total tooth area per pole, $A_w(w)$ is the conductor area, and $L_{d/q}$ are the d/q axis inductances. This current limit is consistent with the specified limits on flux density B_{\max} and current density J_{\max} . The choice of $J_{\max} = 10 \text{ A/mm}^2$ is to limit the temperature rise for the outside coil structure of the LVR motors [7]. Operation with maximum current at radian frequency $\omega = \frac{\pi}{p_t} \dot{x}_{\max}$ is then possible if

$$v_{\max} = \left(\frac{(R + \omega L_d)^2 + (R - \omega L_q)^2}{2} \right)^{\frac{1}{2}} i_{\max} \leq V_{\max} \quad (216)$$

The coil parameters (w, N) are then selected randomly with uniform probability distribution from among the feasible candidates identified above. The detailed derivations are given in Appendix B.

5.5.3 Design Analysis and Optimization

After design parameters for a candidate solution have been randomly synthesized, the next step is to perform analysis to calculate the vector of objective functions. The objective functions related to manufacturing application are already discussed

and demonstrated for a LVR motor in Chapter 4. The additional details to calculate other objective functions are included in Appendix B.

The first objective function is determined by

$$m = \text{moving mass} \quad (217)$$

The associated force function of the LVR motor

$$f(x, i) = \text{force at position } x \text{ due to current } i$$

is based on physical properties as presented in Chapter 3. Two objective functions associated with achievable force, the “smooth” limit and the “average” limit, are calculated according to

$$F_s = \min_{x \in [0, 2p_t]} f^*(x) \quad (218)$$

$$F_a = \frac{1}{2p_t} \int_0^{2p_t} f^*(x) dx \quad (219)$$

where $f^*(x)$ is the solution to the maximum force commutation problem

$$\begin{aligned} &\text{maximize} && f(x, i) \\ &\text{subject to} && |i_j| \leq i_{\max} \quad , \quad j = 1, 2, 3 \end{aligned}$$

for each $x \in [0, 2p_t]$ and i_{\max} is given by (215). Next recall the spatial average power dissipation, previously defined as

$$P_x(f_d) = \frac{R}{2p_t} \int_0^{2p_t} i^{*T} i^* dx$$

where i^* is the solution to the minimum copper loss commutation problem

$$\begin{aligned} &\text{minimize} && i^T i \\ &\text{subject to} && f(x, i) = f_d \\ &&& |i_j| \leq i_{\max} \quad , \quad j = 1, 2, 3 \end{aligned}$$

for each $x \in [0, 2p_t]$ and the desired continuous force satisfies $f_d \leq F_s$. The objective function associated with this performance measure is defined as the average slope of the P_x - f_d curve, i.e.

$$s = \frac{1}{F} \int_0^F \frac{dP_x}{df_d} df_d = \frac{1}{F} P_x \Big|_F = \frac{P_x(F)}{F} \quad (220)$$

To account for numerical errors, the value of $F = 0.95F_s$ is selected for the LVR motor design.

This set of objective functions identifies limits on achievable acceleration (minimum moving mass and maximum force) and average power dissipation with constant velocity operation mode due to constraints imposed on current density, speed, voltage and flux density. These objective functions are clearly competing and therefore the solution to this optimization problem is not a single design. To limit the search, the constraints $F_s \geq 10$ N and $m \leq 25$ kg are imposed.

The stages of synthesis and analysis eliminate some designs because they cannot satisfy all of the specified constraints; other designs are eliminated due to lack of convergence within the magnetostatic analysis during attempts to solve the optimal commutation problems. Those designs that have been successfully synthesized and analyzed are subjected to multi-objective dominance testing to form a database of non-dominated designs. A database maintaining software can be implemented on a computer using the same logic applied for the LPM motor design.

5.5.4 LVR Motor Design Results

The procedure described above was employed for a total of 228795 trials. Of these, 10505 trials were rejected due to coil infeasibility, 158859 trials were rejected due to large mass, 2727 trials were rejected due to convergence problems, and 16761 trials were rejected due to small force. Hence, 39943 candidate designs were identified and, of these, 600 were found to be dominant designs. The database of these dominant designs is characterized statistically by Table 11.

Table 11: Dominant Design parameter distribution of the LVR motors

Parameter	Mean	STD	Min	Max
p_t (mm)	7.41	3.41	2.53	20.87
l_t (mm)	6.83	4.34	1.04	19.89
l_p (mm)	20.67	11.77	2.88	49.97
l_b (mm)	21.18	9.61	5.06	49.92
l_g (mm)	0.20	0.11	0.10	0.79
d (mm)	101.81	34.42	16.04	149.90
n_t	4.31	1.16	2.00	8.00
n_s	2.21	1.06	1.00	4.00
w (AWG)	12.48	2.30	11.00	29.00
N	89.85	65.41	14.00	1050.00

Figure 76 shows the dominant designs with respect to smooth force and moving mass in two formats; reciprocal smooth force $1/F_s$ on the top and smooth force F_s on the bottom. Figure 77 shows the dominant designs with respect to average force and moving mass, with reciprocal average force $1/F_a$ on the top and average force F_a on the bottom. The performance frontiers are particularly apparent when reciprocal force is plotted against mass, since the origin represents the unachievable ideal. Unlike the LPM motor design results, smooth force and average force for the LVR motors are less interrelated due to large ripple force. The trade-off between force and mass attributes along the performance frontiers is clear in these plots.

The dominant designs with respect to average power dissipation slope and moving mass are shown in Figure 78. The trade-off suggests that the motors with larger mass would generate lower average power loss.

Comparative details for several selected dominant designs on the Pareto-optimal frontier of the F_s - m plane, including attributes and design parameters, are shown in Table 12. For this selection, smooth and average acceleration values fall in the ranges 1.33-3.39 g and 3.01-8.12 g, respectively, where $g = 9.8 \text{ m/s}^2$. These acceleration values depend heavily on the constraints imposed within the design software. Other

Table 12: Selected Dominant Designs of the LVR Motors from the F_s - m Plane

m (kg)	0.58	2.61	4.28	7.28	9.63	15.61	19.16	24.42
F_s (N)	10.11	86.62	129.26	162.28	227.13	286.29	333.01	318.25
F_a (N)	17.22	207.52	260.93	353.73	445.12	546.84	693.39	761.80
s (W/N)	1.12	0.40	0.38	0.19	0.45	0.69	0.39	0.23
F_s/m (g)	1.77	3.39	3.08	2.28	2.41	1.87	1.77	1.33
F_a/m (g)	3.01	8.12	6.22	4.96	4.71	3.58	3.69	3.18
i_{\max} (A)	8.22	20.80	33.06	21.28	16.49	41.70	16.49	26.46
v_{\max} (V)	8.36	72.72	43.09	131.09	136.72	66.78	241.45	208.26
R (Ω)	0.11	0.12	0.04	0.09	0.33	0.10	0.51	0.16
L_a (mH)	0.65	3.26	1.31	7.42	13.97	4.67	32.04	16.10
L_u (mH)	0.40	1.92	0.80	4.57	8.68	2.87	19.35	9.44
p_t (mm)	4.64	6.56	7.14	8.51	12.02	20.87	15.47	14.30
l_b (mm)	7.72	7.43	14.61	19.18	18.61	24.36	35.51	45.73
l_g (mm)	0.17	0.22	0.26	0.32	0.47	0.79	0.55	0.47
d (mm)	61.42	138.70	124.22	90.22	148.04	147.40	140.91	117.43
l_t (mm)	4.00	1.92	2.61	2.37	4.47	8.32	4.57	4.49
l_p (mm)	2.88	11.77	6.18	12.78	8.59	8.85	10.10	14.10
n_t	2	2	3	4	3	2	3	4
n_s	2	1	2	2	1	1	1	1
w (AWG)	18	14	12	12	15	11	15	12
N (turns)	32	46	26	64	80	56	120	78

characteristics are tabulated as well, including values for phase resistance, and zero-current values for aligned self inductance L_a and unaligned self inductance L_u . These selected results show that larger wire sizes are preferable for the design objectives under consideration. As mentioned earlier, the direct comparison between the design results of the LPM and LVR motors is not possible because thermal resistances are not calculated.

5.6 Conclusion

In this chapter, a computer-aided design tool for the LPM and LVR motors has been developed based on the multi-objective optimization using Monte-Carlo synthesis. This approach bypasses expert knowledge prejudices that may limit innovation, and prevents sub-optimal results by covering a large space of design parameters; some

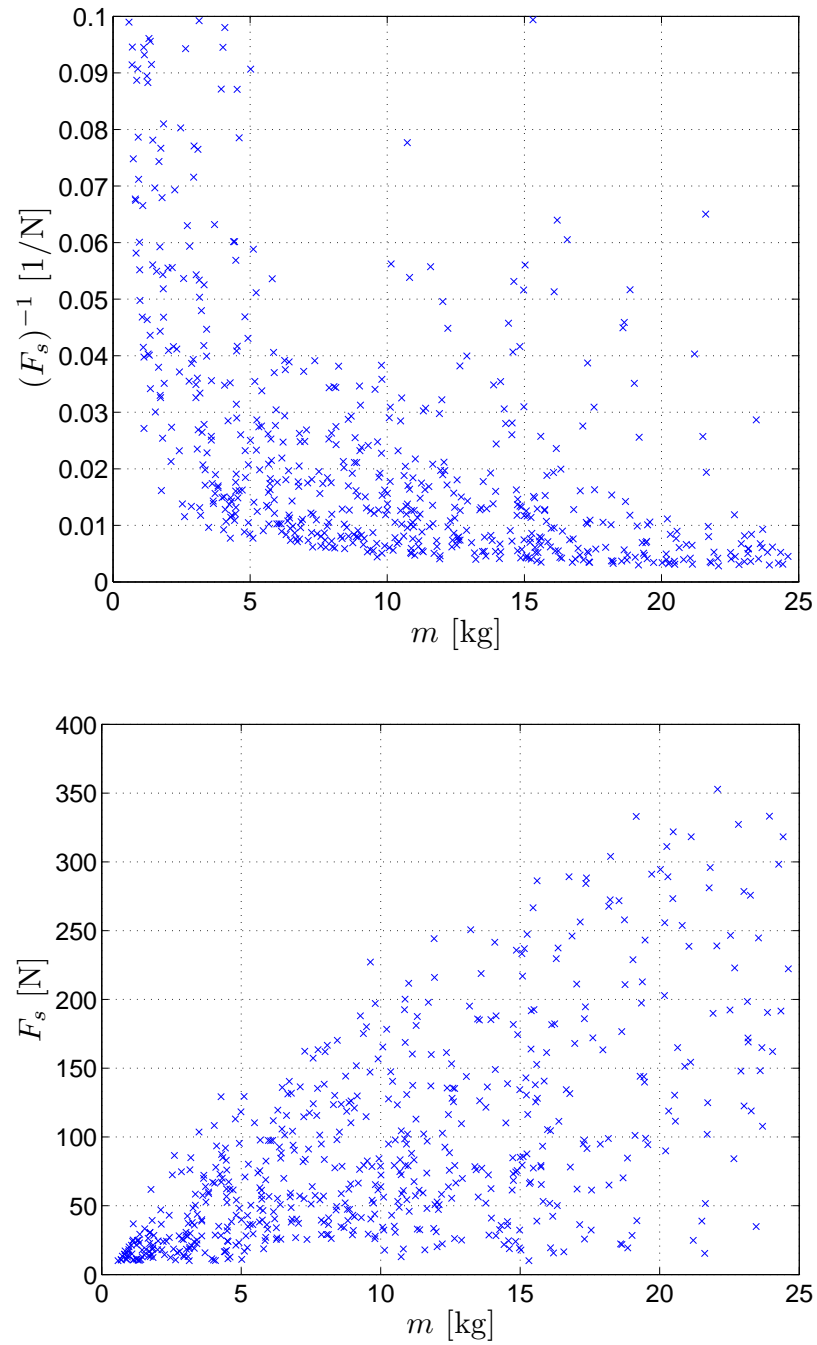


Figure 76: The dominant designs of LVR motors with respect to smooth force and moving mass.

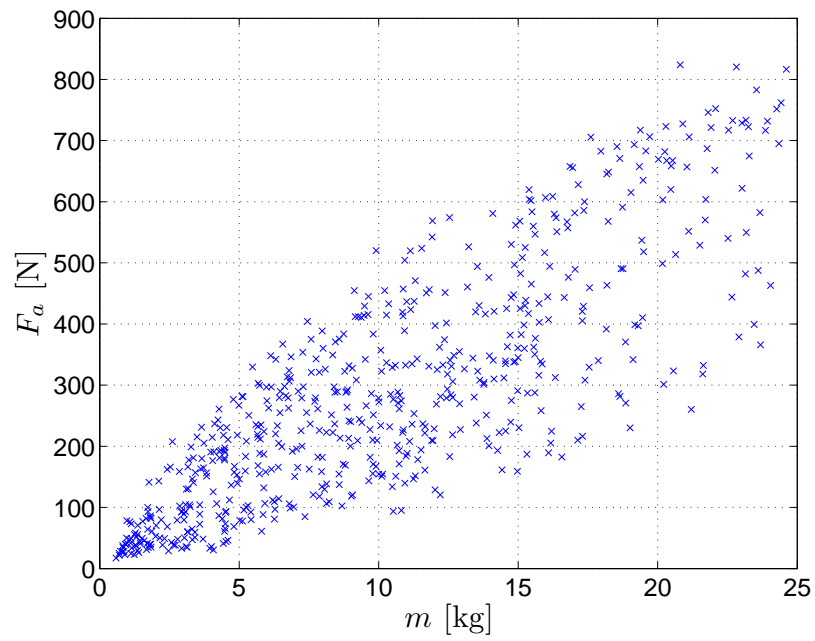
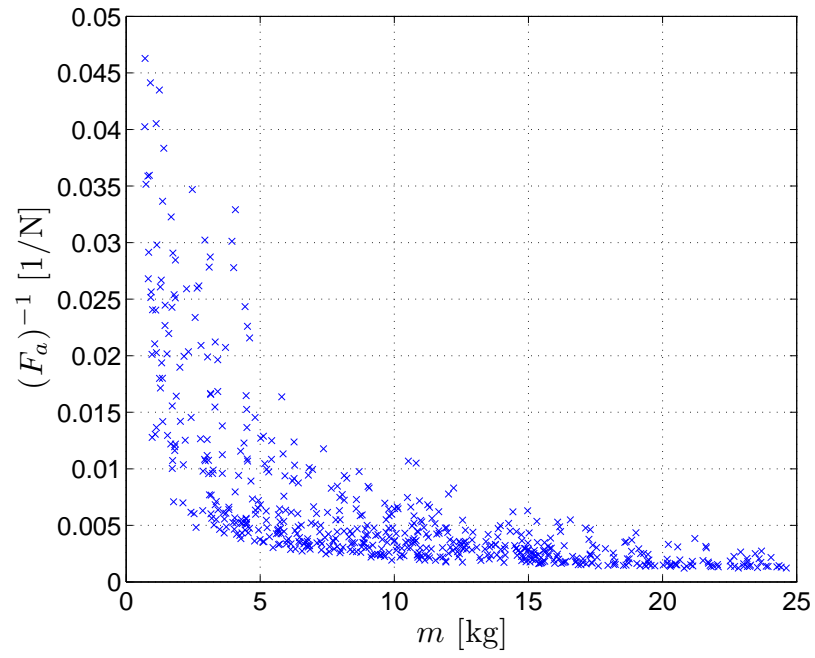


Figure 77: The dominant designs of LVR motors with respect to average force and moving mass.

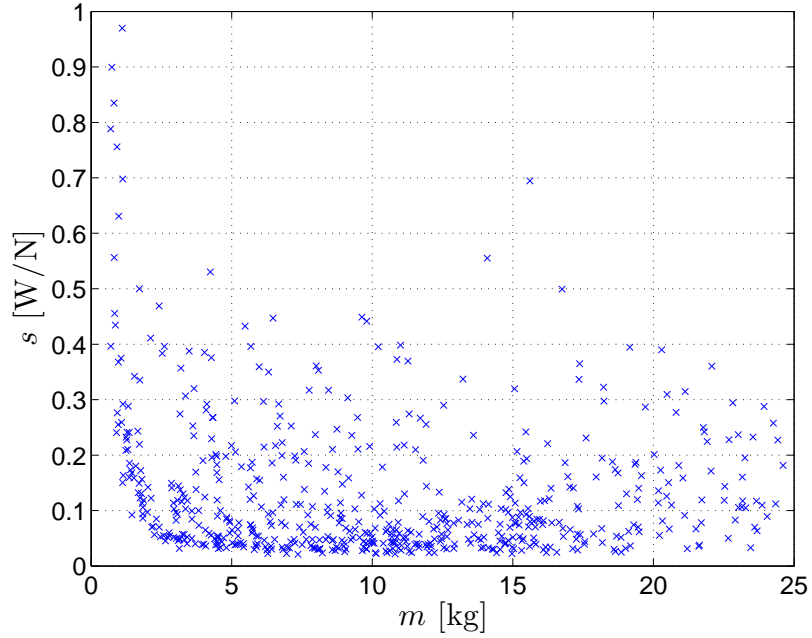


Figure 78: The dominant designs of LVR motors with respect to average power slope and moving mass.

values of the design parameters and material properties are fixed to limit the size of the search space. The design results are then presented with trade-offs between different objective functions. However, direct comparison between two sets of optimal designs is not possible due to the lack of thermal resistance models for both types of motors.

CHAPTER 6

CONCLUSIONS

6.1 Summary of Contributions

The major contributions of this thesis are categorized into three areas: (i) magnetic modeling, (ii) optimal performance assessment and (iii) multi-objective design methodology of the LPM and LVR motors for manufacturing automation applications. The target application is to perform repetitive point-to-point positioning tasks on a continuous basis under temperature constraints. Through simplification, the constraint on temperature rise may be replaced by a constraint on average power dissipation, provided that the thermal resistance is constant and known.

The basic framework of analysis is introduced in Chapter 2 for a class of idealized synchronous motors, where magnetic saturation and spatial harmonics are neglected, to provide clarity and insight to predict the solutions for the “real” motors. In addition, the role of spherical/cubical current limits and 3/6-wire connections are also explored in this chapter.

First, the power-loss-specified time-optimal position control problem (minimize T given P problem) is considered as a means to determine the productivity of a synchronous motor when operating under average power dissipation constraint. This chapter has established that the minimum-copper-loss position control problem (minimize P given T problem) in fact yields the same family of solutions (when T is varied) as the power-loss-specified problem (when P is varied). Moreover, it was determined that computational advantages arise by focusing exclusively on the minimum-copper-loss position control problem.

Analytical solutions to the minimum-copper-loss position control problem are developed for the PM and VR synchronous motors with spherical current limit and 3-wire connection. The analytical expressions of the productivity trade-off curves $T(X, P)$ are also reported. Numerical solutions to the problem are given for the PM, VR and hybrid synchronous motors for the four possible current constraint sets. These results reveal that the cubical current limit with 6-wire connection combination provides the highest performance (i.e. resulting in lowest P when T and X are held equal).

Finally, Chapter 2 explores two optimal commutation problems, namely optimal force control and minimum-copper-loss force control, which are based on solving a family of static optimization problems. The objective of the force control problem is to determine the smooth (ripple-free), average and maximum force limit. The numerical solutions are provided for PM, VR and hybrid synchronous motors for all four possible current constraint sets. These results also indicate that the cubical current limit with 6-wire connection combination provides the highest performance (i.e. resulting in highest smooth and average force range).

The objective of minimum-copper-loss force control is to determine currents that produce a desired force command with minimum power dissipation with or without current limit. The analytical solutions are provided for the problem without current limit, whereas the numerical solutions are provided for the problem with current limit, for PM, VR and hybrid synchronous motors. These results show that both versions of the problem yield identical solutions (same spatial average power dissipation) when the desired force command is small. A small difference becomes noticeable only when the force command approaches very close to the smooth force limit.

Chapter 3 develops the physics-based force models for the LPM and LVR motors where spatial harmonics and magnetic saturation are now considered. Due to the absence of ferromagnetic material in the translator, only spatial harmonics are present

in the force model of the LPM motor, which has been obtained using the analytical solution of the Poisson Equation. The magnetic linearity feature results in a special structure of the force equation that can be exploited. A nonlinear MCA model is developed for the LVR motor that includes both spatial harmonics and magnetic saturation; no special structure can be exploited for the force model of the LVR motor. The accuracy of both force models is verified by FEA.

Applying those force models, the optimal performance assessment of the LPM and LVR motors is explored in Chapter 4 using the mathematical frameworks discussed in Chapter 2. Three approaches to assess the optimal performance of electric motors for manufacturing applications are presented: (i) maximum force limit, (ii) spatial average power dissipation and (iii) productivity trade-off curve. The first two approaches, based on solving static optimization problems, are computationally efficient but less directly related to the target application. The third approach is directly related to the target application but it is more computationally expensive to obtain the productivity trade-off curves. The performance assessment methodologies developed here may be applied to any motor technology used in manufacturing automation applications.

Chapter 5 then discusses the multi-objective design optimization problem. The computer-based design software based on multi-objective optimization is developed using Monte-Carlo synthesis and the performance assessment tools described in Chapter 4. Although Monte-Carlo or unguided random synthesis is time consuming, it has the advantage that design creativity is fully promoted due to its lack of bias. Two performance assessment approaches based on static optimization are implemented because of computational efficiency. The design results of the LPM and LVR motors are finally presented. The two sets of final results are not directly comparable because the thermal resistance models for both types of motors are not available. Hence, the question of which motor technology is more suitable for the target application has been left unanswered. Nonetheless, the preliminary works to develop the thermal

resistance models of the LPM and LVR motors are discussed and presented in the appendices, along with other supplementary materials.

6.2 Future Research

Many research opportunities exist for continuing works in this research direction. Some suggestions are discussed as follows:

Complete Development of Thermal Resistance Model: As an immediate extension to this research work, thermal resistance models of the LPM and LVR motors are required to directly compare their performances. In manufacturing applications where productivity is limited by steady-state temperature, it is necessary to rate the performances of different motor technologies at the same operating temperature to accurately assess their performances. Some preliminary works have been conducted in this direction and are included in the appendices.

Inclusion of Productivity Trade-Off Curve in Design: So far, only computationally efficient objective functions based on static optimization are implemented in the design software. In fact, the productivity trade-off curve $T(X, P)$ is more direct to predict the productivity achieved by each candidate motor design. With a complete development of the thermal resistance model, $T(X, P)$ can be transformed to $T(X, \Theta)$ to vividly show the productivity each candidate design can achieve at temperature Θ . A new problem formulation, namely the time-optimal control problem with temperature constraint, is also another possibility to directly address the coupled nature of the thermal, mechanical and electrical dynamics presented within the systems under consideration.

Further Improvement of LPM and LVR Motor Force Model: The LVR motors are potentially more suitable to operate at high temperature due to the absence of permanent-magnets which tend to degrade at high temperature. Especially, the toothed structure of the LVR motors can be curved such that heat can be removed

more effectively to achieve even better performance. Much research is needed to develop an accurate and computationally efficient force model of the LVR motors with curved-toothed structure. One can always rely on FEA for accurate force prediction of the LVR motors with any arbitrary tooth design, but this is prohibitive for use in the computationally intensive design methodology proposed in this research direction. For the LPM motor, the further improvement should include the thermal effect that degrades the performance of permanent-magnet at high operating temperature.

Numerical Method for Solving Optimal Control Problem: As pointed out earlier, some difficulties were encountered to derive $T(X, P)$ for the LVR motor directly from solving the optimal control problem. Despite being very efficient, the present force model of the LVR motor is still too computationally expensive for the proposed numerical method. In addition to improving the efficiency of the force model, the numerical method itself can be a subject of further improvement, since at present the numerical method does not capture control discontinuity.

Experimental Work for Model Verification: All force and thermal models of the present research have been verified by FEA with reasonable agreements. However, experimental works that include parasitic effects not being modeled in FEA can be carried out to further verify the accuracy of the existing models. This would give an opportunity to further refine and enhance the overall accuracy of the force and thermal models in relation to the actual devices.

Friction Model: Despite being neglected in this research for simplicity, friction can play a big role in determining the achievable performance under optimal control. Hence, the development and inclusion of an accurate friction model to the system dynamics is another important aspect for future research.

Other Heat Sources: In addition to copper losses, the hysteresis losses, eddy-current losses, skin effect losses and mechanical losses are also present and contributing additional heat to the systems. The studies of these losses would further enhance

the ability to accurately predict the achievable productivity.

Feedback Control Implementation: It is necessary to develop a feedback control scheme for actual implementation to verify whether or not the predicted optimal performance is achievable. The development of the feedback controller may be conducted via simulation or experimental work.

Further Consideration of Voltage Limits: In this research, the formulation of the optimal control and optimal commutation problems assumes current sources as controls without any consideration of voltage limits, whereas the actual motors are controlled by voltage sources with finite magnitude. The inclusion of the voltage dynamics equations would add complexity to the problem formulation, but it also increases the overall accuracy of the control design. In addition, a further improvement may include the calculation of voltage limits in motor design that is based on realistic motor models, instead of the idealized models.

Algorithm for Motor Selection: The motors in the non-dominated set from the multi-objective design optimization, in principle, are optimal and “equivalent” subject to the objective functions considered. However, in practice a certain motor must be properly selected from the database for actual construction and implementation. The selection process of the “right” motor from the non-dominated set is apparently not obvious because the choice of such motor closely depends on further specifications such as payload size, smooth/average force requirement and construction cost. The development of such algorithm is undeniably another crucial research direction.

Although many possibilities for future research remain to be explored, this thesis provides a valuable first step for the performance assessment and design optimization of electric motors for manufacturing automation applications under temperature limit. In conclusion, the contributions of this research help establish the framework for analysis and design of LS motors that can be extended for other motor technologies of both rotary and linear types.

APPENDIX A

AIR PERMEANCE MODEL

The air gap model used in this research, introduced in [68], assumes that flux flows across the air gap through flux tubes shaped by straight lines and circular arcs. Representative flux tubes are shown in Figure 79, over one tooth pitch, for several orientations of opposing teeth. The permeance of each flux tube is computed analytically using

$$P_{\text{tube}} = \mu_0 \int \frac{dA}{l} \quad (221)$$

where μ_0 is the permeability of air, l is the length of the tube and dA is the differential cross section of the tube. Evaluation of (221) for all possible cases leads to the following explicit position-dependent expressions for the permeance $P_{\text{tube}}(x)$

$$\begin{aligned} P_1 &= \frac{\mu_0(w_t - x)d}{l_g} & , & \quad 0 \leq x \leq w_t \\ P_2 &= \frac{2}{\pi}\mu_0d \ln \left(1 + \frac{0.5\pi x}{l_g} \right) & , & \quad 0 \leq x \leq 0.5w_v \\ P_{2'} &= \frac{2}{\pi}\mu_0d \ln \left(1 + \frac{0.25\pi w_v}{l_g} \right) & , & \quad 0.25w_v \leq x \leq 0.5w_t \\ P_3 &= \frac{\mu_0d}{\pi} \ln \left(1 + \frac{\pi(0.5w_v - x)}{l_g + 0.5\pi x} \right) & , & \quad 0 \leq x \leq 0.5w_v \\ P_4 &= \frac{\mu_0dx}{l_g + 0.5\pi(w_v - x)} & , & \quad 0 \leq x \leq 0.5w_v \\ P_{4'} &= \frac{\mu_0d(w_v - x)}{l_g + 0.5\pi(w_v - x)} & , & \quad 0.5w_v \leq x \leq w_v \\ P_{4''} &= \frac{\mu_0d(x - w_t)}{l_g + 0.5\pi(x - w_t)} & , & \quad w_t \leq x \leq w_v \end{aligned}$$

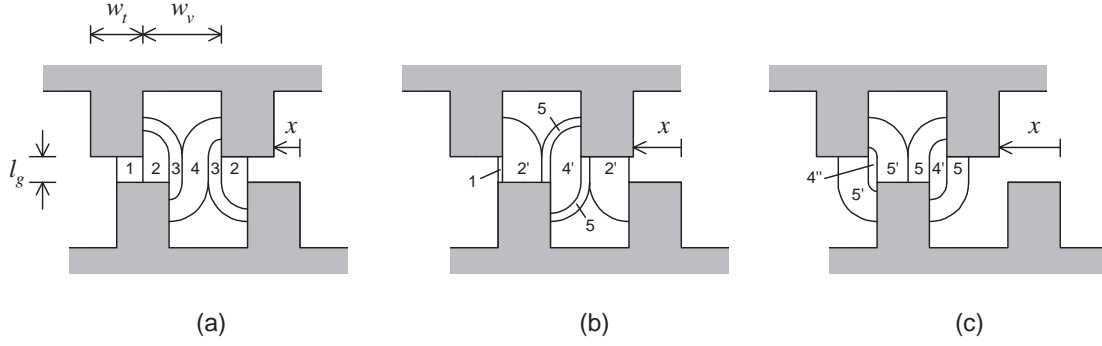


Figure 79: Assumed flux paths between toothed poles at different displacement position: (a) $0 \leq x \leq 0.5w_v$, (b) $0.5w_v \leq x \leq 0.5w_t$ and (c) $w_t \leq x \leq 0.5(w_t + w_v)$.

$$P_5 = \frac{2}{\pi} \mu_0 d \ln \left(\frac{l_g + 0.25\pi w_v}{l_g + 0.5\pi(w_v - x)} \right) , \quad 0.5w_v \leq x \leq w_v$$

$$P_{5'} = \frac{2}{\pi} \mu_0 d \ln \left(\frac{l_g + 0.25\pi w_v}{l_g + 0.5\pi(x - w_t)} \right) , \quad w_t \leq x \leq w_v$$

where w_t is the tooth width, w_v is the valley width, l_g is the air gap length, d is the depth, x is the relative displacement between opposing teeth, and the subscripts are labeled according to the subregions as shown in Figure 79.

The total gap permeance $P_g(x)$ is therefore the sum of all permeances associated with each flux tube. In this research, flux tubes are separated into two distinct groups; overlap flux tubes and fringing flux tubes, corresponding to the overlap component of the gap permeance $P_o(x)$ and the fringing component of the gap permeance $P_f(x)$, defined as

$$P_o = P_1 \tag{222}$$

$$P_f = P_g - P_1 \tag{223}$$

The spatial derivatives of permeances can be calculated analytically using these expressions.

APPENDIX B

DESIGN RELATED DERIVATIONS

B.1 Moving Mass

According to Figure 80(a), the moving mass of the candidate LPM motor is given by the sum of coil mass M_c , epoxy mass M_e and mover mass M_v , i.e.

$$M_m = M_c + M_e + M_v \quad (224)$$

where each quantity is calculated by

$$M_c = (s_c \rho_c + (1 - s_c) \rho_i) \cdot V_c \quad (225)$$

$$M_e = \rho_e \cdot (w_t l_t (d_t + d_g) - V_c) \quad (226)$$

$$M_v = \rho_v \cdot w_t l_t d_v \quad (227)$$

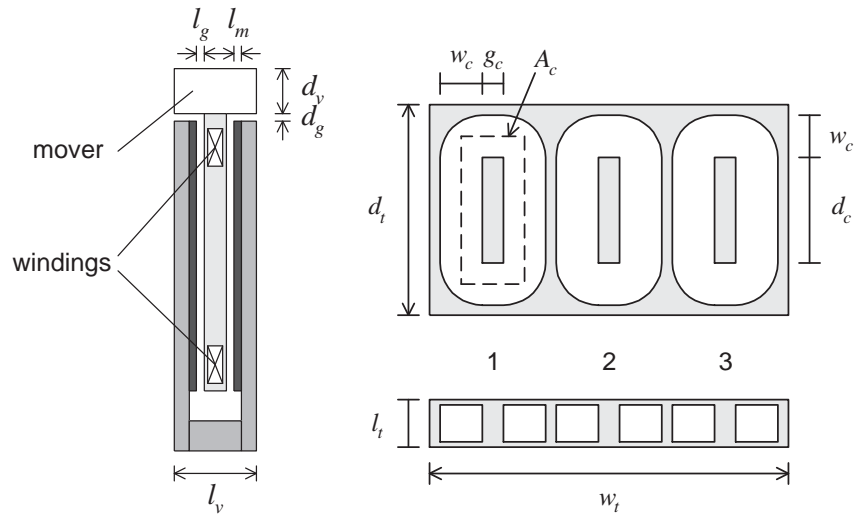
where the coil volume V_c is calculated by

$$V_c = 3 \cdot w_c \cdot l_c \cdot 2(g_c + d_c + 2w_c) \quad (228)$$

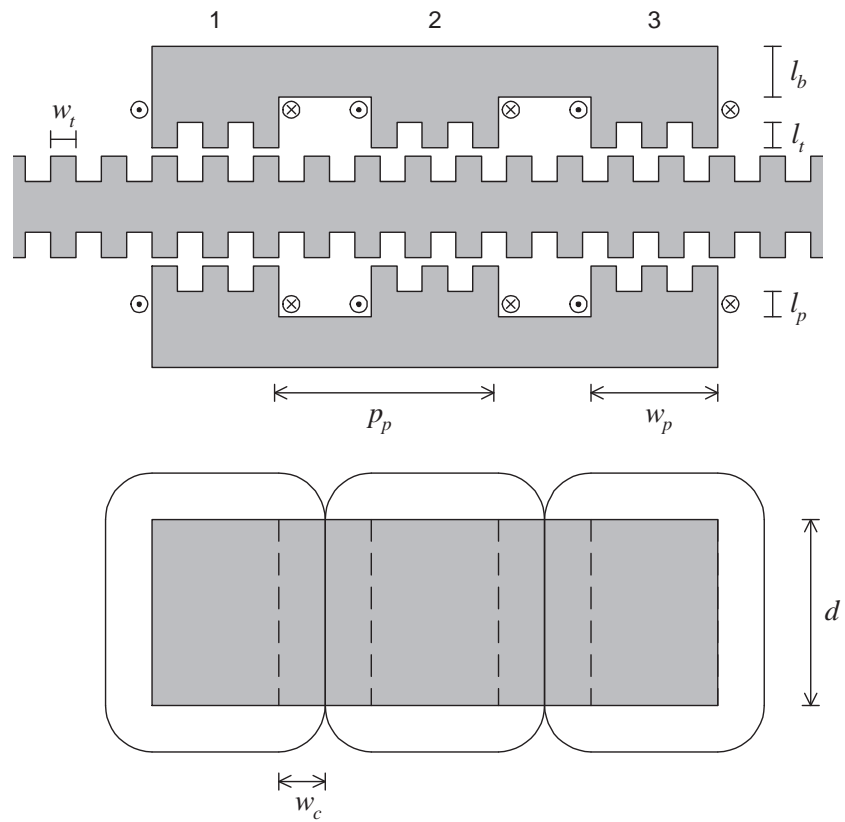
and ρ_c , ρ_i , ρ_e and ρ_a are the density of copper, insulating materials, epoxy and aluminum as listed in Table 13. The insulating materials are assumed to be layers of polyurethane and epoxy and the density is averaged.

According to Figure 80(b), the moving mass of the candidate LVR motor is given by the sum of back iron mass M_b , pole mass M_p , tooth mass M_t and coil mass M_c , i.e.

$$M_m = M_b + M_p + M_t + M_c \quad (229)$$



(a) LPM motor



(b) LVR motor

Figure 80: Motor diagrams with geometry variables defined.

Table 13: Material Density Properties

Material	Symbol	Value (kg/m ³)
Aluminum	ρ_a	2700
Copper	ρ_c	8900
Epoxy	ρ_e	1800
Polyurethane	ρ_p	1300
Silicon steel	ρ_s	7800

where each quantity is calculated by

$$M_b = \rho_s \cdot l_b (2p_p + w_p) d \quad (230)$$

$$M_e = 3\rho_s \cdot l_p w_p d \quad (231)$$

$$M_v = 3\rho_s \cdot n_t w_t l_t d \quad (232)$$

$$M_c = 3(s_c \rho_c + (1 - s_c) \rho_i) \cdot l_p w_c (w_p + d + 2w_c) \quad (233)$$

where ρ_s the density of steel as also listed in Table 13.

B.2 Wire Size and Resistance

According to [11], the bare-wire diameter (conductor only) based on American Wire Gauge (AWG) is given by

$$\text{dia}(w) = 11.68 (0.890526)^{w+3} \text{ mm} \quad (234)$$

where w is the wire size in AWG number. Apparently, the bigger w is, the smaller the wire diameter becomes. The winding resistance is then calculated by

$$R = \frac{\rho N l}{0.25\pi \text{dia}(w)^2} \quad (235)$$

where ρ is the resistivity of copper, N is the number of turns and l is effective circumferential length of the winding as shown in Figure 81. Note that the insulation and bonding material in the winding are taken into account via the coil space factor s_c , which is defined as the ratio between the total conductor area and the total coil area.

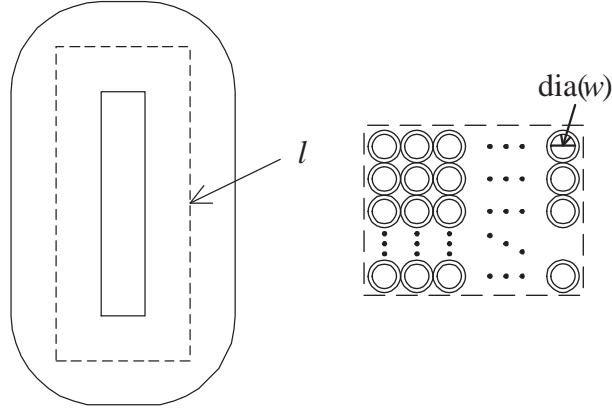


Figure 81: Effective circumferential length and winding cross section for winding resistance calculation.

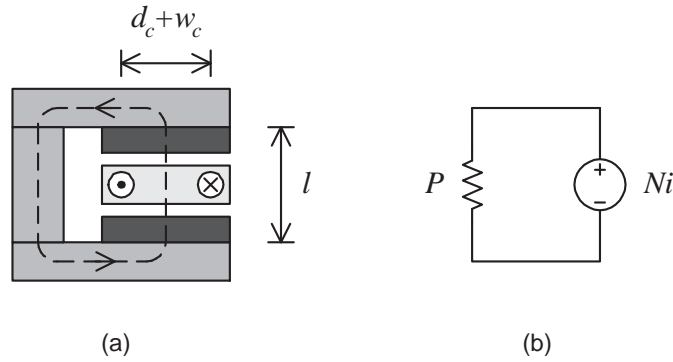


Figure 82: Diagrams for calculating self inductance of the LPM motor: (a) side view of a magnetic flux path linking a coil and (b) the corresponding magnetic circuit.

B.3 Inductances

For the LPM motor shown in Figure 80(a), only self inductance is considered due to the large air gap structure. The diagrams for calculating the self inductance are shown in Figure 82. Assuming magnetic linearity and neglecting flux leakage, the flux linkage λ for the coil is given by

$$\lambda = Li = N\Phi = N^2Pi \quad (236)$$

where L is the inductance, i is the phase current, N is the number of turns, Φ is the magnetic flux and P is the permeance calculated by

$$P = \frac{\mu_0 A}{l} \quad (237)$$

where μ_0 is the permeability of air and A and l are the effective cross section area and effective length, respectively. Note that permeability of steel and permanent magnet are assumed to be infinite and μ_0 , respectively. It follows that the self inductance is given by

$$L = N^2 P \quad (238)$$

and specifically for the LPM motor

$$L = \frac{\mu_0 N^2 (g_c + w_c)(d_c + w_c)}{l_t + 2l_g + 2l_m} \quad (239)$$

where the geometry variables are defined in Figure 80(a).

For the LVR motor shown in Figure 80(b), both self and mutual inductances must be accounted for due to its strong magnetically coupled structure. The inductances may be calculated from air gap reluctances (R_1, R_2, R_3) that vary as functions of relative displacement x . These reluctances are periodic functions of x , with period equal to p_t and with pole-to-pole spatial shifts equal to $p_t/3$, where p_t is the tooth pitch. When spatial harmonics are excluded, the reluctances may be represented by

$$R_j = r_0 + r_1 \cos(\omega x - (j - 1)\frac{2\pi}{3}) \quad (240)$$

for $j = 1, 2, 3$ where $\omega = 2\pi/p_t$ and r_0 and r_1 are the coefficients depending on air gap geometry as considered in Appendix A where permeance is the inverse of reluctance.

By analyzing the equivalent magnetic circuit associated with Figure 80(b), it is possible to relate the air gap reluctances to inductances of the phase windings. For ideal case when steel is infinitely permeable and flux leakage is neglected, the self and mutual inductances are given by

$$L_{jj} = L_s + L_m \cos(\omega x - (j - 1)\frac{2\pi}{3}) \quad (241)$$

$$L_{jk} = -M_s + L_m \cos(\omega x + (j + k - 2)\frac{2\pi}{3}) \quad (242)$$

where

$$L_s = \frac{8}{3}N^2 \frac{r_0}{4r_0^2 - r_1^2} \quad (243)$$

$$L_m = \frac{4}{3}N^2 \frac{-r_1}{4r_0^2 - r_1^2} \quad (244)$$

and $M_s = \frac{1}{2}L_s$ for $j, k = 1, 2, 3$. Finally, the aligned self inductance L_a and unaligned self inductance L_u , which will be used in the design process, are calculated by

$$L_a = L_s + L_m \quad (245)$$

$$L_u = L_s - L_m \quad (246)$$

B.4 System Description Review

A brief description of the ideal LPM and LVR motor system is given here as a basis for determining current and voltage limits.

According to Chapter 2, a change of variables is introduced to eliminate the dependence on position x using the orthonormal transformation matrix

$$S(x) = \sqrt{\frac{2}{3}} \begin{bmatrix} \cos(\frac{\pi}{p}x) & \cos(\frac{\pi}{p}x + \frac{2\pi}{3}) & \cos(\frac{\pi}{p}x - \frac{2\pi}{3}) \\ -\sin(\frac{\pi}{p}x) & -\sin(\frac{\pi}{p}x + \frac{2\pi}{3}) & -\sin(\frac{\pi}{p}x - \frac{2\pi}{3}) \\ \frac{1}{\sqrt{2}} & \frac{1}{\sqrt{2}} & \frac{1}{\sqrt{2}} \end{bmatrix} \quad (247)$$

that maps

$$\underbrace{[\sigma_d \ \sigma_q \ \sigma_0]^T}_{\tilde{\sigma}^T} = S(x) \underbrace{[\sigma_1 \ \sigma_2 \ \sigma_3]^T}_{\sigma^T} \quad (248)$$

where $\tilde{\sigma}$ is a vector of the d -axis, q -axis and 0-axis variable for voltage or current, and σ is a vector of the original voltage or current variables and p is the motor pitch which characterizes the spatial periodicity of the linear magnetic structure. For LPM motors, p is the magnet pitch τ ; for LVR motors p is the tooth pitch p_t .

The resulting voltage equations are given by

$$v_d = Ri_d - \alpha L_q i_q \frac{dx}{dt} + L_d \frac{di_d}{dt} \quad (249)$$

$$v_q = Ri_q + \alpha L_d i_d \frac{dx}{dt} + L_q \frac{di_q}{dt} \quad (250)$$

$$v_0 = Ri_0 \quad (251)$$

where (v_q, v_d, v_0) and (i_q, i_d, i_0) are the q -axis, d -axis and 0-axis component of voltages and currents, respectively; L_d and L_q are given by

$$L_d = L_s + M_s + \frac{3}{2}L_m \quad (252)$$

$$L_q = L_s + M_s - \frac{3}{2}L_m \quad (253)$$

and the constant parameter α is

$$\alpha = \frac{\pi}{p} \quad (254)$$

The force function is given by

$$f(i_q, i_d) = K_a i_q + K_r i_q i_d \quad (255)$$

where K_a is the alignment force constant and K_r is the reluctance force constant. $K_r = 0$ for LPM motors; $K_a = 0$ for LVR motors.

B.5 Current Limit

During the design process, current limits are determined: (i) to conservatively restrict steady-state temperature rise in the windings (both LPM and LVR motor design) and (ii) to prevent over-saturating steel under steady-state operation (only LVR motor design). The design formulas for determining current limit are given by

$$i_{\max} = \begin{cases} A_w J_{\max} & , \text{ LPM motor} \\ \min \left\{ \frac{NA_p}{L_{\text{eff}}} B_{\max}, A_w J_{\max} \right\} & , \text{ LVR motor} \end{cases} \quad (256)$$

where A_w is the cross-sectional area of the conductor, J_{\max} is the maximum instantaneous current density, N is the number of turns per phase, A_p is the cross-sectional

area of the poles, L_{eff} is an effective inductance parameter and B_{max} is the maximum flux density. The analysis method used to calculate (256) is based on the ideal synchronous motor models and the derivation is summarized in the following subsections.

B.5.1 Steady-State Temperature Rise

The thermal model of a motor is greatly simplified by regarding it as a homogeneous body exhibiting a capacity for thermal energy storage and cooled by convection (natural or forced). Under these assumptions, the mean surface temperature ϑ is governed by the power balance

$$C_p M_t \dot{\tilde{\vartheta}} + C_h A_t \tilde{\vartheta} = p \quad (257)$$

where $\tilde{\vartheta} = \vartheta - \vartheta_0$ denotes the rise from ambient temperature ϑ_0 , p is the input power sourcing the heat flow, M_t is the mass experiencing heat flow, C_p is the specific heat of the material experiencing heat flow, A_t is the surface area normal to the direction of heat flow, and C_h is the coefficient of heat transfer. The value of C_h is strongly influenced by the velocity of cooling air. Consequently, the thermal resistance is essentially fixed under forced convection but will depend on the motion trajectory under natural convection.

If the motor provides periodic motion with period T , then the phase currents (i_1, i_2, i_3) and corresponding copper losses $p = R(i_1^2 + i_2^2 + i_3^2)$ will also be periodic with period T . Due to the large thermal time constant, the temperature rise will be primarily determined by the average copper losses computed according to

$$P = \frac{1}{T} \int_0^T p \, dt = \frac{1}{T} \int_0^T R(i_1^2 + i_2^2 + i_3^2) \, dt = R(I_1^2 + I_2^2 + I_3^2) \quad (258)$$

where I_j denotes the RMS value of i_j , i.e.

$$I_j = \sqrt{\frac{1}{T} \int_0^T i_j^2 \, dt} \quad (259)$$

The steady-state solution of the power balance with $p = P$ is given by

$$\vartheta_\infty = \vartheta_0 + \frac{1}{C_h A_t} P \quad (260)$$

If the instantaneous phase currents are bounded by $|i_j| \leq i_{\max}$, then $I_j \leq i_{\max}$ since

$$I_j \leq \sqrt{\frac{1}{T} \int_0^T i_{\max}^2 dt} = i_{\max} \quad (261)$$

Hence, if the instantaneous phase currents satisfy the bound

$$|i_j| \leq i_{\max} = \sqrt{\frac{C_h A_t (\vartheta_{\max} - \vartheta_0)}{3R}} \quad (262)$$

then the steady-state temperature will be bounded by $\vartheta_{\infty} \leq \vartheta_{\max}$. Corresponding to i_{\max} is a bound on instantaneous current density defined by

$$J_{\max} = i_{\max} / A_w \quad (263)$$

Imposing a bound J_{\max} on instantaneous current density is an appropriate way to limit the steady-state temperature. On the other hand, since the steady-state temperature is actually determined by RMS currents, the use of instantaneous current bounds as described above will lead to a conservative (non-optimal) satisfaction of the desired result $\vartheta_{\infty} \leq \vartheta_{\max}$.

Since the LPM motors under consideration usually operate in the linear region of the BH-curve, it is sufficient to consider only current limit from J_{\max} , which may be determined from thermal analysis or expert design rule. However, magnetic saturation must also be taken into consideration to appropriately impose instantaneous current bounds for the LVR motors because the motor usually operates in the nonlinear region of the BH-curve.

B.5.2 Commutation Scheme for Steady-State Operation

Suppose that a three-phase synchronous motor, with linear and sinusoidal magnetics, is commutated with minimum-copper-loss commutation without current limit as discussed in Chapter 2. This commutation scheme can be stated formally as

$$\begin{aligned} & \text{minimize} && \tilde{i}^T \tilde{i} \\ & \text{subject to} && f(i_q, i_d) = f_d \end{aligned} \quad (264)$$

where f_d is a desired force command. This version of the problem has a closed-form solution. If $K_r = 0$ (LPM motors), the solution is

$$\begin{aligned} i_d &= 0 \\ i_q &= i_{\text{PM}}^* \\ i_0 &= 0 \end{aligned} \tag{265}$$

where

$$i_{\text{PM}}^* = \frac{f_d}{K_a} \tag{266}$$

If $K_a = 0$ (LVR motors), the solution is

$$\begin{aligned} i_d &= i_{\text{VR}}^* \\ i_q &= i_{\text{VR}}^* \text{sign}(f_d) \\ i_0 &= 0 \end{aligned} \tag{267}$$

where

$$i_{\text{VR}}^* = \sqrt{\frac{|f_d|}{K_r}} \tag{268}$$

This formulation will be used to estimate current and voltage bounds when the motor operates under steady-state conditions.

B.5.3 Magnetic Saturation

Magnetic saturation are considered to impose instantaneous current bounds only for the LVR motors. According to (247)-(248) and (264)-(267), the excitation current of phase j has the form

$$i_j = I \cos\left(\frac{\pi}{p_t}x + (j-1)\frac{2\pi}{3} \pm \frac{\pi}{4}\right) \tag{269}$$

where the plus sign is used for positive force and the minus sign is used for negative force. The flux density B_j within the poles of phase j is related to the excitation

currents via the flux linkage λ_j and the magnetic flux ϕ_j by

$$\lambda_j = N\phi_j = NA_p B_j = \sum_{k=1}^3 L_{jk} i_k \quad (270)$$

where the self and mutual inductances are given by

$$L_{jj} = L_s + L_m \cos(\omega x - (j-1)\frac{2\pi}{3}) \quad (271)$$

$$L_{jk} = -M_s + L_m \cos(\omega x + (j+k-2)\frac{2\pi}{3}) \quad (272)$$

This leads to

$$\begin{aligned} NA_p B_j &= (L_s + M_s)I \cos\left(\frac{\pi}{p_t}x + (j-1)\frac{2\pi}{3} \pm \frac{\pi}{4}\right) \\ &\quad + \frac{3}{2}L_m I \cos\left(\frac{\pi}{p_t}x + (j-1)\frac{2\pi}{3} \mp \frac{\pi}{4}\right) \end{aligned} \quad (273)$$

It is clear that B_j varies sinusoidally with respect to position. The value of x that maximizes B_j is implicitly defined by the constraint

$$\tan\left(\frac{\pi}{p_t}x + (j-1)\frac{2\pi}{3}\right) = \mp \frac{L_s + M_s - \frac{3}{2}L_m}{L_s + M_s + \frac{3}{2}L_m} = \mp \frac{L_q}{L_d} \quad (274)$$

Applying this constraint, it follows that the flux density within poles is bounded by the peak value of phase currents according to

$$|NA_p B| \leq L_{\text{eff}} I \quad (275)$$

$$L_{\text{eff}} = \sqrt{(L_s + M_s)^2 + (\frac{3}{2}L_m)^2} = \sqrt{\frac{L_d^2 + L_q^2}{2}} \quad (276)$$

Consequently, if B_{max} is the maximum flux density that can be supported by the magnetic material from which poles are constructed, then the phase currents should be limited to i_{max} where

$$i_{\text{max}} = \frac{NA_p}{L_{\text{eff}}} B_{\text{max}} \quad (277)$$

More precisely, if J_{\max} is the maximum current density that can be supported by the wire from which coils are constructed, then the phase currents should be limited according to

$$i_{\max} = \min \left\{ \frac{NA_p}{L_{\text{eff}}} B_{\max}, A_w J_{\max} \right\} \quad (278)$$

The value of B_{\max} is a directly identifiable material parameter, whereas the value of J_{\max} may be determined from thermal analysis or expert design rule.

B.6 Voltage Limit

During the design process, voltage requirements are determined to restrict the values of resistance and inductance in the windings within a reasonable range so that the candidate motors do not require excessively high voltage to operate. The analysis method used to calculate voltage requirements is also based on ideal synchronous motor models, where magnetic saturation and spatial harmonics are excluded.

When a synchronous motor (LPM or LVR) operates under steady-state conditions according to (247)-(248) and (264)-(265), the steady-state physical currents and voltage are given by

$$i = I \begin{bmatrix} \cos(x_1 + \delta_i) & \cos(x_2 + \delta_i) & \cos(x_3 + \delta_i) \end{bmatrix}^T \quad (279)$$

$$v = V \begin{bmatrix} \cos(x_1 + \delta_v) & \cos(x_2 + \delta_v) & \cos(x_3 + \delta_v) \end{bmatrix}^T \quad (280)$$

and the corresponding transformed variables are given by

$$\tilde{i} = I \sqrt{\frac{3}{2}} \begin{bmatrix} \cos \delta_i & \sin \delta_i & 0 \end{bmatrix}^T \quad (281)$$

$$\tilde{v} = V \sqrt{\frac{3}{2}} \begin{bmatrix} \cos \delta_v & \sin \delta_v & 0 \end{bmatrix}^T \quad (282)$$

where δ_i and δ_v are the phase shifts of the currents and voltages, and

$$I = \sqrt{\frac{2}{3}} \|\tilde{i}\| \quad (283)$$

$$V = \sqrt{\frac{2}{3}} \|\tilde{v}\| \quad (284)$$

According to (249)-(251) and (265) when the LPM motor operates under steady-state conditions, the steady-state voltages are given by

$$v_d = -\omega L i_{\text{PM}}^* \quad (285)$$

$$v_q = R i_{\text{PM}}^* \quad (286)$$

where $L = L_d = L_q$ and $\omega = \frac{\pi}{\tau} \dot{x}$. This leads to

$$\|\tilde{i}\| = |i_{\text{PM}}^*| \quad (287)$$

$$\|\tilde{v}\| = |i_{\text{PM}}^*| \sqrt{R^2 + (\omega L)^2} \quad (288)$$

Hence, the bound of voltage v_{max} is given in term of i_{max} as

$$\frac{v_{\text{max}}}{i_{\text{max}}} = \sqrt{R^2 + (\omega L)^2} \quad (289)$$

for LPM motors.

According to (249)-(251) and (267), when the LVR motor operates under steady-state conditions, the steady-state voltages are given by

$$v_d = (R \mp \omega L_q) i_{\text{VR}}^* \quad (290)$$

$$v_q = (R \pm \omega L_d) i_{\text{VR}}^* \quad (291)$$

where the plus sign is used for positive force and the minus sign is used for negative force and $\omega = \frac{\pi}{p_t} \dot{x}$. This leads to

$$\|\tilde{i}\| = i_{\text{VR}}^* \sqrt{2} \quad (292)$$

$$\|\tilde{v}\| = i_{\text{VR}}^* \sqrt{(R \mp \omega L_q)^2 + (R \pm \omega L_d)^2} \quad (293)$$

Since $L_d > L_q$, the bound of voltage v_{max} is given in term of i_{max} as

$$\frac{v_{\text{max}}}{i_{\text{max}}} = \left(\frac{(R - \omega L_q)^2 + (R + \omega L_d)^2}{2} \right)^{\frac{1}{2}} \quad (294)$$

for LVR motors.

In conclusion, the design formulas for determining voltage requirements are calculated according to (289) and (294), as summarized by

$$v_{\max} = \begin{cases} (R^2 + (\omega L)^2)^{\frac{1}{2}} i_{\max} & , \text{ LPM motor} \\ \left(\frac{(R - \omega L_q)^2 + (R + \omega L_d)^2}{2} \right)^{\frac{1}{2}} i_{\max} & , \text{ LVR motor} \end{cases} \quad (295)$$

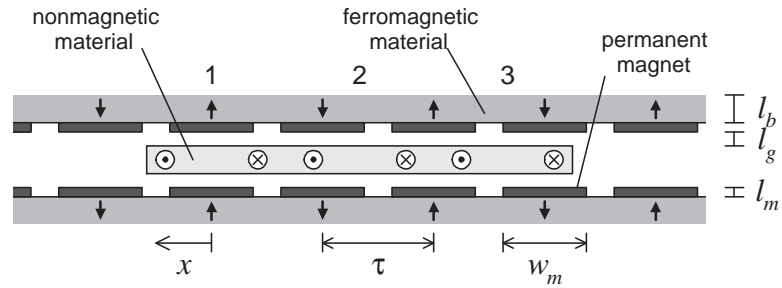
APPENDIX C

THERMAL ANALYSIS OF A LPM MOTOR

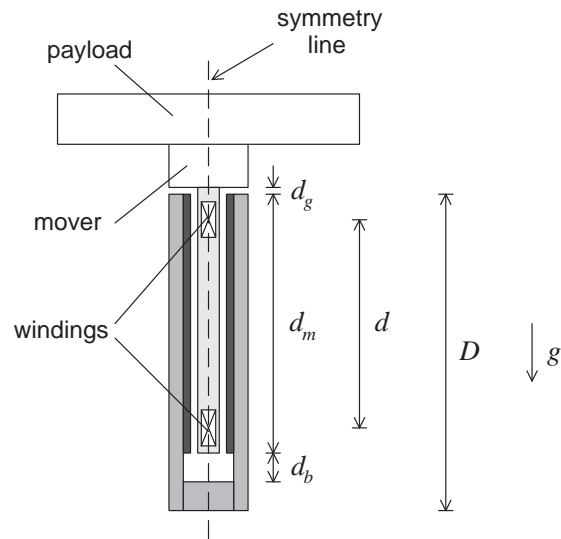
The preliminary work to develop the thermal resistance model (TRM) of a LPM motor is presented in this appendix. In particular, TRM has been a popular tool for thermal analysis in design and optimization of electric motors for its computational efficiency [71, 72, 73, 74, 3]. The resulting TRM is used to determine the “equivalent” thermal resistance that is required to compare performances between different motor technologies for manufacturing automation applications.

Heat transfer analysis of the LPM motor, shown in Figure 83, is complex due to its geometry, and the interrelated modes of heat transfer (conduction in different materials and convection on open surfaces). In addition, the heat convection characteristics are strongly influenced by the intended periodic mode of operation; if forced air or liquid cooling is not available (as considered here), then the cooling air flow arises only from periodic motion. Heat transfer analysis of the motor under consideration has not appeared in the literature.

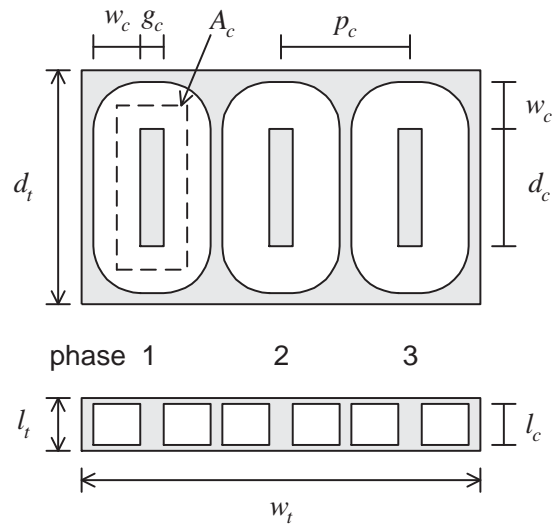
Hence, the objective is to first analyze the heat transfer characteristics of this LPM motor using a TRM that accounts for both conduction and convection. The LPM motor under consideration operates with continuous periodic excitation and *short-stroke* reciprocating motion, resulting in mostly *natural convection* that helps the cooling (forced convection induced by short-stroke motion is small). A full validation of the proposed TRM would require FEA based on coupled conduction and convection wherein computational fluid dynamics is used to determine the velocity field for natural cooling. As a first step, this study validates the TRM using conductive heat transfer results from FEA, obtained assuming consistent heat flux conditions



(a) Top view, with payload removed.



(b) Front view, with payload attached.



(c) Concentrated windings encased in epoxy.

Figure 83: LPM motor with concentrated windings.

on boundary surfaces at which convection occurs.

C.1 Thermal Resistance Model

The main sources of power losses in electromechanical systems are: (i) copper losses, (ii) iron losses from eddy currents and hysteresis, and (iii) friction losses from mechanical contacts and windage. In this study, only copper losses due to periodic operation are considered. The TRM is developed according to the following assumptions:

- The heat generated in the coils is uniformly distributed and conducts in radial directions within cross sectional planes.
- Heat conducts in a single direction within homogeneous materials resulting in isothermal surfaces normal to the heat flux.
- Heat convection occurs only at certain surfaces exposed to air, depending on dimension and orientation.
- Thermal contact resistance between different materials is negligible.

C.1.1 Homogeneous Material

A homogeneous material experiencing heat conduction in one direction has thermal resistance

$$R = \frac{1}{k} \int \frac{dx}{A(x)} \quad (296)$$

where k is the thermal conductivity and A is the cross section area normal to the heat flow direction x . For a block of homogeneous material as shown in Figure 84, with constant area A and vertical heat flow, the thermal resistance is thus

$$R = \frac{L}{kA} \quad (297)$$

where L is the length of the block. Although this model assumes isothermal surfaces normal to the direction of heat flow, it greatly simplifies the network topology and

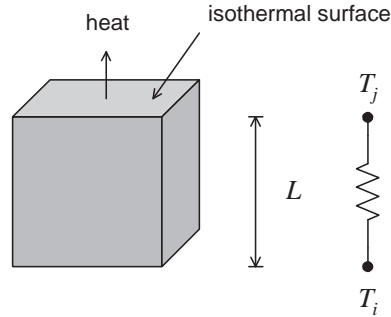


Figure 84: Homogeneous material block and its thermal resistive representation.

can reasonably predict hot spots of the motor. Homogeneous regions of the epoxy, air gap, PM and steel may be modeled in this way.

C.1.2 Windings

The windings are constructed from multiple turns of wire that has a copper core surrounded by electrical insulation (polyurethane, polyester, aluminum oxide, etc.), and coated with adhesive material (epoxy, polyester, etc.). When these windings are heat treated, the adhesive material bonds the coils for mechanical rigidity.

Since the copper is uniformly distributed within the winding, the copper core will be modeled as a single rectangular block with matched cross section area as shown in Figure 85. The layers of the electrical insulation (polyurethane) and adhesive material (epoxy) are grouped together into a single layer to simplify the model.

The copper core is modeled as an ideal heat source

$$q = rI_{\text{rms}}^2 \quad (298)$$

where r is the electrical resistance of the copper and I_{rms} is the rms value of the phase current passing through the coil during one operational period. The phase currents are determined using a model of the electromechanical dynamics to obtain a desired periodic motion. Heat capacitance is not needed when modeling the heat source because only steady-state temperatures are considered.

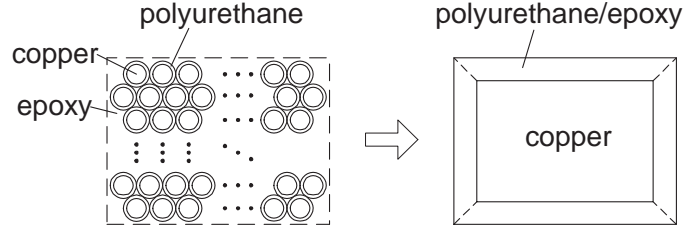


Figure 85: Winding structure and its simplified model.

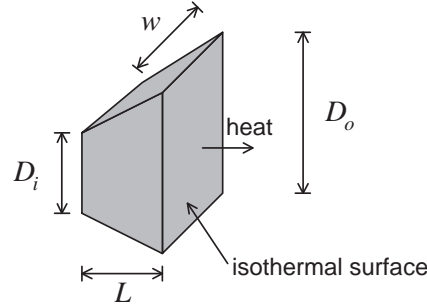


Figure 86: Homogeneous layer of winding material model.

The remaining layer of polyurethane/epoxy is modeled as a one-dimensional thermal resistance using the structure shown in Figure 86. From (296), this leads to

$$R = \frac{L \ln(D_o/D_i)}{kw(D_o - D_i)}, \quad D_o \neq D_i \quad (299)$$

where L , D_o , D_i and w are defined in the diagram.

C.1.3 Natural Heat Convection

Convective heat transfer occurs where motor surfaces are exposed to air. For the LPM motor, convective heat transfer takes place throughout the entire structure and helps the cooling. This convection occurs through thermal resistance

$$R = \frac{1}{hA} \quad (300)$$

where h is the average film coefficient of the particular surface and A is the surface area exposed to the cooling air. The average film coefficient is conventionally obtained from the Nusselt number

$$\text{Nu}_L = \frac{hL}{k} \quad (301)$$

where L is the characteristic length. The Nusselt number is geometry dependent and can be obtained experimentally or by solving the boundary layer equations.

When the LPM motor operates with continuous periodic motion, three possibilities for heat convection exist: (i) predominately natural convection due to negligible amount of relative air flow from short-stroke motion with no forced cooling air, (ii) predominately forced convection due to relative air flow from long-stroke motion with forced cooling air, or (iii) both natural and forced convection. Since the heat dissipation by natural convection is generally lower than by forced convection, the short-stroke motion with minimal cooling represents the true thermal limit of motor performance. Hence only (i) is considered in this study.

Assume that the LPM is set up vertically with payload mounted on the top as shown in Figures 83(b) and 87. The natural convection through surfaces 1, 3 and 7-9 in Figure 87 will be modeled as vertical plates and the Nusselt number for calculating the average heat transfer coefficients is given by [75]

$$\text{Nu}_L = 0.68 + \frac{0.670 \text{Ra}_L^{\frac{1}{4}}}{\left(1 + \left(\frac{0.492}{\text{Pr}}\right)^{\frac{9}{16}}\right)^{\frac{4}{9}}} \quad (302)$$

where Prandtl and Rayleigh numbers are given by

$$\text{Pr} = \frac{\nu}{\alpha}, \quad \text{Ra}_L = \frac{g\beta(T_s - T_a)L^3}{\nu\alpha} \quad (303)$$

where ν is the kinematic viscosity of air, α is the thermal diffusivity of air, g is the acceleration due to gravity, β is the volumetric thermal expansion coefficient of air, T_s and T_a are the surface and ambient temperatures, and L is the characteristic length along the vertical surface. All air-related coefficients are evaluated at the film temperature (average of the surface and ambient temperature).

The natural heat convection through the top and bottom surfaces of the payload will be modeled as horizontal plates and the Nusselt number is given by

$$\text{Nu}_L = 0.54 \text{Ra}_L^{\frac{1}{4}} \quad (304)$$

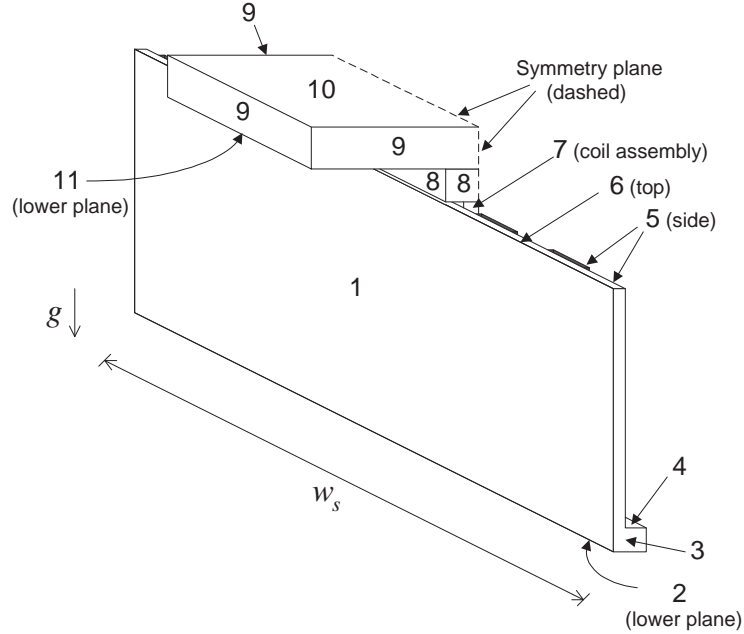


Figure 87: Convective heat transfer surfaces for the steady-state heat transfer analysis for TRM and FEA.

for surface 10, and

$$\text{Nu}_L = 0.27 \text{Ra}_L^{\frac{1}{4}} \quad (305)$$

for surface 11, where the characteristic length $L = A_s/P$; A_s and P are the surface area and the perimeter of the plate. Note that since $\text{Ra}_L \lesssim 10^3$ on surfaces 4 and 6, the heat convection is assumed to be negligible on those surfaces [76].

Surface 2 is where the LPM motor is usually installed on a larger device such as a gantry robot, so it will be modeled as a heat sink. The heat dissipation rate is estimated to be 300 W/m^2 for the body temperature rise of 30 K and average film coefficient of $10 \text{ W/m}^2\text{K}$ over the whole device.

C.1.4 Thermal Network Topology

The TRM shown in Figure 88 represents only half of the thermal system due to symmetry. Nodal temperatures within the windings correspond to the interface between two adjacent materials. Heat sources and heat sinks are represented by current sources

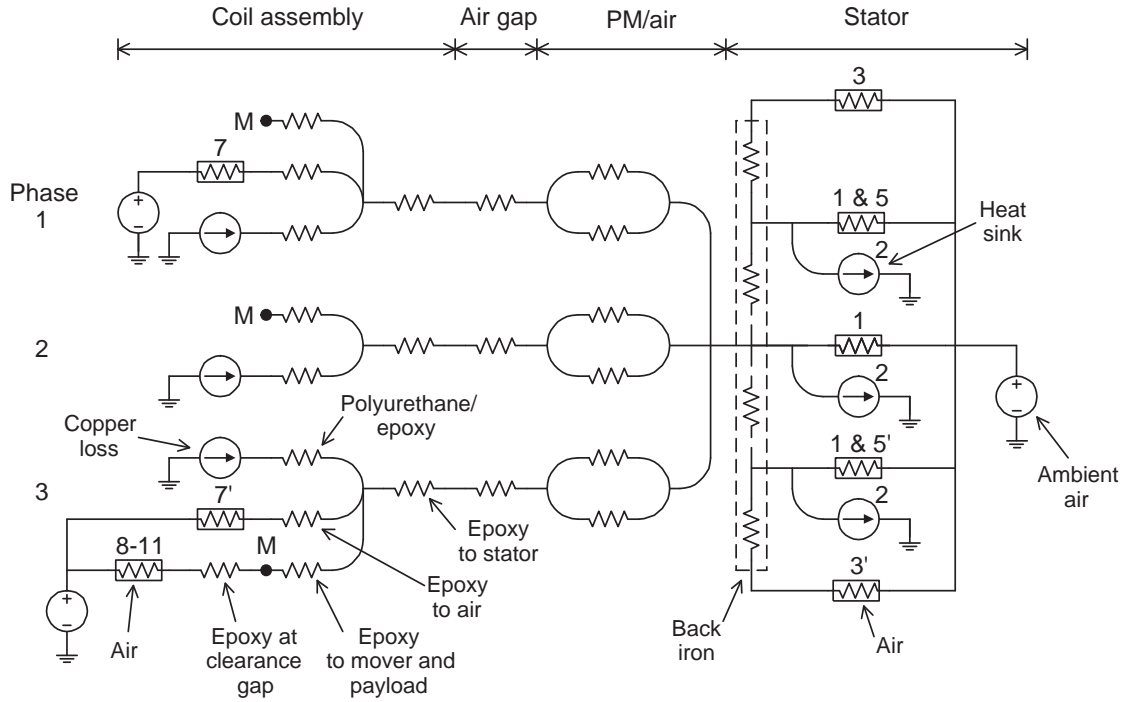


Figure 88: The thermal resistance model of the LPM motor for steady-state heat transfer analysis.

whereas the ambient temperature is represented by voltage sources. The heat conduction through homogeneous materials is represented by linear resistors whereas the natural convection to the ambient temperature is represented by nonlinear resistors due to their surface temperature dependence.

According to the model, heat generated by copper loss is conducted through the polyurethane/epoxy layer to the epoxy case. The heat is then transferred through three possible directions: (i) to the stator (all three phases), (ii) to the air through the sides of the coil assembly (surface 7) and (iii) to the mover and payload (node M to surfaces 8-11). Heat that is transferred to the stator passes the air gap, PMs, steel and then is naturally convected to air via the surface 1, 3 and 5 of the back iron. Some heat is dissipated through heat sinks at the bottom of the U-channel (surface 2). Note that the prime symbol indicates the opposing surfaces on the other side of the device.

Table 14: Material Thermal Properties

Material	k (W/m K)	ρ (kg/m ³)	C_p (J/kg K)
Aluminum	237	2700	903
Copper	385	8900	380
Epoxy	0.8	1800	900
NdFeB magnet	8.95	7500	520
Polyurethane	0.216	1300	1800
Silicon steel	66.1	7800	434

The heat that is transferred vertically passes the epoxy to the mover and the payload, and then is convected through the surfaces of the mover and payload. Since the aluminum mover and the aluminum payload under consideration have good thermal conductivity and are directly attached to the epoxy case, their thermal resistances are negligible and not included in the network. Symmetry along the center of the coil assembly is assumed to reduced the model complexity.

The average film coefficients are calculated using the surface temperature at each location. The surface temperature of surface 1, used for the average film coefficient calculation, is obtained by averaging multiple associated nodal temperatures. The thermal resistance values are determined in accordance with Tables 14-15. For the combined polyurethane/epoxy layer, the material properties are averaged.

C.2 Steady-State Thermal Analysis

At steady state, the temperature rise due to copper loss directly relates to the periodic currents passing through the copper coils. In the TRM, this effect is captured by rms currents $I_{\text{rms},1}$, $I_{\text{rms},2}$ and $I_{\text{rms},3}$. These values are obtained from a model of the electromechanical dynamics as shown below.

Table 15: LPM Motor Parameters

Parameter	Symbol	Value
Coil assembly:		
Coil pitch	p_c	62 mm
Coil width	w_c	23 mm
Coil length	l_c	9.3 mm
Coil gap	g_c	12 mm
Coil depth	d_c	100 mm
Total width	w_t	186 mm
Total length	l_t	10.3 mm
Total depth	d_t	150 mm
Vertical cover	$(l_t - l_c)/2$	0.5 mm
Horizontal cover	$(d_t - d_c - 2w_c)/2$	2 mm
Averaged coil area	A_c	4305 mm ²
Number of turns	N	302
Wire size (AWG)	w	20
Stator:		
Back iron depth	D	180 mm
Back iron length	l_b	10 mm
Magnet depth	d_m	150 mm
Magnet pitch	p_m	93 mm
Magnet width	w_m	35 mm
Magnet length	l_m	5 mm
Air gap length	l_g	0.5 mm
Clearance gap depth	d_g	2 mm
Stator base depth	d_b	15 mm
Total stator width	w_s	569.5 mm
Residual flux density	B_r	1.15 T
Mover & Payload:		
Aluminum mover	-	41.3×186×20 mm ³
Aluminum payload	-	254×254×25.4 mm ³
Moving mass	M	5.51 kg

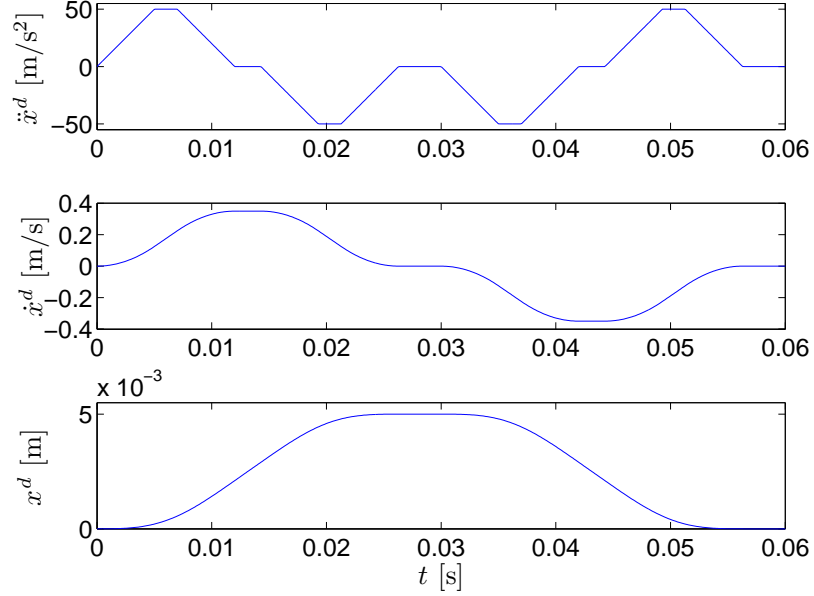


Figure 89: Periodic motion trajectory commands.

C.2.1 Linear Motor Operational Profile

The desired periodic motion is defined by stroke length 5 mm, maximum velocity 0.35 m/s, maximum acceleration 50 m/s², and maximum jerk 10⁴ m/s³. The resulting stroke duration of 26.3 ms, combined with a selected dwell time of 3.7 ms, yields a round-trip period of 60 ms. The desired position x^d , desired velocity \dot{x}^d and desired acceleration \ddot{x}^d are shown in Figure 89.

The phase currents required to produce the commanded periodic motion will be approximated using an idealized model of force production. Neglecting magnetic saturation and spatial harmonics, the force F produced by the LPM motor is given by

$$F = -K_f(i_1 \sin x_1 + i_2 \sin x_2 + i_3 \sin x_3) \quad (306)$$

where i_j is the phase j current, x_j is the phase j electrical position given by

$$x_j = \frac{\pi}{\tau} x + (j - 1) \frac{2\pi}{3} \quad (307)$$

where x is the mechanical position of the motor, and K_f is the force constant given

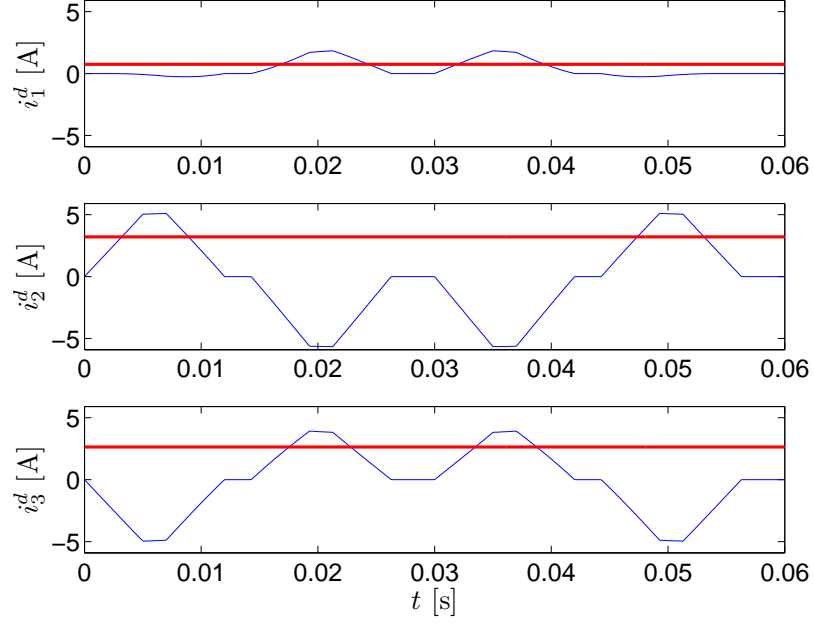


Figure 90: Periodic current commands, with rms currents superimposed.

by

$$K_f = \frac{NB_r l_m A_c}{(l_m + l_g + \frac{l_c}{2})} \cdot \frac{\pi}{\tau} \quad (308)$$

Following a minimum copper loss commutation strategy, the desired phase currents are selected according to

$$\begin{bmatrix} i_1^d \\ i_2^d \\ i_3^d \end{bmatrix} = -\frac{2}{3} \begin{bmatrix} \sin x_1 \\ \sin x_2 \\ \sin x_3 \end{bmatrix} \Big|_{x=x^d} \frac{F^d}{K_f} \quad (309)$$

where the desired force is chosen according to

$$F^d = M\ddot{x}^d \quad (310)$$

where M is the moving mass. The desired current trajectories are shown in Figure 90.

C.2.2 Implementation

The TRM is solved at the stationary position $x = 0$ mm, depicted in Figure 83a, due to the small moving distance of 5 mm. Since the average film coefficients depend on surface temperatures, certain thermal resistances in Figure 88 are nonlinear.

Consequently, nodal analysis of the TRM involves iteration. Iteration is initiated by assuming all convective surfaces have temperature 320 K. Under this assumption, the set of nodal equations for Figure 88 will take a linear form

$$Ax = b \quad (311)$$

where A is a matrix of thermal resistances, x is a vector of nodal temperatures, and b is a vector of heat sources and sinks. This set of linear equations is solved to determine all nodal temperatures. The computed temperatures for the convective surfaces are used to update (311), and the process is repeated until the assumed and computed convective surface temperatures agree to within 0.5 K.

C.2.3 Single-Node Thermal Resistance Model

The single-node TRM, where the motor is regarded as a homogeneous body, can be derived from the existing TRM using simplifying assumptions and circuit reduction, as illustrated in Figure 91. First, the steel elements are replaced by short circuits because metal is usually a much better heat conducting material. Notice that all non-linear elements become linear once the TRM is solved through the iterative process. Then the network topology is reconfigured into a fewer number of lumped elements in Figures 91(b)-(c), where nodes (1,2,3) are assumed to have the same nodal temperature. The Thevenin equivalent circuit is then derived for Figure 91(c) to obtain Figure 91(d) where

$$T_{\text{th}} = T_a - \frac{R_1 R_2 R_3 q_s}{R_2 (R_1 + R_2 + R_3)} \quad (312)$$

$$R_{\text{th}} = \frac{R_1 (R_2 + R_3)}{R_1 + R_2 + R_3} \quad (313)$$

Through circuit analysis of Figure 91(d)-(e), the hot spot temperature T_h of the LPM motor is determined to be

$$T_h = T_{\text{th}} + R_{\text{eq}} \sum_j^3 q_j \quad (314)$$

where q_j is the copper loss of phase j calculated according to (298), and the equivalent thermal resistance R_{eq} is given by

$$R_{\text{eq}} = \frac{1}{3}R_0 + R_{\text{th}} \quad (315)$$

This is the same thermal resistance mentioned in Section 1.1 of Chapter 1 that is required to transform Watt to Kelvin. Note that both (314) and (3) are consistent.

C.3 Finite Element Analysis

C.3.1 PDE Formulation

The FEA computation is conducted to verify the results from the TRM. Since only the short-stroke periodic motion profile is considered in this study, the FEA computation sets the problem as a stationary system. The steady-state heat conduction equation is given by

$$\nabla \cdot (-k\nabla T) = Q \quad (316)$$

where T is the temperature and Q is the heat generation per unit volume. The radiation effect is assumed to be negligible because of the small temperature difference between surfaces.

C.3.2 Computational Settings and Post Processing

The computation is performed using the commercial software COMSOL [77], which is capable of solving (316) in the multi-physics heat conduction mode. Although solving for the stationary system is different from solving for the moving body, the influence of cooling effect due to motion is negligible because of the small travel distance. FEA is conducted in 3D mode because the heat transfer occurs in all directions.

The geometry shown in Figure 87 is solved with the parameters listed in Tables 14-15. The mover and payload are assumed to be solid aluminum blocks. Although some thermal contact resistances are usually present in the actual device, they are omitted in this analysis. Symmetry along the coil assembly is imposed to reduce the problem

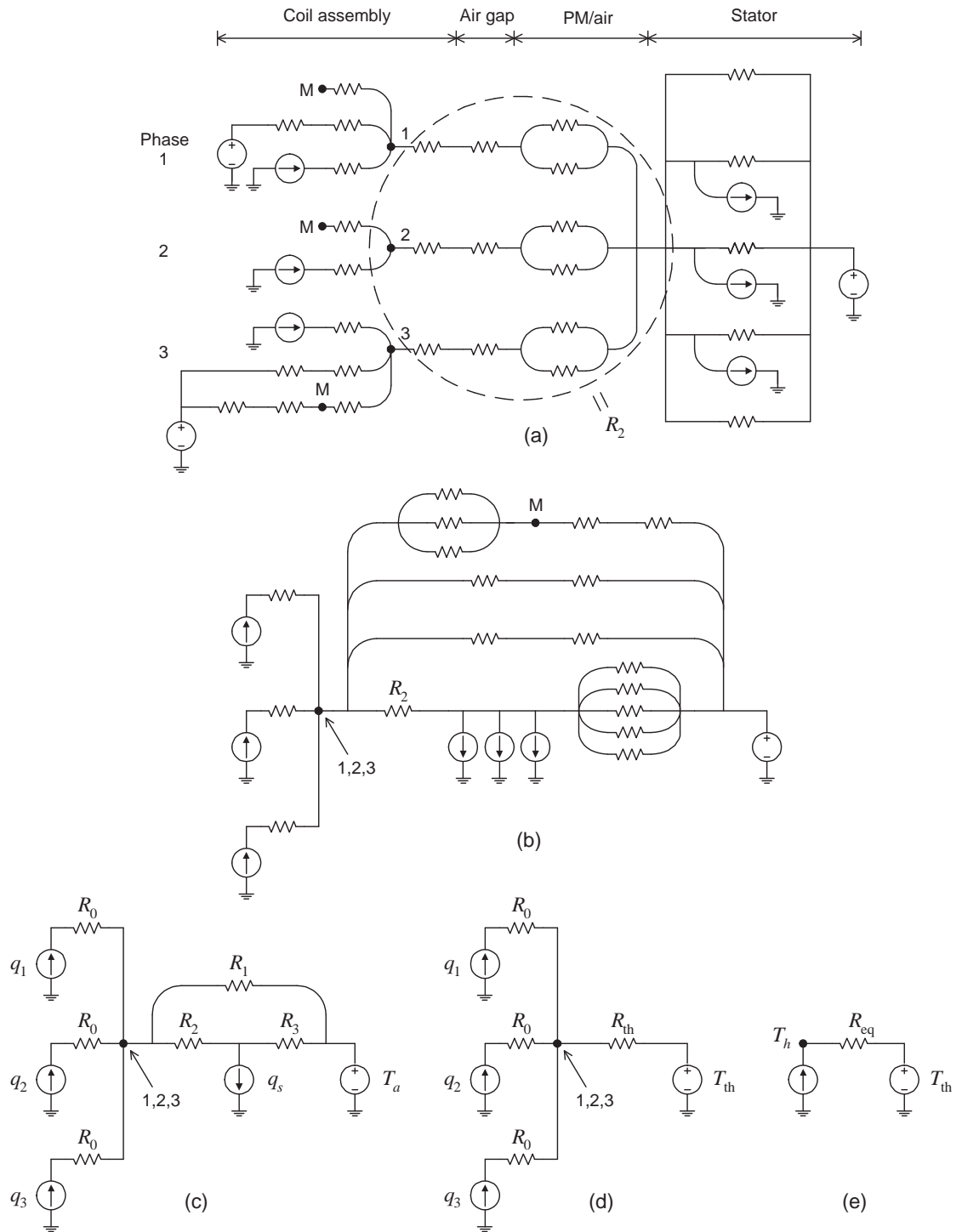


Figure 91: Derivation of the single-node thermal resistance model of the LPM motor: (a) steel elements are replaced by short circuits, (b) network reconfiguration, (c) simplified network topology, (d) simplified network with Thevenin equivalent circuit and (e) single-node TRM.

size. Note that the block of air of the same width as the coil assembly is extended 2 mm vertically upward to include the air between the coil assembly and the mover, and 15 mm vertically downward to include the air space between the coil assembly and the U-channel. The block of air also includes the air space between the stator and the coil assembly.

The boundary conditions used are listed in Table 16, where the boundary numbers correspond to those shown in Figure 87. The average film coefficients derived from (301)-(305) are required to specify all the boundary conditions except surfaces 2, 4 and 6. Since these coefficients are related to the surface temperatures, the FEA computation was iterated, beginning with a set of assumed surface temperatures, until the computed surface temperatures agree with the assumed surface temperatures to within 0.5 K. The initial surface temperatures of 320 K is assumed to start the computation. The converged values of the average film coefficients are listed in the table, where the prime symbol indicates the opposing surface on the other side of the device. These values are different from those obtained from TRM because the computed surface temperatures from the two approaches are different. For surface 2, the heat dissipation rate of -300 W/m^2 is used and thermal insulation (zero heat flux) is assumed on surface 4 and 6 to match the conditions used for TRM. The boundary condition of thermal insulation is also used for all surfaces of air.

To compare the 3D results from FEA to the 1D results from the TRM, the distributed temperature computed from FEA is averaged on boundaries between different materials using the surface integral

$$T_S = \frac{1}{A} \iint T ds \quad (317)$$

where T_S is the surface averaged temperature on the boundary and A is the surface area of the boundary.

Table 16: Boundary Conditions for Steady-State Heat Conduction

Boundary	Types	Settings
1	Heat flux	$h = 4.47 \text{ W/m}^2\text{K}$
2	Heat flux*	$q = -300 \text{ W/m}^2$
3	Heat flux	$h = 4.24 \text{ W/m}^2\text{K}$
3'	Heat flux	$h = 4.30 \text{ W/m}^2\text{K}$
4 (both sides)	Insulation	-
5	Heat flux	$h = 4.44 \text{ W/m}^2\text{K}$
5'	Heat flux	$h = 4.52 \text{ W/m}^2\text{K}$
6 (both sides)	Insulation	-
7	Heat flux	$h = 4.95 \text{ W/m}^2\text{K}$
7'	Heat flux	$h = 5.56 \text{ W/m}^2\text{K}$
8	Heat flux	$h = 7.35 \text{ W/m}^2\text{K}$
9	Heat flux	$h = 6.75 \text{ W/m}^2\text{K}$
10	Heat flux	$h = 5.05 \text{ W/m}^2\text{K}$
11	Heat flux	$h = 2.53 \text{ W/m}^2\text{K}$

* $T_a = 300 \text{ K}$ for all heat flux boundary conditions except boundary 2.

C.4 Comparative Simulation Results

The TRM is used to analyze the heat transfer characteristics of the LPM motor under the periodic excitation. From the current trajectories shown in Figure 90, the rms currents are 0.744, 3.199 and 2.640 A. The electrical resistance of the windings is 2.97Ω per phase and $T_a = 300 \text{ K}$. Note that some of the motor parameters implemented here may be different from those used in the previous chapters.

The temperature distribution on a cross section and on the surfaces of the LPM using FEA are shown in Figures 92-93. The numerical results from the TRM and FEA are compared in Table 17. Since the node temperatures of the TRM represent the average temperatures of each material on the boundary, the surface averages along the boundaries are calculated from 3D FEA to compare with 1D results from the TRM.

From the table, the overall results from the TRM match well with the surface

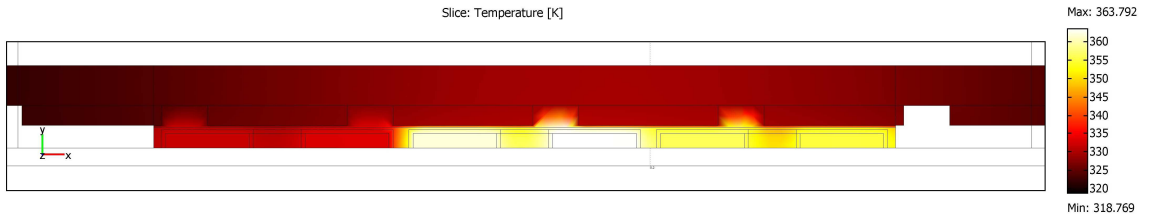


Figure 92: 3D FEA solution on slice located at the center of the coil assembly.

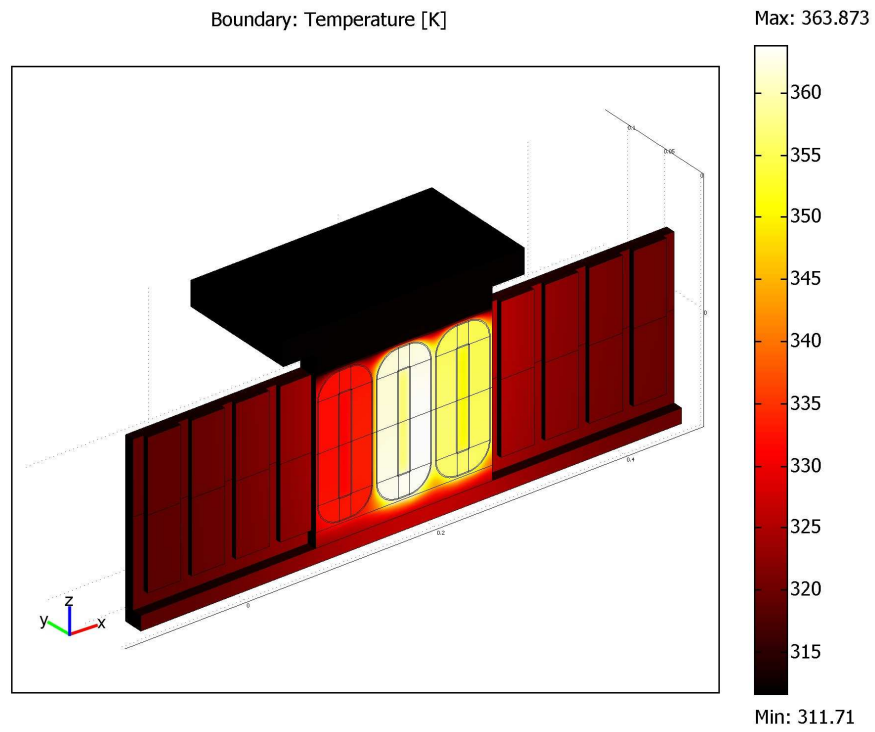


Figure 93: 3D FEA solution on the boundary surfaces.

Table 17: Comparative Thermal Analysis Results, Temperature (K)

Material	Single-node TRM	TRM	3D FEA (surface avg)
Coils (avg)	346.93	346.74	350.39
Phase 1 coil			
Copper-poly./epoxy	-	331.38	332.58
Poly./epoxy-air	-	331.21	332.41
Phase 2 coil			
Copper-poly./epoxy	-	359.27	362.85
Poly./epoxy-air	-	356.14	359.25
Phase 3 coil			
Copper-poly./epoxy	-	349.58	355.72
Poly./epoxy-air	-	347.44	353.29
Payload top surface	-	315.14	311.79
Back iron (outside)	-	323.02	323.32

average data of the FEA results, with the maximum temperature discrepancy being around 5 degrees. Because of the short-stroke motion profile, the electrical load is mainly placed on phases 2 and 3, with phase 2 exhibiting slightly higher rms current, which results in higher temperature rise as expected. Most nodal temperatures calculated by the TRM are lower than the results obtained from FEA except for the temperature of the payload, which may result from the exclusion of the mover and payload model in TRM.

The single-node TRM result is compared with the TRM and FEA results using the average temperature of the three coil windings, as shown in Table 17. The single-node TRM result shows great agreement with a slight deviation from the TRM result because of the absence of the steel elements to simplify the thermal circuit. The numerical value of the equivalent thermal resistance of the LPM motor is $R_{eq} = 1.908$ K/W.

The developed TRM gives satisfactory performance in comparison with the heat conduction analysis from FEA. However, to more accurately simulate the device using

FEA, the buoyancy force that influences the air flow in the natural convection must be solved for. This buoyancy force is closely related to the surface temperature of the material, giving rise to a coupled set of Navier-Stokes and the heat equations [75]. Nonetheless, the simple and computationally efficient TRM overall successfully predicts the hot spot of the LPM motor from heat conduction analysis to within 5 degrees, which is the most critical aspect of this study. More motion profiles may be required to further test the accuracy of the proposed TRM.

C.5 Conclusion

The TRM of the LPM motor has been developed assuming one-dimensional heat conduction in the steel, PM and air gap, and radial heat conduction in the windings. The heat convection of the motor structure is estimated using the natural convection correlations. The thermal resistance model predicts the hot spot to within 5 degrees and the average coil temperature to within 5 degrees.

The single-node TRM is also developed to determine the equivalent thermal resistance of the LPM motor when it is regarded as a homogeneous body. The resulting temperature of the single-node TRM agrees with the average temperature of the three coil windings obtained from both multi-node TRM and FEA. Future improvements may include the thermal contact resistance between different materials and a more elaborate FEA which involves the solving of coupled Navier-Stokes and heat equations for comparison.

APPENDIX D

THERMAL ANALYSIS OF A LVR MOTOR

The preliminary work to develop the thermal resistance model (TRM) of a LVR motor is presented in this appendix. In particular, TRM has been a popular tool for thermal analysis in design and optimization of electric motors for its computational efficiency [71, 72, 73, 74, 3]. The resulting TRM is used to determine the “equivalent” thermal resistance that is required to compare performances between different motor technologies for manufacturing automation applications.

Consider the LVR motor of Figure 94. Because of the open structure, where all materials are exposed to the ambient temperature, heat can transfer in all directions, making thermal modeling quite challenging. Furthermore, the thermal characteristics of the LVR motor are complex due to its mode of operation, i.e. time-varying power dissipation and forced convection induced by motion. Although [3] has investigated related issues for a permanent magnet linear motor, thermal analysis of the LVR motor has not been reported. Since the peak temperature of this device is the major concern in manufacturing automation applications, the continuous periodic mode operation and steady-state temperatures are the main focus in this study.

As a first step, the LVR motor under consideration only operates with continuous periodic excitation and *long-stroke* reciprocating motion, resulting in *forced convection* that helps the cooling (natural convection is small in comparison to the forced convection induced by long-stroke motion). In addition, this allows modeling simplifications based on rms velocity and symmetry. The accuracy of the thermal resistance model is verified by a finite element analysis (FEA) that solves the Heat Equation coupled with the Navier-Stokes Equations. Some materials are repeated here for

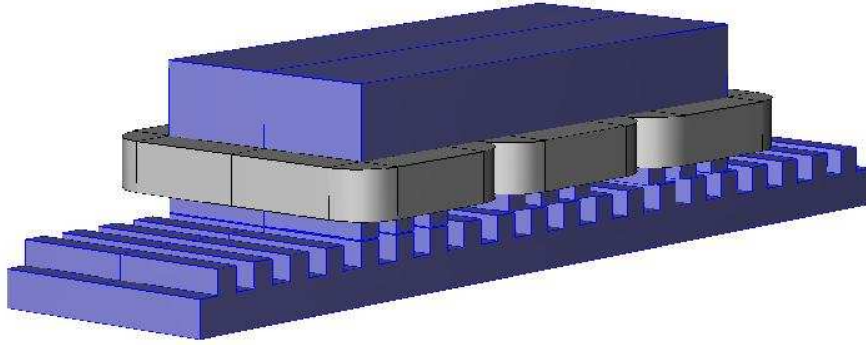


Figure 94: LVR motor (upper half only).

coherence despite previously presented in Appendix C.

D.1 Thermal Resistance Model

The main sources of power loss in electromechanical systems are: (i) copper losses, (ii) iron losses from eddy currents and hysteresis, and (iii) friction losses from mechanical contacts and windage. In this study, only copper losses due to continuous periodic motion are considered.

The primary components in the thermal network are the windings and the steel. Thermal resistances are modeled with the following assumptions to simplify the network:

- The heat generated in the coils is uniformly distributed and conducts in radial directions within cross sectional planes.
- Heat only conducts vertically in steel which results in isothermal layers along the longitudinal direction.
- Heat convection occurs only at certain surfaces exposed to air, depending on dimension and orientation.
- Thermal contact resistance between different materials is negligible.

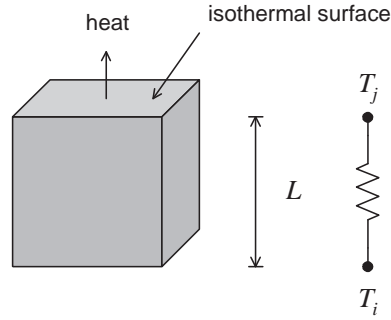


Figure 95: Homogeneous block and equivalent thermal resistance.

D.1.1 Homogeneous Material

A homogeneous material experiencing heat conduction in one direction has thermal resistance

$$R = \frac{1}{k} \int \frac{dx}{A(x)} \quad (318)$$

where k is the thermal conductivity and A is the cross section area normal to the heat flow direction x . For a block of homogeneous material as shown in Figure 95, with constant area and vertical heat flow, the thermal resistance is thus

$$R = \frac{L}{kA} \quad (319)$$

where L is the length of the block. Although this model assumes isothermal surfaces normal to the direction of heat flow, it greatly simplifies the network topology and can reasonably predict hot spots of the motor. Homogeneous regions of steel and air gap may be modeled in this way.

D.1.2 Windings

The windings are constructed from multiple turns of wire that has a copper core surrounded by electrical insulation (polyurethane, polyester, aluminum oxide, etc.) and coated with adhesive material (epoxy, polyester, etc.). When these windings are heat treated, the adhesive material bonds the coils for mechanical rigidity. The

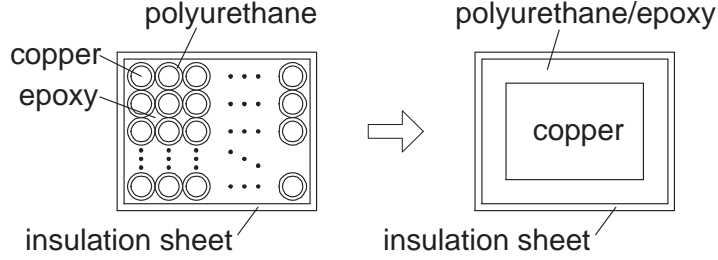


Figure 96: Winding structure and its simplified model.

additional layers of insulation sheet (paper, cotton, etc.) are used to provide surface protection.

Since the copper is uniformly distributed within the winding, the copper cores will be modeled as a single rectangular block with matched cross section area as shown in Figure 96. The layers of electrical insulation (polyurethane) and adhesive material (epoxy) are grouped together into a single layer to simplify the model. The outer-most layer of insulation sheet remains unchanged.

The copper core is modeled as an ideal heat source

$$q = rI_{\text{rms}}^2 \quad (320)$$

where r is the electrical resistance of the copper and I_{rms} is the rms value of the phase current passing through the coil during one operational period. Since the phase currents normally vary according to the motion profile and the control system, I_{rms} is calculated from the periodic current profile obtained by dynamic simulation. Heat capacitance is not needed when modeling the heat source because only steady-state temperatures are considered.

The remaining layers of polyurethane/epoxy and insulation sheet are modeled as one-dimensional thermal resistances using the structure shown in Figure 97. From (318), this leads to

$$R = \frac{L \ln(D_o/D_i)}{kw(D_o - D_i)}, \quad D_o \neq D_i \quad (321)$$

where L , D_o , D_i and w are defined in the diagram.

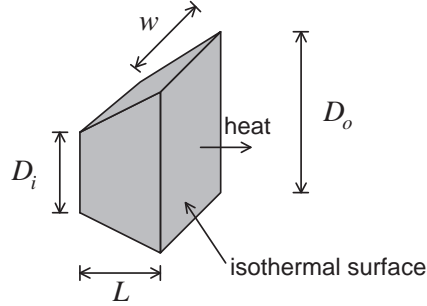


Figure 97: Homogeneous layer of winding material.

D.1.3 Convective Heat Transfer

Convective heat transfer occurs where motor surfaces are exposed to air. For the LVR motor, convective heat transfer takes place throughout the entire structure and helps the cooling. This convection occurs through thermal resistance

$$R = \frac{1}{hA} \quad (322)$$

where h is the average film coefficient of the particular surface and A is the surface area exposed to the cooling air. The average film coefficient is conventionally obtained from the Nusselt number

$$\text{Nu}_L = \frac{hL}{k} \quad (323)$$

where L is the characteristic length. The Nusselt number is geometry dependent and can be obtained experimentally or by solving the boundary layer equations.

Since the LVR motor operates with continuous periodic motion, only forced convection due to relative air flow is considered. To simplify the relative periodic fluid flow dynamic, the inflow air velocity is assumed to be constant in one direction toward surface 4 of the structure shown in Figure 98, and equal to the rms motor velocity (i.e. the constant velocity that yields identical kinetic energy over one period). On average, half of the motor would experience this airflow, and structural symmetry is imposed as shown by the dashed line.

As an approximation, the air flow over surface 1 in Figure 98 will be modeled as a

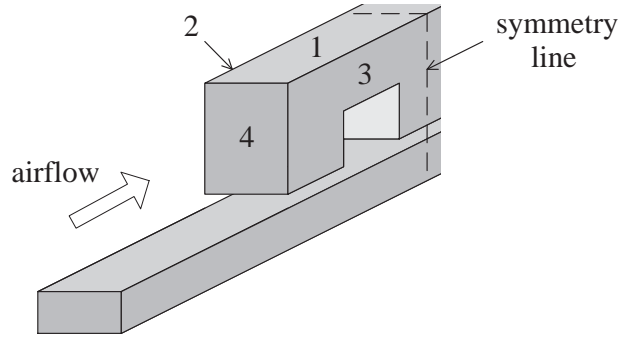


Figure 98: Airflow over the simplified LVR motor structure.

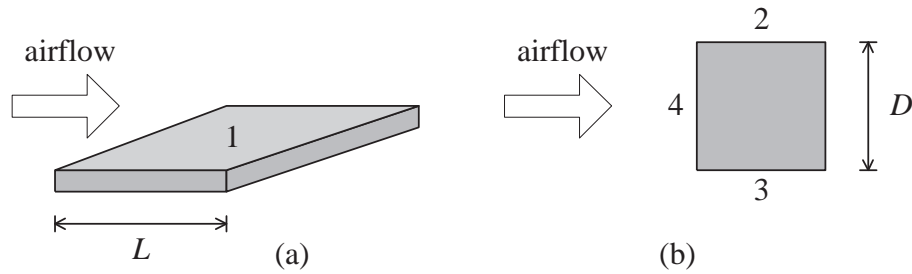


Figure 99: Airflow over (a) a flat surface and (b) a noncircular cylinder.

flow over a flat surface as shown in Figure 99(a). The correlation for calculating the average heat transfer coefficient is given by [75]

$$\text{Nu}_L = 0.664 \text{Re}_L^{\frac{1}{2}} \text{Pr}^{\frac{1}{3}} \quad (324)$$

where the Reynolds and Prandtl numbers are given by

$$\text{Re}_L = \frac{uL}{\nu}, \quad \text{Pr} = \frac{\nu}{\alpha} \quad (325)$$

where u is the upstream air velocity, L is the length along the flat surface, ν is the kinematic viscosity of air and α is the thermal diffusivity of air. Air flow over surfaces 2, 3, and 4 in Figure 98 will be modeled as a cross flow over a noncircular cylinder as shown in Figure 99(b), and the correlation for calculating the average heat transfer coefficient is given by [78]

$$\text{Nu}_D = \frac{hD}{k} = 0.16 \text{Re}_D^{0.699} \quad (326)$$

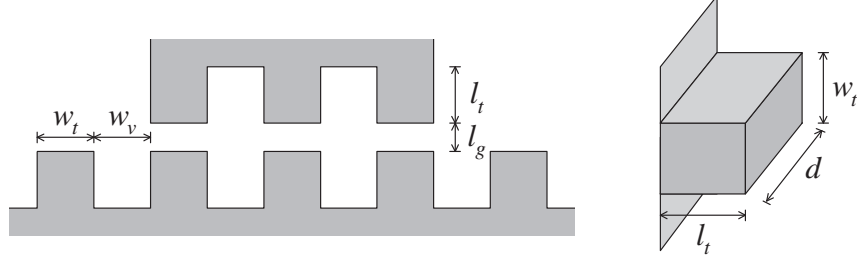


Figure 100: Teeth of the LVR motor having a fin-like structure.

where D is the equivalent diameter. From Figure 98, D is the depth (thickness) of the motor measured horizontally along surface 4. All air-related coefficients are evaluated at the film temperature (average of the surface(s) and ambient temperature).

D.1.4 Toothed Structure

The toothed structures of the LVR motor are fin-like structures, with thermal resistance calculated by [75]

$$R = \frac{1}{\eta_o h A_f} \quad (327)$$

where

$$\begin{aligned} \eta_o &= 1 - \frac{N A_f}{A_t} (1 - \eta_f) \\ \eta_f &= \tanh(m L_c) / m L_c \\ L_c &= l_t + w_t / 2 \\ A_f &= 2 d L_c \\ A_t &= N A_f + A_b \\ m &= \sqrt{h(2d + 2w_t) / k d w_t} \end{aligned} \quad (328)$$

where h is the previously discussed average film coefficient, N is the number of fins, A_b is the surface area of the fin base, d is the device depth, and the dimension parameters w_t , w_v and l_t are shown in Figure 100. For this particular tooth structure, $A_b = (N - 1) d w_v$, where $N = 3$ for the translator and $N = 35$ for the stator. The stator is modeled as a single node and symmetry is imposed along its center.

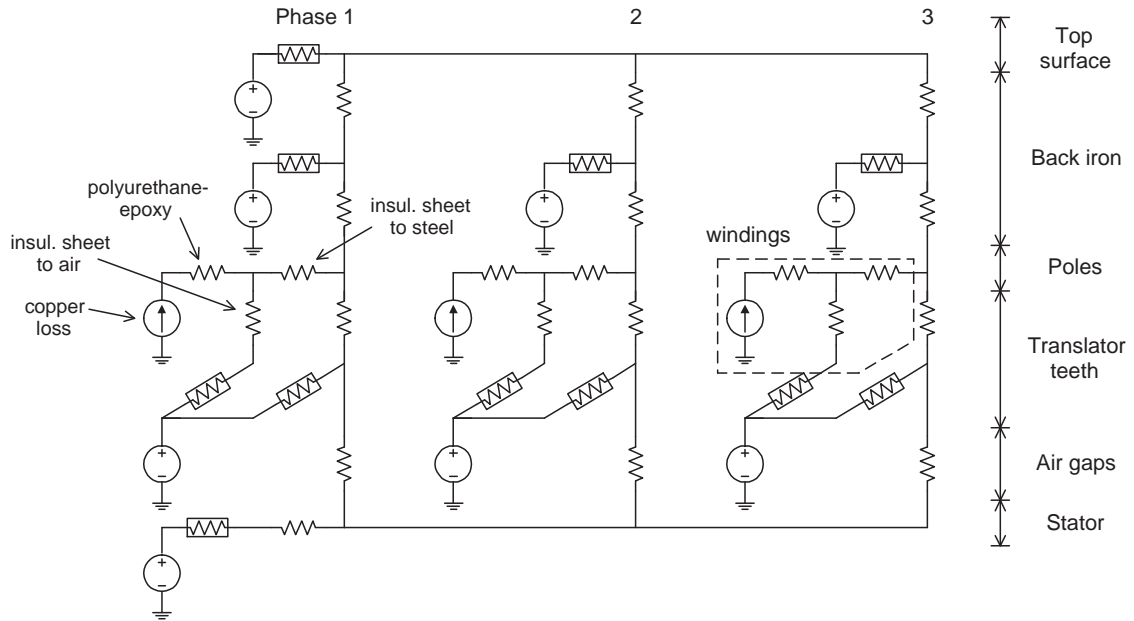


Figure 101: Thermal resistance model of the LVR motor for steady-state heat transfer analysis.

D.1.5 Thermal Network Topology

The complete thermal resistance model of the LVR motor is shown in Figure 101. Nodal temperatures within the windings correspond to the interface between two adjacent materials. Copper losses are represented by current sources whereas the ambient temperature is represented by voltage sources. The heat conduction through homogeneous materials is represented by linear resistors whereas the forced convection to the ambient temperature is represented by nonlinear resistors due to their surface temperature dependence.

According to the model, heat generated by copper losses is conducted through the polyurethane/epoxy layer to the insulation sheet layer. The heat is then transferred either to the steel or to the air. Perfect thermal contact between the insulation sheet and the steel is assumed so that both materials share the same temperature at steady-state. Heat that is transferred to steel is conducted upward to air via the top surface and the sides of the back iron. The remaining heat is conducted downward passing

Table 18: Material Properties

Material	k (W/m K)	ρ (kg/m ³)	C_p (J/kg K)
Copper	385	8900	380
Polyurethane	0.216	1300	1800
Epoxy	0.8	1800	900
Insul. sheet	0.18	930	1340
Silicon steel	66.1	7800	434

Table 19: Motor Parameters

Parameter	Symbol	Value
Device depth	d	50 mm
Tooth width	w_t	5 mm
Valley width	w_v	5 mm
Tooth pitch	p_t	10 mm
Pole pitch	p_p	$\frac{130}{3}$ mm
Tooth length	l_t	5 mm
Pole length	l_p	10 mm
Back length	l_b	15 mm
Stator length	l_s	15 mm
Air gap length	l_g	$\frac{1}{4}$ mm
Teeth per pole	n_t	3
Number of turns	N	200
Wire size (AWG)	w	21
Poly./epoxy thickness	-	0.5 mm
Insul. sheet thickness	-	0.25 mm

the air gap to the stator.

The average film coefficient associated with the top surface is calculated using the surface temperature of surface 1 in Figure 98. The surface temperatures of surface 2, 3 and 4, used for the average film coefficient calculation, are obtained by averaging multiple associated nodal temperatures. Parameters used to compute thermal resistances are listed in Tables 18-19. For the combined polyurethane/epoxy layer, the material properties are averaged.

D.2 Steady-State Thermal Analysis

At steady state, the temperature rise due to copper loss directly relates to the periodic currents passing through the copper coils as well as the convective coefficients that characterize cooling. Therefore, steady-state thermal analysis using the thermal network model requires knowledge of rms current I_{rms} in (320), and rms air velocity u_{rms} for calculating the convective coefficients from (324) and (326). Both I_{rms} and u_{rms} , however, depend on the control system and the motion profile in a complex way. For example, an aggressive motion profile demands larger force and hence larger copper loss, but this also results in larger velocity and hence larger cooling effect. Dynamic simulation is needed to proceed.

D.2.1 Control System for Periodic Motion

The control system considered in this paper is suitable for position control with periodic motion trajectories. It is based on the dq theory of classical synchronous reluctance motors, and it makes use of sinusoidal reluctance and ideal material approximations [79].

The phase voltages are proportional to measured current errors, i.e.

$$v_j = k_i(i_j^d - i_j) \quad (329)$$

where i_j^d is the desired phase current and k_i is a positive feedback gain. The desired phase currents are chosen according to the commutation strategy

$$\begin{bmatrix} i_1^d \\ i_2^d \\ i_3^d \end{bmatrix} = \sqrt{\frac{|F^d|}{\gamma}} \begin{bmatrix} \cos x_1 & -\sin x_1 \\ \cos x_2 & -\sin x_2 \\ \cos x_3 & -\sin x_3 \end{bmatrix} \begin{bmatrix} 1 \\ \text{sgn}(F^d) \end{bmatrix} \quad (330)$$

where F^d is the desired force,

$$x_j = \frac{\pi}{p_t} x + (j - 1) \frac{2\pi}{3} \quad (331)$$

is the electrical position of phase j ,

$$\gamma = \frac{3\pi}{2p_t}(L_d - L_q) \quad (332)$$

is a force constant, p_t is the tooth pitch, and L_d and L_q are constant inductances discussed in [79]. The desired force is chosen according to

$$F^d = Bu + M(\ddot{x}^d + k_d(\dot{x}^d - u) + k_p(x^d - x)) \quad (333)$$

where B is the viscous friction coefficient, u is the motor velocity, M is the moving mass, $(x^d, \dot{x}^d, \ddot{x}^d)$ is the desired trajectory and (k_p, k_d) are positive feedback gains. The implementation of this control algorithm and simulation examples are further discussed in [80].

D.2.2 Linear Motor Operational Profile

Consider the “s-curve” motion profile shown in Figure 102. This motion profile is typically specified by choosing feasible values of maximum jerk j_{\max} , maximum acceleration a_{\max} , maximum velocity u_{\max} , desired displacement X^d and optional dwell time t_d . The desired periodic trajectory x^d considered here is obtained by combining two s-curve motion profiles for position: $0 \rightarrow X^d$ and $X^d \rightarrow 0$. With the use of control software described earlier and the pre-specified motion profile, the steady-state periodic response, and hence the values of I_{rms} and u_{rms} , can be obtained from dynamic simulation.

The dynamic response of the LVR motor is shown in Figure 103 for the choice $j_{\max} = 300 \text{ m/s}^3$, $a_{\max} = 15 \text{ m/s}^2$, $u_{\max} = 1.25 \text{ m/s}$, $X^d = 200 \text{ mm}$, $t_d = 0.1 \text{ s}$, $(k_p, k_d) = (6400, 160)$, and the remaining simulation parameters found in [80]. Notice that the rms values of the three phase currents are practically identical because of the long-stroke periodic motion profile used. This will allow further use of symmetry when FEA is employed to validate the results. For thermal analysis, the effect of periodic motion may be approximated by uniform one-directional airflow, with airflow

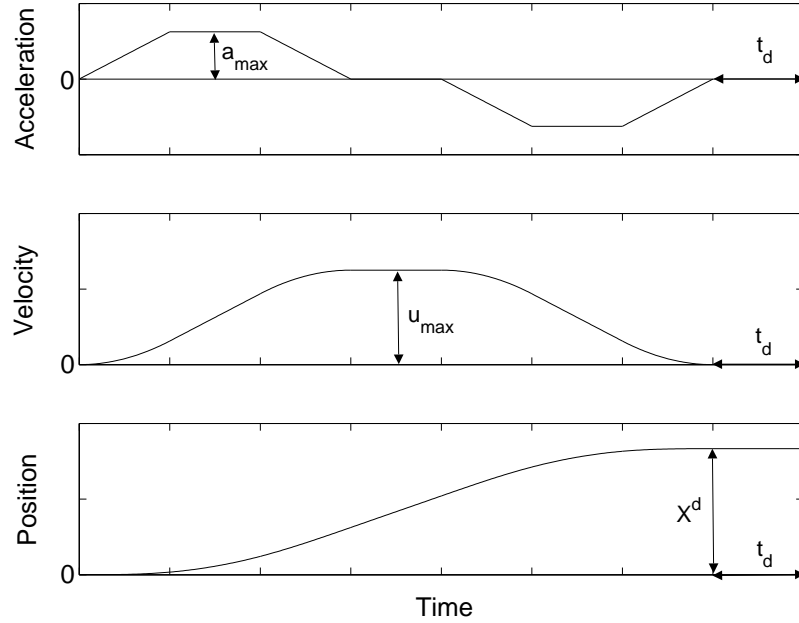


Figure 102: Motion profile using an s-curve.

velocity taken equal to the rms motor velocity obtained through dynamic simulation. This subsequently reduces the periodic transient thermal analysis problem coupled with electrical and mechanical dynamics to the much simpler steady-state thermal analysis problem with constant airflow. Since the thermal time constant is usually several orders of magnitude larger than the electrical and mechanical time constants, thermal analysis can proceed independently after the values of I_{rms} and u_{rms} are known.

D.2.3 Implementation

Since the average film coefficients depend on surface temperatures, certain thermal resistances in Figure 101 are nonlinear. Consequently, nodal analysis of the TRM involves iteration. Iteration is initiated by assuming all convective surfaces have temperature 320 K. Under this assumption, the set of nodal equations for Figure 101 will take a linear form

$$Ax = b \tag{334}$$

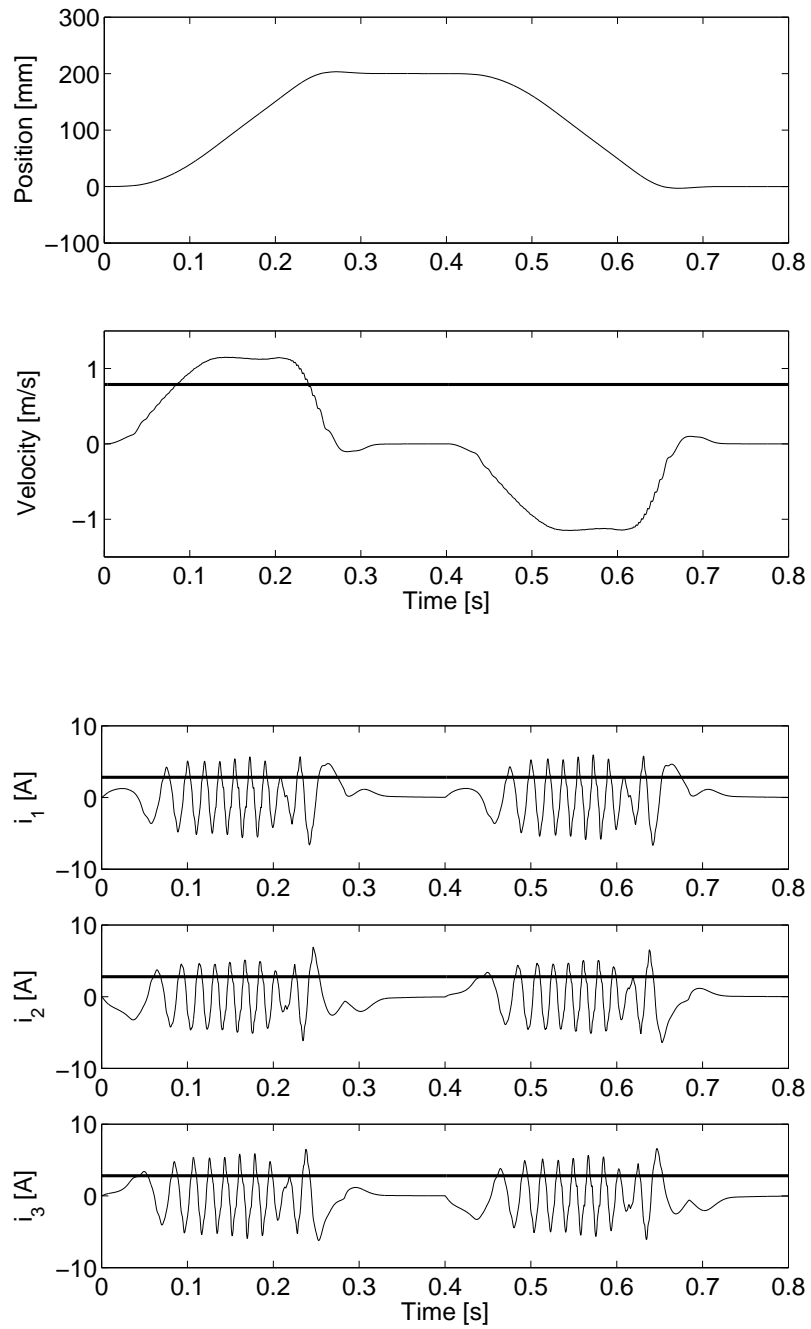


Figure 103: Dynamic response during one operating period of 0.8 s, with rms velocity and rms currents superimposed.

where A is a matrix of thermal resistances, x is a vector of nodal temperatures, and b is a vector of heat sources, i.e. the copper losses. This set of linear equations is solved to determine all nodal temperatures. The computed temperatures for the convective surfaces are used to update (334), and the process is repeated until the assumed and computed convective surface temperatures agree to within 0.5 K.

D.2.4 Single-Node Thermal Resistance Model

The single-node TRM, where the motor is regarded as a homogeneous body, can be derived from the existing TRM using simplifying assumptions and circuit reduction, as illustrated in Figure 104. First, the steel elements are replaced by short circuits because metal is usually a much better heat conducting material. Notice that all non-linear elements become linear once the TRM is solved through the iterative process. Then the network topology is reconfigured into a fewer number of lumped elements in Figures 104(b)-(c), where within each node group: (1,2,3), (4,5,6) and (7,8,9,) they are assumed to have the same nodal temperature.

Through circuit analysis of Figure 104(c), the hot spot temperature T_h of the LVR motor is determined to be

$$T_h = T_a + R_{\text{eq}} \sum_j^3 q_j \quad (335)$$

where q_j is the copper loss of phase j calculated according to (320), and the equivalent thermal resistance R_{eq} is given by

$$R_{\text{eq}} = \frac{1}{3}R_0 + R_1 \quad (336)$$

This is the same thermal resistance mentioned in Section 1.1 of Chapter 1 that is required to transform Watt to Kelvin. Note that both (335) and (3) are consistent.

D.3 Finite Element Analysis

To verify the results from the thermal resistance model, FEA computation is conducted to solve two coupled partial differential equations (PDEs). Solving a system

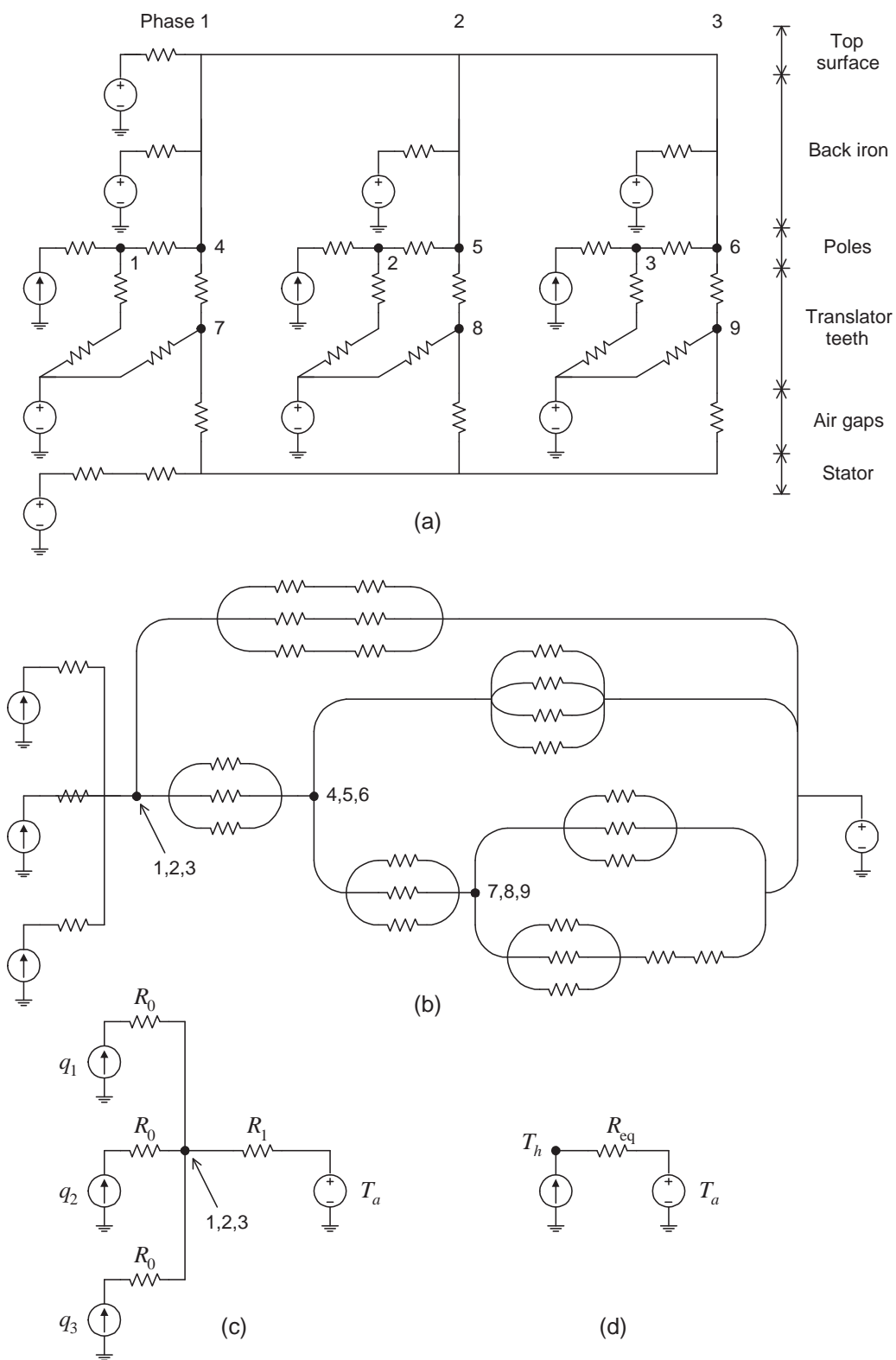


Figure 104: Derivation of the single-node thermal resistance model of the LVR motor: (a) steel is modeled by short circuit, (b) network reconfiguration, (c) simplified network topology and (d) single-node TRM.

of two coupled PDEs is more efficient because the middle step of calculating the convective coefficients from the velocity field solution for use in the heat equation is bypassed. Consequently, this reduces the chance of numerical errors.

D.3.1 PDE Formulation

The steady-state incompressible flow Navier-Stokes equations are given by

$$\begin{aligned} -\mu\nabla^2\mathbf{u} + \rho(\mathbf{u} \cdot \nabla\mathbf{u}) + \nabla p &= 0 \\ \nabla \cdot \mathbf{u} &= 0 \end{aligned} \tag{337}$$

where ρ is the fluid density, μ is the dynamic viscosity, p is pressure, and \mathbf{u} is the velocity field vector. The steady-state heat equation is given by

$$\nabla \cdot (-k\nabla T) = Q - \rho C_p \mathbf{u} \cdot \nabla T \tag{338}$$

where T is the temperature, Q is the heat generation per unit volume, and C_p is the specific heat at constant pressure. The radiation effect is assumed to be negligible because of the small temperature difference between surfaces.

D.3.2 Computational Settings and Post Processing

Computation is performed using the commercial software COMSOL [77], which is capable of solving the coupled equations of (337) and (338) simultaneously in multi-physics mode. When solving the incompressible flow equation, the inflow air velocity is assumed to be constant, and equal to the rms velocity of the motor. Although solving for the fluid flow over a stationary body is different from solving for a moving body through stagnant air, the former problem greatly simplifies the model, and a previous investigation shows good agreement with experimental results [3]. Because of symmetry and periodic motion, the geometry shown in Figures 105-106 is solved in 2D mode with the parameters listed in Tables 18 and 19 and the boundary conditions listed in Table 20. The air flow through the air gap regions is neglected when (338) is solved in order to simplify the model. Although in 2D analysis the end coil is

Table 20: Boundary Conditions for Steady-State Finite Element Analysis

Mode	Boundary	Settings
Incompressible	1	Slip/symmetry
Navier-Stokes	2	Inlet velocity
	3	No-slip
	4	Zero pressure
Convection and Conduction	1	Temperature 300 K
	2	Insulation/symmetry
	3	Convective flux

neglected, the heat source Q has the same value in 2D and 3D analysis. Hence, if the aspect ratio between the depth and width is large, 2D analysis results are reasonably accurate.

To compare the 2D results from FEA to the 1D results from the thermal network model, the distributed temperatures computed from FEA are averaged along boundaries between different materials using the line integral

$$T_l = \frac{1}{L} \int T \, dl \quad (339)$$

where T_l is the line averaged temperature along the boundary, and L is the length of the boundary. In addition, temperatures may also be averaged over the bounded area of each material using the surface integral

$$T_S = \frac{1}{A} \iint T \, ds \quad (340)$$

where A is the area over the integration domain.

D.4 Comparative Simulation Results

The thermal network model is used to analyze the heat transfer characteristics of the LVR motor under periodic excitation. From the dynamic response shown in Figure 103, the rms velocity of the LVR motor is 0.79 m/s, and the rms currents are 2.82, 2.78, and 2.81 A. The electrical resistance of the windings is 1.6 Ω per phase

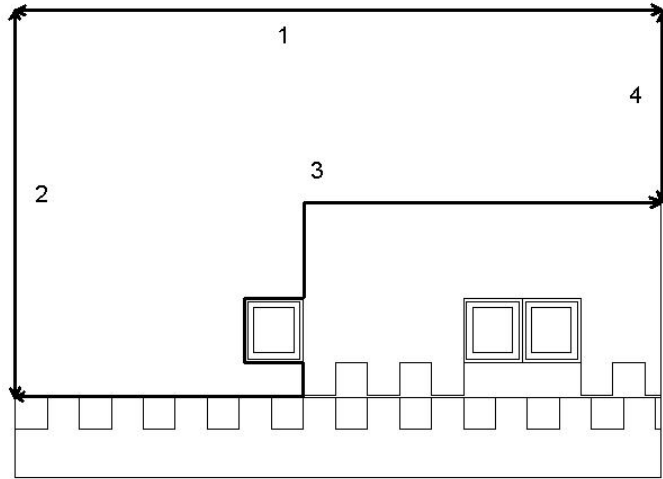


Figure 105: Boundary conditions for solving the steady-state incompressible flow Navier-Stokes equations.

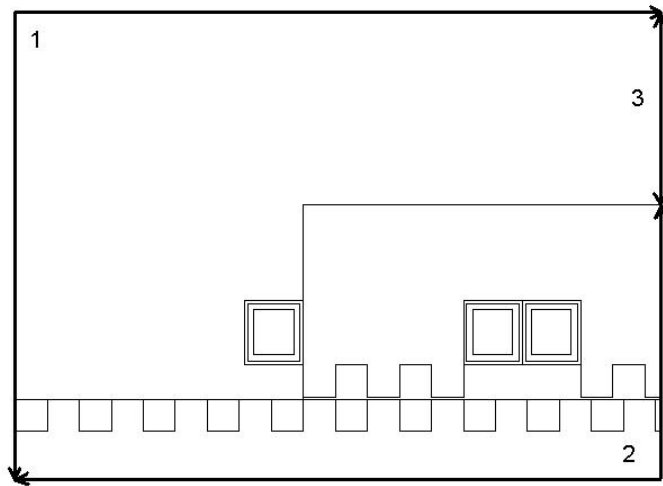


Figure 106: Boundary conditions for solving the steady-state heat transfer equation.

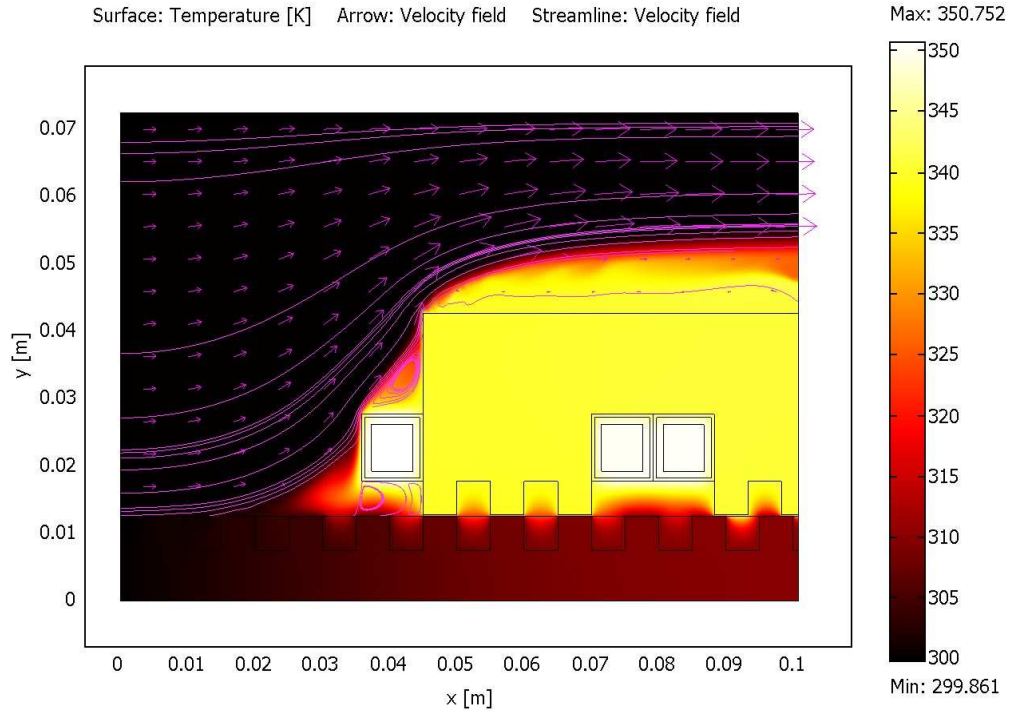


Figure 107: FEA solution of computational fluid dynamics and heat transfer for the LVR motor.

and $T_a = 300$ K. Since the rms values of all three phase currents are very similar (difference is less than 1.5%), symmetry along phase 2 is also imposed in addition to symmetry along the stator bar when FEA is performed. Note that some of the motor parameters implemented here may be different from those used in the previous chapters.

The numerical results from the thermal network model and FEA are listed in Tables 21 and 22. Since the FEA is conducted in the 2D plane, as shown in Figure 107, temperature averaging has been used as described above for direct comparison with the 1D thermal network solution. From these tables, it is clear that the overall results predicted by the thermal network model match well with the averaged FEA results; this makes intuitive sense, because the node temperatures of the thermal network model are intended to represent the average temperatures of each material and region.

Table 21: Comparative Thermal Analysis Results, Temperature (K)

Material	single-node TRM	TRM	2D FEA (line avg)
Coils (avg)	351.26	351.27	350.44
Phase 1 coil (outside)			
Insul. sheet-steel	-	344.19	340.18
Insul. sheet-air	-	346.39	346.61
Epoxy-insul. sheet	-	349.07	348.03
Copper-epoxy	-	351.26	350.74
Phase 1 coil (inside)			
Insul. sheet-steel	-	344.19	340.52
Insul. sheet-air	-	346.39	348.77
Epoxy-insul. sheet	-	349.07	347.56
Copper-epoxy	-	351.26	350.21
Phase 2 coil (inside)			
Insul. sheet-steel	-	344.26	340.87
Insul. sheet-air	-	347.33	348.86
Epoxy-insul. sheet	-	349.11	347.75
Copper-epoxy	-	351.30	350.37
Steel			
Top surface	-	344.03	340.50
Back iron bar	-	344.08*	-
Stator	-	304.95	306.54

* Averaged three nodes.

Table 22: Area Averaged and Maximum Temperature (K) from FEA

Material	2D FEA (area avg)	2D FEA (max)
Phase 1 coil (outside)		
Insul. sheet	346.43	350.30
Epoxy	349.31	350.75
Copper	350.74	350.75
Phase 1 coil (inside)		
Insul. sheet	346.04	350.29
Epoxy	348.82	350.24
Copper	350.23	350.23
Phase 2 coil (inside)		
Insul. sheet	346.24	350.34
Epoxy	348.97	350.39
Copper	350.35	350.39
Steel		
Back iron/pole	343.40	340.90
Stator	308.41	310.19

The node temperatures along the phase one coil are plotted in comparison with the FEA data at $y = 0.02275$ m in Figure 108. The largest temperature difference is at the contact between the insulation sheet and steel. Due to the lack of the third dimension in 2D FEA, the results reported here do not consider the corresponding additional heat source and additional cooling surface area; for that purpose, 3D FEA must be employed.

The node temperatures along the phase one coil are plotted in comparison with the FEA data at $x = 0.0575$ m in Figure 109. The overall temperature predictions are less accurate in steel regions. The discrepancy in the stator temperature is mainly due to the limited length of the stator bar drawn in FEA that results in higher temperature. If the length of the stator bar is extended in the FEA model, its temperature will decrease toward the ambient temperature. Nonetheless, the thermal network model successfully predicts the hot spot of the LVR motor, the most critical aspect of this

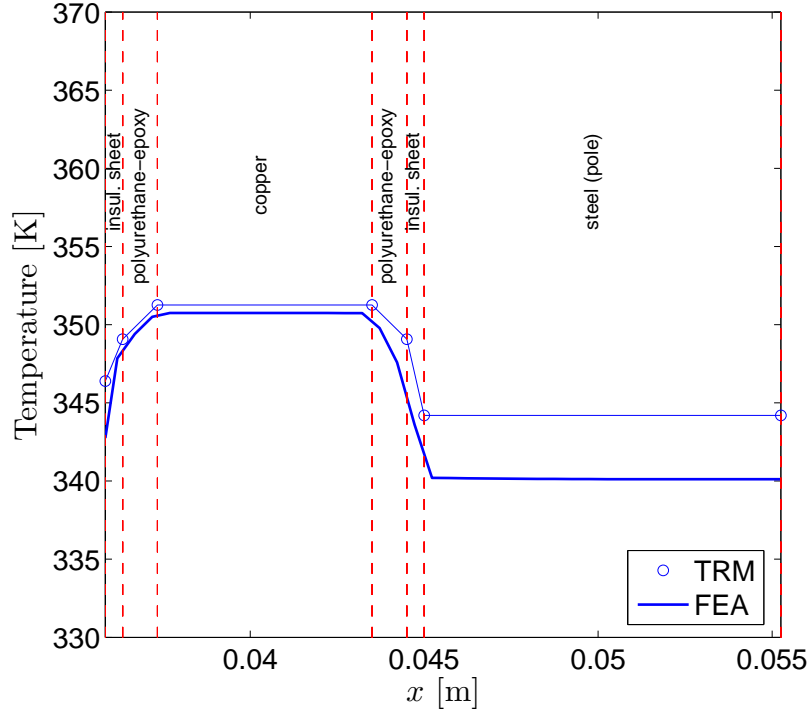


Figure 108: Temperature profile of the LVR motor from thermal network model and FEA results for $y = 0.02275$ m (see Figure 107).

study, within 1 degree.

The single-node TRM result is also compared with the TRM and FEA results using the average temperature of three coil windings, as shown in Tables 21. The single-node TRM result shows great agreement with a slight deviation from the TRM result because of the absence of the steel elements to simplify the thermal circuit. The node grouping also does not greatly affect the average coil temperature because the electrical load is equally distributed among all windings. The numerical value of the equivalent thermal resistance of the LVR motor is $R_{eq} = 2.722$ K/W.

D.5 Conclusion

A thermal resistance model of the LVR motor has been developed assuming one-dimensional heat conduction in the steel and radial heat conduction in the windings. The heat convection of the motor structure is estimated using the rms velocity of

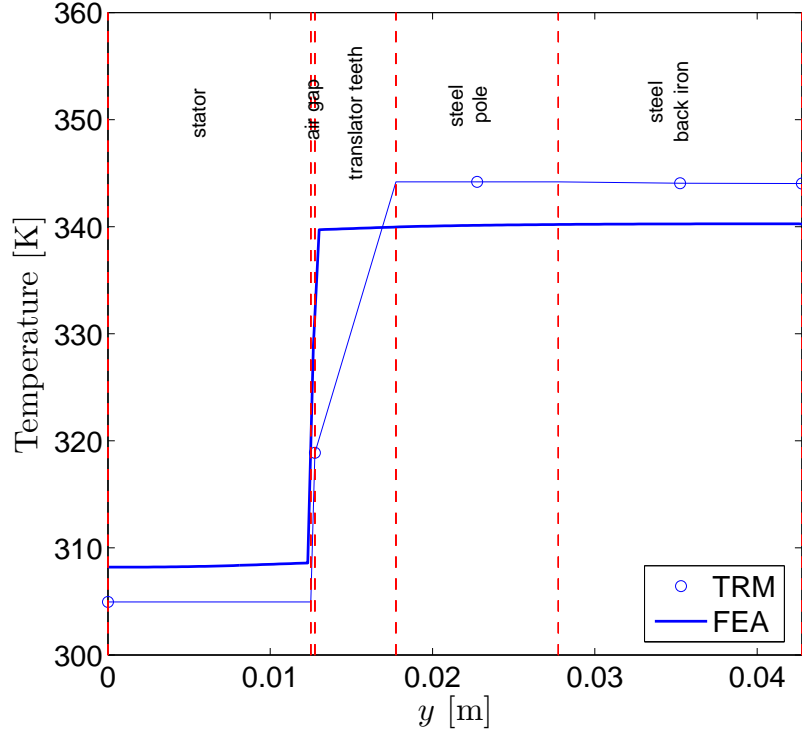


Figure 109: Temperature profile of the LVR motor from thermal network model and FEA results for $x = 0.0575$ m (see Figure 107).

the periodic motion profile. The long-stroke motion results in similar phase current excitations and similar rms currents, further allowing the use of symmetry in the FEA solution. The thermal resistance model predicts the hot spot within 1 degree with a maximum discrepancy of 4 degrees in steel. A 3D FEA could be carried out to obtain a more accurate numerical reference and hence provide more insight for further improvement of the thermal network model.

The equivalent thermal resistance of the LVR motor is calculated by simplifying the existing TRM to obtain the single-node TRM. The hot spot temperature predicted by the single-node TRM corresponds to the average coil temperature from both the TRM and FEA results. However, this development is not yet complete because only long-stroke motion is considered in this study. Future improvements may consider short-stroke motion that requires natural convection for cooling and inclusion of the thermal contact resistance between different materials.

REFERENCES

- [1] I. Boldea and S. A. Nasar, *Linear Electric Actuators and Generators*. Cambridge, UK: Cambridge University Press, 1997.
- [2] J. F. Gieras and Z. J. Piech, *Linear Synchronous Motors: Transportation and Automation Systems*. Boca Raton, FL: CRC Press, 1999.
- [3] C. Jang, J. Y. Kim, Y. J. Kim and J. O. Kim, “Heat transfer analysis and simplified thermal resistance modeling of linear motor driven stages for SMT application,” *IEEE Transactions on Components and Packaging Technologies*, vol. 26, no. 3, pp. 532–540, 2003.
- [4] W. Leonhard, *Control of Electrical Drives*, 2nd edition, New York, NY: Springer, 1997.
- [5] T. J. E. Miller, *Brushless Permanent-Magnet and Reluctance Motor Drives*. NY: Oxford University Press, 1989.
- [6] D. C. Hanselman, *Brushless Permanent-Magnet Motor Design*. NY: McGraw-Hill, 1994.
- [7] T. J. E. Miller, *Switched Reluctance Motors and their Control*. NY: Oxford University Press, 1993.
- [8] B. A. Sawyer, “Actuating system,” United States Patent 3,857,078, December 24, 1974.
- [9] T. M. Jahns, G. B. Kliman and T. W. Neumann, “Interior permanent-magnet synchronous motors,” *IEEE Transactions on Industry Applications*, vol. 22, no. 4, pp. 738–747, 1986.
- [10] M. Sanada, S. Morimoto and Y. Takeda, “Interior permanent magnet linear synchronous motor for high-performance drives,” *IEEE Transactions on Industry Applications*, vol. 33, no. 4, pp. 966–972, 1997.
- [11] H. D. Chai, *Electromechanical Motion Devices*. Upper Saddle River, NJ: Prentice Hall, 1998.
- [12] J. Cros and P. Viarouge, “Synthesis of high performance PM motors with concentrated windings,” *IEEE Transactions on Energy Conversion*, vol. 17, no. 2, pp. 248–253, 2002.

- [13] F. Magnussen and C. Sadarangani, "Windings factor on Joule losses of permanent magnet machines with concentrated windings," *Proceedings of IEEE International Electric Machines and Drives Conference*, Madison, WI, pp. 333–339, June 2003.
- [14] W. Wrobel and P. H. Mellor, "Design considerations of a direct drive brushless PM machine with concentrated windings," *Proceedings of IEEE International Electric Machines and Drives Conference*, San Antonio, TX, pp. 655–658, May 2005.
- [15] J. A. Reyer and P. Y. Papalambros, "Combined optimal design and control with application to an electric DC motor," *Journal of Mechanical Design*, vol. 124, no. 2, pp. 183–191, 2002.
- [16] M. Kim and S. Chung, "Integrated design methodology of ball-screw driven servomechanisms with discrete controllers. Part I: Modeling and performance analysis," *Mechatronics*, , vol. 16, no. 8, pp. 491–502, 2006.
- [17] M. Kim and S. Chung, "Integrated design methodology of ball-screw driven servomechanisms with discrete controllers. Part II: Formulation and synthesis of the integrated design," *Mechatronics*, , vol. 16, no. 8, pp. 503–512, 2006.
- [18] S. J. Salon, *Finite element analysis of electrical machines*. Boston, MA: Kluwer Academic Publishers, 1995.
- [19] P. P. Silvester and R. L. Ferrari, *Finite Elements for Electrical Engineers*, Third Edition. New York, NY: Cambridge University Press, 1996.
- [20] V. Ostović, *Dynamics of Saturated Electric Machines*. New York, NY: Springer-Verlag, 1989.
- [21] M. Cheng, K. T. Chau, C. C. Chan, E. Zhou and X. Huang, "Nonlinear varying-network magnetic circuit analysis for doubly salient permanent-magnet motors," *IEEE Transactions on Magnetics*, vol. 36, no. 1, pp. 339–348, 2000.
- [22] Y. Kano, T. Kosaka and N. Matsui, "Simple nonlinear magnetic analysis for permanent-magnet motors," *IEEE Transactions on Industry Applications*, vol. 41, no. 5, pp. 1205–1214, 2005.
- [23] J. M. Kokernak and D. A. Torrey, "Magnetic circuit model for the mutually coupled switched-reluctance machine," *IEEE Transactions on Magnetics*, vol. 36, no. 2, pp. 500–507, 2000.
- [24] V. Vujčić and S. N. Vukosavić, "A simple nonlinear model of the switched reluctance motor," *IEEE Transactions on Energy Conversion*, vol. 15, no. 4, pp. 395–400, 2000.

- [25] G. Kang, J. Hong and G. Kim, "Design and analysis of slotless-type permanent-magnet linear brushless motor by using equivalent magnetizing current," *IEEE Transaction on Industry Applications*, vol. 37, no. 5, pp. 1241–1247, 2001.
- [26] J. P. Pawletko and H. D. Chai, "Linear step motors," *Proceedings of the 2nd Annual Symposium on Incremental Motion Control Systems and Devices*, Urbana-Champaign, IL, pp. V1–V11, April 1973.
- [27] D. G. Taylor and R. Ahmed, "Analysis of a linear variable reluctance motor with magnetically coupled phases," *Proceedings of the 34th IEEE Southeastern Symposium on System Theory*, Huntsville, AL, pp. 219–223, March 2002.
- [28] D. G. Taylor and R. Ahmed, "Modeling linear variable reluctance motors by finite element analysis and least squares methods," *Proceedings of the IASTED International Conference on Applied Simulation and Modeling*, Crete, Greece, pp. 633–637, June 2002.
- [29] M. Athans and P. L. Falb, *Optimal Control*. New York: McGraw Hill, 1966.
- [30] A. E. Bryson and Y. C. Ho, *Applied Optimal Control*. Washington, DC: Hemisphere, 1975.
- [31] Y. O. Kim and I. J. Ha, "Time-optimal control of a single-DOF mechanical system considering actuator dynamics," *IEEE Transaction on Control Systems Technology*, vol. 11, no. 6, pp. 919–932, 2003.
- [32] S. Ma, "Time-optimal control of robotic manipulators with limit heat characteristics of the actuator," *Advanced Robotics*, vol. 16, no. 4, pp. 309–324, 2002.
- [33] T. Teramoto, K. Ono and O. Turhan, "High-speed motion control of mechanisms under average heat generation restriction," *JSME International Journal—Series C, Dynamics, Control, Robotics, Design and Manufacturing*, vol. 37, no. 2, pp. 315–321, 1994.
- [34] E. S. Sergaki, G. S. Stavrakakis and A. D. Pouliezios, "Optimal robot speed trajectory by minimization of the actuator motor electromechanical losses," *Journal of Intelligent and Robotic Systems*, vol. 33, no. 2, pp. 187–207, 2002.
- [35] D. G. Taylor and R. Ahmed, "Current limited optimal excitation of magnetically coupled linear variable reluctance motors," *Proceedings of International Electric Machines and Drives Conference*, Madison, WI, pp. 857–860, June 2003.
- [36] A. Gray, *Electrical Machine Design: The Design and Specification of Direct and Alternating Current Machinery*. NY: McGraw-Hill, 1913.
- [37] C. G. Veinott, *Computer-Aided Design of Electric Machinery*. Cambridge, MA: MIT Press, 1972.

- [38] D. A. Lowther and P. P. Silvester, *Computer-Aided Design in Magnetics*. NY: Springer-Verlag, 1986.
- [39] R. Krishnan, A. S. Bharadwaj and P. N. Materu, "Computer-aided design of electrical machines for variable speed applications," *IEEE Transactions on Industrial Electronics*, vol. 35, no. 4, pp. 560–571, 1988.
- [40] T. J. E. Miller and M. McGilp, "Nonlinear theory of the switched reluctance motor for rapid computer aided design," *IEE Proceedings B*, vol. 137, no. 6, pp. 337–347, 1990.
- [41] D. G. Luenberger, *Linear and Nonlinear Programming*, 2nd edition. Reading, MA: Addison-Wesley, 1984.
- [42] K. Deb, *Multi-Objective Optimization Using Evolutionary Algorithms*. England: John Wiley & Sons, 2001.
- [43] O. W. Anderson, "Optimal design of electrical machines," *IEEE Transactions on Power Apparatus and Systems*, vol. 30, no. 6, pp. 707–711, 1967.
- [44] A. P. Engelbrecht, *Fundamentals of Computational Swarm Intelligence*. England: John Wiley & Sons, 2005.
- [45] J. A. Moses, J. L. Kirtley, J. H. Lang, R. D. Tabors and F. de Cuadra García, "A computer-based design assistant for induction motors," *Conference Record of IEEE Industry Applications Society Annual Meeting*, Dearborn, MI, pp. 1-7, October 1991. Revision published in *IEEE Transactions on Industry Applications*, vol. 30, no. 6, pp. 1616–1624, 1994.
- [46] C. L. Tucci, J. H. Lang, R. D. Tabors and J. L. Kirtley, "A simulator of the manufacturing of induction motors," *Conference Record of IEEE Industry Applications Society Annual Meeting*, Dearborn, MI, pp. 1353-1358, October 1991. Revision published in *IEEE Transactions on Industry Applications*, vol. 30, no. 3, pp. 578-584, 1994.
- [47] D. E. Cameron, J. H. Lang and D. Belanger, "The computer-aided design of variable-reluctance generators," *Proceedings of IEEE Applied Power Electronics Conference*, Boston, MA, pp. 114–120, February 1992.
- [48] D. A. Torrey and M. Hassanin, "The design of low-speed variable-reluctance generators," *Conference Record of IEEE Industry Applications Society Annual Meeting*, Orlando, FL, vol. 1, p1. 1, pp. 427–433, October 1995.
- [49] S. D. Sudhoff, J. Cale, B. Cassimere and M. Swinney, "Genetic algorithm based design of a permanent magnet synchronous machine," *Proceedings of IEEE International Electric Machines and Drives Conference*, San Antonio, TX, pp. 1011–1019, May 2005.

- [50] D. Cho, J. Kim, H. Jung and C. Lee, "Optimal design of permanent-magnet motor using autotuning niching genetic algorithm," *IEEE Transactions on Magnetics*, vol. 39, no. 3, pp. 1265–1268, 2006.
- [51] S. Vaez-Zadeh and A. H. Isfahani, "Multiobjective design optimization of air-core linear permanent-magnet synchronous motors for improved thrust and low magnet consumption," *IEEE Transactions on Magnetics*, vol. 42, no. 3, pp. 446–452, 2006.
- [52] B. Mirzaeian, M. Moallem, V. Tahani and C. Lucas, "Multiobjective optimization method based on a genetic algorithm for switched reluctance motor design," *IEEE Transactions on Magnetics*, vol. 38, no. 3, pp. 1524–1527, 2002.
- [53] T. Kosaka, C. Pollock, T. Shikayama, T. Nakagami, Y. Kano and N. Matsui, "Ga-based computer aided autonomous electromagnetic design of switch reluctance servomotor drives," *Conference Record of the 2004 Industry Applications Conference, 39th IAS Annual Meeting*, Seattle, WA, pp. 416–423, October 2004.
- [54] M. Hortman, N. Chayopitak and D. G. Taylor, "Multi-objective optimal design of linear variable reluctance motors using genetic algorithms," *Proceedings of International Conference on Electrical Machines*, Chania, Crete Island, Greece, pp. 410:1-6, September 2006.
- [55] G. Q. Bao, D. Zhang, J. H. Shi and J. Z. Jiang, "Optimal design for cogging torque reduction of transverse flux permanent motor using particle swarm optimization algorithm," *Proceedings of International Power Electronics and Motion Control Conference*, Xi'an, China, pp. 260-263, 2005.
- [56] N. Chayopitak and D. G. Taylor, "Nonlinear magnetic circuit model of a linear variable reluctance motor," *Proceedings of the 36th Southeastern Symposium on System Theory*, Atlanta, GA, pp. 170–174, March 2004.
- [57] N. Chayopitak and D. G. Taylor, "Thermal analysis of linear variable reluctance motor for manufacturing automation applications," *Proceedings of IEEE International Electric Machines and Drives Conference*, San Antonio, TX, pp. 866–873, May 2005.
- [58] N. Chayopitak and D. G. Taylor, "Design of linear variable reluctance motor using computer-aided design assistant," *Proceedings of IEEE International Electric Machines and Drives Conference*, San Antonio, TX, pp. 1569–1575, May 2005.
- [59] D. G. Taylor and N. Chayopitak, "Time-optimal position control of electric motors with steady-state temperature constraints," *Proceedings of IEEE International Symposium on Industrial Electronics*, Montreal, Canada, pp. 3142–3146, July 2006.
- [60] N. Chayopitak and D. G. Taylor, "Thermal analysis of a linear permanent-magnet motor with concentrated windings," *Proceedings of the 17th International Conference on Electrical Machines*, Crete, Greece, September 2006.

- [61] N. Chayopitak and D. G. Taylor, "Minimum copper loss position control of linear synchronous motors with current limits," *Proceedings of the 15th Mediterranean Conference on Control and Automation*, Athens, Greece, June 2007 (to appear).
- [62] N. Chayopitak and D. G. Taylor, "Performance assessment of air-core linear permanent-magnet synchronous motors," *Submitted to the 46th IEEE Conference on Decision and Control*, New Orleans, LA, December 2007.
- [63] P. C. Krause, O. Wasynczuk and S. D. Sudhoff, *Analysis of Electric Machinery*, 2nd edition. New York, NY: IEEE Press, 2002.
- [64] D. Kraft, "On converting optimal control problems into nonlinear programming codes," in *Computational Mathematical Programming*, NATO ASI Series, vol. 15, Ed. K. Schittkowski, Germany: Springer, 1985, pp. 261–280.
- [65] R. C. Hargraves and S. W. Paris, "Direct trajectory optimization using nonlinear programming and collocation," *Journal of Guidance, Control and Dynamics*, vol. 10, no. 4, pp. 338–342, 1987.
- [66] O. von Stryk, "Numerical solution of optimal control problems by direct collocation," in *Optimal Control, Calculus of Variations, Optimal Control Theory and Numerical Methods*, ISNM Series, vol. 111, Ed. R. Bulirsch et al., Germany: Birkhäuser Verlag, 1993, pp. 129–143.
- [67] W. H. Hayt, *Engineering Electromagnetics*. New York, NY: McGraw Hill, 1989.
- [68] H. D. Chai, "Permeance model and reluctance force between toothed structures," *Proceedings of the 2nd Annual Symposium on Incremental Motion Control Systems and Devices*, Urbana-Champaign, IL, pp. K1–K12, April 1973.
- [69] C. W. Ho, A. E. Ruehli and P. A. Brennan, "The modified nodal approach to network analysis," *IEEE Transactions on Circuits and Systems*, vol. 22, no. 6, pp. 504–509, 1975.
- [70] J. R. Hendershot and T. J. E. Miller, *Design of brushless permanent-magnet motors*. Hillsboro, OH: Magna Physics Publishing, 1994.
- [71] P. H. Mellor, D. Roberts and D. R. Turner, "Lumped parameter thermal model for electrical machines of TEFC design," *IEE Proceedings-B*, vol. 138, no. 5, pp. 205–218, September 1991.
- [72] J. Faiz, R. Iranpour and P. Pillay, "Thermal model for a switched reluctance motor of TEFC design during steady and transient operation," *Electric Machines and Power Systems*, vol. 26, no. 1, pp. 77–91, 1998.
- [73] A. Boglietti, A. Cavagnino, M. Lazzari and M. Pastorelli, "A simplified thermal model for variable-speed self-cooled industrial induction Motor," *IEEE Transactions on Industry Applications*, vol. 39, no. 4, pp. 945–952, 2003.

- [74] M. F. Momen and I. Husain, "Optimizing the design and performance of a switched reluctance machine using lumped parameter thermal model," *Proceedings of IEEE International Electric Machines and Drives Conference*, vol. 2, pt. 2, pp. 955–961, 2003.
- [75] F. P. Incropera and D. P. DeWitt, *Fundamentals of Heat and Mass Transfer*, 4th edition. NY: John Wiley & Sons, 1996.
- [76] H. Y. Wong, *Handbook of Essential Formulae and Data on Heat Transfer for Engineers*, New York: Longman, 1977.
- [77] Homepage of COMSOL: <http://www.comsol.com/> (date accessed May 2007).
- [78] F. Kreith and M. S. Bohn, *Principles of Heat Transfer*, 5th edition, St. Paul, MN: West Publishing Company, 1993.
- [79] D. G. Taylor and R. Ahmed, "Force control of a linear variable reluctance motor with magnetically coupled phases," *Proceedings of the 34th IEEE Southeastern Symposium on System Theory*, Huntsville, AL, pp. 229–233, March 2002.
- [80] N. Chayopitak and D. G. Taylor, "Dynamic simulation of a linear variable reluctance motor using coupled network models," *Proceedings of the 36th IEEE Southeastern Symposium on System Theory*, Atlanta, GA, pp. 160–164, March 2004.

VITA

Nattapon Chayopitak was born in Chiangrai, a northern province of Thailand on February 9, 1978 and moved to live with his family in Phatthalung, a southern province of Thailand, since 1983. He received a scholarship from the Ministry of Science and Technology of the Thai Government to study abroad in the United States in 1996. In Spring 2001, he finished his B.S. degree in Electrical Engineering from Columbia University, New York and came to Georgia Institute of Technology in the Fall of 2001 to pursue his graduate studies, also in Electrical Engineering.